Limitations to light microscope resolution in biological preparations and methods for enhanced resolution using fabricated microstructures.

Stuart McIntyre

Abstract

Fluorescence imaging has become a vital tool for understanding cardiac cell function. With the advent of calcium-sensitive and fast response voltage-sensitive dyes, it is now possible to gain complex physiological recordings from various cardiac muscle preparations, while simultaneously optically sectioning the samples. However, due to the complexity of these experimental set-ups, it is difficult to set up control samples that allow the user to predict how their sample is affecting the quality of the data being captured.

The aim of this thesis is to assess the strengths and weaknesses of the different types of optical sectioning microscope methods that are currently available in many biological labs. These include confocal, two-photon and selective illumination microscopes . The resolution capabilities of these systems and the associated objective lenses were investigated to determine the optimum conditions for their use. This work includes investigations of the contribution of signal noise and performance of motorised z-stage systems used in these microscope systems to the ability of assess optical resolution..

The optical components of cardiac muscle are investigated individually. This includes the scattering properties of the myocardium and the effects of the refractive index mismatch, as well as the intrinsic fluorescent substances found in cardiac muscle.

Microstructures are used to generate novel ways of overcoming some of the problems faced when imaging cardiac muscle in order to improve the sensitivity and resolution of these systems. Finally, a method is investigated to enhance the the relative concentration of live cardiac:dead cells in after dissociation from intact hearts. This approach would aid the study of isolated cardiac cells be reducing the interference from damaged cells. .

Acknowledgements

I dedicate this thesis to my wife Lanying Zhang and my daughter Jessica Zhang McIntyre, born 12/05/12.


I would like to thank my supervisors Godfrey Smith and Jon Cooper for their help and support.

The following academics from the University of Glasgow:
Norbert Klauke, Francis Burton, Alistair Clarke, Andrew Glidle, Allen Kelly, Iffath Ghouri, Sarah Kettlewell, Martyn Reynolds, Aileen Rankin, Ole Kemi, Johnny Stormonth-Darling, Kamil Rudnicki, All of the JWNC staff, Mike Dunne, David Gillespie, David Patterson and Christopher Syme.

The following people from out with the University of Glasgow:
Brad Amos, Martin Thomas, Gail McConnell, Peter Shaw, Jonathan Woods, Matt Preston, Stephen Fantone and Richard Skilling.

The following people for writing Matlab code and making it publicly available so that I could use as part of my code:
James Blake, Patrick Egan, Phil Larimer, Patrick Pirrotte and Jérôme Mutterer.

Finally I would like to thank my parents.

Index

Figure Legend

Equation Index

Table Index

Abbreviations

AM = Artificial Myocardium

ADC= Analogue to Digital Converter

BSA = Bovine Serum Albumin

CCD = Charged Couple Device

CMOS = Complementary Metal Oxide Semiconductor

Di-4-Anepps = AminoNaphthylEthenylPyridinium,

ECC = Excitation-Contraction Coupling

ECG = Electrocardiogram

EM = Electron Microscope

EMCCD = Electron Multiplying Charge Couple Device

FAD = Flavin Adenine Dinuclotide

FIB = Focus Ion Beam

FPS = Frame Per Second

FWHM = Full Width Half Maximal

ICS = Infinity Colour Corrected System

IPA = Isopropanol

LED = Light Emitting Diode

MTF = Modulation Transfer Function

mW = MilliWatt

NA = Numerical Aperture

NADH = Nicotinaminde Adenine Dinucleotide

NCX = Sodium-Calcium Exchanger

nm = Nanometer

OMX = Optical Microscopy Experimental

PDMS = Polydimethylsiloxane

PMT = Photo Multiplier Tube

PSF = Point Spread Function

QD = Quantum Dot

QE = Quantum Efficiency

RI = Refractive Index

RPM = Revolutions Per Minute

RYR = Ryanodine Receptor

SIMP = Selective Illumination Microscope Prototype

SLM = Spatial Light Modulator

S/N = Signal to Noise Ratio

SR = Sarcoplasmic Reticulum

STED = Stimulated Emission Depletion Microscopy

T-tubule = Transverse Tubule

TMRE = Tetramethylrhodamine Ethyl Ester, Perchlorate

UV = Ultra Violet

W = Watt

μm = Micrometer

λ = Wavelength (Lambda)

3D = Three Dimensions

1.1 Aims

The aim of this thesis is to investigate the detection and resolution characteristics of imaging systems currently in use for fluorescent imaging of physiological events in living specimens, with a particular interest in cardiac muscle. This will involve investigating the resolution capabilities of a variety of imaging systems. This will be done using the following approaches:

1. Calculation of theoretical Point spread function (PSF) and comparison with PSF measurements using confocal laser scanning systems with a range of objectives, and PAM-generated point spread functions.
2. Determination of the optical properties of cardiac muscle in order to establish the effect on image resolution at different tissue depths. This will be achieved by investigating the effects of light scattering and refractive index mismatching on two-photon imaging, in addition to investigating the effects of intrinsic fluorescent dyes on two-photon imaging.
3. Finally, novel methods of high resolution 3-dimensional imaging of cardiac myocytes are attempted with the aid of specifically-designed microstructures in order to improve axial resolution.

Chapter 1: Introduction

Microscopes have been used for many years to reveal detail in biological specimens that is not visible to the human eye. With the advent of fluorescent dyes and labelling, fluorescence microscopy has emerged as a powerful technique for investigating singular aspects of a specimen. It is possible for these systems to optically section specimens, where images are generated from the light that has originated from one plane of the specimen which is normally 1µm thick. Multiple images within a limited depth of the specimen can be taken, in order to build accurate (Three Dimensional) 3D images of the specimen as well as measure fast physiological events. However these imaging systems are not always optimally configured to deliver results close to what is theoretically possible. Therefore it is important to know how the system is configured and what can be causing the sub-optimal performance. As well as thinking of new methods that can be used to circumvent these problems.

1.2 Imaging biological tissue

There are many artefacts that can be generated by current microscope systems. The main areas that biologists are interested in when using optically sectioning microscopes are resolution, speed of capture, field of view and depth of imaging. Resolution is of interest in revealing detailed structures inside cells, and is traditionally limited by the objective lens and the signal/noise ratio (S/N) of the system, when the signal of the specimen is bright enough that the noise is no longer an issue only the optics of the system define the limitations. Typically, high resolution images are acquired at a very slow scan speed to optimise the latter in order to acquire a good signal.

1.3 Interaction of light with molecular structures

The actions of light can be described by two concepts. The first one is photons interacting with molecules which can be described by scattering and absorption. The second concept is waves of light interacting with the surface of a medium which can be described by refraction and polarization.

1.3.1 Photon molecule interactions

When photons hit a molecule there are two processes that may occur; (i) absorption and (ii) scattering. The relative extents of these effects vary from one material to the next. Figure 1.1 shows the different scenarios when a photon travels through any medium.

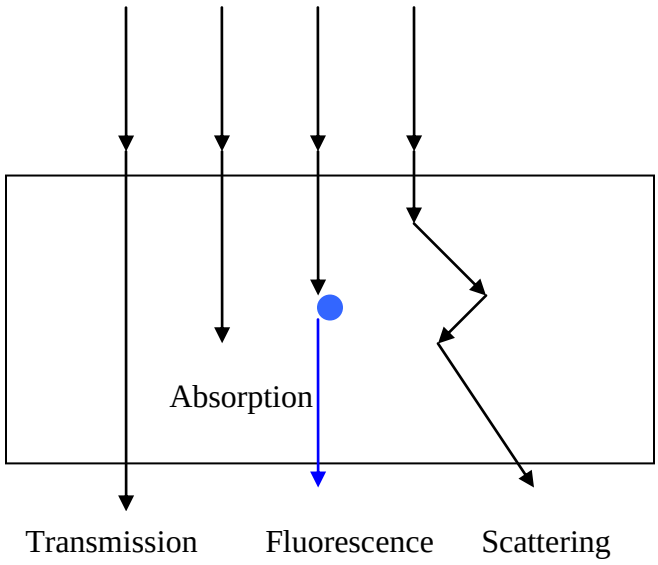

Figure 1.1: The different effects of a photon as it travels through a medium.

1.3.1.1 Absorption

Absorption is where the energy from the photon is converted into another form of energy in the medium it is travelling through. For absorption to occur the incoming photon must have sufficient energy to excite an electron within the atom from its ground state to an excited state. When a photon is being absorbed the incident electromagnetic wave is attenuated when travelling through a medium. This process can be described using the Beer-Lambert law equation (Pawley, 2002):

Equation 1.1

$$I(x) = I_0 \exp[-\alpha x]$$

Where *I(x)* is the output intensity varying with sample thickness *x*, I_0 is the incident intensity and α is the absorption coefficient which describes the amount of photons absorbed is dependent on the medium the photons are passing through; Absorption is wavelength dependent. This is termed optical density and can be described as an extension of the Beer-Lambert law:

Equation 1.2

$$O.D = -\alpha x = \log_{10}\left(\frac{I(x)}{I_0}\right)$$

1.3.1.2 Fluorescence

Fluorescence imaging is a major investigative tool for biological imaging. A sample is stained with a fluorescent dye that can selectively stain structures within a cell, depending on the properties of the fluophore used. Fluorescent material will absorb photons of a relatively selective wavelength and then emit photons of a longer wavelength. There are some substances that will store the absorbed photons and released them slowly over time, this is termed phosphorescence (Vorndran *et al.*, 1995).

Fluorescence is an extension of absorption where the absorption of the photon causes an electron to be raised into an excited state. However, in fluorescence a photon of longer wavelength will be emitted when the electron returns to its ground state (S_0) from S_1. This is shown in figure 1.2 (Amos, 2000)

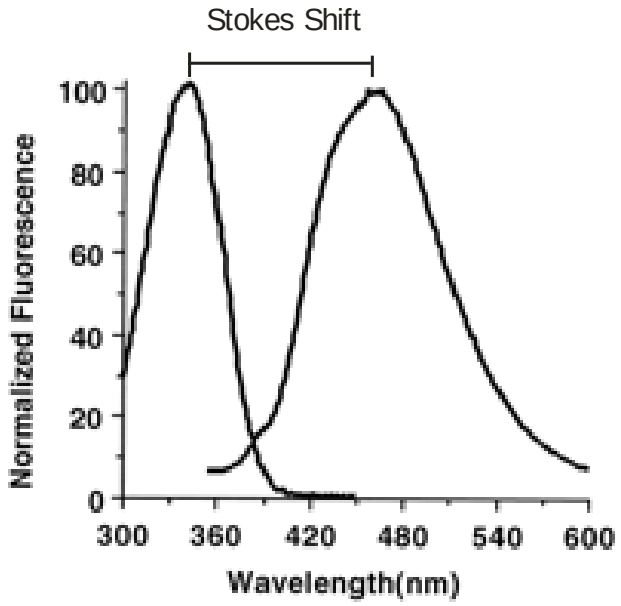

Figure 1.2: Excitation and emission spectra for nicotinamide adenine dinucleotide (NADH) and an annotations showing the stokes shift (Figure from Invitrogen).

There are many biological entities which exhibit fluorescent properties. This is termed intrinsic fluorescence. One of the major examples of this in cardiac muscle and all other cells is NADH which is found in the mitochondria and is excited between 330 nm and 370 nm (Brandes & Bers, 1999;Bessho *et al.*, 1989).

1.3.1.2.1 Stokes Shift

Stokes shift describes the difference between the peaks of the absorption and emission spectra of a dye. When a molecule absorbs a photon it gains energy and goes into an excited state. The molecule will then emit a photon to lose energy. The emitted photon will have less energy and thus a longer wavelength than the absorbed photon. Figure 1.3 shows the different energy states of electron excitement and when this will cause the emission of a photon.

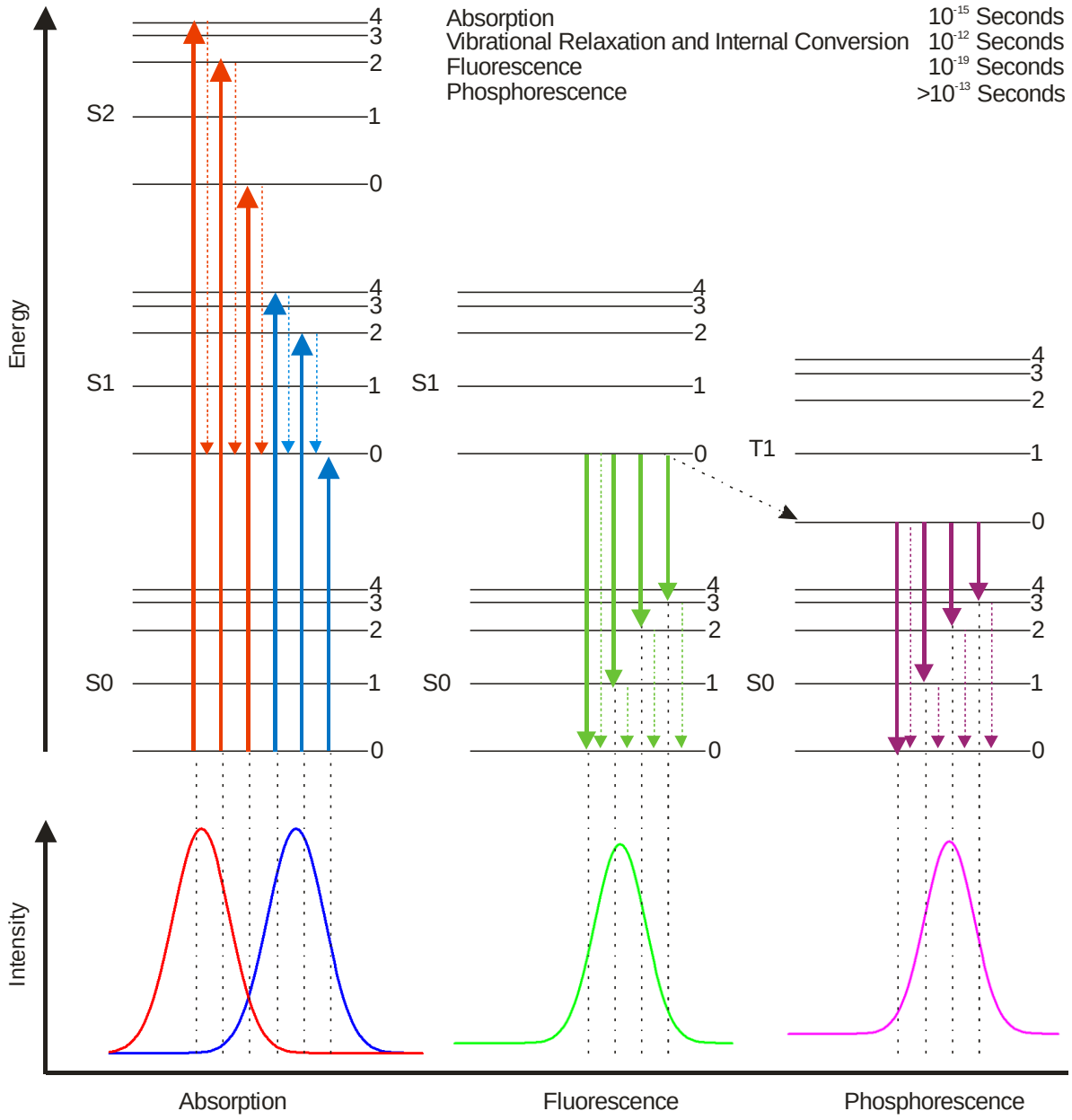

Figure 1.3: The Jablonski diagram. This is a representation of the different type's electronic states of fluorescent molecules and their corresponding spectra. The x axis is grouped by energy stated and the y axis is denotes the spin multiplicity of the electrons of the fluorescent molecule. Solid arrows denote non-radiative transitions while dotted arrows denote radiative transitions. (Pawley J, 2006)

Electronic states are arranged vertically by energy. The solid arrows indicate radiative transitions occurring either during absorption or emission. Dashed arrows represent non-radiative transitions. Internal conversion is a non-radiative transition, which occurs when a vibrational state of a higher electronic state is coupled to a vibrational state of a lower electronic state (James Pawley, 2006).

1.3.1.2.2 Quantum yield

The quantum yield (QY) describes the efficiency of the fluorescence of a particular molecule. This is calculated as the number of photons emitted over the number of photons absorbed. The QY will be wavelength-dependent. The most effective fluorescent molecule can have a QY of 1 meaning it will emit a photon for every photon absorbed, however molecules that have a QY of 0.1 are still considered quite fluorescent (Garini *et al.*, 2006).

1.3.1.3 Scattering

Scattering is where the direction of a photon will change upon interacting with the medium through which it is travelling. Some tissues scatter photons less than others, as scattering is dependent on the density of organelles in the specimen. In cardiac tissue this can arise from very small changes in the refractive index. Scattering can occur when light travels only a few μm into a cell. As multiple scattering events can happen to the same photon this can be a large factor in two-photon imaging and is a major limiting factor when performing deep tissue imaging. There are several different types of scattering which are described below (Popp *et al.*, 2003;Dong *et al.*, 2003).

1.3.1.3.1 Rayleigh scattering

Rayleigh scattering occurs when the wavelength of light is less than the size of the objects within the material. With this form of scattering the path the light follows has an equal chance of changing to any direction. Rayleigh scattering can be described by the equation

Equation 1.3

$$\frac{I(\theta)}{I_0} = \frac{\left(1+\cos^2\theta\right)k^4\left|\alpha\right|^2}{2r^2}$$

Where $I(\theta)$ is the scattered intensity at angle θ, I_0 is the incident intensity $k=2\pi/\lambda$, r is the distance from particle to detector and α is the electrical polarisability of the particle.

It can be seen that the scattered intensity is inversely proportional to the fourth power of λ. Thus longer wavelengths are scattered less and will generally propagate deeper into tissue.

1.3.1.3.2 Mie scattering

Mie scattering occurs when the wavelength of light is greater than the size of the objects within the material; this process is not wavelength-dependent and will tend to change the photons path by an angle less than 90 degrees. Modelling Mie scattering is more complicated than with Rayleigh scattering. There is a simulator available at http://omlc.ogi.edu/calc/mie_calc.html. This program can provide the scattering coefficient and the average cosine of the phase function as well as graphical outputs of the simulation. The input data required is the size of the spherical objects, the wavelength of light and number of angles.

1.3.1.3.3 Anisotropy

An anisotropic material is defined as a material in which the properties of the scattering will depend on the direction the photons enter the media. The direction of the light scatter can be defined as g which is the mean cosine of the angular phase function. If g is 0 then the scatter is isotropic. For a g value of -1 the scatter is purely backscatter and if g=1 purely forward. g is defined by the following equation

Equation 1.4

$$g = \frac{\int_{4\pi} p(\theta)\cos(\theta)d\omega}{\int_{4\pi} p(\theta)d\omega}$$

The solid angle is calculated by

Equation 1.5

$$d\omega = \sin\theta d\theta d\varphi$$

Where $d\omega$ is the solid angle as defined, $p(\theta)$ is the probability function also known as the phase function and θ is the scattering angle. Almost all cardiac tissue is anisotropic, with typical values ranging from 0.7 to 0.99 which indicates that the angle of scatter will be between 8˚ - 45˚.

1.3.1.3.4 Turbid media

As photons pass through biological material there will be a proportion of the photons which are absorbed and scattered. The total attenuation coefficient can be expressed as the sum of the absorption and scattering coefficients. The ratio of scattering to absorption is known as the optical albedo which is defined below.

Equation 1.6

$$a = \frac{\alpha_S}{\alpha_T} = \frac{\alpha_S}{\alpha + \alpha_S}$$

Where α_s is the scattering coefficient, α is the absorption coefficient and α_T the total attenuation coefficient. Thus an optical albedo of 0 would be for a medium which does not exhibit scattering and conversely 1 for a media which only exhibits scattering.

1.3.2 Wave interactions

1.3.2.1 Transmission and reflection

A fundamental process to fluorescence biological imaging is that the photons pass through the medium and are not reflected. Most media will partly reflect light and partly transmit light, and this is described by

Equation 1.7

$$T = \frac{I}{I_0} = 1 - R$$

Where *T* is the transmission coefficient *I* and I_0 are the output intensity and incident intensity respectively. *R* is the reflection coefficient and is defined as 1-T.

When light propagating at an angle to normal incidence is reflected from the surface or interface of a material it also undergoes refraction, whereby, the refracted light travels through the medium at a different angle to the incident beam. This is given by the law of refraction. As the angle gets shallower there is more reflection and less refraction.

1.3.2.2 Refraction

Refractive index (RI) is an optical property of tissue substance, which is defined in terms of a real part n_r and an imaginary part n_i as

Equation 1.8

$$n = n_r + in_i$$

Where n_i is equal to the extinction coefficient κ. Where κ indicates the amount of absorption loss when the electromagnetic wave propagates through the material as dindecated by the beer-lambert law.

Refraction is when the angle of a wave changes at the surface of a medium, this is due to the phase velocity of the wave is changed the frequency of the wave remains constant. This can be described by Snell's law. Figure 1.4 shows a diagram of an incident ray being refracted.

Equation 1.9

$$\frac{\sin\theta_1}{N_1} = \frac{\sin\theta_2}{N_2}$$

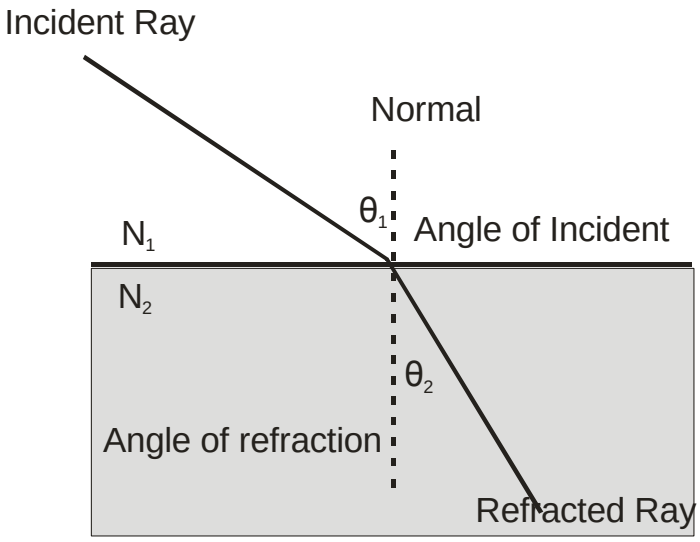

Figure 1.4: The effects of a refracted light ray. Where N_1 it the refractive index of the first material, N_2 is the refractive index of the second material, θ_1 is the angle of indecent ray from the normal and θ_2 is the angle of the refracted ray from the normal.

However, tissues are not homogeneous structures and small refractive index changes exist. Soft tissues consist of tightly packed groups of cells in a network of fibres through which water percolates. Figure 1.19, taken from (Schmitt & G.Kumar, 1998) shows the actual refractive indexes of differing mediums (Qing Ye *et al.*, 2011)

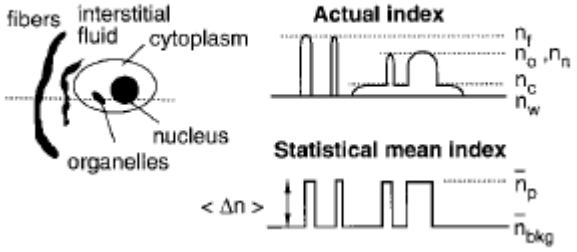

Figure 1.5: The inhomogeneities in refractive index within a cell.(Schmitt & G.Kumar, 1998)

The major refractive index variations are found to be caused by the nuclei, fibres and organelles. The dry weight fractions of each component can be used to calculate the mean

index variation $\langle \Delta n \rangle$ as shown in the following equation. In cardiac tissue 45% is made up of collagen and elastin fibres

Equation 1.10

$$\langle \Delta n \rangle = f_f (n_f - n_s) + f_n (n_n - n_c) + f_o (n_o - n_c)$$

Where, $f_{f,o,n}$ is the dry weight fraction of fibre, organelles and nucleus, respectively and, $n_{f,o,n}$ are the refractive indices of the fibre, organelles and nucleus, respectively.

1.3.2.3 Polarisation

Polarisation describes the orientation of the oscillation of light waves which is perpendicular to the direction of propagation. Light contain is electric and magnetic wave vectors at oriented at 90° to each other as shown in figure 1.19. The light may be oriented in a single direction which is termed linear polarisation, or it may rotate as the wave travels which is known as circular polarisation. Figure 1.6 shows a semantic representation of the electric field component is 90 degrees from the magnetic field component.

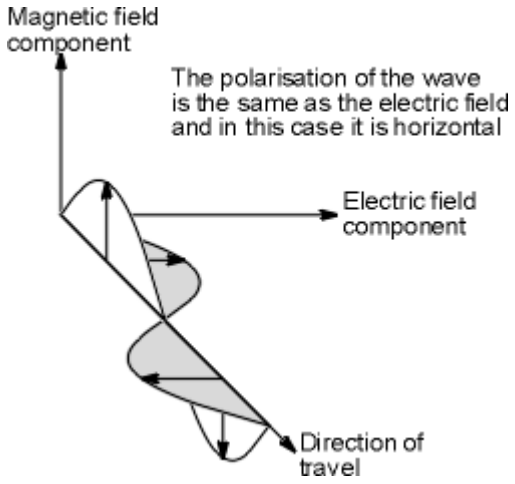

Figure 1.6 This figure shows the polarisation of an electromagnetic wave.

The polarisation of light is used in many ways in optical microscopy. To measure the polarisation properties of tissue a polarised excitation source can be used with a second

polariser blocking the excitation light. When a specimen is imaged only the light that has had its polarisation changed by the tissue is able to be imaged. The Stokes vector describes the polarisation of light mathematically by the following equation

Equation 1.11

$$\vec{S} = \begin{pmatrix} S_0 \\ S_1 \\ S_2 \\ S_3 \end{pmatrix} = \begin{pmatrix} I \\ Q \\ U \\ V \end{pmatrix}$$

Where I represents the overall intensity of the beam, Q gives the intensity of linear polarization along horizontal and vertical axes, U represents the intensity of linear polarization at $\pm 45^{o}$, and V gives the intensity of light that is (right- and left-) circularly polarized (de Boer *et al.*, 1999).

1.4 Review of cell and heart structure

The human heart is a four-chambered organ consisting of two atria and two ventricles. The left and right sides of the heart are composed of an atrium and a ventricle, responsible for supplying blood to the systemic and pulmonary circulations, respectively. While the contraction of the atria actively contributes in part to ventricular filling, it is not essential for this process. Instead, the distensible atrial walls allow the atria to fill with blood rapidly following atrial systole, facilitating continuous, non-pulsatile venous inflow to the heart. The right side of the heart receives de-oxygenated venous blood from the body and pumps blood to the lungs via the pulmonary artery. The blood pressure in the pulmonary circulation is lower than the rest of the body, one reason why the right ventricle is smaller than the left ventricle. The tricuspid value prevents the backflow of blood from the ventricle to the atrium during contraction (systole). The blood then leaves the right ventricle and enters the pulmonary artery via the pulmonary valve. The left chambers supply the rest of the circulatory system via the aortic arch. Oxygenated blood returning from the lungs enters the left side of the heart and fills the left atrium and left ventricle via the pulmonary vein during the relaxation phase of the cardiac cycle, known as diastole. The bicuspid valve prevents blood from returning to the left atrium during systole. In systole the blood is forced out into the aorta via the aortic valve which also stops backflow of blood back into the ventricles. The anatomy of the heart is shown in figure 1.7.

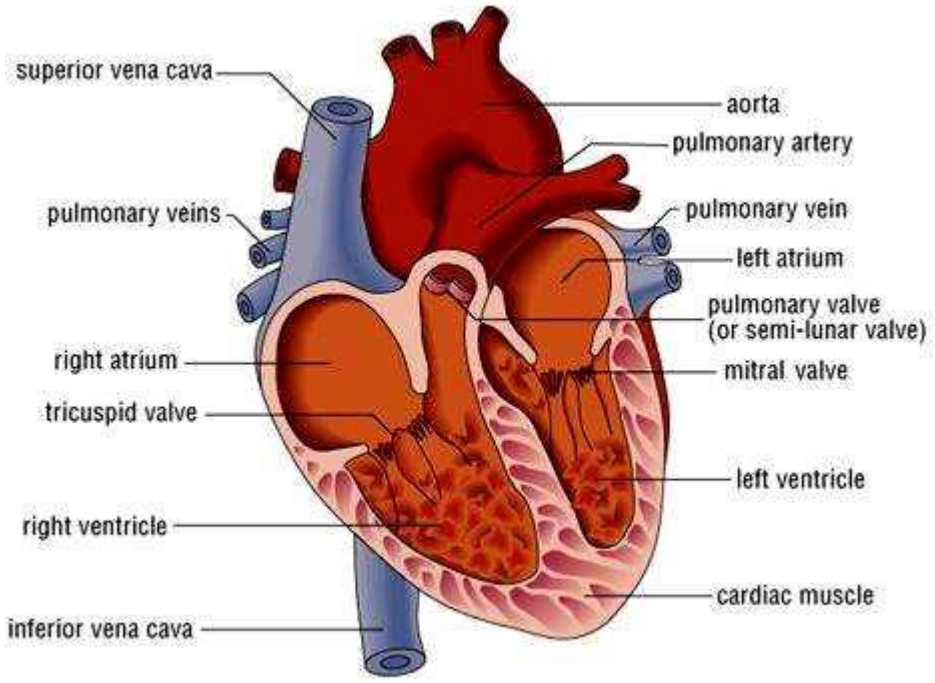

Figure 1.7: The structure of the heart. Figure from dihisham.com/archives/21579

Cardiac muscle cells, also known as cardiac myocytes, exhibit automaticity, meaning they can spontaneously depolarise in the absence of an external stimulus. As such, initiation of electrical activation of the heart is determined by pacemaker cells located in the sino-atrial node of the right atrium, which exhibit the fastest spontaneous depolarisation. This stimulates the atria first and causes the cells to depolarise and contract. This initiating electrical impulse spreads to another group of specialised pacemaker cells at the atrio-ventricular node, and the impulse is conducted via the bundle of His, down the left and right bundle branches of the interventricular septum towards the apex, finally spreading through the purkinje system. This results in the near-synchronous contraction of the ventricles, which initiates at the apex first, aiding the pumping efficacy of the heart (J R Levick, 2003). Figure 1.8 shows the blood volumes and pressure achieved in a typical cycle with the ECG information.

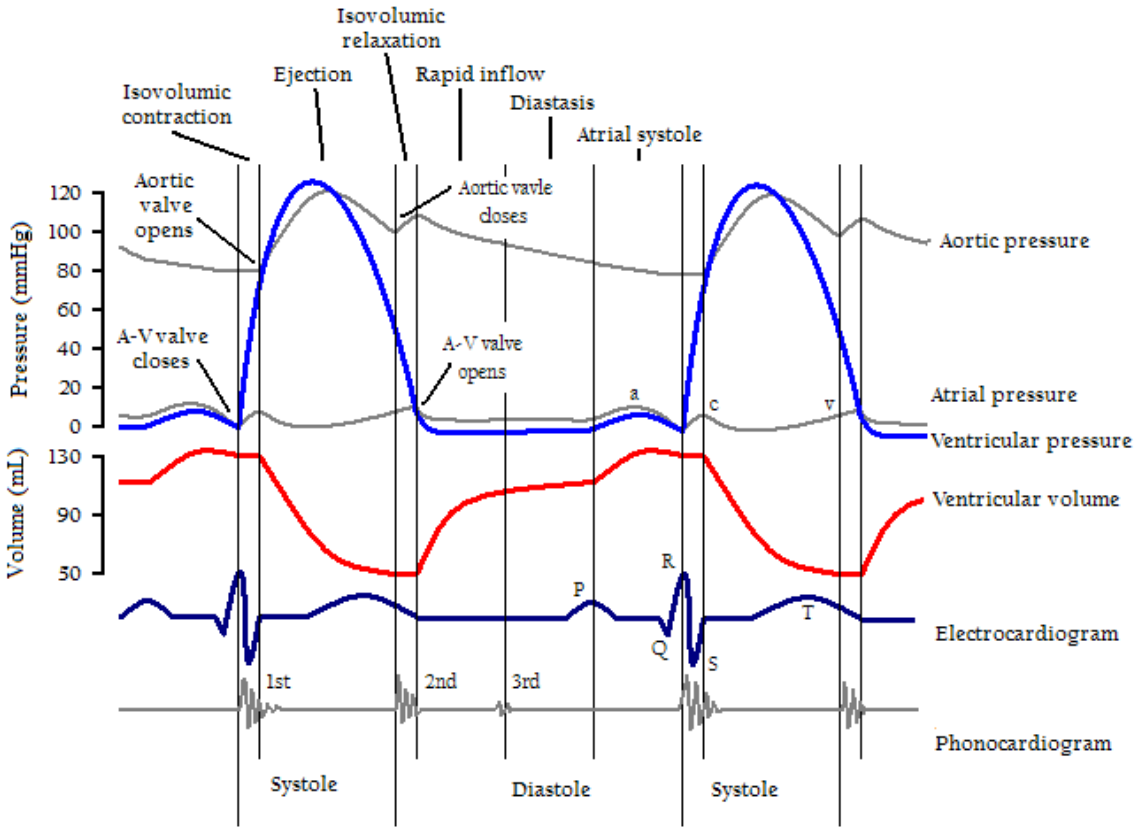

Figure 1.8 The cardiac cycle of the left ventricle, showing the phonocardiogram, electrocardiogram (ECG), blood volumes and typical pressures in a human subject.

In the intact heart, cardiac myocytes are organised in distinct sheets, with individual cells joined end-to-end and tightly electrically coupled at structures known as intercalated disks, allowing the near synchronous depolarisation and subsequent contraction of the atria and ventricles. It is possible to isolate and study individual cardiac myocytes from mammalian hearts by enzymatic dissociation of cells using a collagenase. A healthy ventricular myocyte is approximately 120 µm in length and 20x30-40 µm in width and depth, respectively. When dissociated these living cells are described as rods. If the cell membrane becomes permeable to calcium the muscles units in the cardiac cell will activate and the cell will hyper-contract. These hyper-contracted cells are termed balls due to their appearance.

1.4.1 Cell to cell structure

Human cardiac myocytes are mono-nuclear, whereas rabbit cells are di-nuclear. Cells are attached at each end via intercalated disks, which contain gap junctions to allow rapid communication of electrical impulses between cells. The gap junctions have connexin units that span the gap junction (2-4 nm), 6 connexon subunits form a connexin unit. As these gap junctions are open to the cytoplasm and as cells can form "Y" shaped ends the cardiac cells will work as an electrically activated sheet (Soeller *et al.*, 2009).

1.4.2 Intracellular anatomy

Each myocyte is composed of contractile units of myofibrils that have a diameter of 1 μm, these myofibrils are composed of sarcomeres, the basic contractile unit. They are 1.8-2 μm long in the uncontracted state. These units lie between two Z-lines. Z-lines are partitions formed by α-actinin proteins. There are two types of filaments that cause contraction; thin actin filaments which have a diameter of 6 nm and length of 1 μm and thick myosin filaments which are 11 nm and 1.6 μm in length. These form the basic contractile mechanism for cardiac muscle.(DM Bers, 2002)

Transverse tubules (T-tubules) penetrate in from the membrane surface of the cardiac cell and reach deep within the cell. T-tubules are essential for fast and even depolarization of the cardiac myocyte, this is shown in figure 1.9. (Andreas Ohler *et al.*, 2009;Brette & Orchard, 2003;Lyon *et al.*, 2009;Soeller & Cannell, 1999).

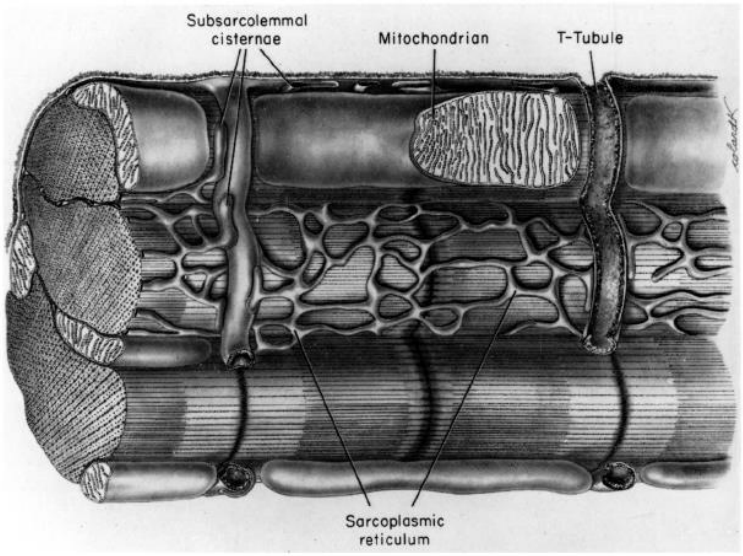

Figure 1.9: The intracellular structure of a cardiac myocyte with the SR network positioned around the myofibrils and mitochondria placed in between the myofibrils (DM Bers, 2001).

1.4.3 Excitation-Contraction Coupling

The process whereby electrical depolarisation of the cardiac myocyte induces activation of the contractile elements is known as excitation-contraction coupling. Under normal conditions, electrical depolarisation will spread across the surface membrane and down into the T-tubules, activating voltage-gated L-type Ca^{2+} channels located here. This leads to an initial influx of Ca^{2+} into the cell, measured as an inward Ca^{2+} current. This in turn triggers a proportionately greater release of Ca^{2+} from an intracellular Ca^{2+} store, the sarcoplasmic reticulum (SR), by activating Ca^{2+}- sensitive ion channels, Ryanodine receptors, located on the SR membrane. This process is known as calcium-induced calcium release (CICR). This raises the intracellular Ca^{2+} concentration sufficiently to allow activation of the contractile elements and initiation of contraction. For relaxation to occur, Ca^{2+} must be removed from the intracellular space and returned to its resting concentration. This is performed by a number of processes; re-uptake back into the SR by the sarco-endoplasmic reticulum ATPase (SERCA); extrusion from the cell via the sodium calcium exchanger (NCX) or the sarcolemmal Ca^{2+} ATPase; uptake into the mitochondria by the mitochondrial Ca^{2+} uniporter (Radwanski *et al.*, 2010;Soeller *et al.*, 2007). Disruption of normal EC-coupling mechanisms has long been known to be a

feature in many cardiac disease states. Therefore, understanding how this process is altered in disease is a key goal for current researchers.

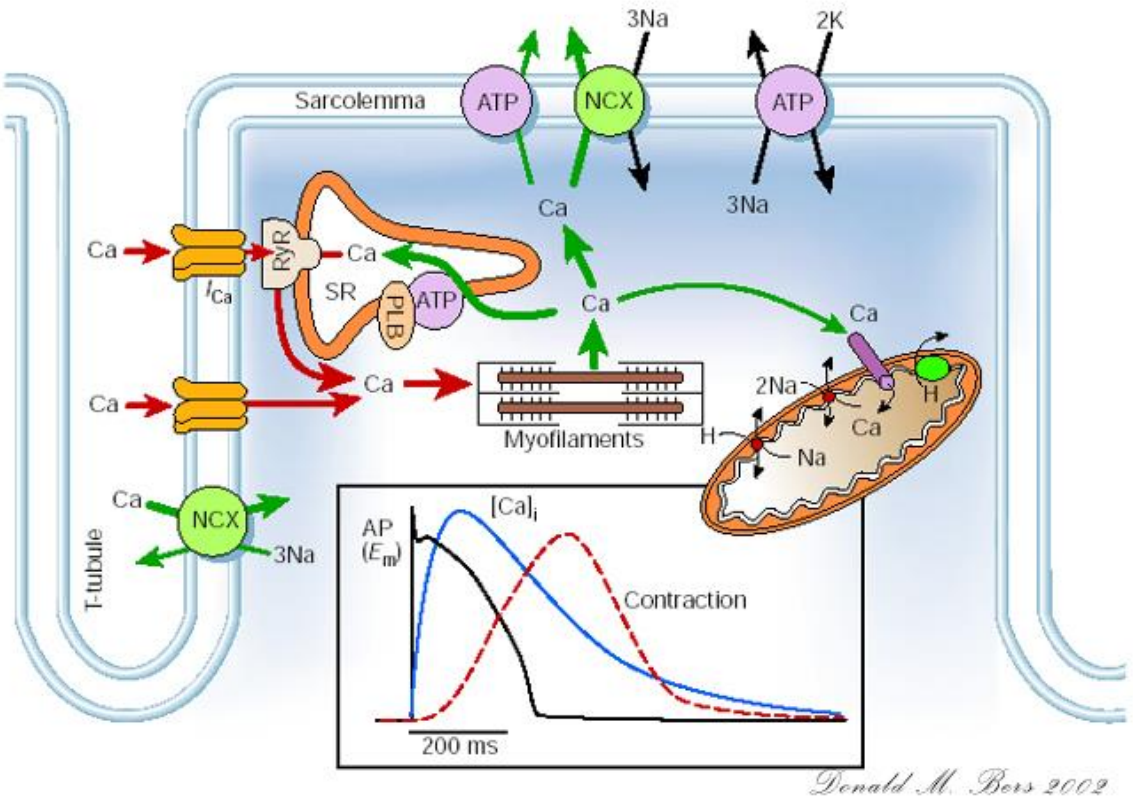

Figure 1.10: Diagrammatic representation of E-C coupling in cardiac myocytes. Schematic indicates the major calcium fluxes within the cardiac myocyte, with relative time course of the cardiac action potential (AP), intracellular calcium transient and cell contraction, shown in the inset graph.(DM Bers, 2002)

1.5 Optical properties of myocardium.

Cardiac muscle has many factors that contribute to its optical properties, it is desirable to study each of these phenomena individually in order to quantify the loss of resolution and light absorption in order to better understand the final images captured when imaging cardiac muscle. This method may also help reduce the number of experimental animals needed.

1.5.1 Scattering and Absorption

Scattering of photons in the myocardium, along with absorption, is known to cause light loss. There have been many simulations to try and separate the effects of absorption and scattering in the myocardium, however these have proven to be inaccurate with depths of tissue less than 2 mm (Gandjbakhche *et al.*, 1999). In this project the effects of scattering and absorption will be studied as one phenomenon (Bishop *et al.*, 2007).

1.5.2 Refractive index of cardiac muscle.

Cardiac muscle has been found to have an average refractive index of 1.38. This has been measured in canine cardiac muscle using a method discussed in Chapter 2, and in human cardiac muscle through the use of optical coherence tomography (Tearney *et al.*, 1995;Kuypers *et al.*, 2005).

1.5.3 The interaction of polarised light with cardiac muscle.

When polarised light is used with cardiac muscle there can be retardance when the polarisation changes orientation, or depolarisation, where the light waves enter a state of multiple polarisations. The polarity of laser light has been used to measure sarcomere length by directing the beam into slices of muscle where there will be columns of diffracted light from which the sarcomere length can be calculated (Leung, 1982;Yeh & Pinsky, 1983). There is a birefringence associated with the extracellular collagen network. Therefore there is a change in the polarisation properties in diseased hearts with myocardial infarction for example, where the infarcted regions of the heart are composed mainly of fibrous connective tissue.

1.5.4 Inhomogeneous refractive index

Blood vessels that run through the cardiac muscle are refractive when being imaged as they contain a fluid that has a different index to cardiac muscle. This has been found to interfere with the wave of light and cause distortions. If the inhomogeneities can be measured it is possible to correct for them using adaptive optics (Helmchen & Denk, 2005).

1.5.5 Tissue absorbance

The absorption of photons in cardiac muscle is wavelength dependent. Longer wavelengths interact less with cardiac muscle this is shown in figure 1.11 which displays up to 600nm.

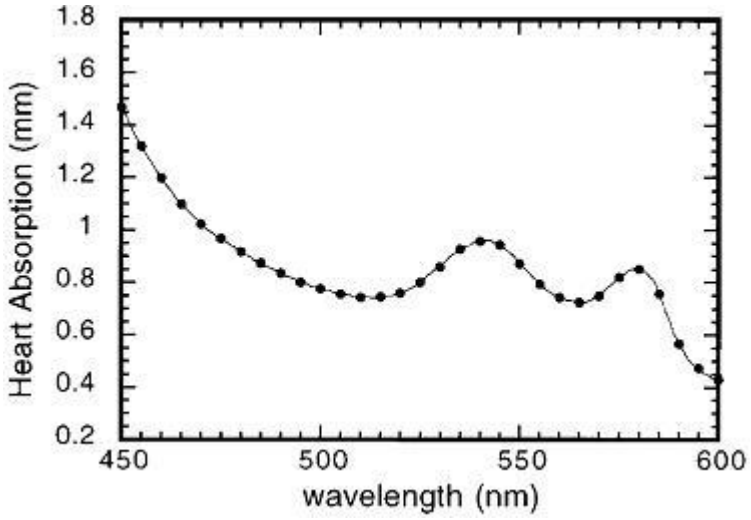

Figure 1.11 The absorption of photons in the visible part of the spectrum in pig heart (Gandjbakhche *et al.*, 1999).

1.5.6 Intrinsically fluorescent substances in tissue

Cardiac muscle contains NADH and Flavin Adenine Dinuclotide (FAD), both these substances are known to be auto-fluorescent. It is possible that they cause bleed through on the two channels that are being used to record signals from other dyes. Thus causing a detection of a signal that will contribute to background or possibly a signal that could be misinterpreted (Rocheleau *et al.*, 2004).

1.6 Use of fluorescence probes to study heart function.

In addition to studying microscopic structures, fluorescent indicators are useful for investigating physiological function, e.g. voltage, Ca^{2+} and mitochondrial membrane potential.

1.6.1 Tetramethylrhodamine Ethyl Ester Perchlorate (TMRE)

TMRE is a dye with a very high quantum yield that is cell-permeant and stains the mitochondria inside cells with an intact membrane. TMRE binds to inner mitochondrial membrane. It can be used to measure mitochondrial depolarization related to cytosolic calcium transients and to image time-dependent mitochondrial membrane potentials (Xu & Webb, 1996;Loew *et al.*, 1994).

TMRE can be used for measuring membrane potentials of mitochondria. It can be excited at 545 nm and emission is at 590–630 nm.(Gordienko *et al.*, 2001)

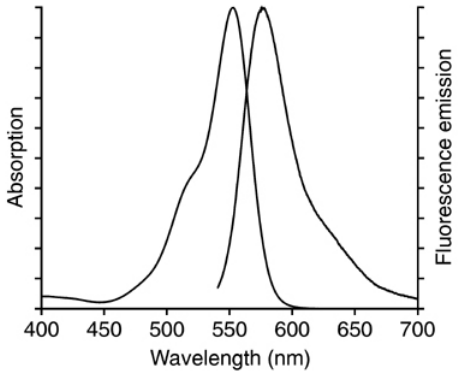

Figure 1.12 The excitation and absorption spectra of TMRE. Figure supplied by Invitrogen

1.6.2 Fura-2

Fura-2 is a dye that binds to free intracellular calcium and can be used to make ratio metric measurements. Its peak excitement is at 340 nm and it emits at 510 nm. This dye is a carboxylic acid with an AM ester group attached. This causes the molecule to have no charge and thus can permeate the cell membrane. Once the dye is inside the cell, esterases cleave the molecule at which point the dye becomes fluorescent. Figure 1.26 shows the emission and excitation spectra of fura-2.

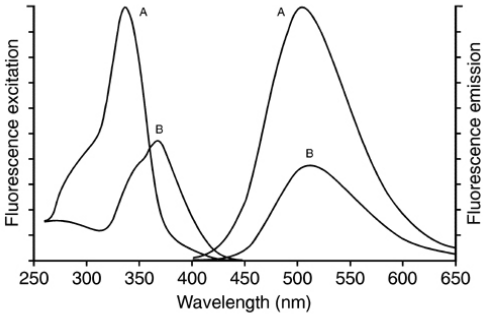

Figure 1.13: The excitation and absorption spectra of Fura-2: A shows Ca2+-saturated and B shows Ca2+-free Fura-2 in pH 7.2 buffer. Figure from Invitrogen.

1.6.3 ANEPPS dyes

The ANEPPS family of dyes is a very useful fluorescent dye for studies of cardiac muscle. Di-4-ANEPPS stains the extracellular cell membrane by binding to amphiphillic molecules in a lipid membrane via a pair of hydrocarbon chains on the dye molecule, with the chromophore oriented perpendicular to the cell membrane (Loew, 1996) The dye will not cross the membrane of a healthy cardiac cell. However, if the membrane is damaged then the dye will stain intracellular structures and the cell will appear many times brighter than a healthy cell. This can be a useful indicator of cell health. However, Di-4-ANEPPS has been documented to cause photodynamic damage to the cell. Documented effects of Di-4-ANEPPS are prolongation of the action potential duration, reduction of the membrane resting potential and eventually of excitability (Schaffer *et al.*, 1994). Isolated rabbit myocytes seem to be less prone to these effects than their rat equivalents (Katerina Fialova *et al.,* 2010). Di-4-ANEPPS' main use is as an extremely fast response dye to monitor voltage changes in excitable cells. These dyes operate by means of a change in their electronic structure, and consequently their fluorescence properties (Montana *et al.*, 1989). The excitation peak of Di-4-ANEPPS is around 475 nm and in this work a 488 nm laser or a 470 nm LED was used in the Selective Illumination Microscope (SIM) (Wokosin *et al.*, 2004;M Nováková *et al.*, 2008;Schaffer *et al.*, 1994;Schaffer *et al.*, 1994) It stains the outer membrane and T-tubules making anatomical measurements from a cardiac specimen possible. However ANEPPS main use is for making millisecond temporal optical voltage recordings from cardiac cells, making

it possible to track the time course of very fast electrical events in cells, such as the upstroke of the cardiac action potential. The disadvantage is that the dynamic range of the dye is relatively low; changes in the fluorescence are 10% per 100 mV. This means that some physiological changes which are very subtle may be difficult to resolve (Campagnola *et al.*, 1999;Millard *et al.*, 2004;Dumas & Kinisley, 2005;Schaffer *et al.*, 1994)

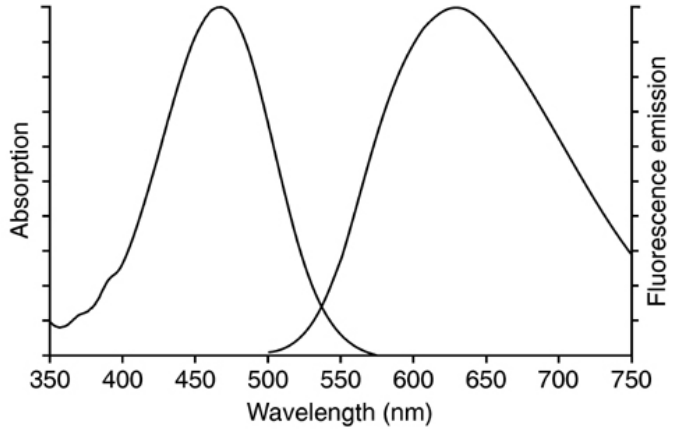

Figure 1.14 shows the excitation and emission curve of Di-4-ANEPPS (figure supplied by Invitrogen)

A more accurate way to measure small voltage changes with Di-4-ANEPPS is to make ratiometric measurements. Ratio of emission intensities peaks change at 560 nm to 620nm as the voltage increases, this makes it possible to measure Di-4-ANEPPS in two channels with a dichroic mirror splitting the light around 590nm and make spectral ratiometric measurements to estimate voltage measurements of a sample (Montana *et al.*, 1989).

1.6.4 Congo Red

Congo red is a sodium salt it is a secondary diazo dye with an absorption peak around 502nm and excitation peak around 614 nm. It is used in this project to bind to agar so Agar can be imaged accurately in solution (Erdemoglu *et al.*, 2008)

1.7 Resolution

In optical microscopy, resolution is defined as the minimum separation between two points that can result in a certain contrast change between the points. The contrast is described as a percentage change of the signal, where a 10% difference between two points results in a high resolution but a weak contrast. This can be described in more detail by the Rayleigh citation described in section 1.7.5 (James Pawley, 2006). In the perfect microscope, the resolution will depend on both the wavelength of the emission and the numerical aperture of the objective lens.

In fluorescence microscopy, the image is determined by the total number of photons collected from the specimen, optical aberrations from the imaging system itself and the number of pixels in the final image.

Low signal to noise ratio can be a feature of biological measurements. As the signal to noise (S/N) becomes lower, the resolution will drop as it will be harder to discriminate the contrast between points. The contrast used to define two objects is determined by accepting the highest achievable light intensity as 1 and no fluorescence as 0. Thus the highest contrast value can be one. The two points would need to be a greater distance from each other for the lowest value to be one. As the two points become closer, the lowest value will rise thus the contrast value will tend towards zero. Once the contrast value is zero the points can no longer be distinguished. This is known as the contrast cut off distance. Although any value above zero is technically a detectable difference in contrast, it is considered that any value over 0.26 is considered significant when dealing with fluorescence microscopes (Pawley, 2002).

1.7.1 The objective lens

The objective lens on a microscope is the most important aspect of the microscope, it is the closest part of the microscope to the specimen, and determines the image that is formed and the amount of light that is collected from the specimen figure 1.15 shows the simplest from of microscope set up, a wide field transmission illumination system.

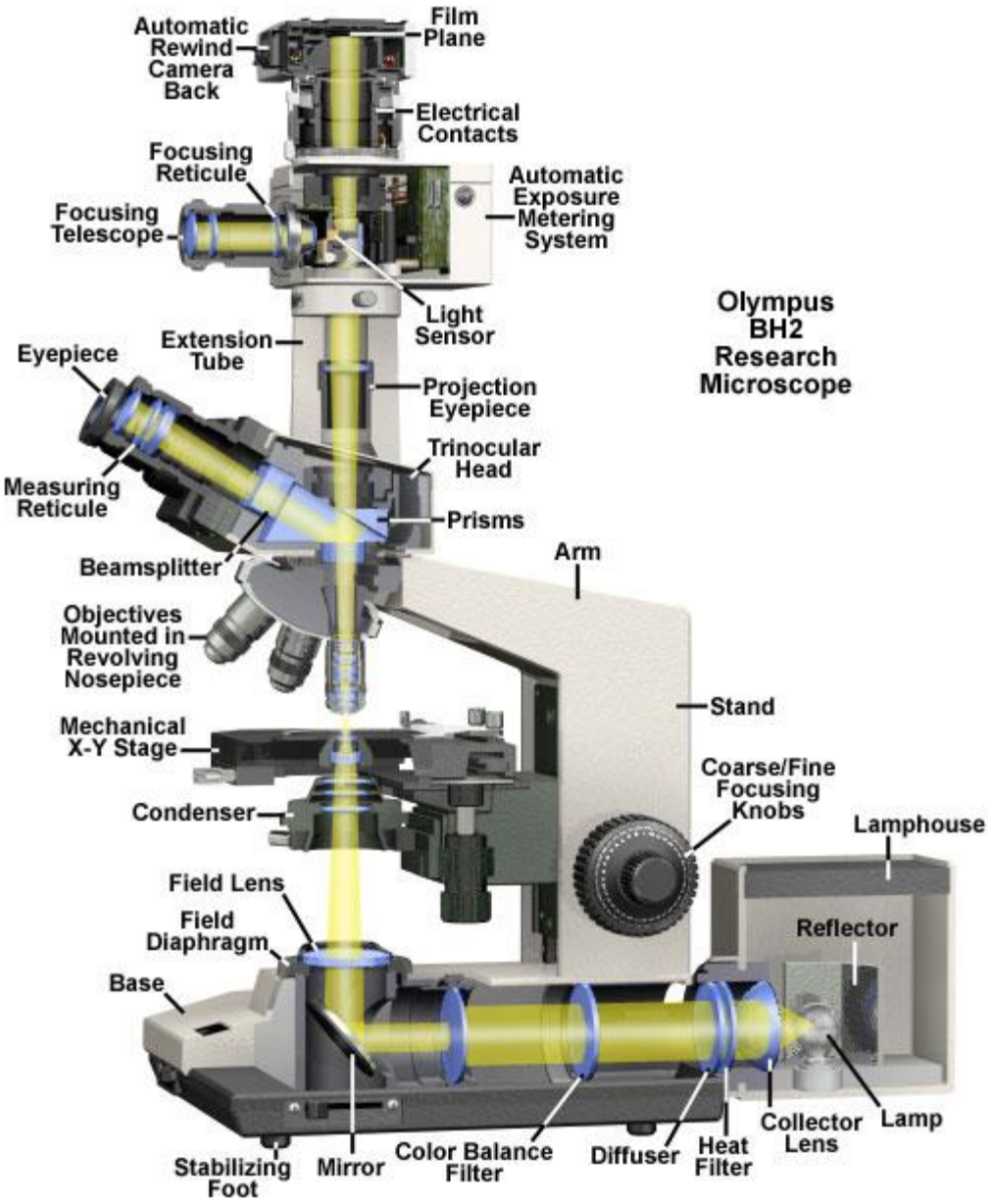

Figure 1.15 show where the objective lens is in reference to the rest of a microscope system. Figure supplied by Olympus.

Modern objective lenses are built with many glass elements inside them. The glass elements are there to correct the many different types of aberration that can occur such as coma, astigmatism, geometrical distortion, field curvature, and spherical and chromatic aberration. There are three factors that determine the resolution of the objective lens: (I) the refractive index of the medium between the lens and the specimen, (ii) the wavelength

of light being used and (iii) the numerical aperture of the lens (Mortimer Abramowitz *et al.*, 2002).

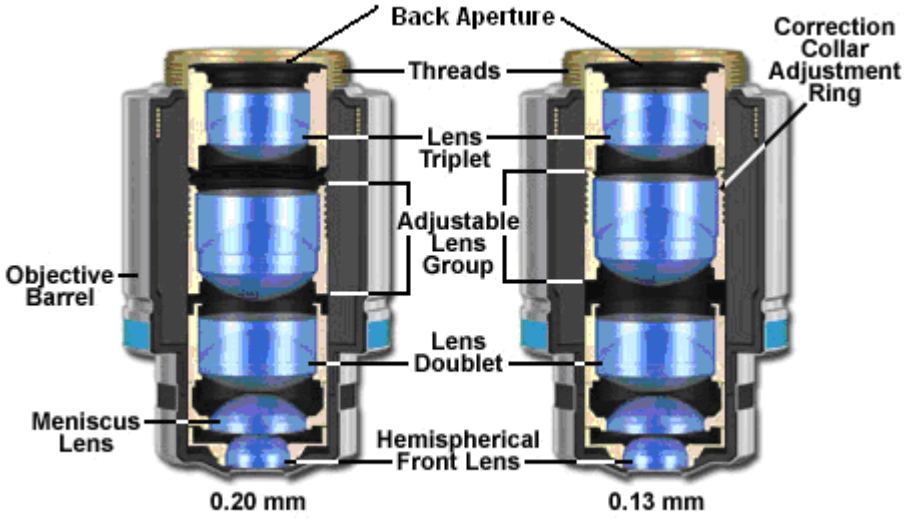

Figure 1.16: Construction of an objective lens showing a number of separate elements housed within. Supplied by Zeiss

An airy pattern is a description of the pattern of concentric rings the can be generated around the smallest focus spot that can be achieved by an objective lens with an evenly illuminated back aperture. The rings are caused by diffraction. The term airy disc normally refers to the first ring in the pattern .

The lateral resolution of an airy disc is defined by the following equation:

Equation 1.12

$$R_{airy} = 0.61\left(\frac{\lambda}{NA}\right)$$

The axial resolution can be described as:

Equation 1.13

$$Z_{\min} = \frac{2\lambda\eta}{NA^2}$$

where λ is the wavelength, η is the index of refraction and numerical aperture is the numerical aperture, R_{airy} describes the radius of the airy disc. Figure 1.17 shows the effect of the changes of NA. (Miks *et al.*, 2007).

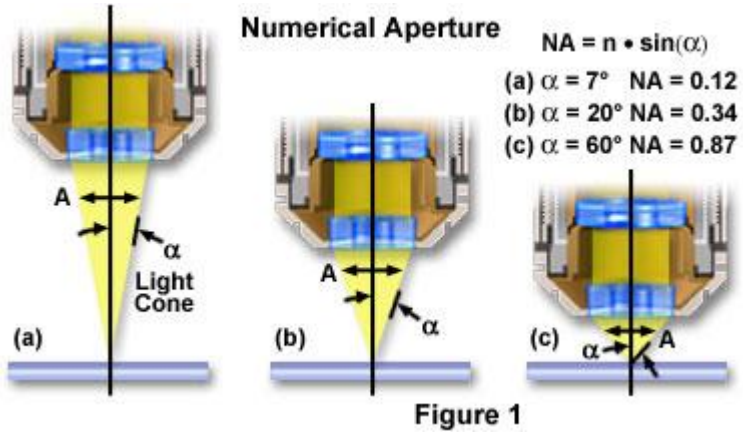

Figure 1.17: Schematic of different numerical aperture lenses along with a demonstration of the reduction in the working distance. This figure also demonstrates the important of fully illuminating the back aperture of the lens. Figure supplied by Nikon

The numerical aperture is one of the most important aspects of a lens as it describes the cone of light captured by the objective from the specimen or the angle of light. This can be described as:

Equation 1.15

$$NA = n \times \sin(a)$$

Where NA is the numerical aperture, n is the refractive index and α is the one-half angular aperture of the objective. This is the major contributing factor to resolution and sensitivity;. The amount of light that will be collected by an objective lens can be calculated as:

Equation 1.16

$$BI = \frac{NA^4}{M^2 TR}$$

Where BI is the brightness index, M is the magnification, NA is the objective numerical aperture and the Transmission Ratio (TR) is presumed to be 100,000. The TR describes the total power of a transmitted wave relative to the incident wave. (Patterson *et al.*, 2010)

The flowing Table 1.1 shows the brightness index for a series of lenses that could be used in biological research.

Magnification	NA	BI
40x	0.8	25.6
40x	1	62.5
60x	1	27.7
60x	1.2	57.6

Table 1.1 shows the brightness index of various specifications of objective lenses.

The one disadvantage of high numerical aperture objectives is they can have shorter working distances. In the most recent generation of microscopes the back apertures have become larger, by effectively scaling the optics up the newer objectives have higher NAs at lower magnifications than the previous generation.(Miks *et al.*, 2007)

Most objective lenses use one of four immersion mediums: air, water, glycerine and oil. Air lenses tend to be low magnification and low numerical aperture with larger working distances. Oil is the preferred objective lens for high resolution imaging as the oil shares the same refractive index as glass which is 1.51. There is a slight refractive index variation between some of the microscope manufacturers; Zeiss design the lenses to be used with oil of refractive index 1.513 while Olympus use oil with a refractive index of 1.515, therefore it is important to use the correct oil or there will be a loss of resolution.

Water immersion lenses are a popular choice for biological work, as many biological samples are immersed in water/saline on the other side of the cover slip. As the angle of refraction is less steep there is also an increased working distance. As demonstrated by figure 1.8

The maximum numerical aperture of an objective lens is limited buy the immersion medium used. If incorrectly spherical aberration may occur or in sever cases total internal reflection.

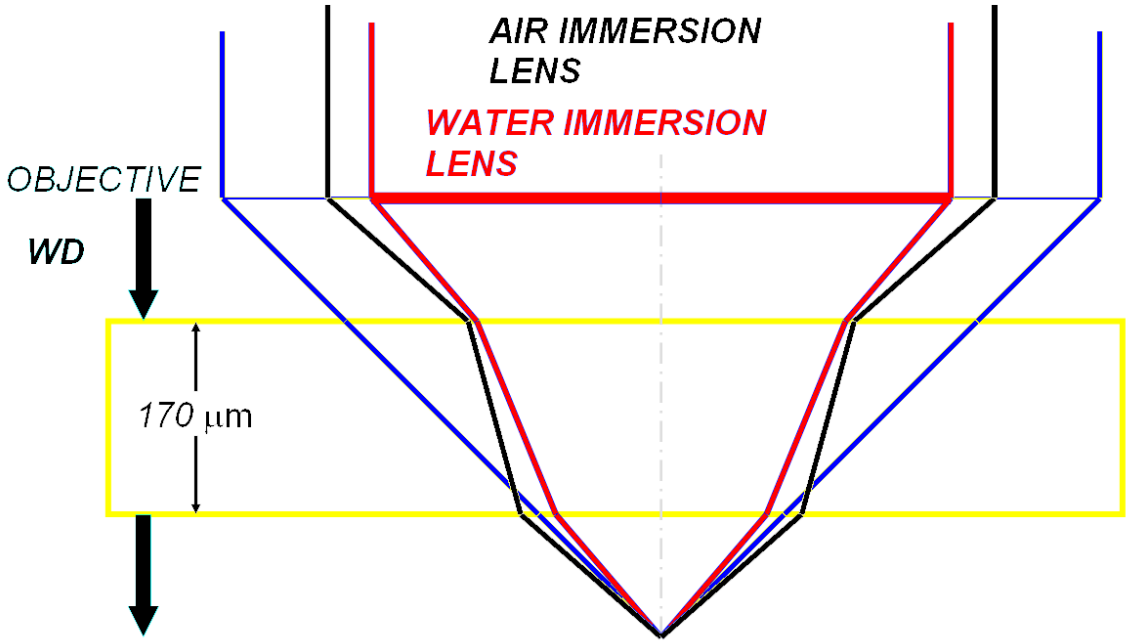

Figure 1.18: The influence of different immersion mediums on the working distance and numerical aperture of the objective lens (Wokosin, 2007).

Most water and some air lenses have correction collars to work with thicker or thinner cover slips, this can be useful if thin cover slips are used to try and increase the working distance of the lens. If the lens does not have a correction collar it will be designed to work with a 170 µm thick cover slip which is an agreed microscope imaging industry standard (Teh *et al.*, 2005).

1.7.2 Point spread function

The Point Spread function (PSF) of the lens describes the smallest point that can be resolved by an objective lens. These are used extensively through out this thesis as a method of comparing systems. PSF is described showing a Gaussian cross section in each axis by taking the full width measurement at half the maximal peak of the system.

1.7.3 Nyquist rate in spatial and temporal situations

In PMT-based scanning systems the choice of how the system is set up is very flexible. The voxel size, voxel dwell time and the amount of voxels an image is composed of can be varied independently. It is important to consider these options and how they relate to each other when an image is being acquired. It is important to have an idea of the requirements that are needed to capture the relevant information (Nicolas DEY *et al.*, 2010). It is important to consider the pixel size and sensor size when specifying cameras that have to meet resolution requirements of imaging systems. as discussed in more detail in section 1.95.

The Nyquist–Shannon sampling theorem is a vital principle for choosing a sampling rate. It states that the sampling rate must be at least twice that of the frequency that is trying to be resolved. In spatial terms it is useful to calculate or measure the PSF of the objective lens and calculate the sampling rate needed if maximum resolution is required. However, it is worth knowing the size of the smallest object of interest in the specimen being imaged and setting the Nyquist rate to sample for that as larger pixel sizes will gather more light in the same amount of time.

The speed of the event can also be calculated using the same principle; it is unlikely that the two sampling rates will marry so that the optimum resolution is captured at the optimum acquisition speed. There are several ways to get around this problem. The first approach is to reduce the region of interest and only image part of the sample. If this is undesirable then there is the line scan option where one glavo mirror is locked in place and a scan is taken in one axis, this will result in a high speed scan that has a high resolution on one axis only. If this is undesirable another approach is to perform two separate scans, a slow high resolution scan and then faster scans using larger pixel sizes. The two images can then be superimposed. For this method to work effectively there must be no movement of the sample and it must be in a stable state when performing multiple scans (Rossmann, 1969).

1.7.4 Factors that determine noise in imaging systems.

The major factor in determining the speed of an imaging system is the signal to noise ratio. It is complicated to estimate what an adequate signal to noise ratio will be, as it is dependent on what information is being extrapolated from the signal. It is helpful to understand the nature of noise that is detected in optical microscopy and its source. There are four different types of noise:

1.7.4.1 Photon noise

Photon noise, also termed shot noise, can be found in all optical systems due to the quantum nature of light. It can be described as the ability for statistically significant fluctuations to be detected due to the low levels of photons being recorded. Photon noise follows Poisson distribution where the variance is equal to the mean.

1.7.4.2 Dark noise

The Dark current is the signal from photosensitive devices such as PMTs or CCDs even when no photons are entering the device. There are a number of factors that can contribute to dark noise. In the case of PMTs, thermal stimulation of the cathode and dynodes can cause electrons to break free of the surface. Dark noise from this source follows Poisson distribution. (Peter Bankhead, 2012;Peter Bankhead, 2009)

1.7.4.3 Read noise

Read noise is caused by the analogue to digital signal conversion and is directly proportional to the speed that the analogue to digital conversion is carried out. Read noise follows a normal distribution. $N(\mu,\sigma^2)$ where μ is the mean, σ^2 is the variance and N is the normal distribution.

1.7.4.4 Amplification noise

During any amplification process when a signal is amplified, the input noise is also amplified. However the amplification can add additional noise. This additional noise is typically represented by a factor called the noise factor which represents the additional noise over the noise expected from the amplification process.

1.7.5 Quantum Efficiency of detectors

Quantum efficiency (QE) describes the sensitivity of a detection system. It is a number between 0 and 1. It quantifies the chance that a photon falling onto the system will be detected, 1 = 100% detection and 0 = 0% detection. This is not a constant term; it is dependent on the wavelength of the photon.

1.7.6 Rayleigh criterion

The Rayleigh criterion quantifies the spatial resolution. It is the minimum distance between two points before they become irresolvable. This is defined as the radius between the point of maximum intensity of the Airy disc and the first diffraction minimum.

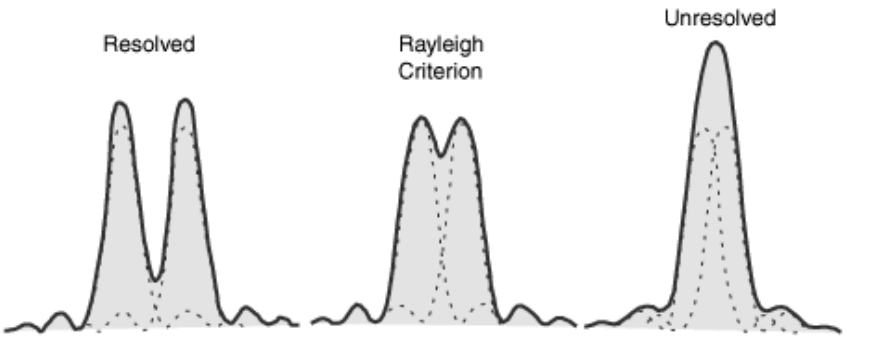

Figure 1.19: Schematic representation of the Rayleigh criterion. Image from http://hyperphysics.phy-astr.gsu.edu

The following formulae describe the Rayleigh criterion when using a confocal imaging system.

Equation 1.17

$$\Delta x = \frac{\lambda ex}{(8n\sin\alpha)}$$

Equation 1.18

$$\Delta z = \frac{\lambda ex}{(4n(1-\cos\alpha))}$$

Where

Equation 1.20

$$a = \sin\left(\frac{NA}{n}\right)$$

n= refractive index (water =1.333, Oil =1.515, Air= 1)

λex = the excitation wave length

The diffraction barrier (Heintzmann & Ficz, 2007) (also known as Abbe Resolution) is a term used to describe the minimum resolvable point, and is derived from the Rayleigh criterion. This is described in the following equations. Lateral resolution can be described as:

Equation 1.21

$$R=\frac{\lambda}{2NA}$$

and for axial resolution:

Equation 1.22

$$R=\frac{2\lambda}{NA^2}$$

Where R = Resolution, λ is the wavelength of light and NA is the numerical aperture of the imaging objective lens (James Pawley, 2006). There are now several new imaging methods that are capable of breaking the diffraction barrier such as photo-activated localization *microscopy* (PALM), Stimulated emission depletion microscopy (STED) or Stochastic optical reconstruction *microscopy* (STORM). It is important to consider the scale of the specimen that is being imaged. The field of view of the microscope is dependent on many factors. In many situations certain types of imaging system may not utilise the full field of view that the objective offers. This may due to factors such as the sensor size of the camera or limitations of scanning head system.

A typical adult cardiac myocyte is ~120 µm in length, and ~20 µm wide, making it easily resolvable by almost any microscope objective. The nucleus inside a cell is a spherical shape around 6 µm whereas the mitochondria are around 0.5-1 µm, so they are on the threshold of what is able to be resolved although it is still possible to detect them with

fluorescence staining. T-tubules run throughout the cell and have a diameter of 100 nm (Haemmerle *et al.*, 2011;Brette & Orchard, 2003).

Speed of acquisition is desirable to image fast physiological events, the speed the image is acquired is dependent on the sensitivity of the system. These experiments are usually noise limited. This can be overcome by reducing the spatial resolution in-order to increase the temporal resolution so that one pixel collects more light which averages out noise. More excitation light can be used to achieve higher light levels; however, this may induce a higher rate of bleaching and damage the cell (McDonald *et al.*, 2012) and hence shorten the time that physiologically relevant data can be taken from it. Deep tissue imaging in intact tissue is desirable as the tissue is more physiologically relevant than dissociated cells that have been separated by enzymatic digestion. The typical penetration depth of a confocal microscope in cardiac muscle is ~50 μm, beyond which the scattering, absorption and refractive index change of the tissue becomes an issue and there is no longer a usable signal. For deep tissue imaging, two-photon microscopy (described in section 1.8.4) is a good alternative as longer wavelengths are not so easily absorbed or scattered by tissue (Mortimer Abramowitz *et al.*, 2002;Centonze & White, 1998;Ntziachristos, 2010;Ghauharali & Brakenhoff, 2000).

1.8 Common imaging systems used in biological research.

Fluorescence microscopy has become a major research tool in the field of biological research. Advances in microscopy with the availability of line scanning confocal systems and 2P systems have allowed researchers to capture images of optically sectioned specimens or high speed images of specific biological events (Bass & Van Stryland, 2010). It is important to understand the principles of how these systems operate and what they can achieve.

1.8.1 Wide field

Wide field imaging is one of the simplest setups on a fluorescence microscope system. This will capture all the light whether it is in or out of focus. This is done by using a light source, there are many light sources for wide field imaging as there is a lot less power needed than in other optical sectioning imaging systems. However it is important that these light sources are stable so that comparative intensity measurements can be made over different time periods. It is possible to achieve optical sectioning with the use of a high numerical aperture objective where only a very limited part of the specimen will be in focus and specialist analysis software that can identify the out of focus regions and remove them. However there are limitations to this approach, such as a limited field of view and short working distance of the objective(Swedlow & Platani, 2002).

1.8.2 Line-scanning confocal microscopy

Confocal is one of the most commonly used laboratory techniques. Confocal microscopy offers several advantages over wide field microscopy. While a conventional wide field image shows all of the depth of the specimen in a single image, the confocal microscope can optically section the specimen being viewed. Most of the out of focus light from a specimen with thickness that exceeds the plane of focus is discarded. This section, termed the depth of field, can be varied to some extent although it cannot penetrate too deeply into the specimen. Due to absorption of the light, the working distance for most confocal systems is about 50 µm in cardiac muscle (F B Sachse *et al.*, 2008). There is a pinhole that can be set so that only the photons emitted from the plane of focus will pass through

a pinhole that is placed in conjugate focal plane. All the photons that have originated from a different location in the z axis will have a corresponding lateral position on this plane, the pin hole will occlude this light, This pinhole is usually variable in diameter. The operator can vary the pinhole diameter thus is able to “thicken” the focal plane.

Confocal microscopes need a powerful and coherent light source at a specified wavelength. Lasers are used extensively in confocal microscopy. Laser light will pass through the objective lens and will focus the majority of the light onto the plane of focus. Depending on the numerical aperture of the lens, the diameter of the beam is 0.25-0.8 µm. As the laser light passes through the specimen, there will be a brighter patch on the plane of focus. (Pawley, 2002;Cheng *et al.*, 1999), Figure 1.20 show a schematic diagram of a confocal system, where the pin hole is just in front of the PMT and there are ray diagrams showing what happens to the light that does and dose not originate from the focal plane of the specimen.

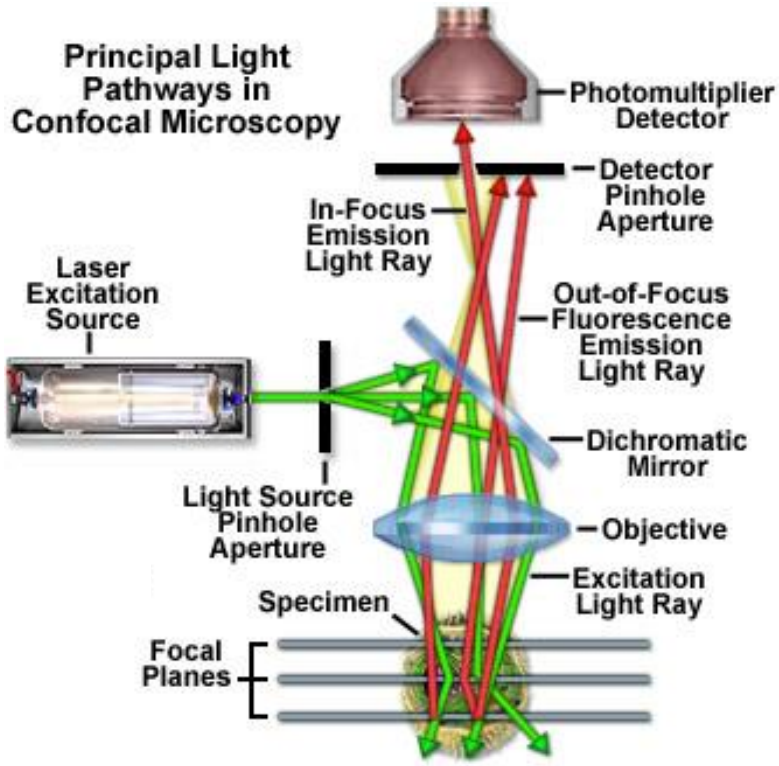

Figure 1.20: This diagram shows the operating principle of a confocal microscope where the green arrows denote excitation light and the red arrows denote emission light. Figure supplied by Nikon.

1.8.3 Slit scanning confocal (Zeiss Five/Seven Live)

The Slit scanning confocal system, developed by Zeiss, works in a similar principle to a confocal system but with a few fundamental changes compared to a standard confocal microscope; the pin hole is in fact a slit with a lens focusing the light to that slit and the photomultiplier tube (PMT) has been replaced with a special Charge couple device (CCD) that is an array of 512 pixels. This setup makes the detectors spatially aware in one axis, although there is loss of Z resolution due to the imperfect pinhole shape. The specimen is then illuminated by a modified laser beam that is rectangular in shape. One disadvantage of this system is that a much higher intensity of laser light is needed to illuminate the specimen in comparison to traditional confocal microscopy due to the fact that the light source is illuminating a larger region of interest than the equivalent confocal system. This coupled with the fact that the laser light can scan a selected region of interest at up to 120 Hz, the specimen can be rapidly damaged, and thus the experiments are only valid for the first few seconds of imaging.

Figure 1.21: The operating principle of a slit scanning confocal.
The numbers on the diagram denote 1 DUO beam combiner, 2 Beam shaper for line scan, 3 AchroGate beam splitter (wavelength dependant), 4 confocal apertures, and 5 High quantum efficiency detectors. Figure supplied by Zeiss

1.8.4 Multi-photon imaging

Multi-photon imaging differs from traditional confocal imaging in many aspects. Multi-photon imaging uses near infra-red wavelengths to excite fluorescent molecules. This gives multi-photon imaging an advantage since it has been found that infra-red wavelengths are far less damaging to cells than visible wavelengths. This means longer experiments are possible without causing damage to the cell. The depth of tissue that can be imaged is considerably higher (confocal: ~50 µm vs two-photon: ~ 500 µm) (Andreas Ohler et al., 2009;Leray et al., 2008;Scherschel & Rubart, 2008). The illumination method is fundamentally different to confocal microscopy. As the name suggests, it takes more than one photon to excite the dye molecules, which is not the case in confocal imaging. In multi-photon imaging, two and sometimes three photons are needed to provide enough energy to excite a fluorescent molecule. As a result, the excitation light is channelled to a defined point in the sample. The PSF of the lens will be the only region where the photon density is high enough for the molecules to fluoresce. The fluorescent molecules within the plane of focus will become excited. This eliminates the need for a pinhole. As only the photon intensity in the psf of the lens is high enough to generate the two-photon effect, there is a sharp drop off in the intensity of the photons out with the PSF of the lens so those photons will not become excited. This is effect is demonstrated in figure **1.3** One of the drawbacks with this technique is that there is a lot less emission light returning to the detectors than conventional confocal (Rubart *et al.*, 2003;Soeller & Cannell, 1999). To deal with the lower signal intensity, most two-photon systems employ the use of non-descanned PMTs). These PMTs are placed in the light path so that the emission light does not have to pass through the scan head mirrors in order to research them they are placed as close to the back aperture of the objective as is practically possible, thus minimising light loss that normally occurs from the light train through the optics, thus to some degree compensating for the lower signal intensity from the reduced light emission.

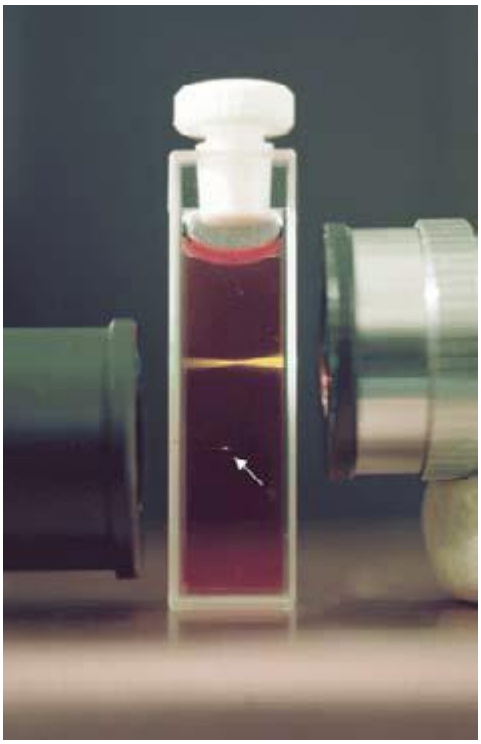

Figure 1.23 this figure is a classic diagram showing the fundamental difference between conventional confocal excitation and two-photon excitation. (Figure supplies by Amos)

Light sources are an important factor in two-photon imaging as well as need long wavelengths (typically into the near IR) the light source must be pulsed, omitting the photons in pulse typical between 100-200 femto-seconds, this is to increase the photon density required to generate the two photon effect while keeping the average power of the laser light down to a minimum amount. Ti-sapphire lasers have been the traditional choice of light source for two-photon imaging due to there ability the tune wavelengths as well as produce pulsed laser light at the near-IR wavelengths. A second important aspect of two-photon system design is the effect the glass has on the pulse width, glass causes the pulse widths to broaden, shorter pulse widths are effected more severely by the effects of scattering, thus limiting the depths of tissue imaging that can be obtained, longer pulse widths will reduce the two photon efficiency. It is difficult to know the optimum pulse width for cardiac muscle as there are no lasers that are able to offer a tuneable pulse width. Whoever both Coherent and spectra physics perceive the ideal pulse width for two-photon imaging two be 140 femto-seconds and design there lasers accordingly.

1.8.5 Structured light

Structured light is a relatively new method for achieving optical sectioning by patterning the excitation light of an imaging system. It has applications for both high speed imaging as well as super resolution. This is achieved by controlling the illumination patterns of the excitation light. This patterning of the light can be achieved by different methods that are detailed below (Fedosseev *et al.*, 2005).

1.8.6 Spinning disk confocal

Multiple beams of light can be used to capture data at a much faster rate, the speed of capture for these systems is determined by the specifications of the camera used. These confocal microscopes are called spinning disk confocal microscopes, which are equipped with a dual set of disks known as Nipkow disks. The first disk has an array of pinholes with micro-lenses which are designed to focus light on to the pinhole of a second disk. In-between the disks, there is a dichroic mirror that reflects the emission light towards a CCD camera. The spinning disk system will generate a set illumination pattern that will be determined by the pinhole array on the disk. One limitation of the spinning disk is that the pinholes are of a fixed size. This can cause a number of problems; the optimum pinhole size will change depending on emission wavelength. If the pinhole is too wide, it will affect the Z sectioning capabilities. There is also a threat of "crosstalk" where emission light from one pinhole could travel through a different pinhole. Most spinning disk manufacturers opt for a very small pinhole size that will increase the Z sectioning capability and nearly eliminate the "crosstalk" problem. The down side of this is that a lot of emission light is lost. Figure 1.24 show a schematic representation of the spinning disc system. (Wang *et al.*, 2005).

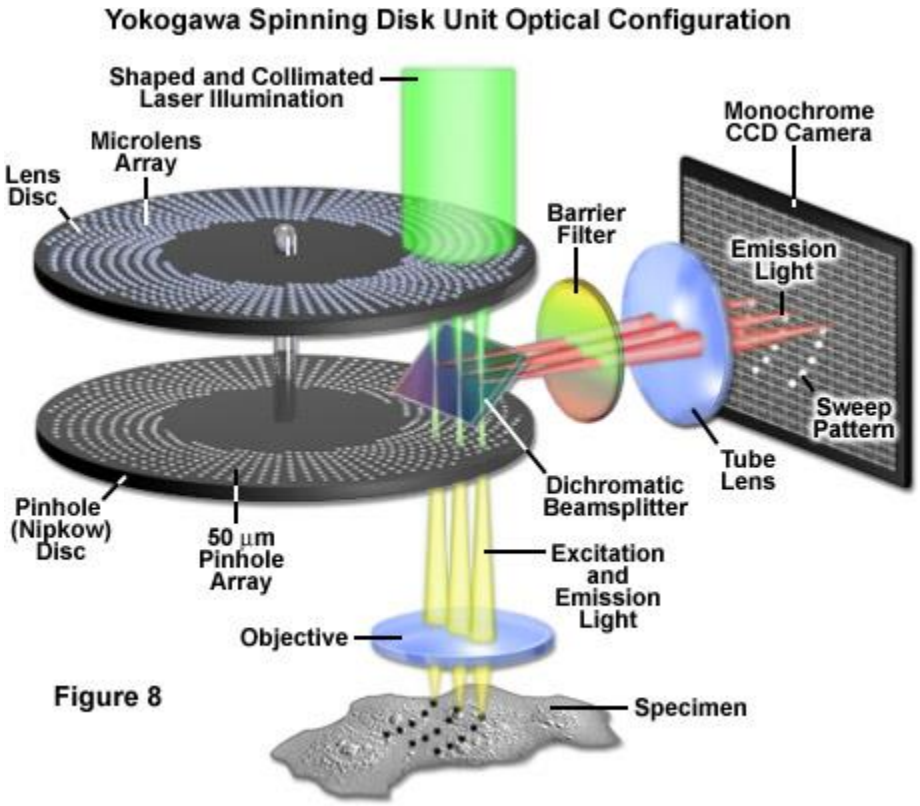

Figure 1.24: The operating principle of a spinning disc confocal microscope. Figure supplied by Zeiss

1.8.6.1 Selective illumination device

The selective illumination device has two aspects which shall be discussed in this review. The first is the Spatial Light Modulator (SLM) and the second is simultaneous acquisition of the conjugate and non-conjugate image. The spatial light modulator and pattern generation will be discussed in more detail in chapters 2 and 3 (Fulwyler *et al.*, 2005; Fedosseev *et al.*, 2005a, 2005b;Hagen *et al.*, 2007;Beversluis *et al.*, 2008;Neil *et al.*, 1997).

1.8.6.2 The Potential of the Selective Illumination Device

It is possible for the selective illumination microscope prototype to optically section samples. The result is similar to a Nipkow spinning disk system. However, the selective illumination microscope prototype system will be able to generate a series of patterns determined by the operator. It is also possible to have some crude control over the

pinhole size by activating neighbouring pixels. Figures 1.25 and 1.26 show how the excitation light enters the SIMP and is directed through the system.

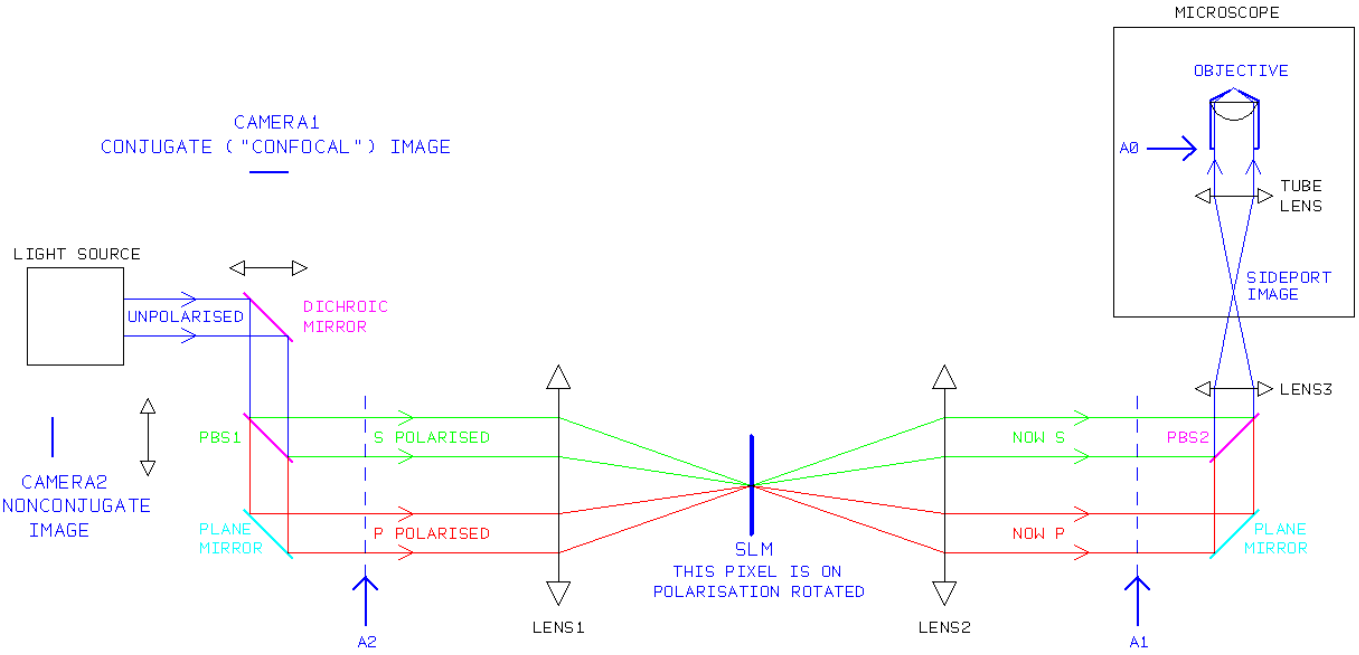

Figure 1.25: Theoretical layout of the SIMP. The a excitation light path through to an "on" pixel where the polarisation of the light has been rotated thus the light is reflected into the microscope. The SLM sits on an image plane. A1 and A2 denoted the aperture planes.

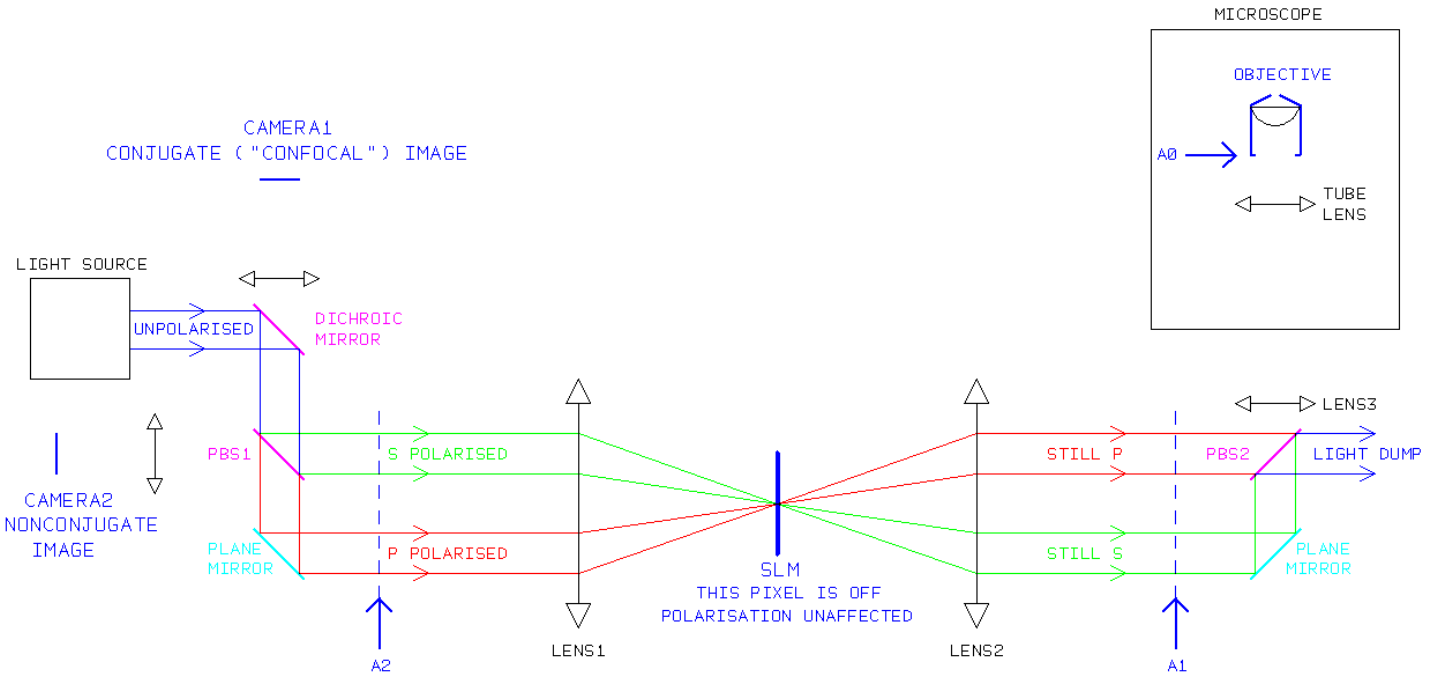

Figure 1.26: Theoretical layout of the SIMP. Where the excitation light is being put through the system and transmitted to an "off" pixel where the polarisation of the light has left as its original polarisation, the light in this path is reflected into a beam dump.

The spatial light modulator is actually a reflective polarising device it so that lenses one and two in Figure 1.5 are in fact different parts of the same parabolic mirror acting as a lens, this enables the beams to be steered towards separate beam splitters. This means that the emission and excitation light paths are travelling along the same beam path most of the time. The excitation light is then reflected onto a polarized beam splitter, which splits the light into P and S polarizations. Where the light is split into two pathways, they both will be directed through the SLM. If the light hits an "ON" pixel, the light's polarization will be rotated, and then the light will travel along the first pathway through the polarized beam splitter where it will be reflected into the microscope objective lens. If the light hits an "OFF" pixel, it will travel along the second pathway, then through into the second polarized beam splitter where the light will be discarded.

The emission light that returns from the microscope will hit the second beam splitter and will be split into P and S polarizations. The two distinct light paths are then directed onto the SLM. If the light hits an "OFF" pixel, the light's polarization remains unchanged, and

it travels to the Camera collecting the non-conjugate image. If the light is to hit an “ON” pixel, the polarization will be rotated by 90 degrees and then will be directed into the conjugate camera image. this is show in figures 1.27 and 1.28

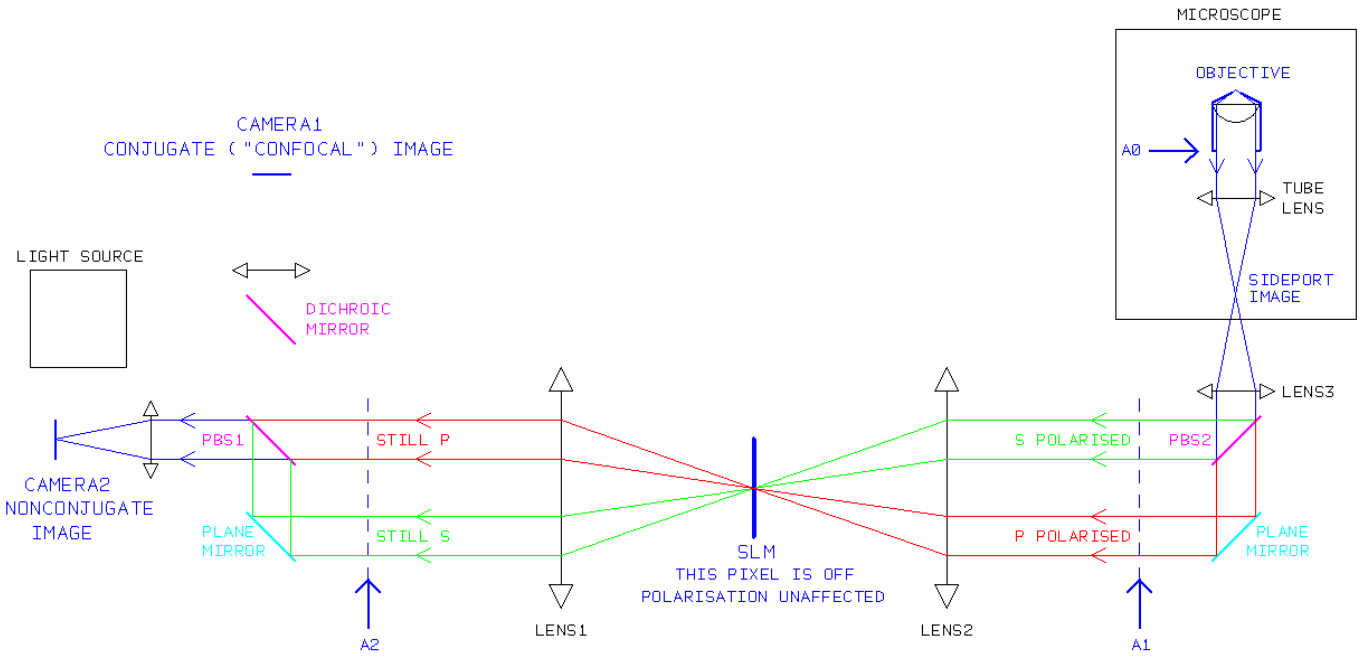

Figure 1.27: Theoretical layout of the SIMP. Where the emission light is returning from the microscope, light is being put through the system it is transmitted to an “off” pixel where the polarisation of the light has left as its original polarisation, the light in this path is reflected into camera 2 which is forming the non-conjugate image.

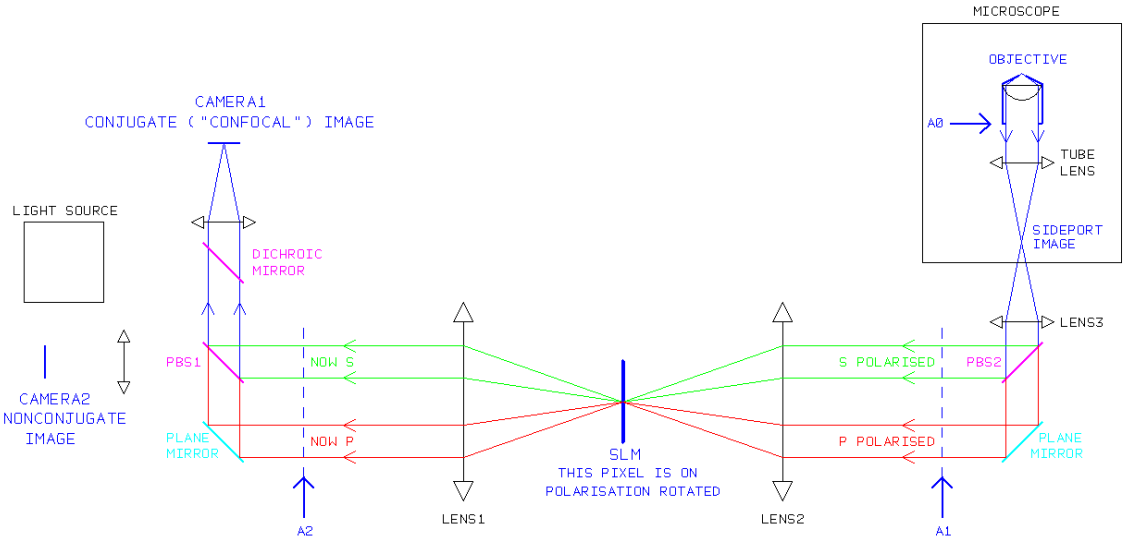

Figure 1.28: Theoretical layout of the SIMP. Where the emission light is returning from the microscope. Light is being put through the system it is transmitted to an "on" pixel where the polarisation of the polarisation of the light is rotated, the light in this path is reflected into camera 1 which is forming the conjugate image.

1.8.6.3 Spatial Light Modulator

A spatial light modulator is an array which a beam pathway can be passed through or reflected depending on the spatial light modulator design. The spatial light modulator can modify the intensity or the polarity of different parts of the beam. It is constructed via a series of pixels. In the case of the Selective Illumination Microscope Prototype (SIMP), there is a matrix which is 1280x1040 pixels. Each of these pixels has two states, ON and OFF. When a pixel is active, it will change the polarity of the light that passes through the pixel by 90 degrees. When a pixel is inactive, the polarity remains unchanged. The spatial light modulator has a display rate of 1440 Hz. With the use of a polarized beam splitter, it enables twin path illumination (Hanley *et al.*, 1999).

1.8.6.4 Conjugate and Non-conjugate Image Pathways

When the spatial light modulator has split the emission light into two separate light paths, the information from one light path can be thought of as a confocal image where the

image has been optically sectioned. The second light path can be thought of as information regarding the wide field image. (Heintzmann *et al.*, 2001).

1.8.6.5 Light sources for the Selective Illumination Microscope Prototype

The selective illumination microscope prototype has a port through which a variety of LEDs can be attached. This means that it is possible to use a variety of wavelengths at a relatively low cost. Using LEDs as a light source has been very successful. However, for some uses of the selective illumination microscope prototype there may not be enough power generated by the LED, for instance, illuminating tissue markers that are only weakly stimulated by the wavelength in use. The largest laser diameter is 3 mm, which is produced by a Nd:YAG laser which produces light at 355 nm. The light source in the selective illumination microscope prototype will need to evenly illuminate the back aperture if the objective attached to the spatial light modulator which has a diameter of approximately 2 cm. This means that whatever laser is used it will need to undergo beam expansion.

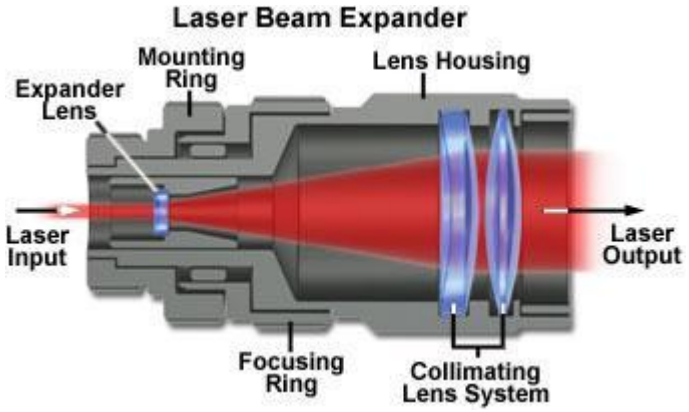

Figure 1.27: The basic layout of an optical beam expander. Figure supplied by Olympus.

1.8.6.6 Laser Beam Expander

There are two types of laser beam expander. A Keplerian beam expander will cause the beam to invert itself and to broaden, while a Galilean beam expander will expand the beam while not inverting it. One problem associated with laser beam expansion is laser speckle, which is a random intensity pattern produced by the interference from a set of

wave fronts. Laser speckle can become a major issue when a laser beam is expanded due to the waves becoming incoherent and interfering with each other causing a random wave motion. If there is laser speckle on the SLM, this will have disastrous consequences as the field of view will be unevenly illuminated. Laser speckle can be eliminated by vibrating the light guide at a frequency greater than the frequency which is being imaged this was done in a similar PAM set up in Oxford (Faivre Olivier, 2012)

1.9 Types of detector used in imaging systems

There are two types of detector, cameras, and photomultiplier tubes.

1.9.1 Photomultiplier tubes (PMT)

A PMT is a detector commonly used to detect photons. It is capable of responding to a single photon. The main component of the PMT is the photocathode. It is located at the aperture, which is covered with a sheet of glass or quartz. The photocathode will transfer the energy of a photon to an electron. The surplus energy from the transfer will turn to kinetic energy that will enable the electron to negate the draw of the photocathode surface. Figure 1.28 shows a schematic representation of the PMT.

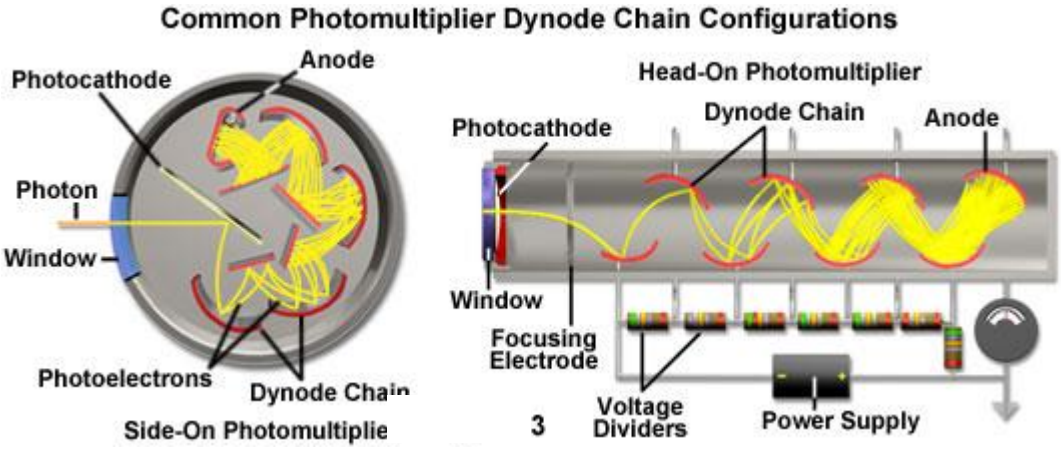

Figure 1.28: Diagram of a photo multiplier tube. The diagram highlights how a photon entering the PMT would be converted to an electron and the resulting cascade event that occurs through the dynode chain. Figure supplied by Olympus.

The PMT consists of a series of electron multipliers called dynodes. The last piece in the PMT is the anode which completes the circuit. The voltage to the dynodes can be controlled, the higher the voltage the more electrons it will generate when the dynode is stimulated by electrons coming into contact with a dynode. There are focusing electrodes that direct the electrons to the first dynode so that the electrons do not "skip" dynodes.

The PMT photo cathode is constructed from alkali metals or semiconductors and is designed to respond to a wavelength region dependent on what base metal was used to make the PMT. The sensitivity of the PMT can be calculated by:

Equation 1.23

$$R = \frac{q.QE.q}{hc}$$

Where R is the response. q is the charge of an electron, QE is the quantum efficiency of the photosensitive surface, h is Planck's constant and c is the speed of light. The QE of PMTs can vary greatly; the first PMT made in 1935 had a peak QE of 0.04, now the highest peak QE is 0.36 (Mirzoyan *et al.*, 2006).

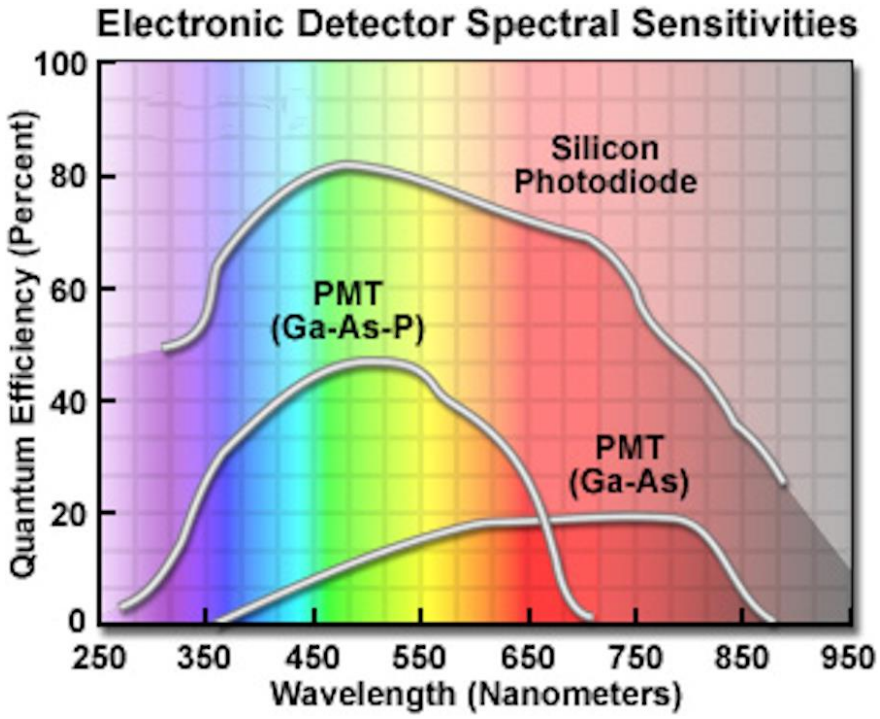

Figure 1.29: How different compositions of photocathode react across the spectrum. The quantum efficiency (QE) is shown as a logarithmic percentage. This shows how the composition of the metal will determine how the PMT responds to various wavelengths of light as well as the quantum efficiency of each wavelength. Figure supplied by Hamamatsu**.**

1.9.2 Charge-Coupled Device

A Charge-Coupled Device (CCD) is a grid of charge registers that have the capability to store charge. This grid is exposed to a stream of photons over a set period of time. Each area of the grid will then have an associated charge dependent on the number of photons that was detected by each charge register. Most CCDs have a sense zone and a read zone; once the sense zone has been exposed the charges are moved down to the read zone and read out while the sense zone is exposed again. The charge is moved through a series of registers to a line of registers at the side of the grid one row at a time. This line of registers then moves the line forward one space at a time where the signal for that grid space is amplified and fed through an analogue to digital converter. The CCD camera has high QE but can be prone to read out noise. Measures have been developed to limit the different types of noise. Cooling the CCD will reduce the dark noise dramatically;

cooling the camera by 20^{o}C can cause a reduction in noise by a factor of 10. Read noise can be generated by the amplifier and analogue to digital converter. Slowing the speed at which the analogue to digital converter processes the signal will cause a reduction in noise. Adding spaces in the grid together will increase the signal to noise ratio and will effectively increase the speed at which a frame can be digitised but there will be a loss of resolution. Back thinned CCD cameras use a novel arrangement of the imaging elements to increase the amount of light captured and thereby increase the QE.

Figure 1.30 shows the two different types of architecture that exists with high performance CCD sensors, the first type is frame transfer CCD, where the accumulated charge from the sensors must be shifted vertically row by row into the serial output register, a disadvantage of this system is “light smearing” where light falls on the pixels while they are being read out. This can be over come by moving the entire frame down into a storage section, which is similar to the CCD. However this slows the speed at which the camera can be driven. Alternatively a mechanical shutter could be used or the illumination light source could be deactivated.

Interline CCDs have there transfer channels immediately adjacent to each photodiode, this make the process faster, however they have a disadvantage that the interline reduces the light sensitive area of the sensor, this can be partially compensated for by micro lens arrays.

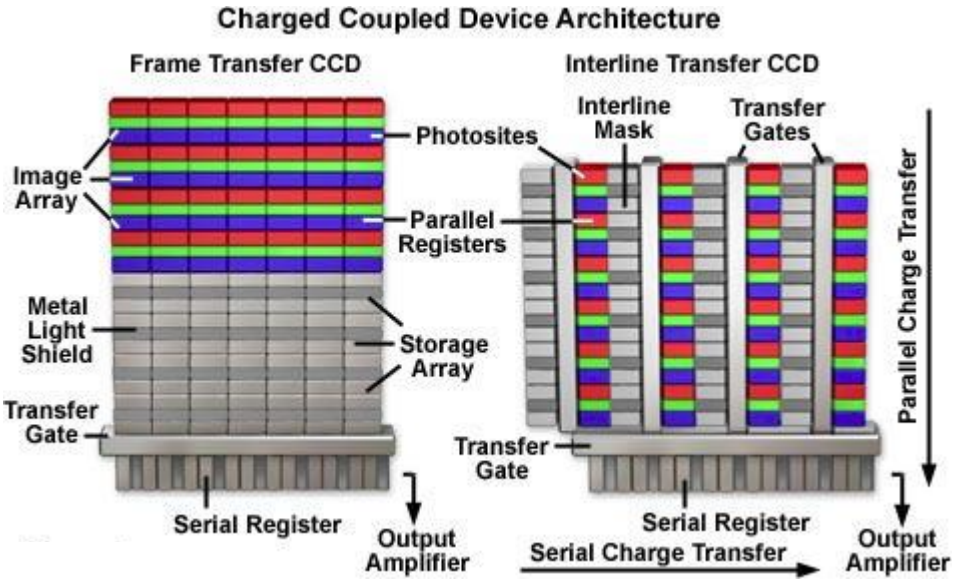

Figure 1.30: The two different types of CCD Architecture.
Image supplied by http://micro.magnet.fsu.edu.

Interline-transfer CCD arrays normally contain micro lens array to focus the light on to the photo sensitive part of the array. The charge transfer channel is immediately adjacent to the well so that the charge can be transferred to the channel. Frame transfer CCDs have a second part of the sensor that is covered with a mask. The charge from the photo-sensitive part of the CCD is move down the register where it is read out.

1.9.3 Electron Multiplying Charge-Coupled Device

An electron multiplying Charge-Coupled Device (EMCCD) has a gain register between the charge registers and the readout amplifier. The gain register acts can be thought of as an array of small PMTs, multiplying the number of photons before it hits the charge register. When the gain register is active the electrons per photon is increased. However when the gain registers are not active the QE is much lower than that of a normal CCD camera as the photons have to pass through the gain register apparatus before hitting the charge register. When charge is shifted pixel to pixel towards the output amplifier there is a very small probability that charges cause additional charges. In a conventional CCD this event is almost undetectable. However in an EMCCD camera this erroneous charge will be amplified through the gain registers, leading to a significant noise factor. EMCCD cameras are useful because they are capable of generating an acceptable signal to noise

ratio where signals are to weak for other cameras to generate acceptable signals. As figure 1.11 demonstrates

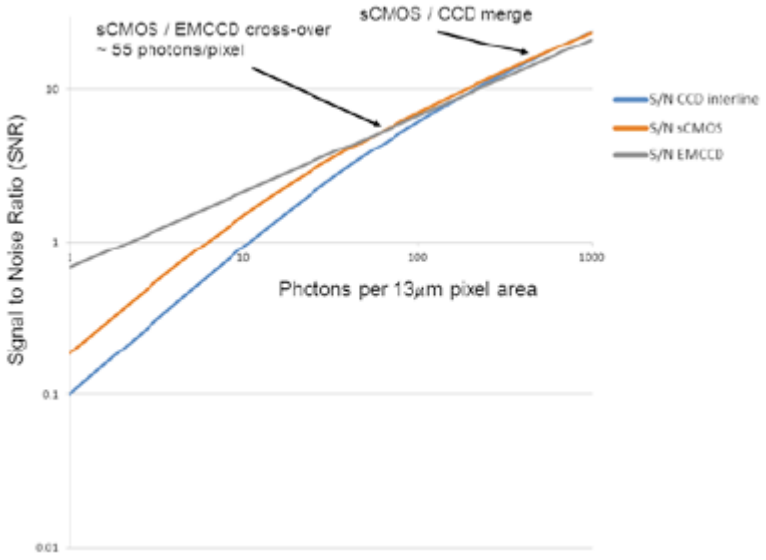

Figure 1.31 Shows the signal to noise ratio of different sensor types as light levels become lower. Figure supplied by Andor.

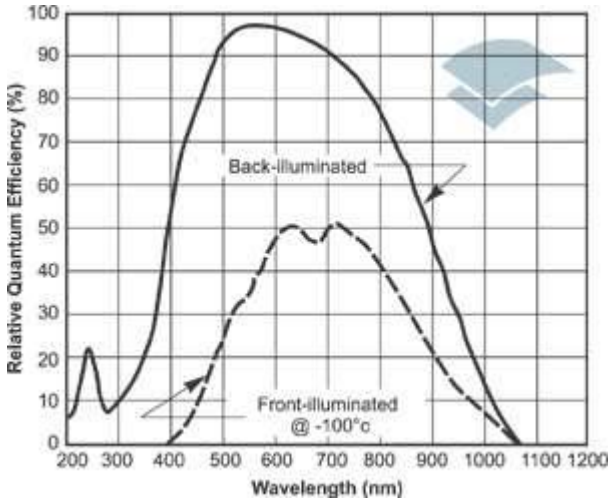

Figure 1.32 QE of front illuminated and back illuminated CCD cameras across the spectral range. Figure supplied by Andor.

1.9.4 Scientific Complementary Metal Oxide Semiconductor (SCMOS)

CMOS chips were invented around the same time as CCDs, however these were traditionally thought of as a poor compromise to CCDs due to the potential of the well

being different sizes, therefore no pixel could be compared to its neighbour. CMOS sensors convert charge to a voltage that can immediately be read off, meaning that CMOS sensors can read data at a far faster rate than a CCD. This has stimulated research into producing high quality scientific CMOS cameras. Recently Andor and Hamamatsu have released scientific grade CMOS cameras. Andor's camera is termed the Neo sCMOS Camera and Hamamatsu is termed the flash sensor. These cameras offer fast frame rates (of up to 100 frames per second), low read noise and high dynamic range, but are not as sensitive as the EMCCD cameras currently on the market and do not have the same binning advantages of CCD systems, making them less versatile.

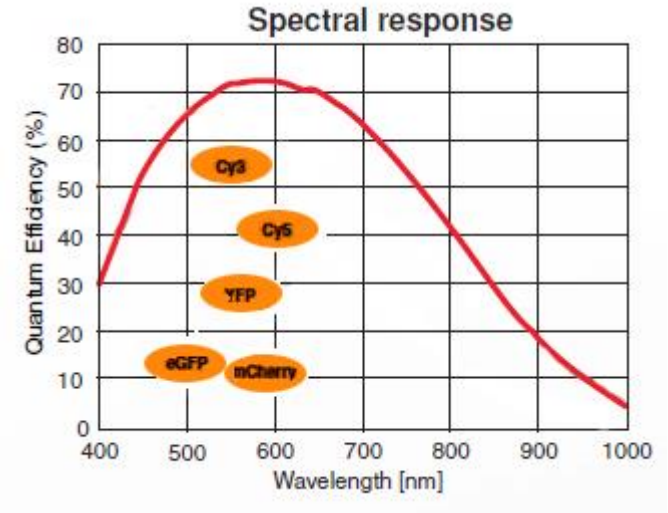

Figure 1.33: The QE of a sCMOS camera across the spectral range. Figure supplied by Hamamatsu.

1.9.5 Cameras and Pixel size

Pixel size is of vital importance on cameras as they do not have the advantage of PMT based scanning system where the pixel size of the image based on the setting selected by the scanning head can be altered (the smallest point that can be resolved is calculated by Equation 1.24). This means that the pixel size is dependent on the wavelength used and the objective used. To gain maximum resolution benefits the resolution should be sampled at the Nyquist rate.

Therefore the optimum pixel size for an imaging system can be calculated as

Equation 1.24

$$P = \left(\frac{\left(\frac{0.61\lambda}{NA} \right) M}{2} \right)$$

Where P= pixel size, λ= wavelength, NA= Numerical aperture, and M= magnification,

To calculate the optimum magnification, Equation 1.25 is rearranged to

Equation 1.25

$$M = \frac{2P}{\left(\frac{0.61\lambda}{NA} \right)}$$

2 Chapter 2: Methods

2.1 Cell dissociation

To isolate single heart cells from the myocardium the connective tissue matrix surrounding the cells has to be digested using the enzyme collagenase. This is done by perfusing isolated hearts with a collagenase containing solution as described below (These procedures were slightly different when applied to rabbit and rat hearts).

The physiological saline solution (Krebs' solution) used had the following composition (in mM); NaCl (120), HEPES (20), KCl (5.4), NaH_2PO_4 (0.52), $MgCl_2$ (3.5), taurine (20), creatine (10), Glucose (11.1). The solution is set to a pH of 7.4 at 37^{o}C with NaOH.

2.1.1 Rabbit Cell Dissociation

Surgical removal of the heart was a licensed procedure, performed by one of two technicians (Aileen Rankin or Michael Dunne) licensed to carry out the procedure. Male New Zealand White rabbits (3.0-3.5 kg body weight) were given an intravenous injection of 2500 IU Heparin together with an overdose of sodium pentobarbitone (100 mg/kg) via the left marginal ear vein. The heart was excised and immersed in chilled (4°C) Krebs' solution. The heart was then cannulated via the aorta onto a Langendorff perfusion system and perfused retrogradely at a constant flow of 25 mL/min. 200 mL of nominally Ca^{2+}-free Krebs' solution, maintained at 37°C, was initially perfused through the heart to wash out blood. The heart was then perfused with collagenase/protease solution (3 mg Protease and 50 mg collagenase type II, dissolved in 75 ml Ca^{2+}-free, sterile Krebs' solution for approximately 5 minutes). The enzyme solution was washed out of the heart by perfusion with 100 mL sterile Krebs' solution containing 1 % (w/v) Bovine Serum Albumin (BSA) for approximately 2 minutes. The ventricles were then cut from the heart and finely chopped. The myocytes were dissociated by lightly titurating the solution using a plastic Pasteur pipette. The dissociated cardiac myocytes were filtered through a gauze mesh to remove undigested and other tissues.

2.1.2 Rat Cell Dissociation

Male Wistar rats (250-350g body weight) were sacrificed by a concussive blow to the head followed by cervical dislocation. The heart was then removed and placed into a beaker with 25 ml of chilled Krebs' solution with 1250 IU of heparin to prevent the blood from coagulating. The heart was then attached to a cannula of a Langendorff perfusion system and perfused with Krebs' solution at 37^{o}C until all the blood has been washed out of the heart. After this, a solution consisting of 70 ml Krebs' solution containing 50 mg collagenase type 1 (Sigma Aldrich) and 3 mg protease (Sigma) was perfused through the heart. The heart was carefully monitored for signs of digestion, as the perfusion proceeds the heart becomes soft and slimy to touch and the atria have become translucent. The process normally takes 6 to 10 minutes. Once the heart has been suitably digested, the heart is then cut down from the Langendorff perfusion system and immersed in Krebs' solution containing bovine serum albumin (BSA, Sigma Aldrich), the role of the bovine serum albumin is to disable the collagenase enzyme and stop the digestion process. The heart is then cut into pieces and shaken so that cardiomyocytes break away from the main body of the tissue.

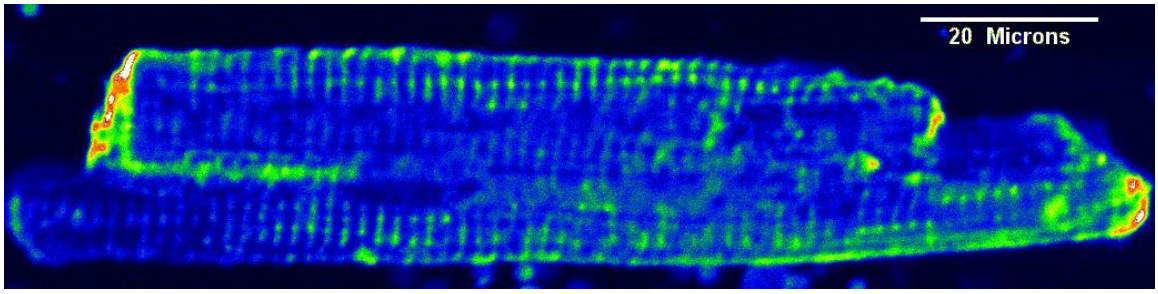

Figure 2.1 shows a typical healthy cardiomyocyte stained with Di-4-anepps excited at 488nm and collected at 505nm and longer and imagined confocal using a Nikon 60x NA 1.2 on a Biorad Radiance 2000.

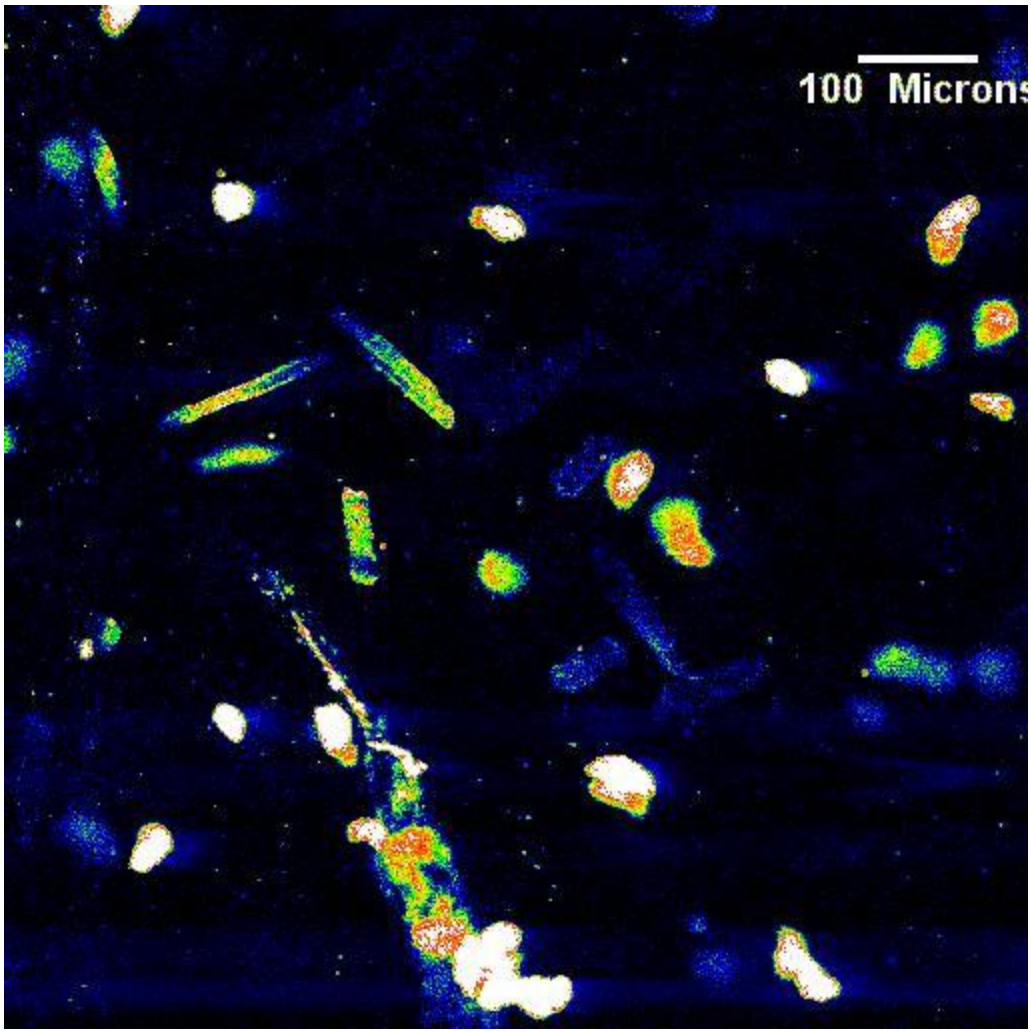

Figure 2.2 A typical sample of cells from a digested rat heart. The approximately round structures are hyper-contracted (damaged) cells, the rod shaped structures are intact, viable heart cells.

A healthy cardiac cell is approximately 120 µm in length and 20x30-40 µm in width and depth. These living cells are described as "rods". The digestion process used to dissociate heart cells damages many cells. Once the membrane of a cell has been ruptured, calcium freely enters the cell causing the cell to hyper-contract into a structure approximately 50 µm in all dimensions. These cells are described as "balls". A typical dissociation process can yield anything from 60% to 80% of the cells as balls (Goldman & Wurzel, 1995).

2.2 Purification of living cardiac cells

There are many reasons that a 100 % rod solution would be desirable. Cardiac cell culture requires a high ratio of rods:

(i) Western blots, protein phosphorylation and measurements of large collections of cells become more meaningful if the balls are removed or at least are present in a constant ratio.

(ii) Microstructures can become blocked with balls and therefore need special skills to move rods into structures. With a 100% rod solution, it would be possible to make microstructures for a wider audience and speed up the experimental process.

(iii) Unpublished observations from laboratory work suggest that the life-time of the rods is longer when in a solution containing fewer balls.

2.2.1 Separation by fluid dynamics

2.2.1.1 Sedimentation

It has been observed that balls settle in solution at a faster rate than rods. This can be explained when calculating the Stokes drag forces, which are represented as:

Equation 2.1

$$F_d = -bv$$

Where b is dependent on the properties of the fluid and the dimensions of the object, and v is the velocity of the object.

For a spherical object b is given as:

Equation 2.2

$$b = 6\pi\eta r$$

Where r is the Stokes radius of the particle and η is the fluid viscosity. The drag force for a rod can be representation of a series of spheres in parallel, as the rod will orientate itself

to present the shape that will present the least drag. Due the much smaller diameter of the end of the rod compared to the ball the rod is observed falling at a faster rate than the balls, thus showing that it maybe possible to separate the cells with the use of flow gradients.

In order to purify the rod solution a simple set up was created using an~60cm column with an inner diameter of 0.5 cm. A pipe was attached at the bottom to form a "U" bend, and then the tubing went to the same height as the top of the column. A peristaltic pump fed the end with the pipe so the flow rate could be controlled. The concept was to match the flow rate of the rods so the balls would fall to the bottom of the column (Murthy *et al.*, 2006). The flow rate was started at 25 mL/min, as the diameter of the inside of the tube was 5 mm. The volume for a one 1 cm segment of the tube can be calculated using the following formula.

Equation 2.3

$$V= \pi r^2 h$$

V is calculated at 0.19 cm^2 Therefore to calculate ml/min at 25 ml/min entering a 5 mm pipe, 0.95 cm of pipe is needed to contain one ml of fluid. Therefore the flow is 0.23 m/min. It was assumed that the Krebs' solution in which the cells were suspended has similar fluidic properties to water at room temperature. The dynamic viscosity of water at 20°C is 1.002, the kinematic viscosity is 1.004 and the fluid density is 998.2 kg/m^3. For this principle to work, laminar flow would need to be established in the tube with the rising flow. For laminar flow there needs to be a Reynolds number less than 2000.

The Reynolds's number can be expressed as:

Equation 2.4

$$\mathrm{Re} = \frac{\rho V d}{\mu}$$

Where Re is the Reynolds number, ρ is the fluid density and μ is fluid viscosity, V is the characteristic velocity give in metres/s and *d* is the characteristic length of flow in mm. the Reynolds number for this particular set up is calculated as 139260. This Reynolds

number is far higher than 2000. Therefore, very turbulent flow can be expected. This was what was observed in practice and thus the rods where unable to be separated from the balls.

For laminar flow to be achieved the formula is rearranged to:

Equation 2.5

$$V = \frac{\mathrm{Re} \bullet \mu}{\rho d}$$

V is calculated as 0.0033 in this set up, the diameter of the tube would need to be impractically small for the rod and ball solution not to become blocked.

2.2.2 Elutriation

Elutriation works on a similar principle to the method above. However, the column is in a centrifuge so the force of gravity can be altered by the cycle rate. There is also a chamber in the return path which increases in diameter so that flow slows and different sizes of particles sit on various parts of the chamber and can be removed by increasing the flow or slowing the spin speed (Diamant *et al.*, 1989; Goldman & Wurzel, 1995,).

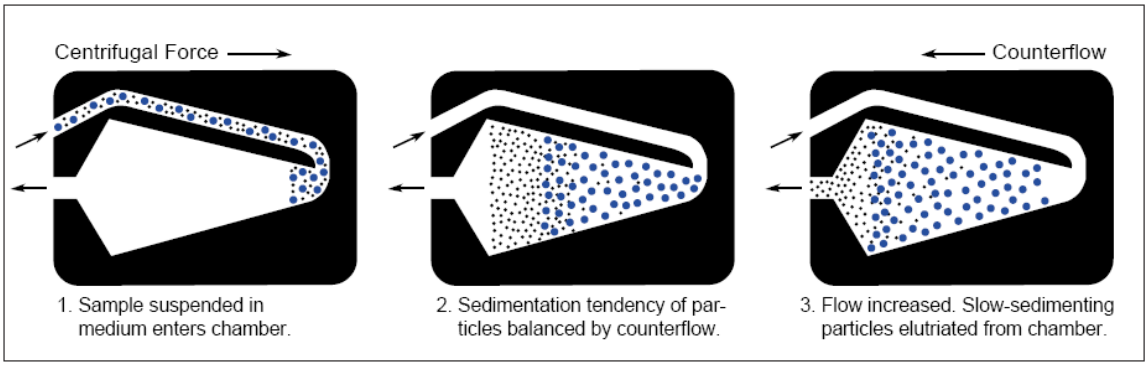

Figure 2.3 Diagram highlighting the operating principles of elutriation. Figure supplied by Beckman Coulter.

A Beckmann Coulter elutriation system was set up with a JE-5.0 rotor and a single 40 ml chamber and peristaltic pump. The first tests were conducted using blood, as one of the primary purposes of the device is to isolate different blood cell fractions and should represent the normal working range of the system. The chamber was photographed to monitor the position of the blood cells in the chamber.

In theory, blood cells are fairly uniform and should have a thickness of around 2-3 µm and a diameter of 7 µm. This should create a banding of red blood cells in the chamber. What was observed there was a continuous presence of blood cells in the chamber, this suggests that the cells are of different sizes, this is possibly because the cells were dying due to bursting causing the haemoglobin would leak out, and because of its small size (80 – 200 nm) haemoglobin would then immediately leave the system (Bauer & Hannig, 1988; Boerma *et al.*, 2002).

Table 2.1: Elutriation buffer

Chemical	Formula Weight	Concentration	2L
NaCl	58.44	125mM	14.61g
KCl	74.55	2.6mM	0.387g
Na_2HPO_4	141.95	8.1mM	2.299g
KH_2PO_4	136.08	1.4mM	0.381g
Glucose	180	50mM	18g
BSA	0.5%		10g

Table 2.1 contains details on the solution that was used in the elutriation system.

Above is the solution used to separate red blood cells into different categories. The solution would be expected to be viscous towards the thinner end of the chamber where the larger molecules where being held. This is not what was observed, which suggested that cells were becoming deformed.

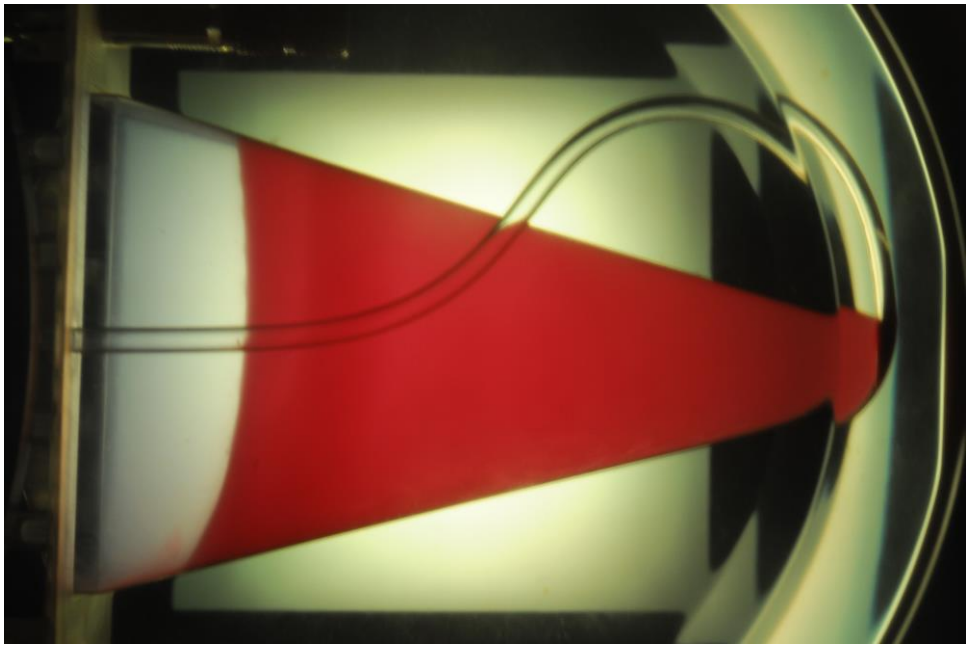

Figure 2.4 shows the chamber of the elutriation system while it is active, there are red blood cells in the chamber with 18 mL/min flowing through and the centrifuge is set to 2,000 RPM. There is no banding of the blood cells and there is a small "leak" from the left-hand side of the chamber.

2.2.2.1 Protocol for elutriation

Use the 5 ml chamber, suspend the cells in 1 or 2 ml, adjust the rotor speed such that 200-300 g are effective at the peripheral end of the chamber (where the cells enter), After equilibration of the chamber (removing air bubbles, etc.), the counter flow is turned off. Fill the hose between cell injection point (e.g. three-way valve) and the point where the hose reaches the centrifuge (do not inject cells into the rotor at this point) Turn on the counter flow and drive the cells into the rotor with a counter flow rate of >80 mL/min. Collect about 100 mL of the fluid leaving the centrifuge. Check whether the cells were driven through the rotor. If the cells were driven through, repeat the experiment at a lower counter flow rate (at a counter flow rate were only about 50% of the cells can be collected you may check whether one or the other type of cells are enriched in the fluid leaving the centrifuge by examining the fluid with a light microscope).

The formula for converting the G-force into revolutions per minute (RPM) in a centrifuge is:

Equation 2.6

$$G = (1.118\text{x}10 - 5)\text{RS}^2$$

Where G = relative centrifugal force (which can be expressed as G-force), R is the radius of the rotor arm to the point where the specified force should be exerted expressed in cm, and S is the rpm that the rotor is turning (Thompson *et al.*, 1984).

To calculate the RPM needed to exert 200-300g of force at the end of the chamber the formula is rewritten to.

Equation 2.7

$$S = \left(\frac{G}{(1.118\text{x}10 - 5)\text{R}} \right)^{0.5}$$

The distance from the end of the chamber to the centre point on the Beckmann Coulter J.E 5.0 rotor is 17cm. therefore 200g S= 1025.8rpm For 300g S= 1256.4rpm.

However this method was still found to be unsuitable for separating rods and balls mainly due to the size of the chamber being too large to allow the desired flow rates to be achieved due to the impractically large volume that would be required of the peristaltic pump to move.

2.2.3 Separation with the use of Percoll gradients

Percoll is a substance used to separate many cell types, although its main use is for separating much smaller specimens than cardiac myocytes. Percoll works by separating objects based on their density. This is done using low speed centrifugation where a density gradient is set. Percoll is iso-osmotic, non toxic and can easily be removed from the solution after purification, making it an ideal medium to use with live cells.

A low G-force centrifuge was used with 7.5 ml chambers. Tubes loaded with a 5 ml mixture of 60 % Krebs' solution and 40 % Percoll solutions (Sigma Aldrich) were spun at 20 kg of force for 50 minutes, slow speed up and soft stops were used to ensure the gradient was not disturbed. Then 2 ml of Krebs' solution containing live ("rods") and dead ("balls") cardiomyocytes were gently added to the top of the tube, and spun in the centrifuge at 15 kg for 4 minutes. This was able to produce an upper "scattered" band of balls with some rods. Once this was carefully removed there was a thin band that contained a 100% rod solution.

2.3 Imaging systems

The confocal and two-photon systems were used mostly in frame scanning mode and used to acquire optically sectioned Z-stacks. The pinhole was set to one Airy disc, which gave optimum optical sectioning capabilities of the system. Slower scanning or Kalman averaging was used where noise became an issue.

2.3.1 Confocal systems

A variety of confocal and two-photon systems were used in this project. They were:

Microscope System	Objectives
Zeiss 510	C-Apochromat 63x/1.2 W Corr
	Plan-Apochromat 20x/0.75
	Plan-Apochromat 63x/1.4 Oil DIC
BioRad 2000	Nikon Plan Flour 10x NA 0.3
	Plan Flour 20x NA 0.75
	Plan Flour 40x NA 1.2
	Plan APO 60x NA 1.2
Olympus FluoView	Uplsapo 60x Oil NA:1.35
TM FV1000	Plapon 60x Oil NA:1.42

2.3.2 Two –photon systems

Microscope System	Objectives
Zeiss 510	Achroplan IR 40x/0.8 W
	N-Achroplan 10x/0.3 W
BioRad 2000	Nikon Plan Flour 10x NA 0.3
	Plan Flour 20x NA 0.75
	Plan Flour 40x NA 1.2
	Plan APO 60x NA 1.2

2.4 Point Spread Function Methods

2.4.1 Calculating PSF

It is possible to calculate the theoretical FWHM of the PSF for confocal microscopes using the following formula (Miks *et al.*, 2007);

Equation 2.8

$$\bar{\lambda} = \frac{\lambda_{ex}\lambda_{em}}{\sqrt{\frac{\lambda_{ex}{}^2 + \lambda_{em}{}^2}{2}}}$$

Equation 2.9

$$FHWM_r = \frac{0.36\bar{\lambda}}{NA}\sqrt{\frac{\lambda_{ex}{}^2 + \lambda_{em}{}^2}{\lambda_{em}{}^2 + \frac{\lambda_{ex}{}^2}{1+\left(\frac{1.552NA \bullet PH_d}{\lambda_{em}Mm}\right)^2}}}$$

Where;

λ_{ex} = wavelength of excited light (nm)

λ_{em} = Wavelength of emitted light (nm)

NA = numerical aperture of objective lens

n = refractive index of medium

m = magnification of the objective

M = Secondary magnification

PH_D = pin hole aperture (μm)

2.4.2 Measuring point and edge spread functions

The best method for measuring the PSF is by imaging sub-resolution highly fluorescent beads somewhere in the order of 50 nm-200 nm. The imaging system will be able to detect the fluorescence but will be unable to resolve the bead. Hence, the bead will appear as the smallest item the objective can resolve with the edges blurred. A variation of the measurement of a sub-resolution point is to measure a sub-resolution edge spread

to generate an edge-spread function, which is taken individually for the X, Y and Z axes. As the edge is highly polished any defects in the surface are smaller than the resolving power of an optical microscope. Edge spread functions also have an advantage as it is easy to identify any non-evenly illuminated surfaces caused by misalignment of the system. It will also give a higher signal-to-noise ratio making intensity measurements more accurate. However, this method will not reveal as many imperfections in the optics as the comparable PSF, for example, detecting spherical aberrations and coma (Rossmann, 1969).

Beads measuring 200 nm in diameter were used. The beads used in the data presented were supplied by Invitrogen (TetraSpeck™ Fluorescent Microspheres Size Kit Cat. No. T14792). These beads came premounted and have been coated with four different dyes; with excitation peak at 365 and emission at 430 nm (blue), excitation peak at 505 and emission at 515 nm (green), excitation peak at 560 and emission at 580 nm (orange), and excitation peak at 660 and emission at 680 nm (dark red). These dyes have been selected so that the emission and excitation peaks are separate.

Beads were tested against a second method in which 170 µm thick cover slips were cleaned, and the beads were left to adhere to the cover glass by a process of evaporation. It was found that the Invitrogen slide produced reproducible results. The lab prepared slide had some beads which did not bind to the cover slip, introducing a refractive index change between the cover slide and the bead. It was also observed that there could be fluorescent material found in the immersion medium of the beads using the lab prepared slide.

Another advantage to the Invitrogen slide is the four dye system. This enables the Invitrogen slide to be used in a variety of machines where the excitation wavelengths were limited. However, it is less than ideal to compare imaging systems that using different wavelengths as the resolution is dependent on the wavelength. The Invitrogen slide was constructed in such a way as to avoid these problems. Due to the manufacturing process, the beads are within 10% of their target 200 nm sizes, therefore this did not

present a problem as they are beyond both the lateral and axial resolution limits with the exception of the 1.4 numerical aperture lenses which might be able to resolve the beads laterally.

This method of bead measurement can be used to detect different types of aberration and the varying resolution from the objective lenses. This report does not take these effects into account. Therefore, different beads at different distances from the optical axis were measured.

2.5 Point Spread Function Data analysis

These data from the imaging systems were read into Matlab where custom software had been written to analyze the beads.

Step 1:
Differing methods were used to read in the z-stacked images of the bead. This is because there were differences in how the data was stored depending on which brand of microscope was used. The data was then projected into a 3D cube of the greyscale values.

Step 2:
The next step was to create a summation of all the grey scale values on the XY, XZ and YZ planes, this was done by adding the values together in each axis respectively. Then a summation of each line was made, and the line with the highest grey scale was noted. In theory it will contain the axial position in which the centre of the bead is located. At this point if the data still looked noisy, the original data cube is put through a simple filter to increase the signal-to-noise ratio. The filter was a direct form II transposed implementation of the standard difference equation.

Step 3:
An image of each of the XY, XZ and YZ image planes is displayed with the lines of intersection shown so that the user can check that it is the correct bead being analyzed.

Step 4:

A cropped section of the grey scale values for the three axial points is taken from the centre of the bead, the crop was large enough to include some of the baseline in every axis but not analysis all the data that had been captured and the base level is estimated and subtracted from the data set, this was done by taking the mean of the background values and subtracting off the mean value from every element in the array. When looking at the Z-sectioning this method has proven to be simplistic as there can be decreasing light levels as the scan goes deeper into the specimen. This can lead to negative values, which will affect the Gaussian fit.

Step 5:

A Gaussian fitting algorithm (shown in equation 2.10) was then applied to the X, Y and Z axis of the beads. The Gaussian fit will force itself through 0 so it was important to check that the data was baseline corrected. The Gaussian fitting algorithm "fitgauss" was downloaded from the Matlab file exchange. This code had a small modification from the standard code to allow a change to the priorities of the conditions by which the Gaussian curve was fitted.

Equation 2.10

$$f(x) = ae^{\frac{(x-b)^2}{2c^2}}$$

Equation 2.10 shows the formula used to fit the Gaussian curves, e is eulers number (2.718),a describes the height of the Gaussian distribution, b described the position of the peak and c describes the width of the Gaussian distribution.

Once the Gaussian curve had been fitted, a full width at half maximum measurement (FWHM) was made. The "fwhm" subroutine was downloaded from the Matlab file exchange server. The FWHM measurement is multiplied by the pixel-to-size ratio and reported back as the PSF of that axis in µm.

2.5.1.1 File formats

This project involved the analysis of images taken from microscopes made by Nikon, Zeiss, Olympus, Perkin Elmer, Cairn and Bio Rad. Nikon, Olympus and Perkin Elmer instruments all use a similar method of storing the data where the image is saved as a TIFF file and the meta data is stored as a separate file which is either a TXT or an XLS file. These files can be read directly into Matlab. The BioRad instrument generates a PIC file with the image and the meta data is stored in the same file. The module "ReadPIC" was used to create an object in Matlab where the information could easily be accessed.

At the time of writing the code a Matlab module that could read a Zeiss LSM v5 file could not be found. So the LSM files were read by LSM tool box version 4.0e in ImageJ where the LSM files are broken into TIFF image files and XLS Meta data files, which can be loaded into Matlab.

2.5.2 Deconvolution

Deconvolution is a mathematical operation used in image restoration to recover an object from an image that is degraded by blurring and noise. The blurring is largely due to diffraction-limited imaging by the instrument. The largest factor of the different types of noise is photon noise (Young I *et al.*, 2010). If an image is constructed of PSFs, deconvolution attempts to refine the PSF and construct the image from the finer PSF.

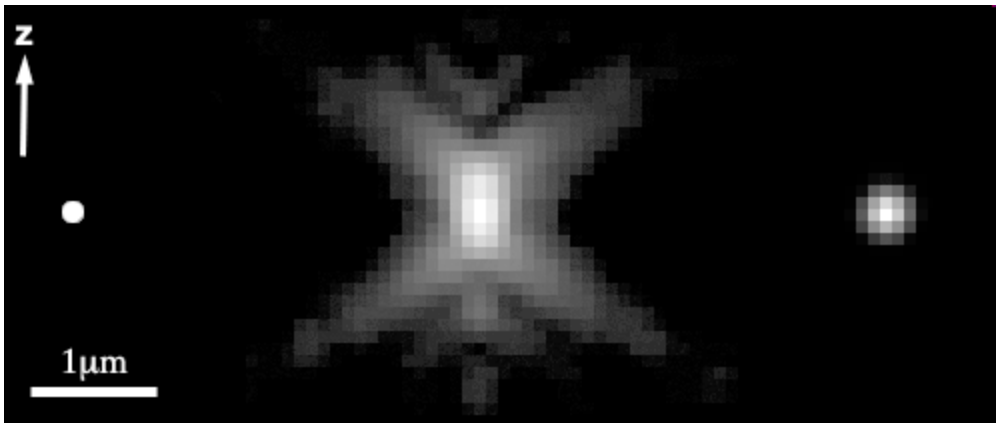

Figure 2.5: Huygens representation of a deconvolved PSF. On the left is an idealized image of a 175nm bead. The centre image is the PSF from a Zeiss 100X NA1.4 objective lens, and on the right is a deconvolved image of a single bead image using this PSF, performed using Huygens deconvolution software (Jacques Boutet de Monvel *et al.*, 2001).

Deconvolution is an iterative process meaning that the process repeatedly updates the recovered image. This is done by convolving an estimate image with the PSF, and comparing this convolved image against the original image. The difference is computed and then used to update the estimated image (Sarder & Nehorai, 2006). Most algorithms can use a theoretical or measured PSF from a sub-resolution bead. A theoretical PSF is a model of the imaging process in a microscope assuming it is perfectly aligned and configured. Any misalignment can have severe consequences for the PSF size. Therefore, it is best to use a PSF that has been measured from the imaging system.

It is important to discriminate between image restoration, where information about the imaging system is used to extrapolate more data from the image, and image enhancement, where the image is made more pleasing to the human eye. This includes methods such as sharpening algorithms and boosting contrast. Not every image taken from an imaging system can be deconvolved. Deconvolution requires that the image be finely enough resolved so that the image is composed of point spread functions rather than pixels. This means the image that is intended to be deconvolved means that the Rayleigh criterion must be sampled at the Nyquist rate or finer (Laasmaa m, 2010).

A review of the free distributed deconvolution software was undertaken. This included the plugins for ImageJ Deconvolution Lab and 3D_ deconvolution, which uses the Richardson Lucy algorithm and an estimated PSF, the Richardson Lucy algorithm is an iterative procedure for recovering a latent image that has been blurred by a known point spread function. It was found that there was a massive loss of dynamic range in the image (approximately 40 times). A Matlab program was written which took an image to be deconvolved and an image of a sub-resolution bead. The program then called the subroutine that finds the bead and fits a FWHM in X, Y and Z. A theoretical PSF was then created from these measurements to eliminate noise problems that may arise. However, this program encountered the same problem. Another problem encountered was that the algorithm would use all of the computer's memory as the whole file was deconvolved as a single unit. This is because the edges of the image can be mistaken for sharp contrast lines and are then drawn into the image, causing artefacts. Eventually Huygens deconvolution software was used. It is a very powerful deconvolution engine which breaks the image into "bricks", dealing with the edges of images more effectively. No evidence of these "bricks" could be detected in the final image (Mehadi, 2010; de Monvel *et al.,* 2001; de Monvel *et al.,* 2003).

The user interface is excellent. It will alert the user if the sampling intervals are insufficient and also allows the user to use an image of a sub-resolution bead as a PSF. However, it gives the user no feedback on the PSF measurements taken form the image

that was used in the input, so it is hard to know if the image has been analysed correctly. Results from deconvolution are shown in Chapter 4 (Shaevitz & Fletcher, 2007; Shaw, 1994; Sun *et al.*, 2009; Von Tiedemann *et al.*, 2006).

2.6 Edge spread function measurement.

It can be difficult to obtain a valid PSF measurement from some imaging systems. This is the case with the Zeiss LSM 510 two-photon system when used for deep tissue imaging, as it is hard to achieve a good signal-to-noise ratio using sub resolution beads within a highly scattering medium such as cardiac muscle.

This system has been fitted with a Chameleon Ultra II Ti:sapphire laser system (Coherent Inc.). This is a tuneable laser operating between 680 nm to 1080 nm and is capable of a peak power output of 4.5W at 850 nm. In comparison to conventional confocal imaging, there are much lower levels of light emitted from two-photon imaging even when descanned detectors are used. This means that conventional bead imaging is impossible as the power output settings from the laser required for an adequate signal-to-noise ratio will cause the medium containing the beads to burn. Under these circumstances, there are many advantages to imaging a fluorescent edge. The edge should be absolute to generate a reduction in fluorescence over a distance that is much less than the optical resolution. Microscope objective optics will blur this edge in relation to the PSF on that axis with the higher numerical aperture lenses, resulting in a sharper gradient than the lower numerical aperture lenses. The gradient tends to be a sigmoidal curve. It is possible to differentiate the sigmoidal curve and then measure a FWHM. However, there can be differences in the extremities of the curve due to the rate of rise at the extremes of the curve occurring at slightly different rates. Therefore, a FWHM taken from an edge spread is not directly comparable to a PSF measurement due to the fact that the edge is the measurement of one edge where as the PSF is a measurement of two edges which are in extremily close proximity. The test slide that was used was a Chroma fluorescent slide that had a finely polished surface.

2.7 Edge Spread Function data analysis method

To test the effects of different factors of cardiac muscles, a suitable test standard must be obtained. As discussed previously, edge spread functions work very well for two-photon systems. There are further advantages of using edge spread functions; 5 µm fluorescent beads will be used to mark the surface of the artificial myocardium. Locating an area with a bead on the surface, and then scanning down to the fluorescent edge provides a better method than trying to locate a sub-resolution bead beneath the 5 µm bead and in many cases may not be possible.

Normally, the PSF is estimated using sub-resolution beads, but this technique is unsatisfactory in this application for several reasons: (i) single beads would need to be suspended throughout a medium with a low density to ensure no clustering (ii) fluorescence from sub-resolution beads is poor, and any further loss of signal would make detection marginal. In contrast, edge spread functions are ideally suited for deep imaging because; (i) the specimens have high and stable fluorescence (ii) the slide is at a fixed distance from the objective and therefore easy to locate. For these reasons, a slide was designed to assess optical aberration by measuring the ESF under a range of conditions. It was also important to use low concentrations of 5 µm beads so that they did not affect the measurements as the beads are opaque they can block out light immediately beneath the area of the bead.

Figure 2.6 shows an axial summation of all the greyscale values taken of the surface of a Chroma test slide clearly showing a blurring of the edge of the surface which is shown in image 2.6. Figure 2.7 shows the differentiated data from figure 2.8 this shows a clear Gaussian shape that a FWHM can be fitted.

Figure 2.5 Shows the Axial image of the surface of a Chroma test slide clearly showing the blurring of the edge of the surface.

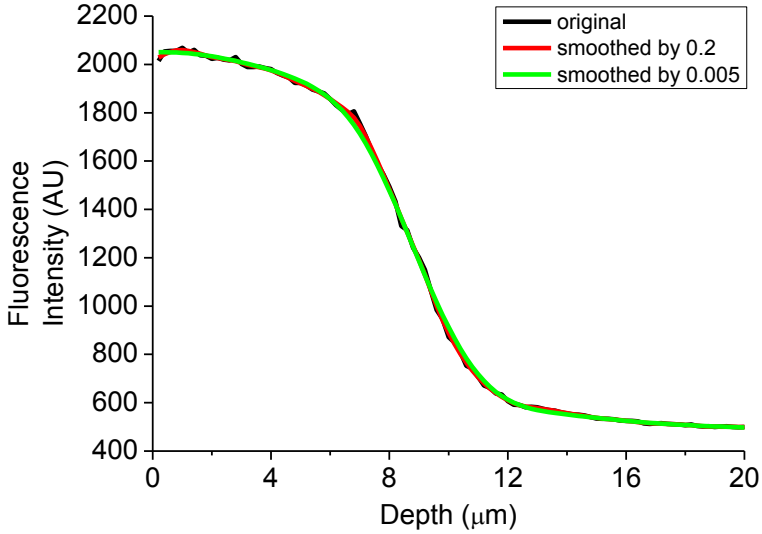

Figure 2.6 This graph shows typical edge spread function data with two levels of smoothing splines.

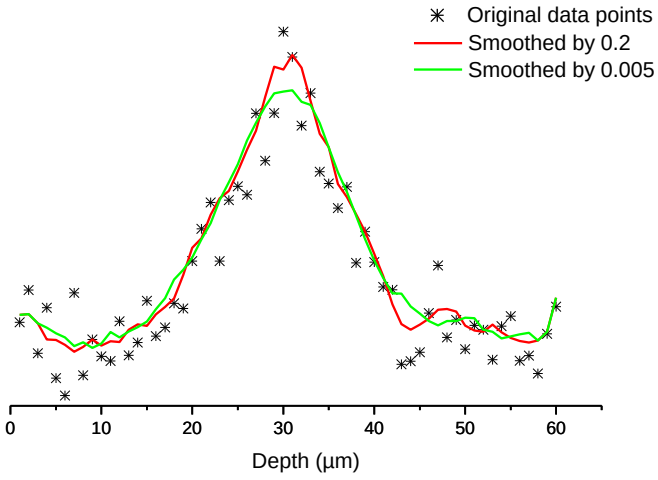

Figure 2.7 shows the differentiated edge spread function original data plot from Fig 2.8 above, along with the smoothed signal using a smoothing factor of 0.2 and 0.005. the smoothing algorithm is a moving average filter.

Typical edge spread function data is shown in Figure 2.8, along with spline fits of the data at two different values, 0.2 and 0.005. The artefacts that are present in the 0.2 trace have been removed in the 0.005 without altering the shape of the distribution. A measurement of FWHM for the data set in Figure 2.8 is shown in Figure 2.7. A Gaussian curve is fitted to the curve that was smoothed by the 0.005 factor. It shows two smoothed differentiated edges and the original data points, the FWHM where found to be more accurate when using the smoothed data on multiple measurements This is caused by the significantly smaller peak of one of the Gaussian fits.

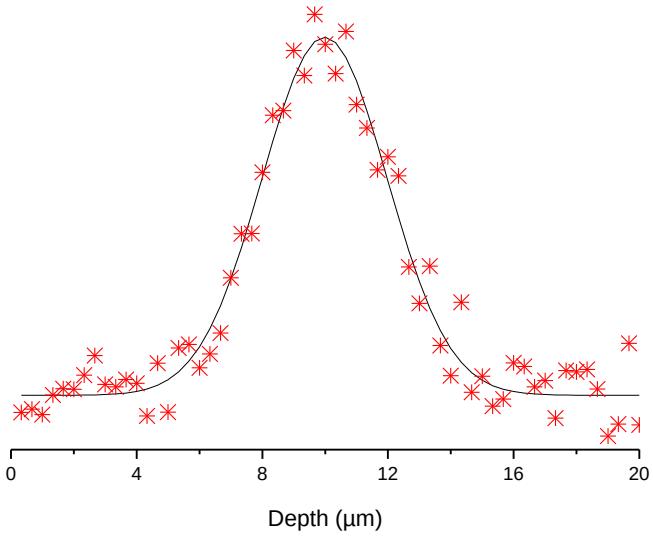

Figure 2.8 shows the final smoothed fitted Gaussian to the original data with the baseline subtracted. This method of measuring edge spread functions yielded very reproducible results from which accurate estimates could be made.

2.8 Monitoring Z stage movement

Attempts were made to accurately measure Z-stage movements. These measurements were taken with a Heidenhain MT 60K (Encoders UK Ltd, Unit 5a The Courtyard Reddicap Trading Estate, Sutton Coldfield, Birmingham, West Midlands, B75 7BU). This is an accurate probe that reports the postion in one axis with extreme accuracy, the Heidenhain MT 60K has a 60 mm length of travel and a quoted margin of error of ± 0.5 µm (0.8%). The Heidenhain MT 60K was carefully and firmly clamped to the stage of the microscope and the probe lowered on to the moving part of the mechanism. Great care was taken to ensure that the probe was at 90 degrees from the surface it was measuring. Coarse measurements were made initially, where the Z-stage (objective turret) was raised or lowered in 10 x 5 µm steps and then reset back to the original position in one 50 µm step. A fine measurement experiment was then undertaken where the turret was moved 10 x 1 µm steps before being reset with a single 10 µm step.
In three of these microscopes, the precision of a 0.2 µm step was examined, where the microscope was moved 5 x 0.2µm steps and then the measurement was taken. This measurement was performed in order to ascertain movement accuracy when scanning a sub-resolution bead.

The Heidenhain MT 60K probe was last calibrated in 2006, and found to have a 0.4 µm margin of error across the entire 60 mm of the probe's travel. No more recent calibration of the probe was available. The probe's accuracy was validated by measuring the height of finely manufactured metal plates that were gently cleaned in alcohol. These plates increased in the order of 2.54 µm (0.0001 of an inch.)

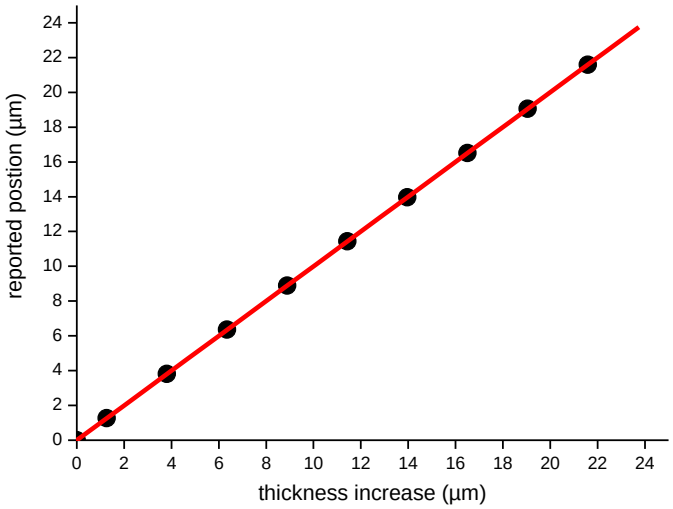

Figure 2.9: This figure shows the thickness increase of the metal plates and the reported thickness that the Heidenhain MT 60K measured.

Linear Regression through the origin for the probe calibration data showed an R-value insignificantly different from 1 and a P value of <0.0001, demonstrating that the probe is highly accurate and working as expected. The probe uses gravity to exert a constant down force of 44 g. Considering that the weight of the average objective lens is much larger than 44 g, this should not affect the performance of the microscope turret.

2.9 Measurement of the refractive index of liquids.

Measurement of the refractive index of liquids can be made accurately using a refractometer. A known thickness of the liquid is placed beneath a prism and light of a certain wavelength is directed into the prism, the refraction of the beam can then be measured.

2.9.1 Measured refractive index of agar and cardiac muscle

To measure the refractive index of a material a procedure was set up where a slice of the material was cut to an appropriate depth (typically 40 µm), such that the imaging system could scan through the bottom of the material to the top. A sharp edge is cut and a fluorescent substance of known refractive index is placed next to it. The preparation is

then sandwiched between a slide and cover slip. As the confocal microscope scans through the preparation it will report slightly different heights between the material of interest and the known fluorescent substance. The heights are divided to determine an axial scaling factor as described previously (Dirckx *et al.*, 2005).

The refractive index is then calculated by:

$$n = \frac{ASF + (0.155 \pm 0.004)}{(0.8717 \pm 0.0028)}$$ For Water immersion, NA=1.2

$$n = \frac{ASF + (0.135 \pm 0.004)}{(0.7435 \pm 0.0027)}$$ For Oil immersion, NA=1.3

Where n is the refractive index and ASF is the axial scaling factor, which is the distance in µm between the theoretical z position in a substance with the refractive index matched to the lens and the reported z distance.

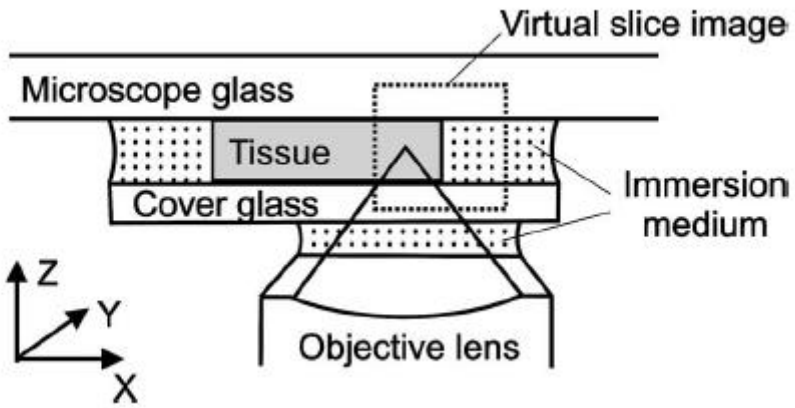

Figure 2.10: This diagram shows the experimental setup used to measure refractive index changes caused by a given material.

In this case water was mixed with fluorescein (Life Technologies Ltd, 3 Fountain Drive Inchinnan Business Park, Paisley PA4 9RF, UK). The gel was created by mixing a 2% agar concentration and was staining the agar with Congo red (Sigma Aldrich the Old Brickyard, New Road, Gillingham, Dorset, SP8 4XT). The preliminary results show the 2

% agar mix having a refractive index between 1.351 – 1.443. The Z-stage inaccuracy will make more precise measurements harder (Erdemoglu *et al.*, 2008).

2.9.2 Scattering and absorption set up.

To test the scattering properties of the 100nm polystyrene beads (Sigma Aldrich), logarithmic concentrations were mixed with water and used as the immersion medium for the lens, so the depth of scattering medium between the lens and the sample will be the working distance of the lens (3.6 mm on the 40X 0.8 NA which is used throughout chapter 4).

2.10 Quantum dots

One of the major problems with imaging beads is knowing whether a single bead is being imaged or if there are multiple beads adhered together. There can be problems if the beads are too close together. An alternative to beads is quantum dots (QD). These are 5-50 nm in size and are highly fluorescent. Quantum dots emit a wavelength dependent on their size. This means the manufacturing of quantum dot has to be done with very high quality control (Rauf *et al.*, 2010;Gorodetsky *et al.*, 1996). Therefore, it is possible to generate test slides that have high quantum efficiency and are sub-resolution structures that would be in known locations.

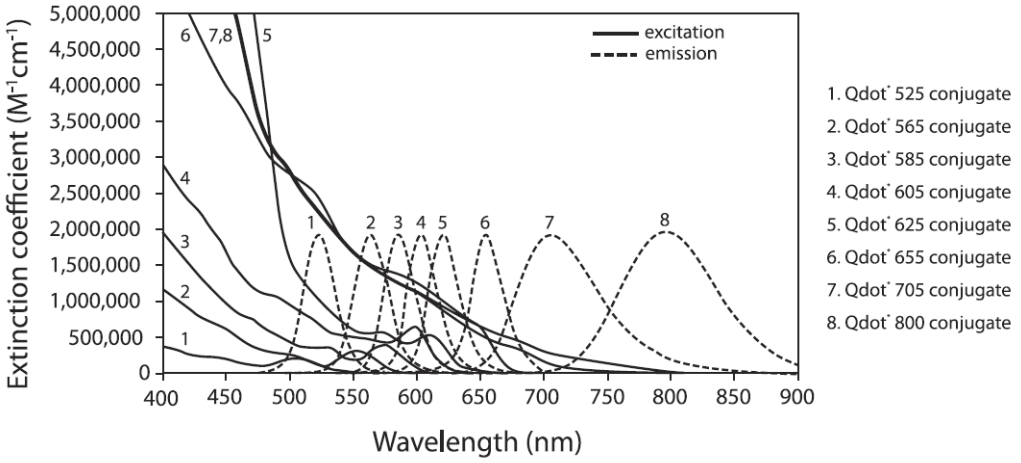

Figure 2.11: shows the excitation and emission spectra of 8 different types of quantum dots that are commercially available. Figure supplied by Invitrogen

2.11 The generation of micro and nano-structures

Many of the experiments in this thesis used microstructures to manipulate specimens under a microscope.

2.12 Building SU8 structures using photo-lithography

SU8 (Shipley Europe Ltd, Herald Way, Coventry, West Midlands, CV3 2RQ.) is a photo-resist that can be used to create structures ranging from ~30 to 100 µm high. It can be bonded to glass but bonds better to silicon . A wafer of either glass or silicon is cleaned in an ultrasonic bath and is immersed in acetone then isopropanol (IPA) and finally Opticlear (AGTC Bioproducts Unit 4 Fleet Business Park, Itlings Lane Hessle, HU13 9LX.) for a period of 5 minutes each. The samples are then washed down in distilled deionised water and blow-dried in nitrogen so as to avoid drying marks. The wafers are then placed in an oven at 120 ^{o}C overnight (Yoon *et al.*, 2006;Han *et al.*, 2007). SU8 is a substance with a known viscosity. To set the depth of SU8 it has to be spun at a certain speed for a set amount of time. The most viscous SU8 (3050) was used. The nomenclature states the thickness of the layer achieved for a given spin speed. This denotes that 3050 will form a uniform 50 µm layer when spun at 3000 rpm. The wafer was placed on a spinner and a quantity of SU8 was poured on. This was then spun at 1000 rpm to create a layer 100 µm high (Han *et al.*, 2007;Walsh & Franses, 2003).

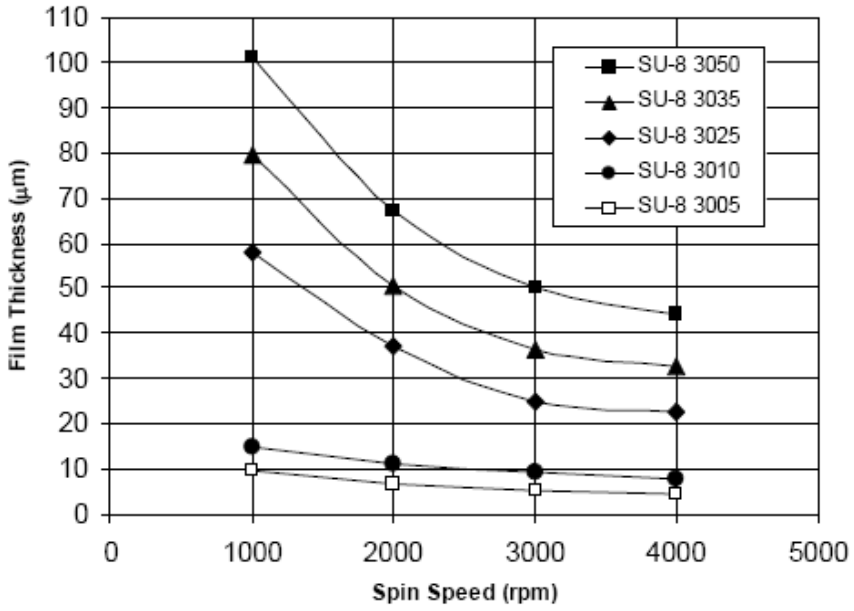

Figure 1. Spin speed vs. Thickness
for SU-8 3000 resists (21°C US & EU)

Figure 2.12: Diagram demonstrating the different heights SU8 can be built up to. From the SU8 technical data sheet

The sample was then baked for 15 to 20 minutes on a hotplate at a maximum temperature of 90 ^{o}C to evaporate the solvents and to set the SU8. There will be a border region around the edge of the sample of non-uniform thickness (bead). In order to make a structure with well defined edges, these needed to be removed. On thin wafers, this was done by scoring the wafer and snapping the edges off. On a thick wafer, it cannot be cut because it will generate particles in the clean room. In this case, EC solvent was carefully applied to the broader region of the sample to dissolve away this part of the SU8 and thus enable a uniform contact of the mask with the SU8 surface for faithful pattern transfer. The sample was then ready to be exposed. A mask of the micro-structure was then made. This is usually a 4" or 6" quartz wafer with a pattern imprinted on it in chrome (Using e-beam lithography, alternative masks have been written on acetates with a high resolution printer). SU8 requires a bright field mask. This means that the parts of the SU8 that are exposed to ultra violet (UV) light become cross linked and form the structure.

With the border region of the SU8 (bead) removed, the SU8 can come into contact with the chrome side of the mask. This minimises the diffraction from the UV light coming through the holes in the mask (proximity exposure). Diffraction can be a major problem in tall structures because the edges will become sloped, which causes them to become unstable (Klauke *et al.*, 2003). Once the sample had been exposed it was heated on a hotplate at ~90 ^{o}C for 1 minute to allow further cross linking of the exposed areas (post exposure bake). The sample was then developed in EC developer, mixed in a 1:1 ratio with distilled water for 5 minutes, washed down in distilled water to stop development of the SU8 and dried with nitrogen. This process created a master copy that inverse structures could be cast from.

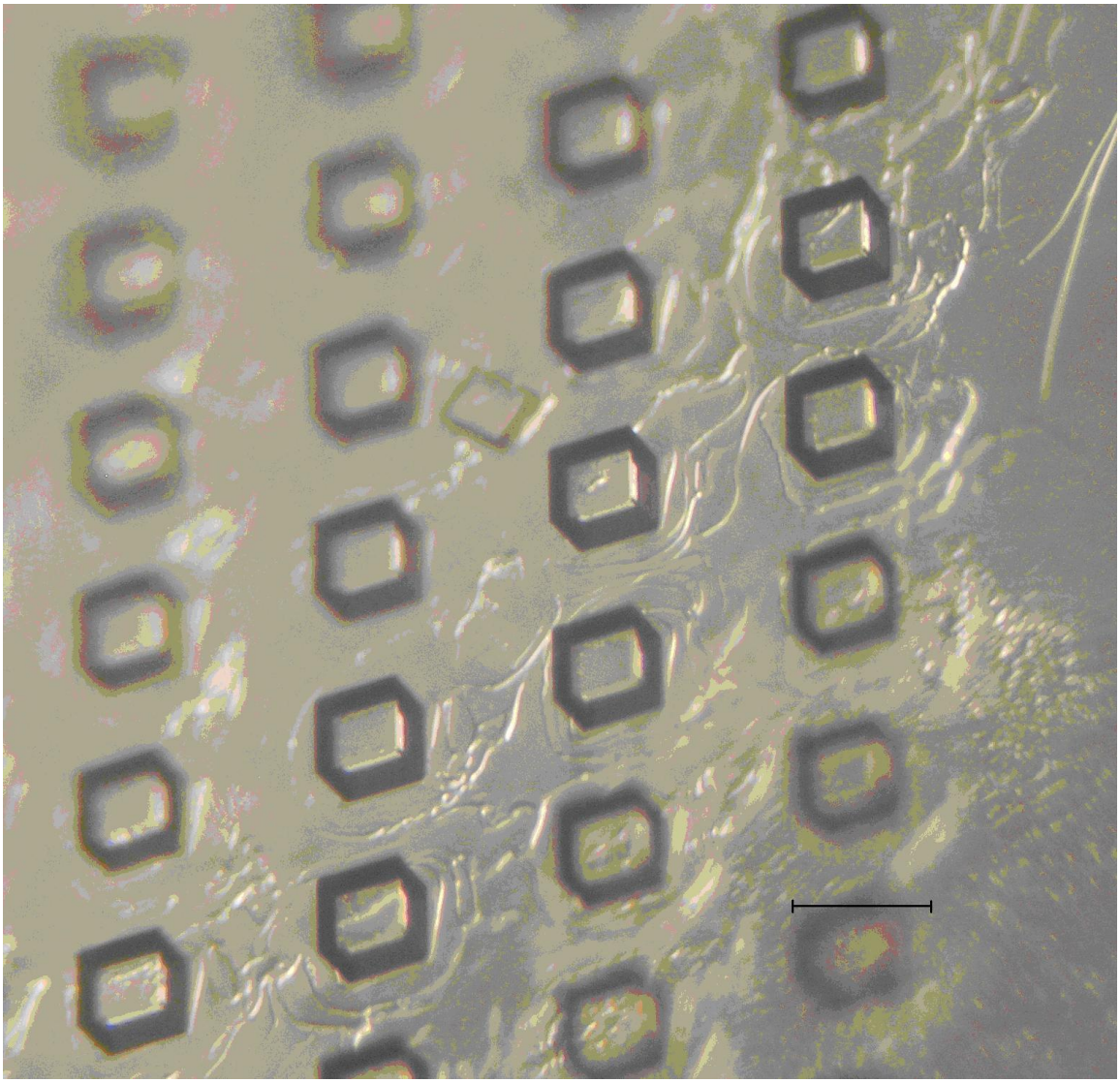

Figure 2.13: Photograph of a micro-structure as it leaves the clean room. Note the SU8 is still covering the glass. If the structure is developed further, the bond between the exposed SU8 and the glass weakens. This greatly increases the useable life of the structure. The scale bar represents 150µm.

2.13 Silicon orientation

Silicon wafers are extremely pure discs that can be a variety of thicknesses. In this project, 380 µm thick wafers were used. Silicon wafers have a complex crystalline orientation that is defined using Miller's index. When a wafer is cut, the surface of the

wafer is oriented to one of the crystalline planes of the silicon . In this project, 100 and 110 wafers were used (Strandman *et al.*, 1995), (Tellier, 1998).

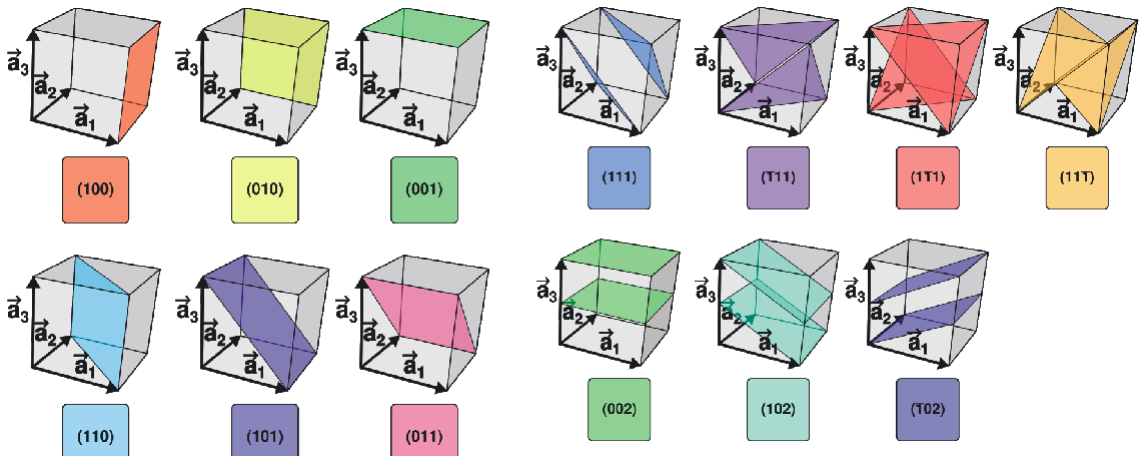

Figure 2.14 shows the various angles as described by Miller's angle. The Miller orientations are critical to define the etch angle of the silicon.

Angle	***100***	***110***	***010***	***001***	***101***
100	0.00	45.0	90.0	90.0	45.0
011	90.0	60.0	45.0	45.0	60.0
111	54.7	35.3	54.7	54.7	35.3
211	35.2	30.0	65.9	65.9	30.0
311	25.2	31.4	72.4	72.4	31.4
511	15.8	35.2	78.9	78.9	35.2
711	11.4	37.6	81.9	81.9	37.6

Table 2.2 Table showing the etch angle in degrees at the primary and secondary planes. More information can be found at http://www.cleanroom.byu.edu/EW_orientation.phtml.

2.14 Potassium hydroxide (KOH) wet etch method

A structure was created using a potassium hydroxide (KOH) wet etch method. Initially a 100 orientation silicon wafer was used, where the orientation of the crystal runs at 54.74°. This will give a very steep angle to the mirror. Both sides of the wafer were coated in a silicon nitride layer, this was to protect the wafer as both sides would be immersed in KOH. Primer was then spun on to one side of the wafer followed by S1818 (micro resist technology GmbH, Koepenicker Str. 325, 12555 Berlin, Germany) photo-resist to a depth of 1.5 µm, followed by a soft bake at 90°C for 30 minutes and a pattern was developed on the wafer so that the photoresist was protecting the regions that are not to be etched.

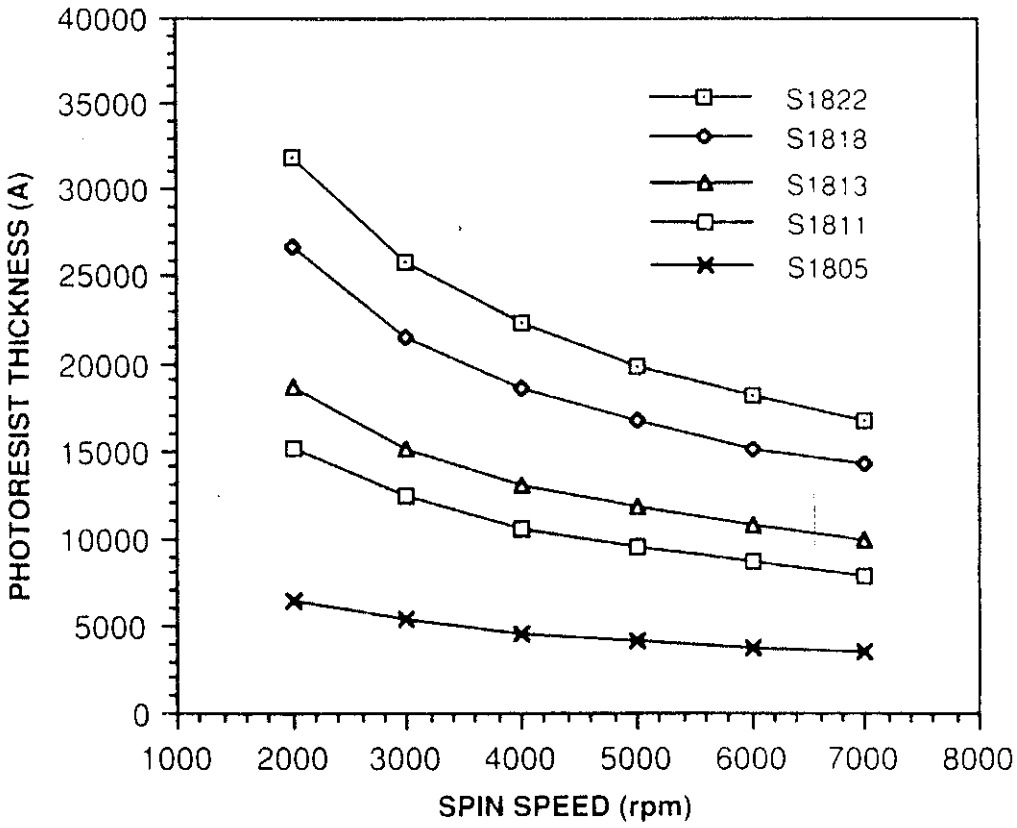

Figure 2.15: this graph shows the resist thickness of the s1800 series of photo resist spun at variable speeds. Taken from the S1800 product information sheet.

After the exposure to UV light, the wafer was then baked at 120 ^{o}C for nine or ten minutes and then developed with a 1:1 mixture of Microposit MF -319 (micro resist technology GmbH) and distilled water. A plasma etch was then performed to remove the silicon nitride that was not protected by the photoresist, then the wafer could be etched in 30 % KOH + 25 % isopropanol and water at 80 ^{o}C. The depth of the structure was dependent on the length of time the wafer was etched. There are many factors that contribute to the smoothness of the surface. The wafer is shown in the electron microscope images below (Figure 2.16).

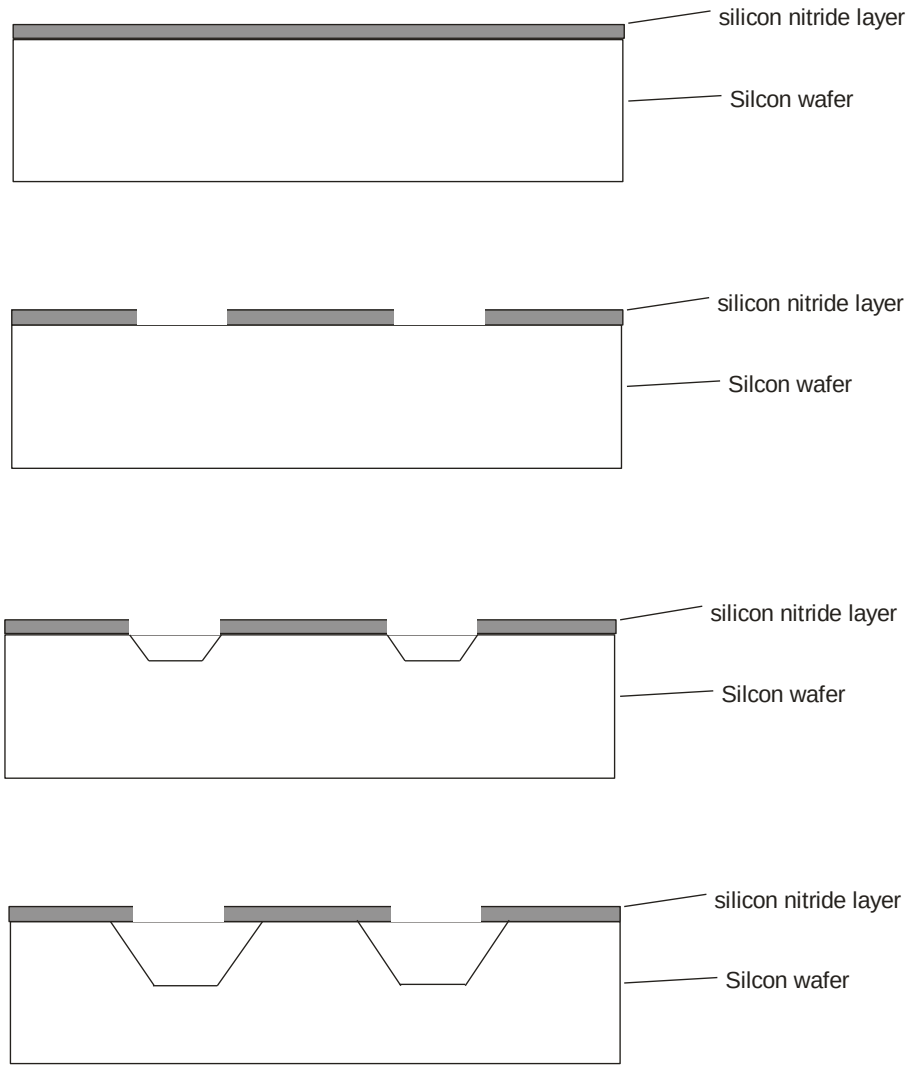

Figure 2.16: is a schematic representation of the etching process. Representing a 100 orientation silicon wafer with a protective layer of silicon nitride being etched by KOH.

2.15 The use of nano-imprinting to create a standard test slide.

Microscopes that are set up for fluorescent imaging techniques currently depend on the imaging of sub resolution beads to measure the resolution of the system. This technique is time consuming and requires some skill from the operator. When the results are interpreted and found to be larger than expected operators sometimes lack the confidence to believe there results, therefore this task is frequently neglected.

Therefore it is desirable to generate a test slide that is of a known standardised pattern would be of great interest to users how are interested in the resolving capabilities of there system. Additionally as the pattern is known it is possible to write software that would automate the data analysis.

2.15.1 Requirements

The resolution should be around 100nm or below, this will require the use of E-beam patterning. There must be defined fluorescent regions it is desirable the regions are composed of quantum dots due to there bright signal and resistance to bleaching, making the test slide very robust.

It is possible to use epi-illumination to locate and focus on a fluorescent target. However it is easier to use a transmitted image to find and focus on the pattern. Therefore it is desirable to use a translucent substrate such as glass or quartz and have the fluorescent pattern material to be sitting on opaque metalized areas to increase contrast.

2.15.2 Using quantum dots it use in a standard test slide

Calcite crystals are very similar to quantum dots. However, they are not fluorescent, which is not needed in EM. Quantum dots will repel each other and will therefore settle at a certain distance apart from one other, the particles that have done this have settled at distances apart that are over the expected lateral PSF of most imaging systems, although it should be noted that these crystals are about 1.5 µm in size rather than the 5-50 nm that quantum dots are. However, there are still areas where crystals are adhered together. This poses a risk of the sub-resolution features being larger than expected (Kraus et al., 2007).

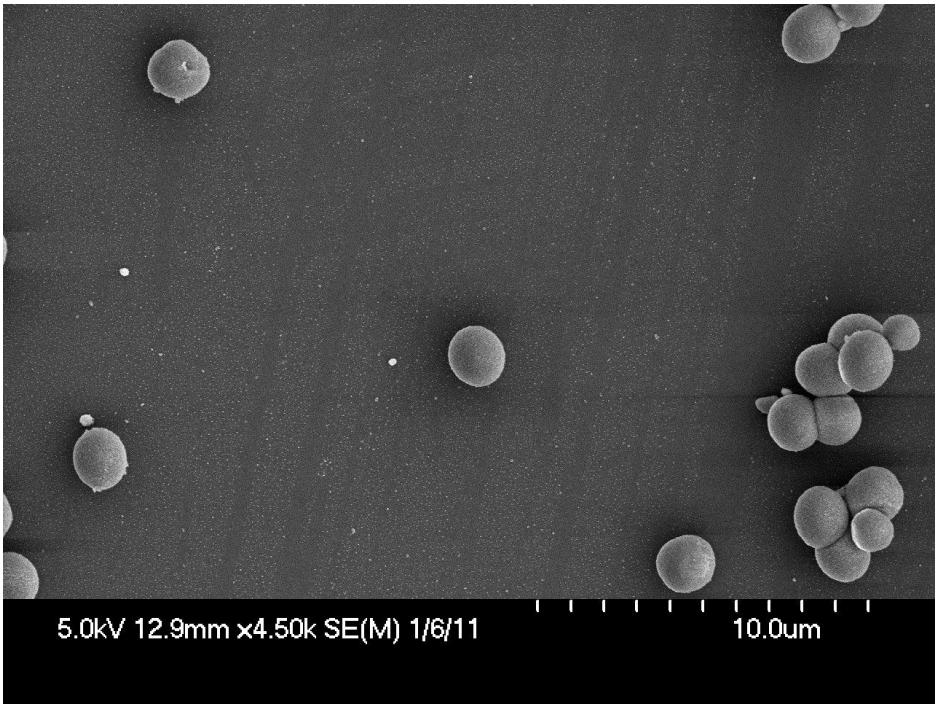

Figure 2.17: this electron microscope image shows calcite crystals at 8mM. 3µlX50µl were sampled, diluted on a cover slip and left to dry.

A test slide that can hold fluorescent particles at set positions would be an advantage as it would greatly simplify the process of taking a PSF from a microscope.

Nano-imprinting was used to create wells 200 nm wide and approximately 400 nm deep. These wells were placed 2 µm apart. Then micro beads or quantum dot solutions were poured over the structure, and the fluorescent molecules fell into the wells. Subsequently, the rest of the solution could be removed by a gentle side flow of solution with no fluorescent material present, while the beads were still located in the wells (Lee *et al.*, 2009;Maisch, 1981;Goldman & Wurzel, 1995). This test structure was ideal for testing the optics of imaging systems that are mainly designed for imaging slides and thin biological preparations,

A silicon wafer was cut to 25 mm square. The wafer was cleaned, and HDMS primer was spun on at 4000 rpm for 30 s and then baked at 120 ^{o}C for ten minutes. This left an even

coating with a thickness of a few nanometres. Next, ma-N 2401 photo resist was spun on to the sample to achieve a thickness of 100 nm. The resist was spun at 3000 rpm for 30 seconds. The sample was then baked on a vacuum hotplate at 90 ^{o}C for 3 minutes. The sample was then exposed on the VB6 at 100 kV patterning a regular array of 200 nm squares on a pitch of 2 µm with a 16 nA beam current and a dose of 650 µC/cm^2. Once the sample had the design patterned onto the photo resist, the sample could be developed. This was done in Microposit MF^{tm} -319 for 3 minutes and then rinsed in distilled water for ten minutes to ensure that development had stopped before the sample was dried under a stream of nitrogen, The sample was then ready for dry etch. Dry etch was used to bore directly at 90° from the surface to generate pillars that were 261 nm in height as confirmed by atomic force microscopy (AFM). Once the sample had been etched, it was immersed in a mixture or 30 µl of silane and 50 ml of heptanes. The fluid was then evaporated on a hotplate. The structure had a thin coating of silane which helps protect against mechanical damage as the structure is used as a stamp.

2.15.3 Pattern

To take a regular resolution measurement across the field of view lines will be spaced 5µm apart and run in along the X and Y axis to make a grid. 3 2µm square regions will be patterned to aid on focusing the slide.

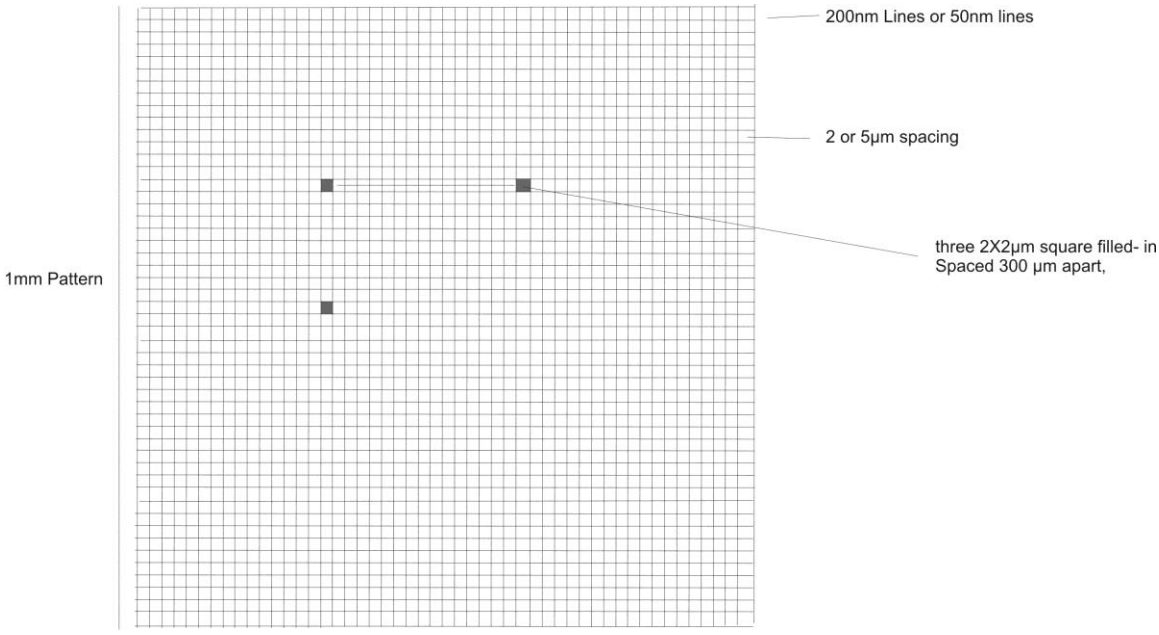

Figure 2.18 shows the theoretical pattern that con be used to take multiple line measurements across the field of view of and objective.

2.15.4 Proposed method

The most cost effective method of procuring such a slide is to use Electron beam on a fused silica substrate, generating a 1mm pattern on to a 10mm chip for ease of handling. SAL resist will be mixed with quantum dots with an excitation peak around 490nm. There can be a spectral shift when QDs are in high concentrations. It is also important that the QD are not exposed to temperatures over 150 degrees Celsius.

The planned procedure is to Clean a 4" glass wafer in O_2 Plasma coat the wafer in SAL resist mixed with QDs and bake for 110 C for 10 min. use Ebeam to write the patterns on to the sample, post bake at 110 C for 10 minutes and develop the photoresist, multiple washes to remove excess QDs. Then the sample will have a protective layer of SAL spun on and the wafer will be cleaved into 1cm chips, the SAL will be developed the any contaminants from the cleaving will be removed. The chips will then be boxed and shipped.

2.16 Manufacturing structures out of the clean room.

It is desirable to create cheap structures that can be made easily and used in biological experiments. Therefore the following method was developed in order to generate a constant supply of cheap micro structures.

Quartz pipettes (CM Scientific Ltd. 1 Ryefield Court, Ryefield Way, Silsden, BD20 0DL) were used to load individual cells into the micro-structures. These have an outer diameter of 170 µm and an inner diameter of 150 µm and have to be pulled to produce a tapered end of ~90 µm inner diameter. The melting point of the quartz is approximately 1200 ^{o}C. A P2000-F laser pipette puller (Sutter Instruments) designed specifically for quartz pipettes was used. This differs from the standard P2000 puller as the laser is focused to a smaller point to generate the heat required.

A pipette puller was built; and it works by driving a large current through platinum wire. The pipette is stretched across it and the length is slowly changed as the quartz melts. It is then mounted and the end is crushed until it is at the appropriate diameter. A Polydimethylsiloxane (PDMS) (Dow Corning Limited, Cardiff Road, Barry, Vale of Glamorgan, CF63 2YL) solution was made by mixing PDMS with the curing agent in a 9:1 ratio. It was then mixed in a 1:3 ratio with heptane. This lowers the viscosity and allows it to flow through the pipes. The SU8 will bond to the PDMS making it very hard (impossible) to lift off. The SU8 structure is placed in a vacuum chamber with a 100 µl of a fluoro-silane for one hour to expose the SU8 surface to the fluoro-silane vapour. This covers the structure in fluoro-silane and allows the PDMS to be separated from the SU8. An upright dissecting microscope was used to view the structure. A quartz (fused silica) pipette is attached to a micro-manipulator and a Hamilton syringe driver and the pipette lowered into the PDMS and the PDMS drawn into the pipette. Once this was done the pipette was run along the posts in the SU8 structure, making sure the PDMS does not cover the posts. The structure was baked in an oven at 100 ^{o}C for 40 minutes. The PDMS was lifted away from the SU8 and placed on a cover slip. Because of the silane, the structure floats, so it is placed in an ultrasonic bath with some alcohol for five minutes. Figure 2.18 shows one of these structures, it is an array of wells that will be used to

orientate dissociated myocytes end on so that the intercalated discs can be imaged with greater resolution, the results of this are shown in chapter 5.

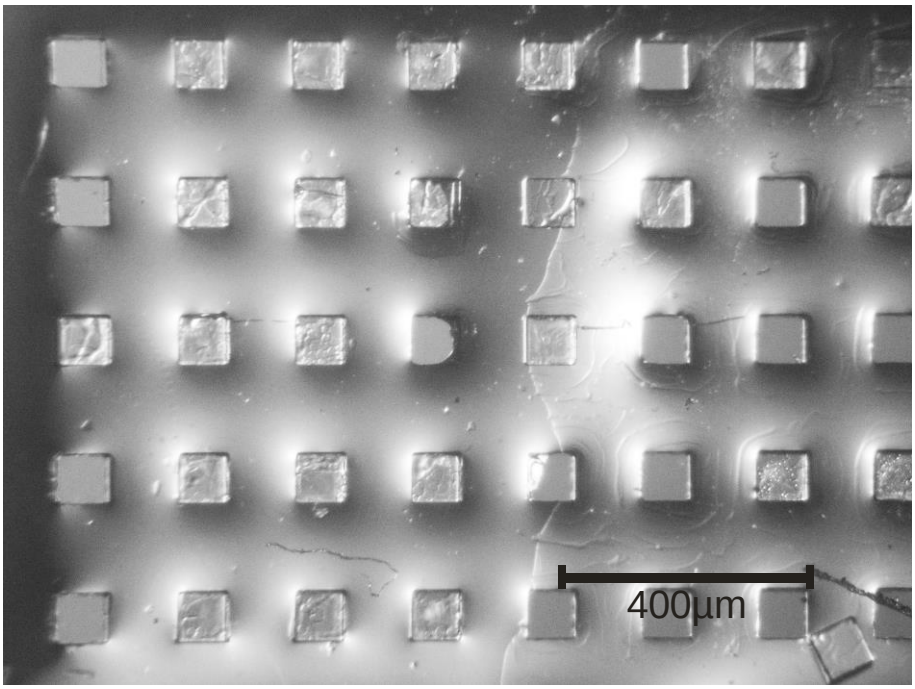

Figure 2.19: is a light microscope transmission image of an Example of a finished PDMS structure that is used in experiments. It shows a matrix of wells that have been formed out of PDMS. In the bottom right there is an SU-8 block visible that has become detached from the glass substrate.

3 Chapter 3: Microscope resolution measurement

The work presented in this chapter describes a detailed analysis of different objectives and imaging systems, and compares the theoretical resolution to the measured resolution. It also examines the accuracy of Z-drive mechanisms used within microscope systems; errors in this aspect of microscope operation may be part of the explanation as to why theoretical and actual PSF values differ.

The aims of this chapter are:

1. Calculation of theoretical point spread function (PSF)
2. PSF measurements using a confocal laser scanning system and a range of objectives.
3. Investigate PAM-generated PSFs
4. Investigate the accuracy of Z-drive movements

3.1 Measuring resolution:

The methods used to measure resolution are described in Chapter 2 page 9.

3.1.1 Calculating theoretical resolution

The methods used to calculate the theoretical resolution are described in Chapter 2 page 8 Equation 1. All results are given as FWHM of the minimum resolvable unit in the X/Y and Z axes and can be illustrated by generating an image of an elongated spheroid the dimensions of which are dictated by the FWHM in X/Y and Z. This chapter addresses the subject of resolution and sensitivity of various objective lenses in various systems. Lenses produce different renditions of the specimen they are used to image. As a result objective lens choice is a very important issue; for example Figure 3.1 shows two images of the same specimen imaged in the Z-plane with two different objectives. The specimen was a thin membrane of collagen (approximately 20µm thick)stained with a fluorescent dye. The thickness of the membrane was accurately imaged in the Z-axis using a 40 x objective but not measured accurately with a 10 x objective.

A

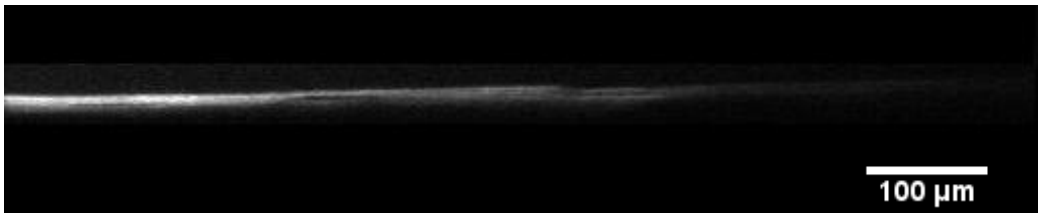

B

C

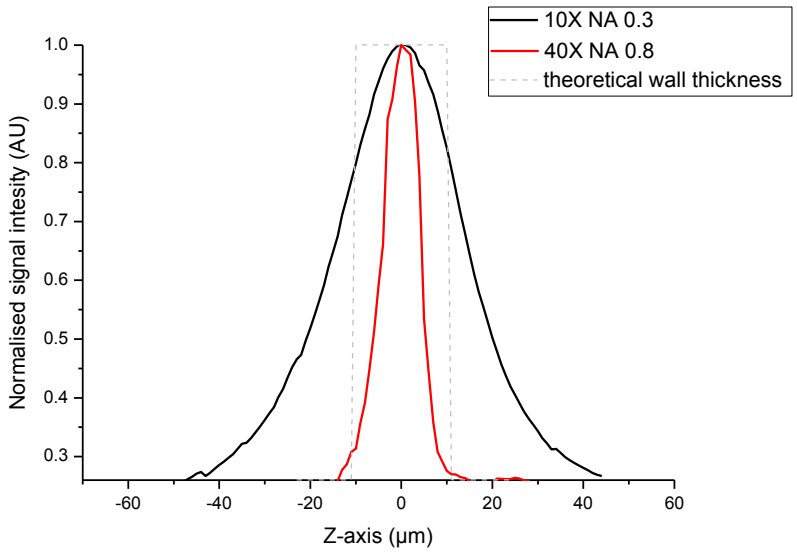

Figure3.1 shows the difference that can occur when imaging the same specimen with different objectives. Figure A shows an X/Z-image of a 20µm thick collagen network wall composed of collagen fibres stained with Fluorescein being scanned with a 40x NA 0.8 objective. Figure B shows an X/Z-image of the same specimen on the same imaging set up being scanned with a 10x NA 0.3 objective, the resolution and the interpretation of signal intensity is quite different between the two objectives, Figure C shows a summation of the X and Y greyscale values of a selected region through the Z section of the same section of the sample. It is possible to distinguish between the edge that is

pressed up against the cover slip using the plan-Apochromat 40x NA 0.8 W, however this information is lost using the Achroplan 10x NA 0.3 W.

3.2 Results:

3.2.1.1 Zeiss Achroplan 10x NA 0.3 W Ph1

The Achroplan 10x NA 0.3 W Ph1 has an estimated PSF of X/Y = 1.11 µm and Z = 18.18 µm at 960 nm, which is the preferred wavelength for exciting a number of membrane binding dyes. The preferred wavelength for exciting Rhodamine is 800 nm, which would provide an estimated PSF of XY= 1.13 µm and Z= 17.3 µm

3.2.1.2 Zeiss Plan-Apochromat 40x NA 0.8 W

The plan-Apochromat 40x NA 0.8 W has an estimated PSF of X/Y = 0.417 µm and Z = 2.33 µm at 960 nm, which is the preferred wavelength for exciting Di-4-ANEPPS. The preferred wavelength for exciting Rhodamine is 800 nm, which would provide an estimated PSF of X/Y = 0.425 µm and Z = 2.21 µm.(Wokosin *et al.*, 2004; Xu & Webb, 1996)

3.2.2 Results from calculated PSF

Microscope type: Confocal
Numerical aperture (NA): 1.2
Excitation wavelength: 488 nm
Emission wavelength: 530 nm
Number of excitation photons: 1
Lens medium refractive index: 1.333
Back projected pinhole radius: 300 µm
Specimen medium refractive index: 1.333

FWHM
X/Y= 0.215µm
Z= 0.639µm

The calculated PSF (above) and the variables used in the calculation are shown above using formulae 2.8 and 2.9.. The same variables are used to calculated the measured PSF values.

Results from Measured PSF

The measured PSFs are larger than the theoretical PSFs measured from the BioRad Radiance 2000 using a Nikon 60x NA1.2 oil objective: which contrasts from the calculated results.

Microscope type confocal
Numerical aperture 1.2
Excitation wavelength 488 nm
Emission wavelength 530 nm+
Number of excitation photons 1
Lens medium refractive index 1.333
Back projected pinhole radius 300 µm
Specimen medium refractive index 1.333

FWHM

X= 0.570 µm

Y= 0.548 µm

Z= 2.837 µm

The above shows the measured PSF results with the same variables as the calculated PSF

3.2.3 The effect of NA on the resolution

The PSF of an optical sectioning system is dependent on the numerical aperture of the lens and the wavelength of excitation and emission light being used. As the numerical aperture is decreased, the PSF will become elongated until it looks more like a column of light. Figure 3.26 below demonstrates this:

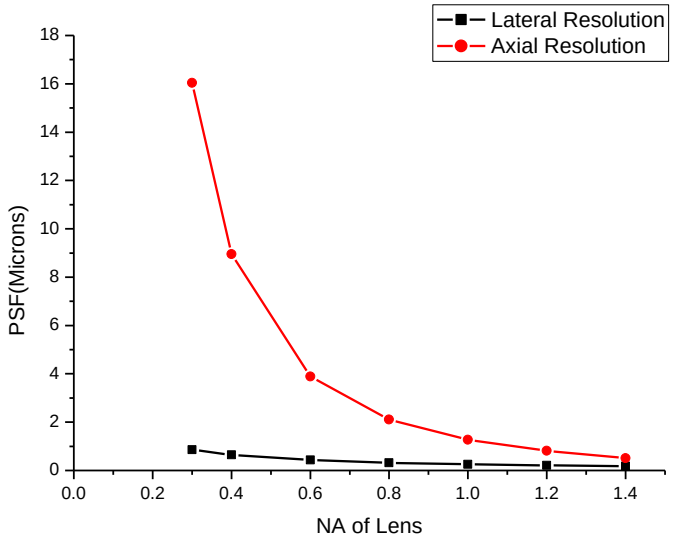

Figure 3.2: A simplified calculated PSF and its dependence on the NA. Fine opticalsections cannot be achived using a low NA objectives. due to the collimating shape the PSF adopts with a low numerical aperture lens. This technique is used to create fine structures in photo-resist (Teh *et al.*, 2005) **.**

Summary of Calculated PSF

Imaging system	NA	X/Y(µm)	Z(µm)
Zeiss 5Live (Plan-Apochromat 20x/0.75)	0.75	0.34	2.08
Zeiss upright Two Photon (Achroplan IR 40x/0.8 W)	0.8	0.41	2.33
Zeiss 510 A (C-Apochromat 63x/1.2 W corr)	1.2	0.21	0.63
Zeiss 510 B (C-Apochromat 63x/1.2 W corr)	1.2	0.21	0.63
Zeiss 510 C (Plan-Achromat 63x/1.4 Oil Ph3)	1.4	0.18	0.51
Zeiss Exciter (plan-Apochromat 63x/1.4 Oil DIC)	1.4	0.18	0.51
Olympus (plapon 60x o na:1.42)	1.42	0.18	0.48
Olympus (uplsapo 60x W NA:1.20)	1.2	0.21	0.63
Olympus (uplsapo 60X O NA:1.35)	1.35	0.19	0.46
BioRad (60x PA Water / 1.2)	1.2	0.21	0.63

Table 3.1: shows the theoretical FWHM values in the X, Y and Z axes for a series of objectives readily available within the Biomedical and Bioengineering laboratories at the University of Glasgow.

The PSF from the objectives listed measured using fluorescent microspheres using single photon excitation at 488 nm as most confocal systems have either a 488 nm Argon or diode laser Two-photon systems used 960 nm, as this is the longest wavelength the older Coherent Ti-sapphire Chameleon laser can emit and is very close to double 488 nm (although it is important to note that many dyes do not have a two-photon excitation spectrum that is simply the one-photon excitation spectrum doubled).

3.2.3.1 Summary of measured PSF

Imaging system	NA	X/Y(µm)	Z(µm)
Zeiss 5Live (Plan-Apochromat 20x/0.75)	0.75	1.9	2.76
Zeiss upright Two Photon (Achroplan IR 40x/0.8 W)	0.8	0.41	1.74
Zeiss 510 A (C-Apochromat 63x/1.2 W corr)	1.2	0.44	2.97
Zeiss 510 B (C-Apochromat 63x/1.2 W corr)	1.2	0.49	1.44
Zeiss 510 C (Plan-Achromat 63x/1.4 Oil Ph3)	1.4	0.51	4.28
Zeiss Exciter (plan-Apochromat 63x/1.4 Oil DIC)	1.4	0.45	2.03
Olympus (plapon 60x o na:1.42)	1.42	0.31	1.76
Olympus (uplsapo 60x W NA:1.20)	1.2	0.34	2.4
Olympus (uplsapo 60X O NA:1.35)	1.35	0.31	1.42
BioRad (60x PA Water / 1.2)	1.2	0.52	2.52

Table 3.2: Shows the measured PSFs from various microscopes. All variables were kept the same except for the pinhole, which was calculated by the manufacturers' software to the optimal pinhole size which is one Airy Diameter, unless two-photon was used.

Single-photon systems use a 488 nm excitation source as most confocal systems have a 488 nm laser, whilst two-photon systems excite at 960 nm. This is the longest wavelength the older Coherent Chameleon laser can emit. Note the two-photon imaging system is highlighted in red. This is because there has been an insufficient signal-to-noise ratio and the PSF has been calculated to be smaller than what is theoretical possible. This is discussed in the next section.

Below is the technical detail of some of the objectives used in this project along with details of the measure PSF data taken from these objectives. All of which where being used as single photon confocal systems.

3.2.3.2 Olympus Uplsapo 60X NA:1.35

Magnification	60X
Numerical Aperture	1.35
Working Distance [mm]	0.15
Coverglass Thickness [mm]	0.17
Immersion	Oil
Field of View [mm]	26.5
Correction Ring [Korr]	No

A

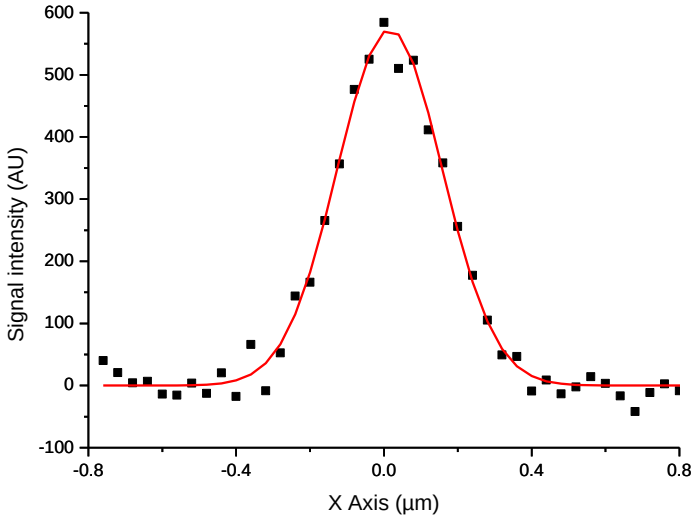

FWHM = 0.27µm

B

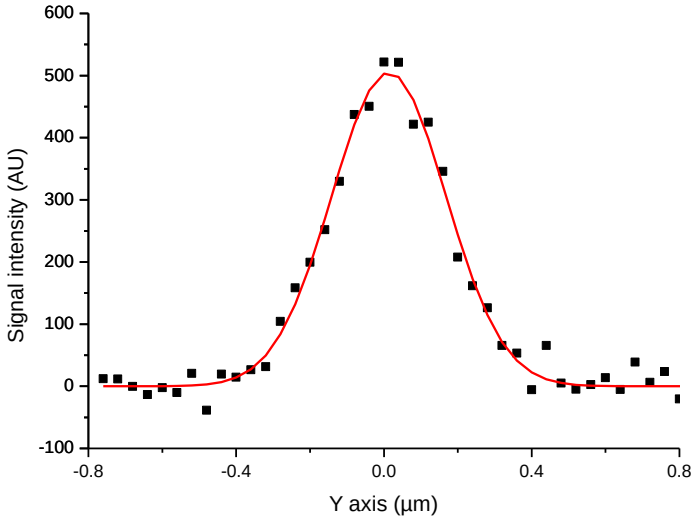

FWHM = 0.35µm

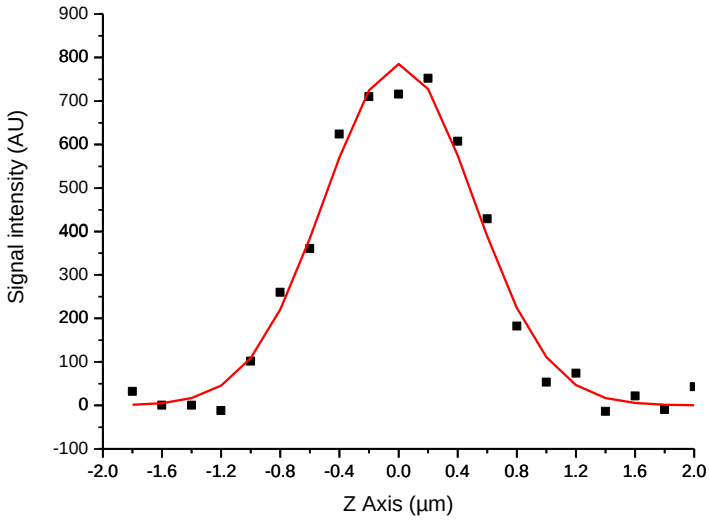

FWHM = 1.42µm

D E

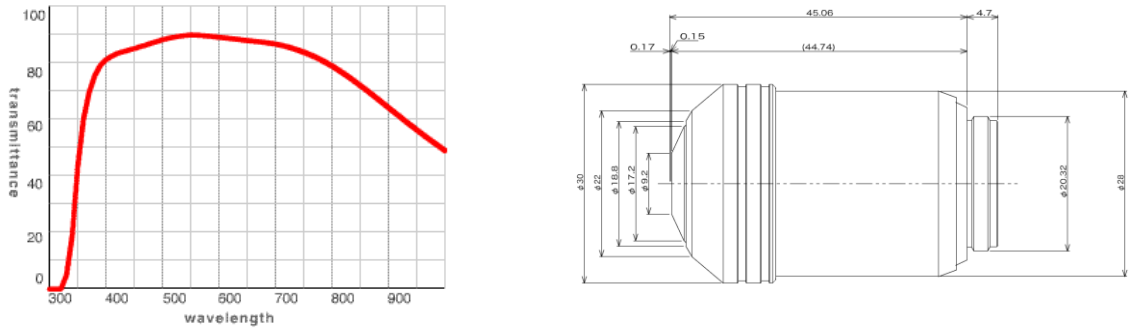

Figure 3.3 shows data from the Olympus Uplsapo 60X NA:1.35. Figures A, B and C show the Gaussian fits to the original data in the X, Y and Z axes. Figure D shows the transmission efficiency at various wavelengths. Figure E shows a technical drawing of the objective lens used (supplied by Olympus).

3.2.3.3 Olympus Uplsapo 60X NA:1.2

Magnification	60X
Numerical Aperture	1.20
Working Distance [mm]	0.28
Coverglass Thickness [mm]	0.13-0.21
Thread Type	
Immersion	Water
Field of View [mm]	26.5

A

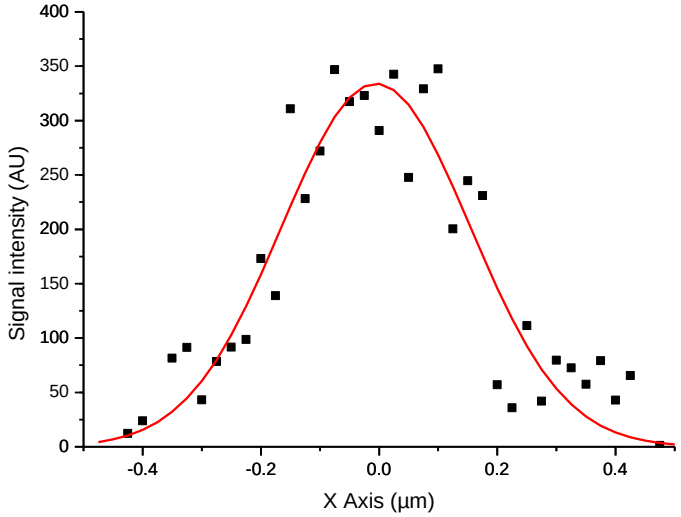

FWHM = 0.33µm

B

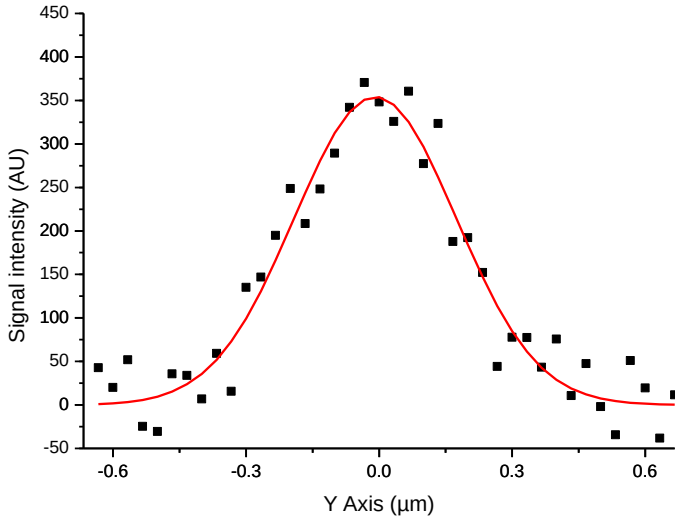

FWHM = 0.35µm

C

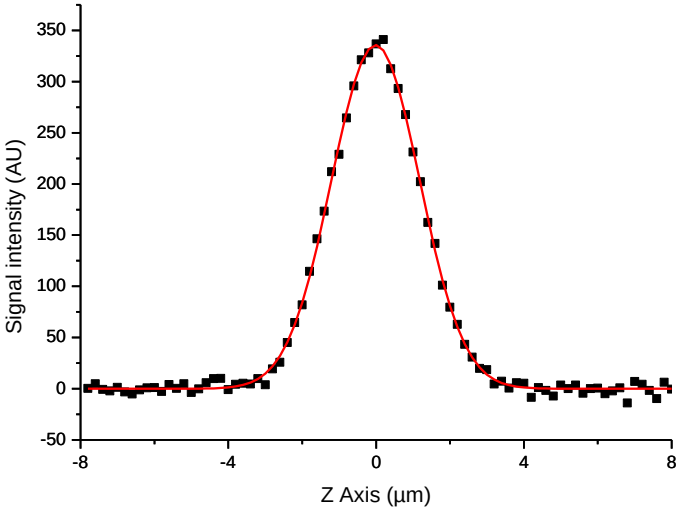

FWHM = 1.74µm

D E

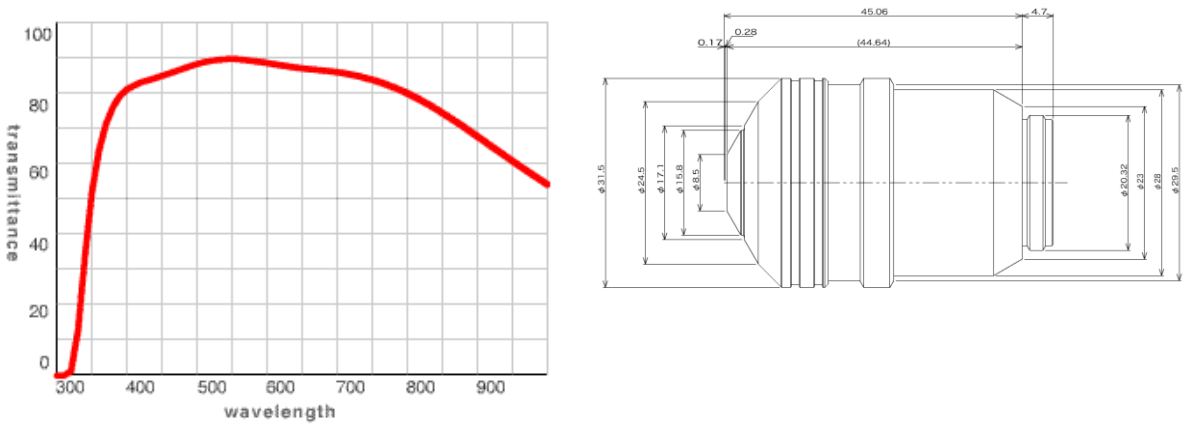

Figure 3.4 shows data from the Olympus Uplsapo 60X NA:1.2. Figures A, B and C show the Gaussian fits to the original data in the X, Y and Z axes, respectively. Figure D shows the transmission efficiency at various wavelengths. Figure E shows a technical drawing of the objective lens used (supplied by Olympus).

Olympus Uplsapo 60X NA:1.42

Magnification	60X
Numerical Aperture	1.42
Working Distance [mm]	0.15
Coverglass Thickness [mm]	0.17
Thread Type	M27x0.75
Immersion	Oil
Field of View [mm]	26.5
Parfocal Length [mm]	45.06
Optical System	ICS
Correction Ring [Korr]	No

A

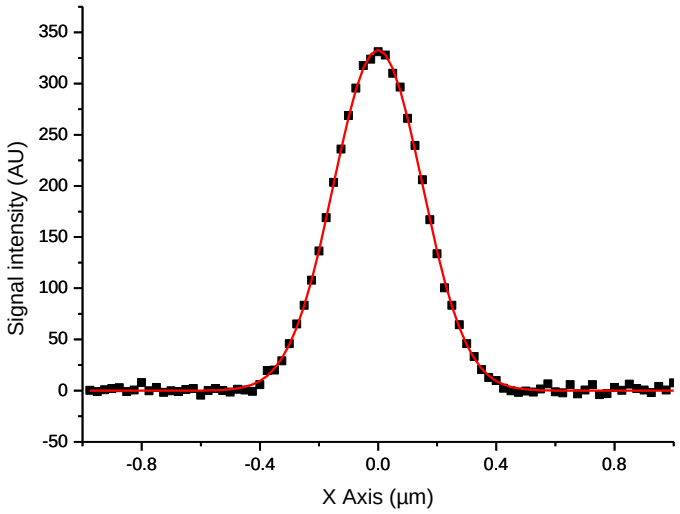

FWHM = 0.32µm

B

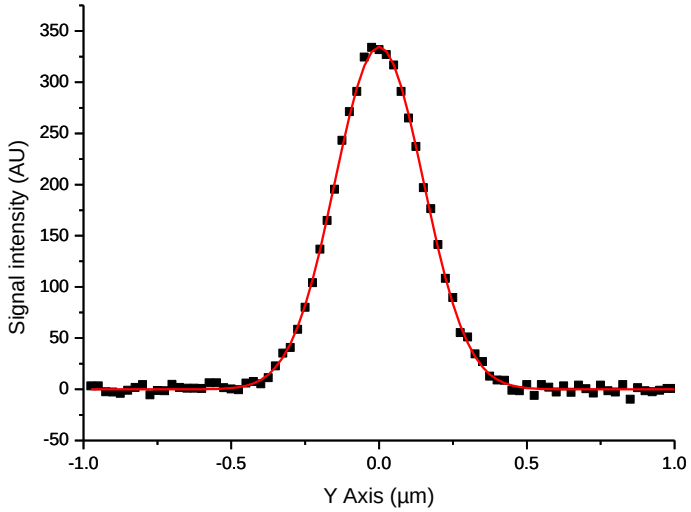

FWHM = 0.32µm

C

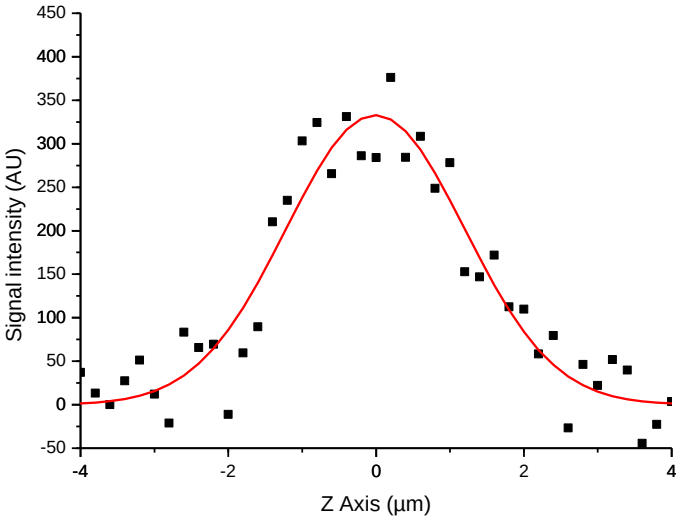

FWHM = 2.4µm

D

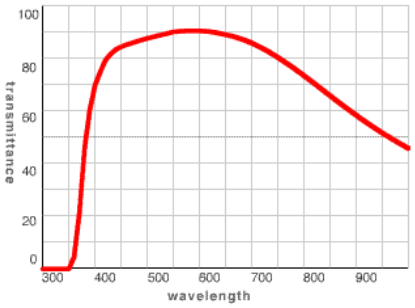

E

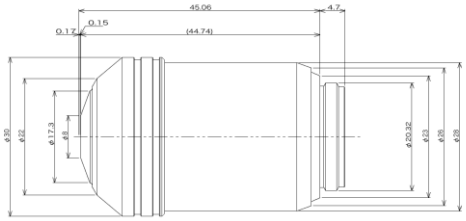

Figure 3.5 shows data from the Olympus Uplsapo 60X NA:1.42. Figures A, B and C show the Gaussian fits to the original data in the X Y and Z axis. Figure D shows the transmission efficiency at various wavelengths. Figure E shows a technical drawing of the objective lens used (supplied by Olympus)

3.2.3.4 Zeiss C-Apochromat 63x/1.2 W corr

Magnification	63X
Numerical Aperture	1.2
Working Distance [mm]	0.28 at cover glass 0.17
Coverglass Thickness [mm]	0.14-0.19
Thread Type	M27x0.75
Immersion	Water
Field of View [mm]	25
Parfocal Length [mm]	45.06
Optical System	ICS
Correction Ring [Korr]	Yes

A

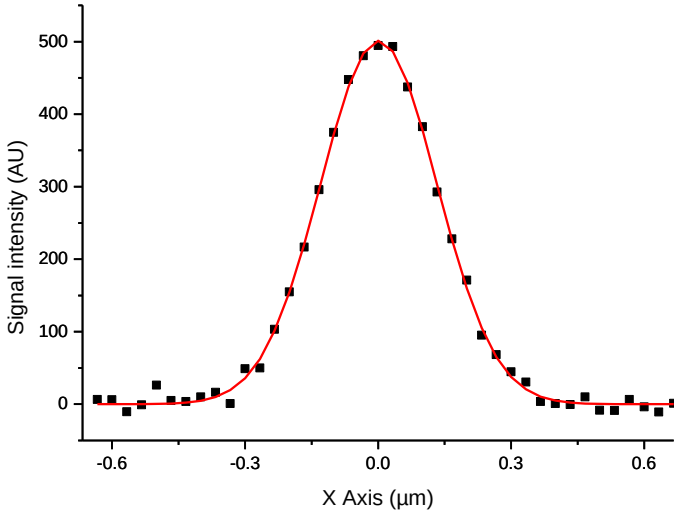

FWHM = 0.29µm

B

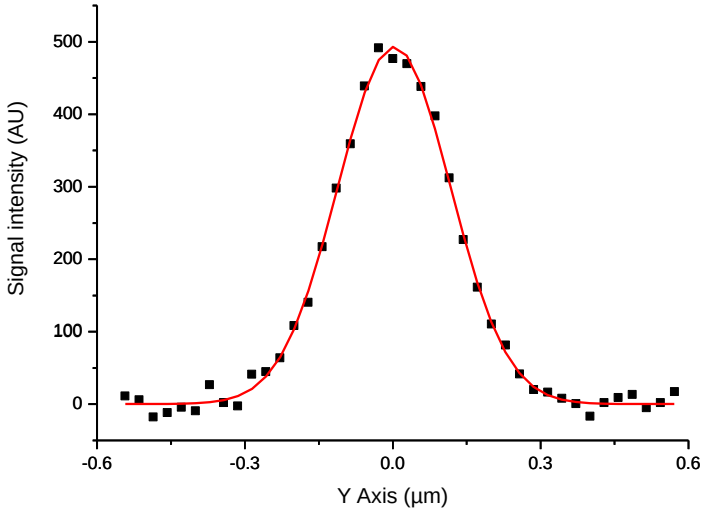

FWHM = 0.35µm

C

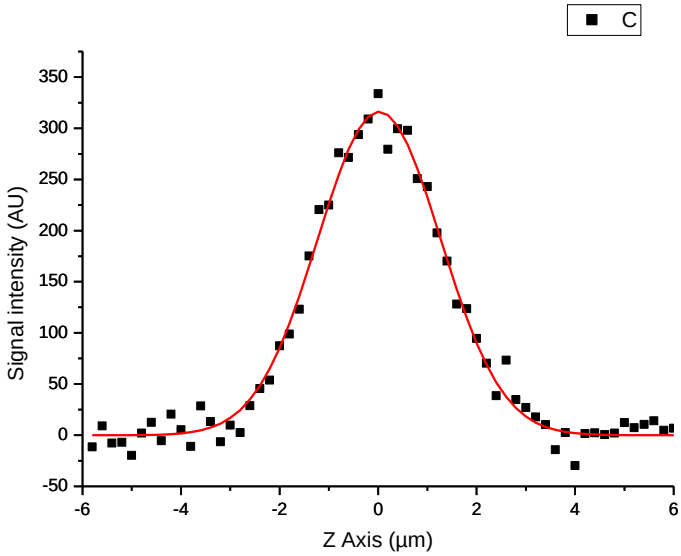

FWHM = 2.88µm

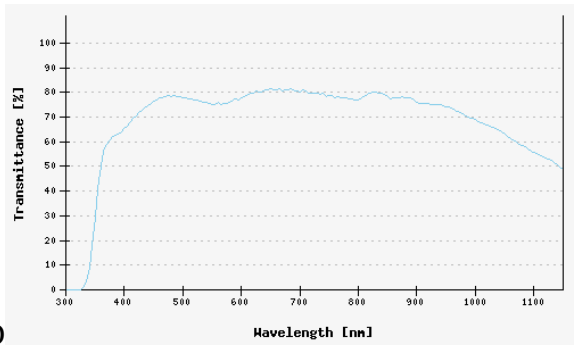

D

E

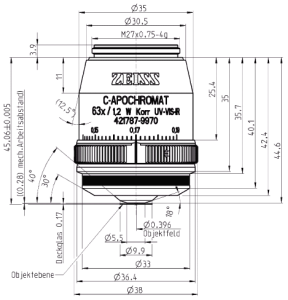

.

Figure 3.16 shows data from the Zeiss C-Apochromat 63x/1.2 W corr. Figures A, B and C show the Gaussian fits to the original data in the X Y and Z axis. Figure D shows the transmission efficiency at various wavelengths. Figure supplied by Olympus. Figure E shows a technical drawing of the objective lens used. Figure supplied by Zeiss

3.2.3.5 Zeiss plan-Apochromat 63x/1.4 Oil DIC

Magnification	63X
Numerical Aperture	1.4
Working Distance [mm]	0.19
Coverglass Thickness [mm]	0.17
Thread Type	M27x0.75
Immersion	Oil
Field of View [mm]	25
Parfocal Length [mm]	45.06
Optical System	ICS
Correction Ring [Korr]	No

A

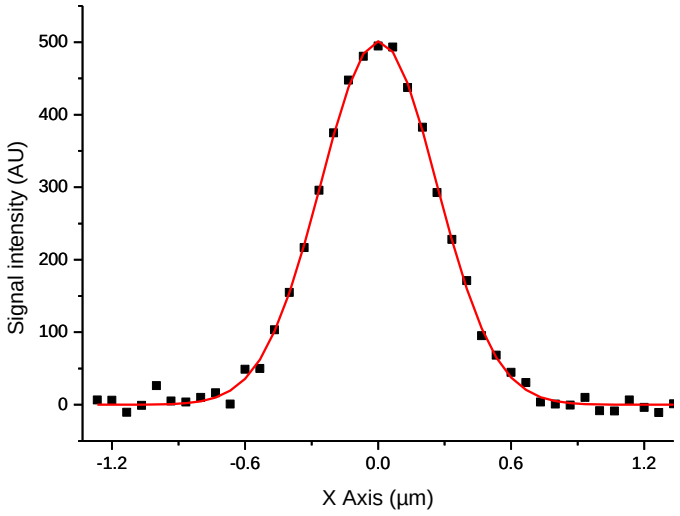

FWHM = 0.57 µm

B

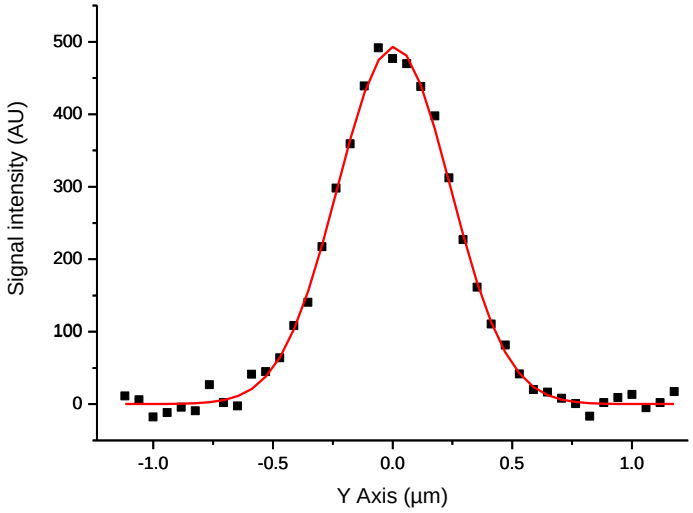

FWHM = 0.60 µm

C

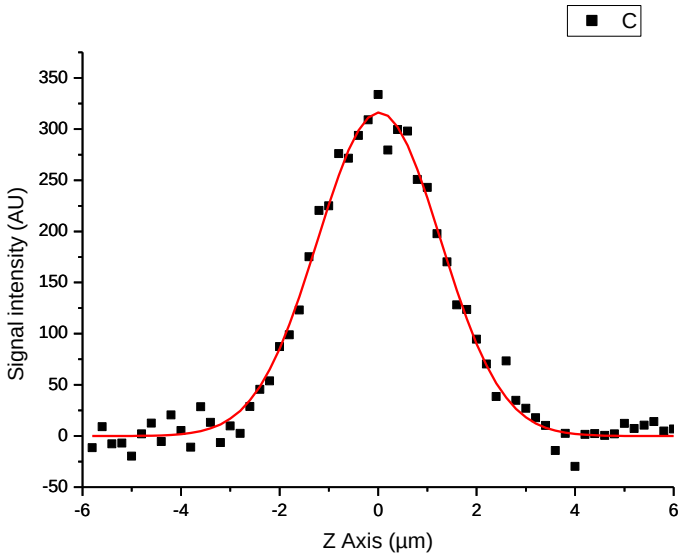

FWHM = 2.20 µm

D

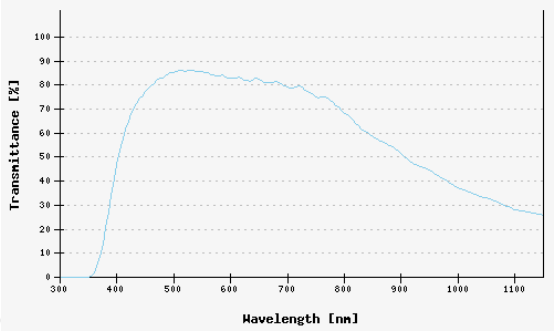

E

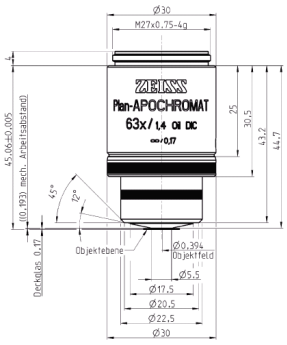

Figure 3.7 shows data from the Zeiss plan-Apochromat 63x/1.4 Oil DIC. Figures A, B and C show the Gaussian fits to the original data in the X Y and Z axis. Figure D shows the transmission efficiency at various wavelengths. Figure E shows a technical drawing of the objective lens used. Figure supplied by Zeiss

3.2.3.6 Nikon Plan Apo 60x PA Water / 1.2

Magnification	60x
Numerical Aperture	1.2
Working Distance [mm]	0.22
Coverglass Thickness [mm]	
Transmission wave lengths	340–1100nm
Immersion	water
Field of View [mm]	14
Parfocal Length [mm]	
Optical System	
Correction Ring [Korr]	yes

Figures supplied by Nikon

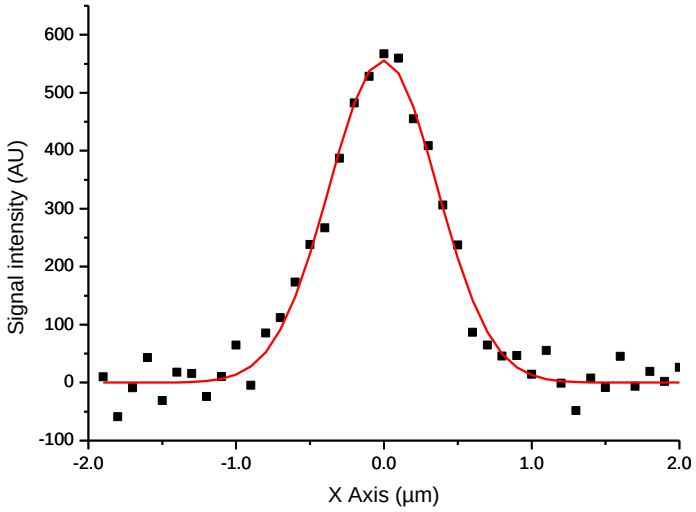

FWHM = 0.70µm

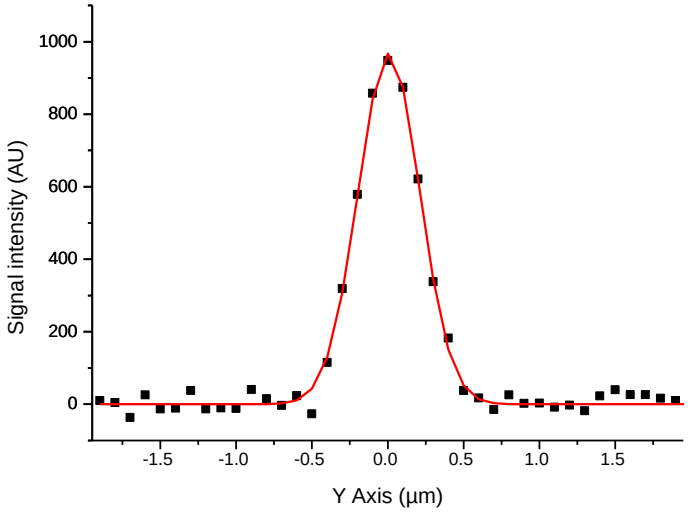

FWHM = 0.45 µm

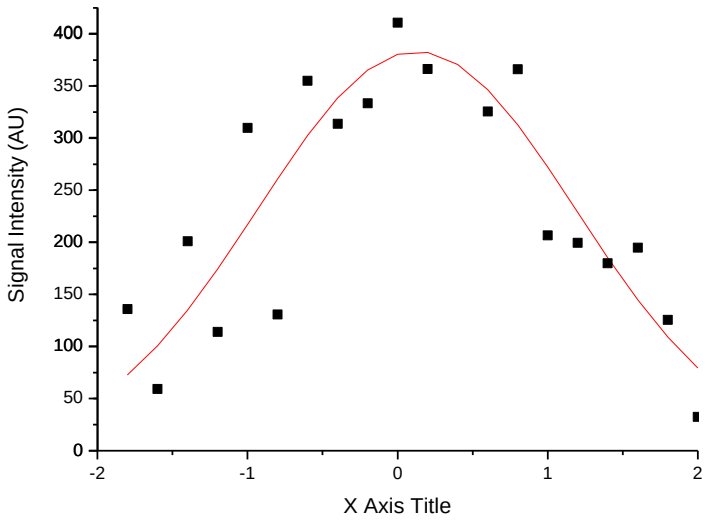

FWHM = 2.72 µm

Figure 3.8 shows data from the Nikon Plan Apo 60x PA Water / 1.2. Figures A, B and C show the Gaussian fits to the original data in the X Y and Z axis. Figure D shows the transmission efficiency at various wavelengths.

3.3 Measurement of resolution using a structured light microscope

The optical abilities of the selective illumination microscope prototype are entirely dependant on the pattern that is being displayed on the SLM. In this project there were patterns used to simulate wide field imaging as well as scanning pinhole arrays and faster scanning slit arrays

3.3.1 Preparing patterns to display on the Spatial Light Modulator

The spatial light modulator takes 24-bit bitmap images and displays them in a rapid series of on and off pixels. In order to generate the appropriate bitmap images a Matlab code was written that creates binary tiles of the patterns desired and then fills the 1280x1040 array with the tile pattern and then saves it as a bitmap image. The following patterns shown are the tile bitmap images. (Neil *et al.*, 1997)

3.3.2 Patterns used

Patterns were used to image the 1 μm beads and the dimensional measurements of the beads were taken. The patterns were:

3.3.3 Wide field patterns

This is the simplest pattern where all the pixels are on. This simulates a simple wide field image. Similarly, all the pixels could be turned off and the light would travel down the non-conjugate pathway, and there would be an added light to this pathway because of the issue with the light only being rotated by 60 degrees. The wide field pattern simply displays a series of white pixels.

Figure 3.9 show the conjugate channel on the left and the non-conjugate panel on the right. A Chroma test slide is being imaged at the stage to give a uniform background. The SLM is displaying the University of Glasgow's logo in the conjugate channel it is clear that the "off" pixels on the SLM cause the channel to have no light in these areas, however in the non-conjugate channel the blacks are not true blacks, this is caused by the light leak caused to the partial polarisation of the light to 60 degrees instead of 90. the dirt that is visible in this image is either on the SLM as it is a focal plane or on the aperture blades of the system.

3.3.4 Scanning pinhole patterns

There were two basic patterns generated by a grid of two-by-two with one active pixel. This will channel 25% of the light into the conjugate channel and 75% of the light down the non-conjugate channel. When the light rotation issue is taken into account 17.5% of

the light will go into the conjugate channel and 82.5% into the non-conjugate. Depending on the pixel size, there is a chance of cross-talk between the active pixels. One of these patterns is shown in Figure 3.10:

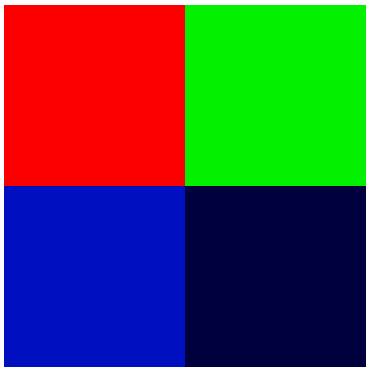

Figure 3.10 shows the first sample confocal pattern used with the SIMP. The colours represent the sequence that the pixel will be turned on or off. This is a representation of a single point, the pattern is repeated to fix the SLM array. These colour images are the physical image that is generated by the Matlab program. However the SLM will interpret these files as a series of 24 on/off commands for each pixel.

The second pattern is a 3X3 tile with one active pixel. This has a slower scan speed and should give better optical sectioning, however as the maximum number of frames this pattern can occupy are 18 has if the full 24 frames where used this would cause uneven illumination of the sample, this means that the last 6 frames must be set to off. This is effectively a 25% light loss, as the pattern will only channel 11% of light down the conjugate light path when it is working optimally due to the 60 degree polarisation issue. This coupled with the light rotation issue, and we can only expect 5.7% of the light to be channelled into the conjugate path. This can cause problems as there is a high probability that the side of the chip of the EMCCD being exposed to the non-conjugate channel will saturate before the conjugate channel has had enough exposure for an adequate signal to noise ratio. This can be solved by completely blocking the light from the non-conjugate channel and exposing for longer periods of time, this was done in all of the high confocal patterns that where run in this chapter.

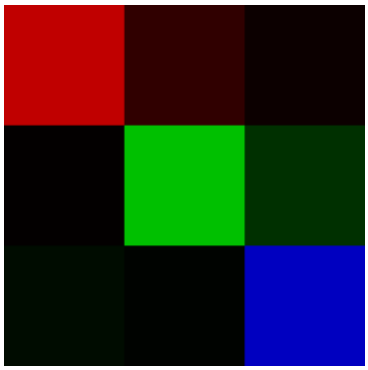

Figure 3.11 This pattern generates a slower scanning rate but a more highly confocal pattern for the SIMP. The colours represent the sequence that the pixel will be turned on or off. These colour images are the physical image that is generated by the Matlab program. However the SLM will interpret these files as a series of 24 on/off commands for each pixel.

3.3.5 Scanning slit patterns

The second type of pattern that can be generated is a pattern where the pinhole is actually and slit and is scanned across the image. These lose some confocal ability. Figure3.12 below shows two generated patterns, one of which has one of four lines active, and the second pattern has one of twenty four lines active:

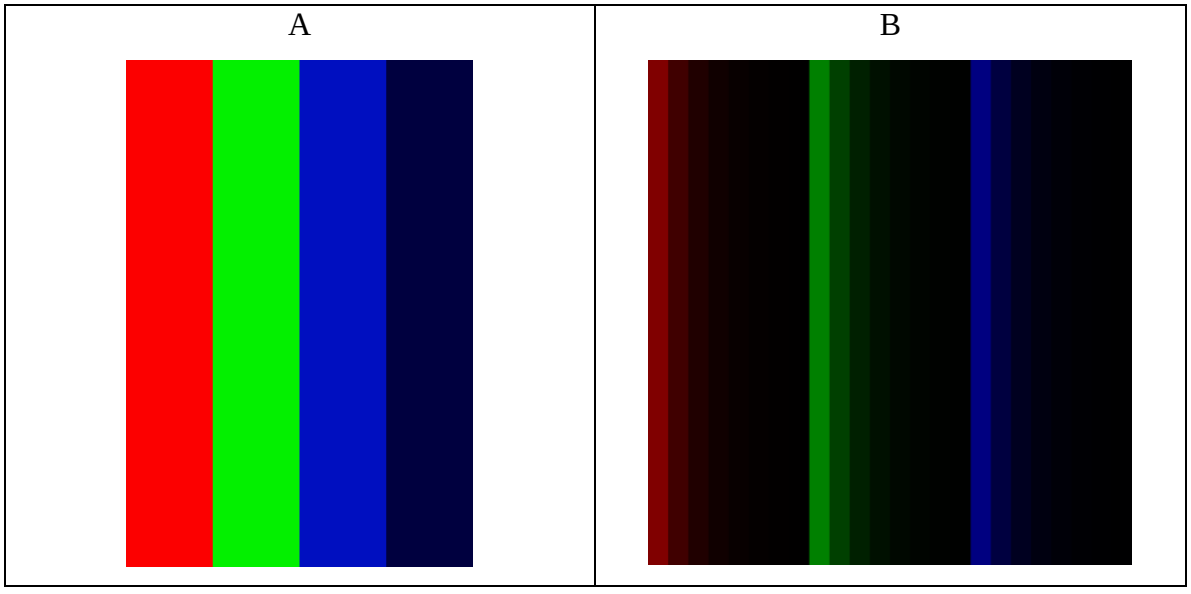

Figure 3.12 shows two simulations of slit scanning confocal patterns that could be used with the SIMP. These colour images are the physical image that is generated by the Matlab program. However the SLM will interpret these files as a series of 24 on/off commands for each pixel.

3.3.6 Experimental data from PAM

The PAM was setup using several EMCCD cameras. However, the PAM seemed to be suffering large amounts of light loss that dramatically affected the sensitivity. As a result 1 µm beads had to be imaged, PSF measurements could not be make, however the edges of the bead can be examined. With the long exposure times these long exposure times caused very noisy images on the EMCCD due to the dark noise there. As the non-conjugate image would cause saturation and possibly blooming on the EMCCD the non-conjugate channel light was not collected, therefore it was not possible to subtract the non-conjugate channel from the conjugate channel.

The following diagrams show PSF measurements fitted to three Z stacks of 1 µm beads using an Olympus Uplsapo 60x NA 1.25 lens. The first recording was taken with the EMCCD camera mounted directly onto the microscope side port. The second was taken through the PAM with all the pixels on the spatial light modulator on so it is simulating a wide field microscope. The third image was taken with the PAM running a highly confocal pattern.

No PAM PSF

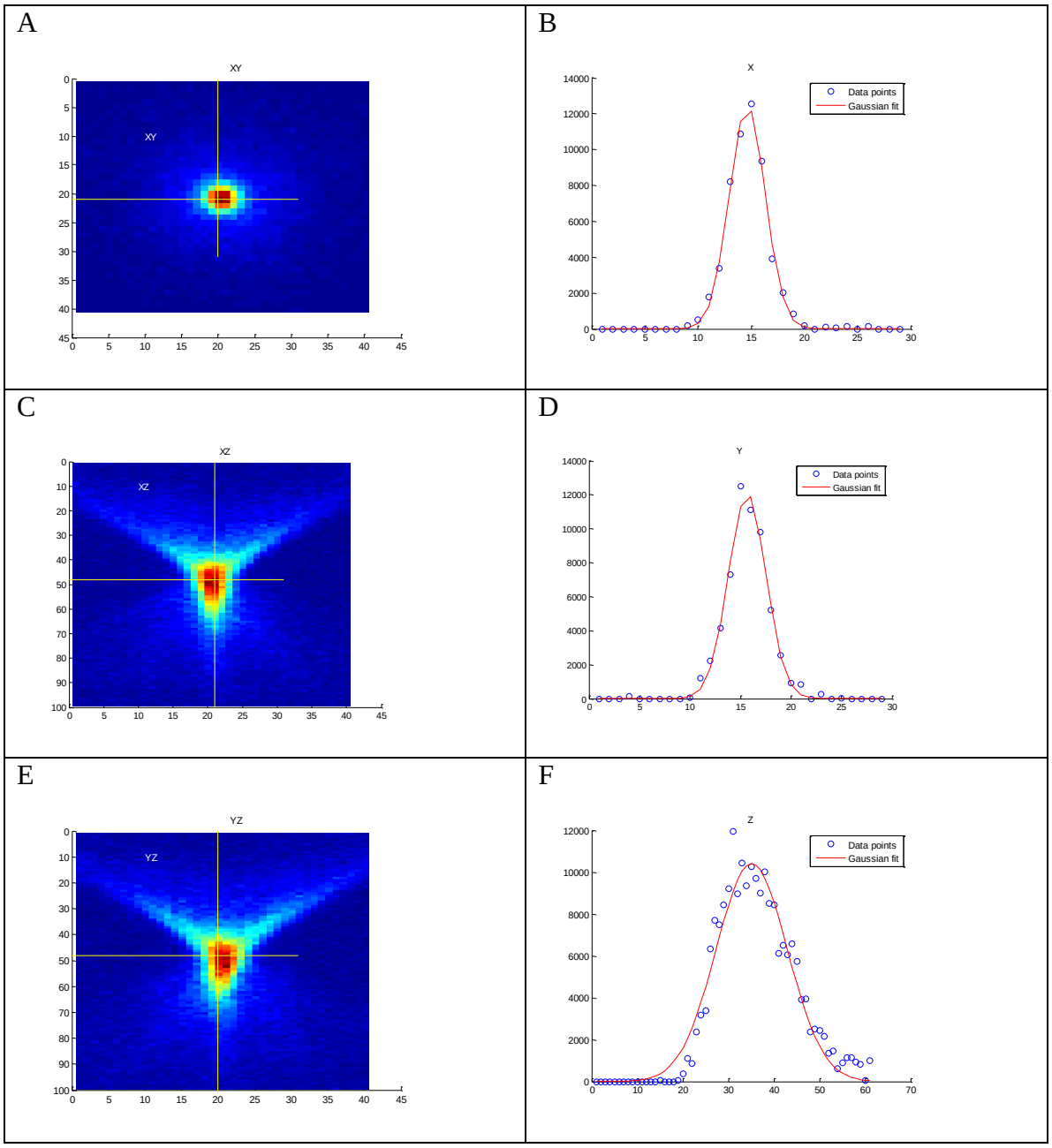

Figure 3.13 Show experimental results from the camera being mounted directly on to the Microscope with out the SIMP. Figures A, C and E show the fluorescent bead and where it is being sectioned at 0.2µm intervals. Figures B,D and F show original data of the section bead on the X, Y and ZA axes along with a Gaussian fit.

Simulated wide field

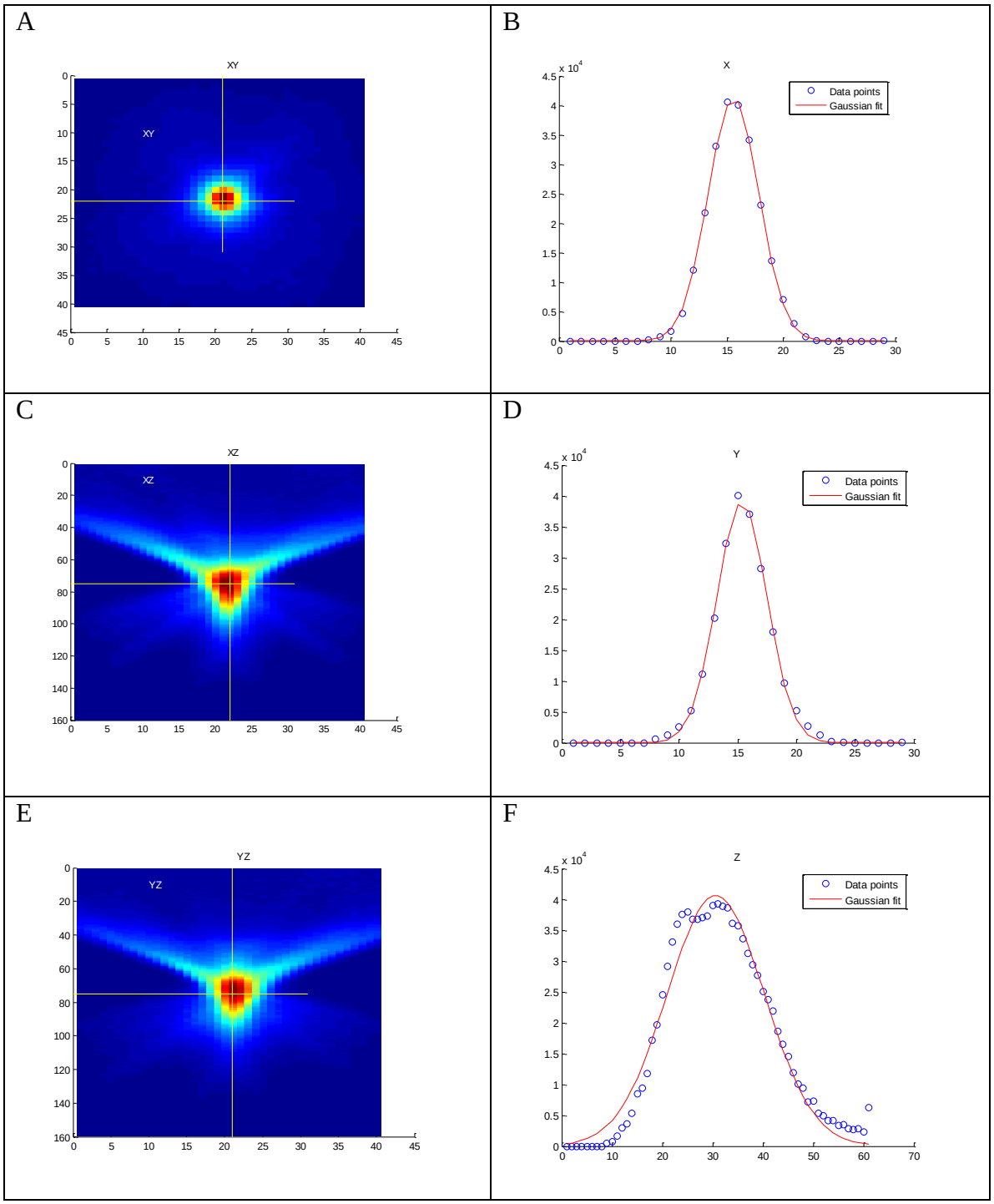

Figure 3.14 Show experimental results from the selective illumination microscope prototype where the pattern was simulating a wide field microscope. Figures A, C and E show the fluorescent bead and where it is being sectioned. Figures B, D and F show original data of the section bead on the X, Y and ZA axes along with a Gaussian fit.

Pinhole =2 pixels, tile diameter =12 pixels

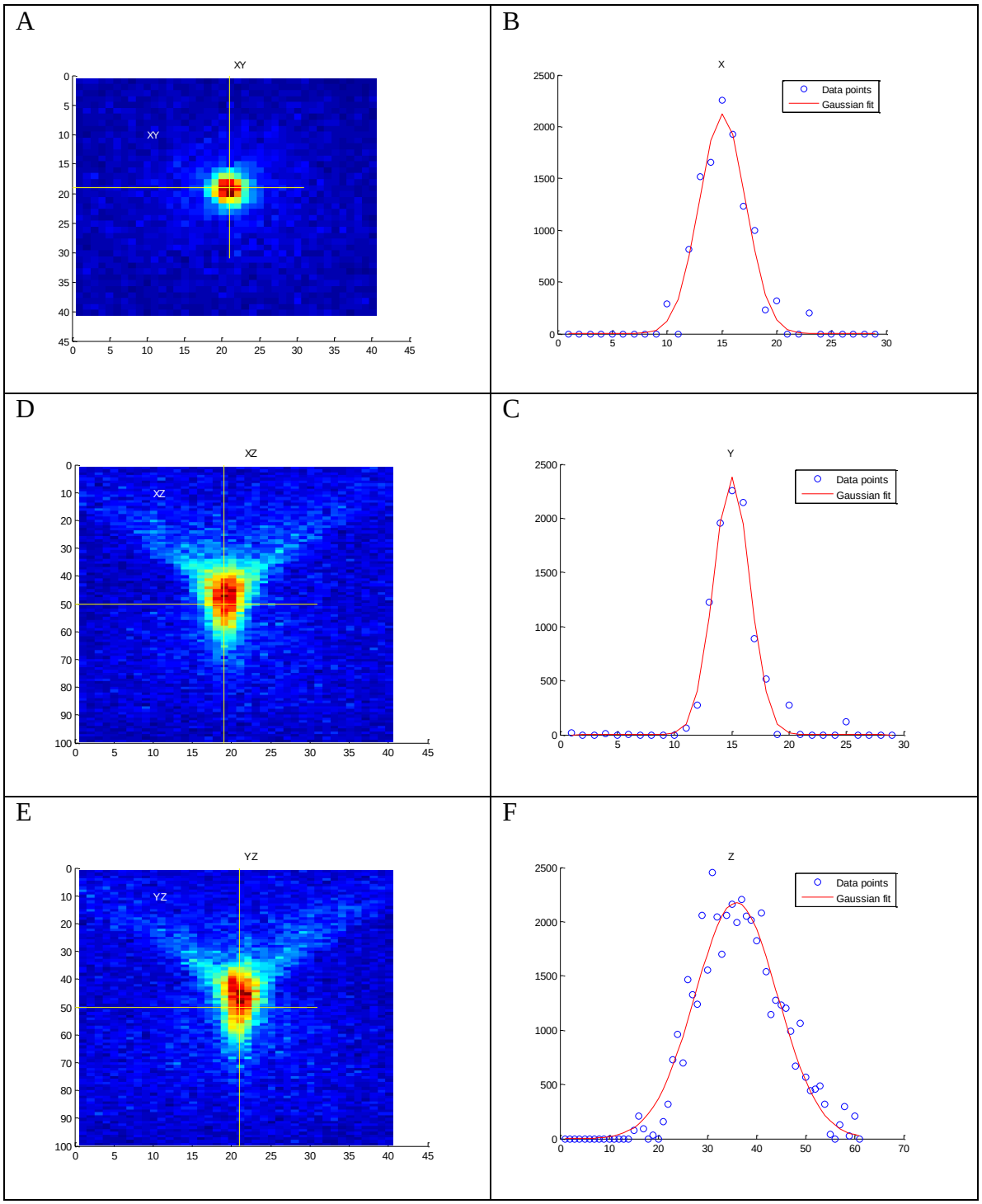

Figure 3.15 Show experimental results from the selective illumination microscope prototype where the pattern was simulating a spinning disk microscope (The pattern from Figure 3.4). Figures A, C and E show the fluorescent bead and where it is being

sectioned. Figures B,D and F show original data of the section bead on the X, Y and ZA axes along with a Gaussian fit.

Pattern	X(µm) Mean± STD	Y(µm) Mean± STD	Z(µm) Mean± STD
White	1.54 ± 0.3	1.4 ± 0.12	3.55 ± 0.18
SlitScan Pin=1 Speed =4	1.35 ± 0.10	1.33 ± 0.10	3.58 ± 0.13
PointScan Pin=1 tile =3	1.13 ± 0.07	1.10 ± 0.13	3.79 ± 0.10
PointScan Pin=1 tile =2	1.29 ± 0.12	1.3 ± 0.07	3.71 ± 0.13
PointScan Pin=2 tile =12	1.32 ± 0.12	1.25 ± 0.02	3.7 ± 0.13
PointScan Pin=2 tile =8	1.44 ± 0.04	1.28 ± 0.09	3.8 ± 0.05
NoPam	1.66 ± 0.24	1.73 ± 0.10	3.2 ± 0.12

Table 3.3 shows the FWHM from various different modes of the selective illumination microscope prototype set up where from the 1 µm beads imaged with a 60X NA 1.2 oil lens.

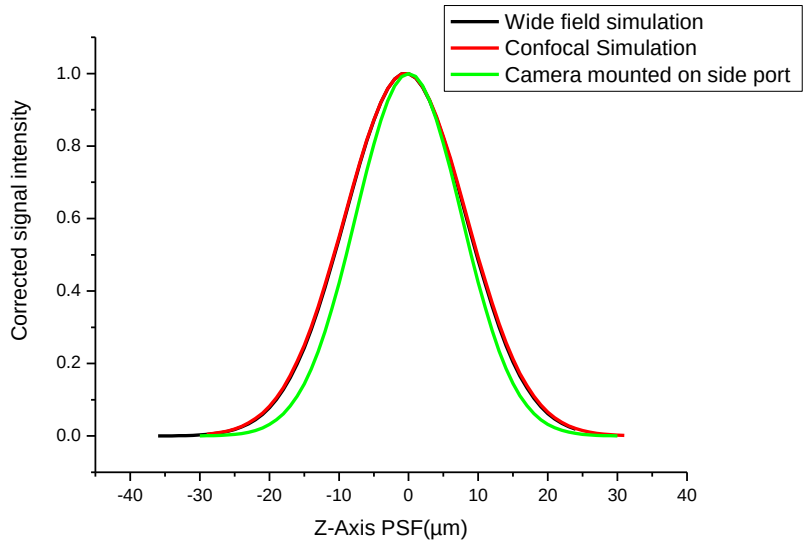

Figure 3.16 Shows the Z-axis in different modes of the SIMP. None of the patterns used demonstrate optical sectioning or an improvement in resolution.

From the results from the SIMP show that there is no significant optical sectioning acquired by the SIMP system, there is a small improvement in X/Y resolution however it is not significant enough to justify the use of the system. There are two likely causes of the lack of Z sectioning. The optical surfaces of the SIMP had become contaminated by dirt and it was not possible to clean these surfaces without risking damage to the system. This could cause diffraction in the light paths causing a loss of resolution from the SLM. The second issue is the lack of light, this system had to illuminate a $20mm^2$ surface and this was being done with a 470nm LED. This was meant that very little signal was arriving at the specimen, and was causing issues with acquiring the image.

3.3.7 Z-stage movement

All commercially available optically sectioning microscopes depend on stepping motors moving either the specimen or the objective lens relative to the specimen in order to image different planes. To further investigate the accuracy of Z-axis imaging, the accuracy of the stepping motors was assessed. This was achieved by measuring the moving part of the microscopes position relative to the rest of the microscope using a Heidenhain MT 60K probe. The methods that are used are described in more detail in Chapter 2 Page 90.

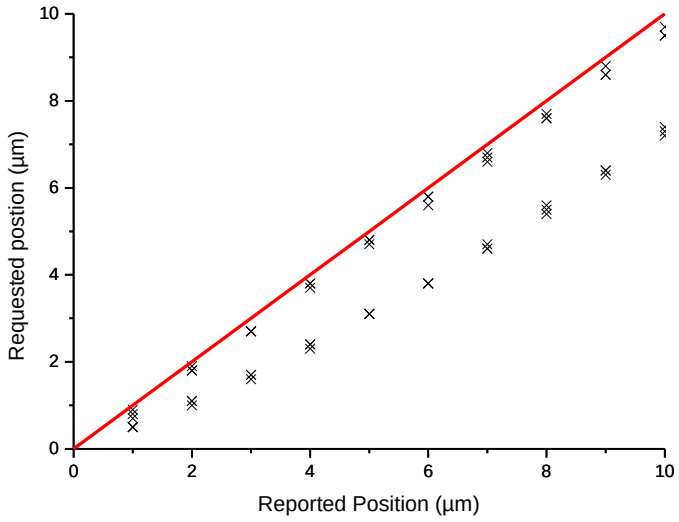

Figure 3.17 Shows the initial positional measurements from a confocal Zeiss 510 microscope when requested to move 1µm steps three times, the solid line is the line of identity. It is noticeable that the microscope underestimates the step size. It also does not produce reproducible movements.

Graphs 3.18-21 show single µm steps taken with a variety of microscopes in ascending and descending modes. A series of 5 200 nm steps where also preformed in order to see if the error was cause every time there was a move command or where the error was associated with distance travelled.

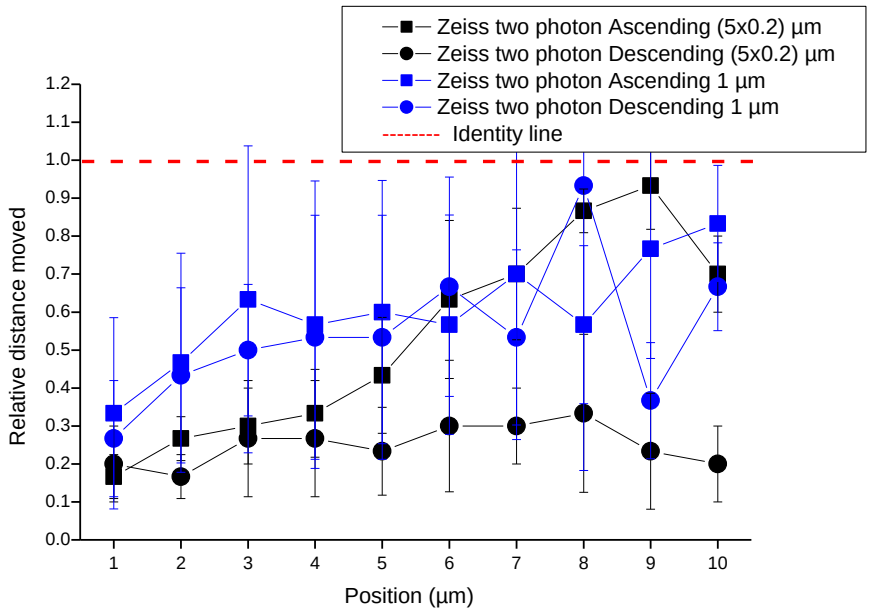

Figure 3.18 shows the data from the Zeiss 510 two-photon microscope after performing a 10 step procedure 3 times.

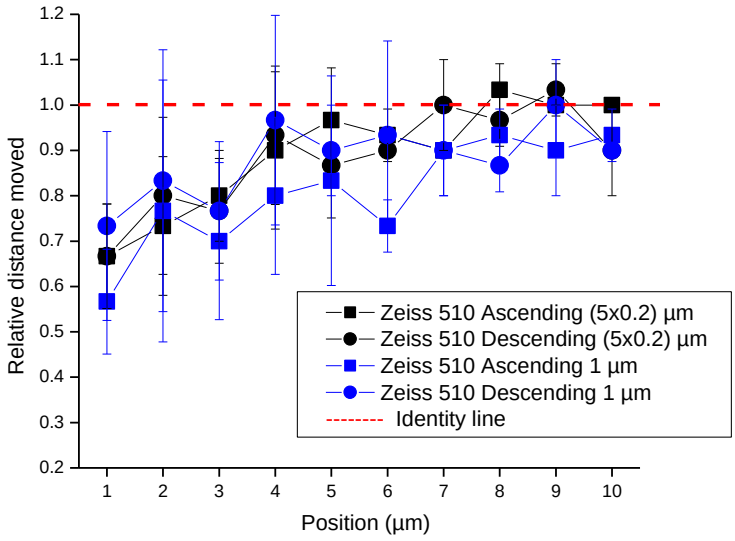

Figure 3.19 shows the data from a different Zeiss 510 confocal microscope after performing a 10 step procedure 3 times.

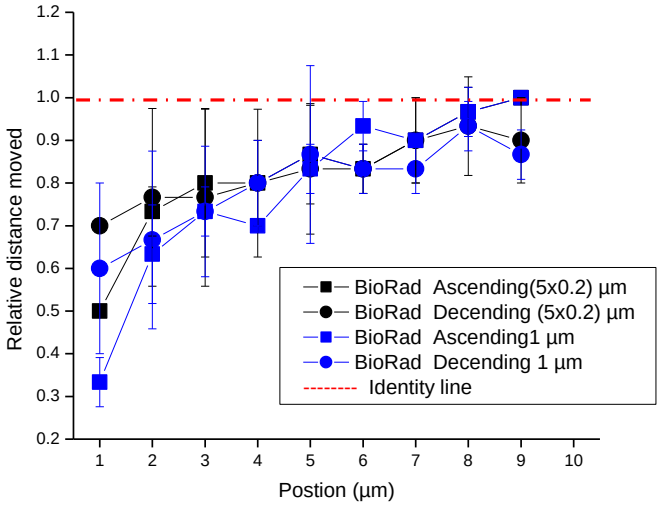

Figure 3.20 shows the data from the BioRad confocal microscope after performing a 10 step procedure 3 times.

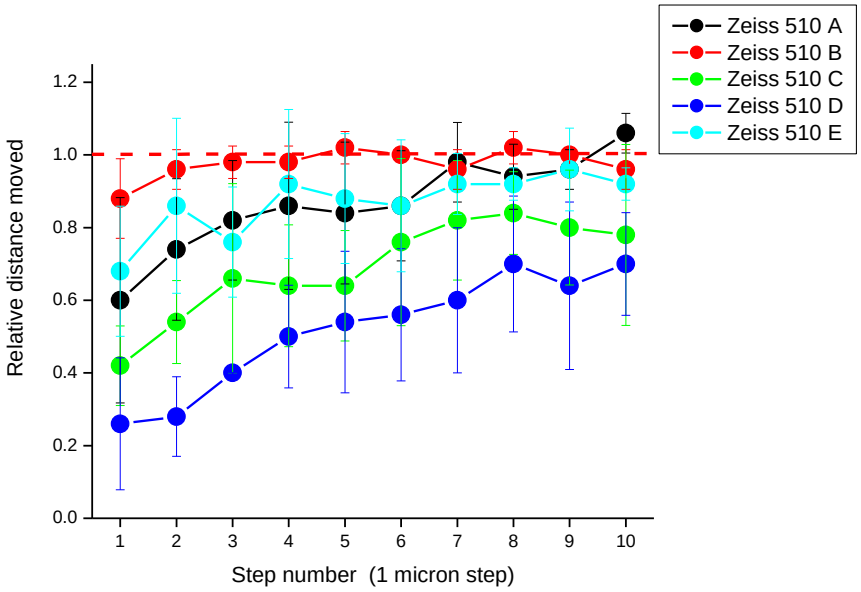

Figure 3.21: shows all the Zeiss 510 microscopes that were tested. This demonstrates how much variation there was between the systems that have very similar set ups.

Graphs 3.18 to 3.21 show that there is a large in accuracy in Z stage drives that shows no hysteresis when being driven in either direction. The Figures 3.22 to 3.24 show the same systems when performing 5µm steps.

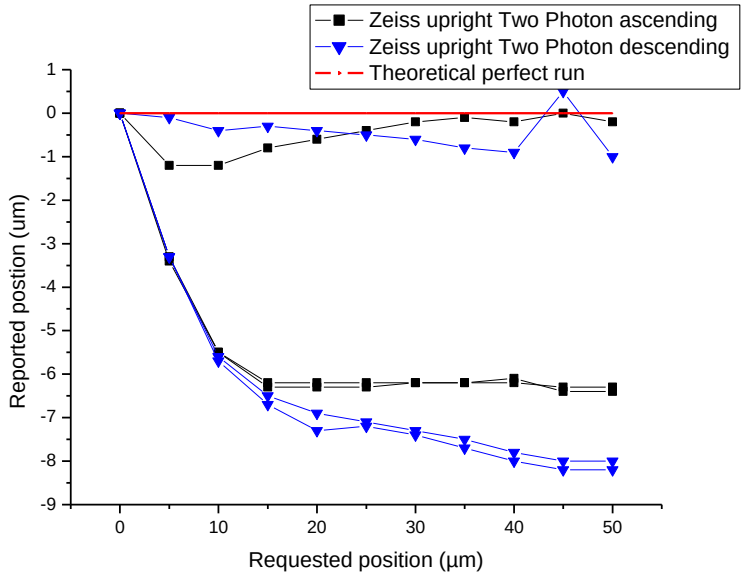

Figure 3.22 This figure shows the Zeiss upright two-photon system moving in 5µm steps. On some runs the accuracy is high however there are runs where the system underestimates the first three steps. The format of this graph shows the cumulative effect an inaccuracy in Z-stage positioning can have.

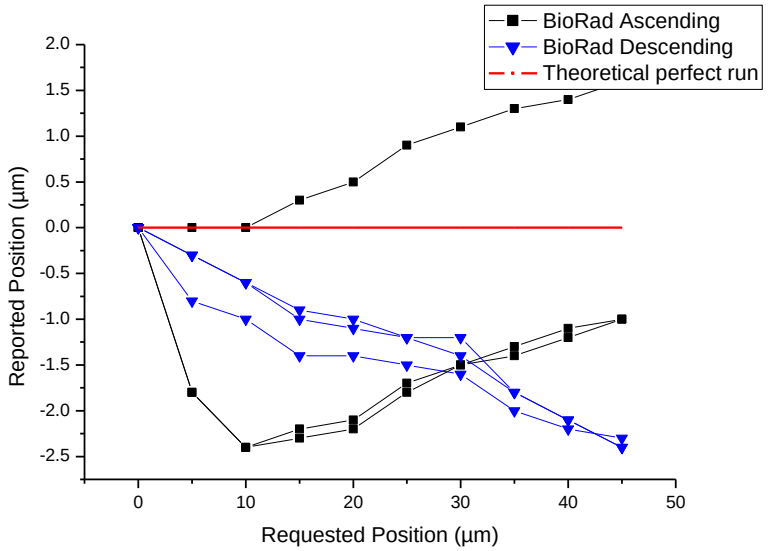

Figure 3.23 Shows the BioRad confocal system moving in 5µm steps. The BioRad system shows highly reproducible and accurate Z-stage movements.

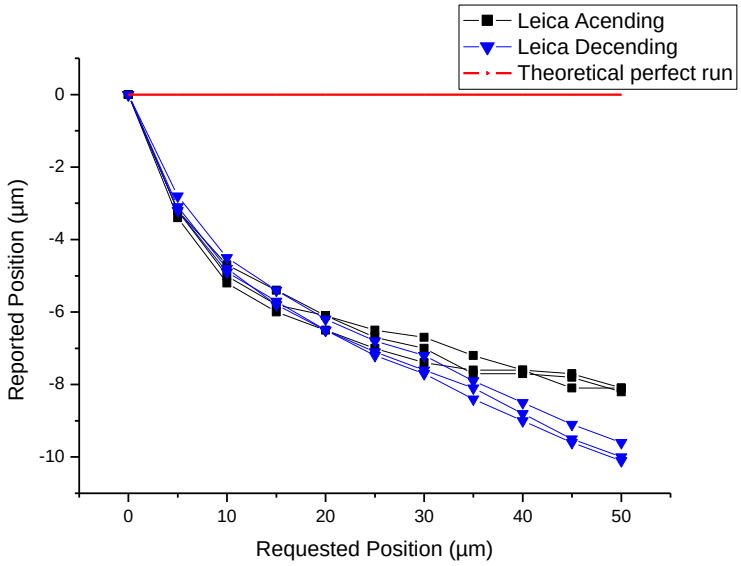

Figures 3.24 The Leica SP5 show reproducible results but the system continuously underestimated the step size.

System	steps 1-3 (1µm steps)	steps 4-10 (1µm steps)	steps 1-3 (5 µm steps)	steps 4-10 (5 µm steps)
Zeiss upright 2P (after moving)	0.60±0.31	0.77±0.32	3.66± 1.38	4.94±0.38
Zeiss upright Two Photon	0.66±0.33	0.62±1.58	4.95± 0.48	5.16±0.41
Olympus	0.8±0.13	0.94±0.11	4.71±0.53	5.16±0.41
Leica SP5	0.43±0.29	0.65±0.24	3.1±0.99	4.55±0.22
Zeiss Five Live	0.60±0.57	0.79±0.57	3.2±1.53	4.84±1.03
Ziess 510 A	0.54 ± 0.19	0.75 ± 0.18	3.54±1.03	4.92±0.22
Ziess 510 B	0.72±0.22	0.92±0.14	4.3±0.81	5.00±0.12
Ziess 510 C	0.94±0.08	0.99±0.04	5.01±0.18	4.79 ± 0.69
Ziess 510 D	0.31±013	0.60± 0.18	3.53 ± 0.79	4.79 ± 0.69
Ziess 510 E	0.76±0.19	0.91±0.12	4.48 ± 0.61	5.02 ± 0.13
BioRad	0.61±0.2	0.89±0.10	4.56±0.63	5.04±0.244

Table 3.3 Shows results from the monitoring of the Z stage movements of various imaging systems used for research.

3.4 Discussion

3.4.1 Uniformity of resolution across the field

One of the important factors that can effect the resolution measurements is if the back aperture is not illuminated properly as described in chapter 1 section 1.3.1. It would also mean that the resolution measurements would be different across the field of view. In order to check for this a fluorescent Perspex slide was imaged and ESF measurements taken at different point in the field of view as described in Chapter 2 section 2.6.

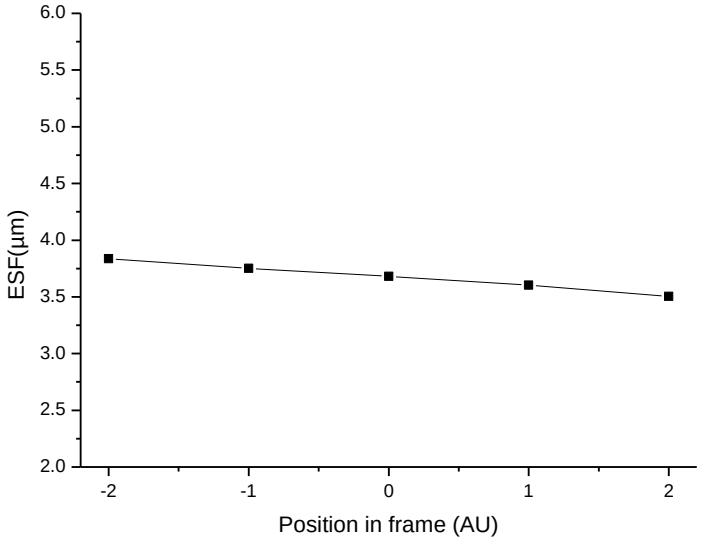

Figure 3.25 shows several ESF measurements across the same field of view. A Chroma test slide was images and a z-step frequency of 0.2µm was used (the ESF was calculated using the method described in section 2.7), Region 0 is the centre of the frame while regions 2 and -2 are the outer extremities of the field. There is a small increase in Z-resolution however it would be expected to be in the middle of the frame rather than in one corner of the field.

From the results of this scan it is apparent that the illumination of the back aperture is fairly uniform.

3.4.2 The effect of noise on point spread function measurement.

Separate computer simulations were run to estimate how varying levels of noise affect the point spread function. This established whether or not noise had a greater influence on the PSF measurements than the optical aberrations of the objective lens. A program was created that generated a perfect Gaussian curve which had a large Z FWHM measurement of 2.33 µm, which is the calculated theoretical PSF (as described in section 2.4). Then a certain amount of Poisson noise could be added to the Gaussian distribution after the distribution had been created:

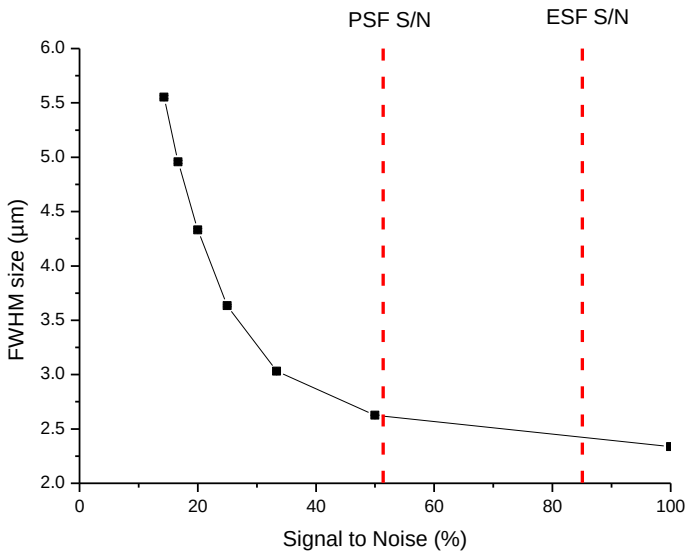

Figure 3.27 This graph shows the results of adding increasingly larger noise signals to the Gaussian distribution. Each level of noise was simulated and measured 1000 times. The errors where so small that they cannot be drawn on this scale. There is very little error in the measurements however there is a large detrimental effect on the FWHM measurements. The red dotted lines show the measured signal to noise ratio of the recording taken earlier in this chapter. The ESF measurements have a much more advantages signal to noise ratio, The PSF signal to noise ratio is slightly lower but still not in the range where a lack of signal would be adversely effecting the measurements.

In order to estimate the noise levels the where present in live cell recordings, measurements were taken from the Zeiss 510 Descanned detectors which were held at a constant gain of 629. Varying levels of laser power were used to generate different signal intensities. The mean of the signal along with the variance was then measured. It is important to maintain an exposure where there is an even Gaussian distribution. If the signal becomes too close to the extremities of the PMTs dynamic range, the signal will start to become cropped and will no longer be representative of a Poisson distribution, due to the clipping of the sides of the distribution due to the limitations of the dynamic range. A Chroma test slide was imaged so that fluorescence occurred and photon noise could be taken into account as it is one of the largest contributors to the noise levels. It was important that there are no filters in the system, the PMT defines the maximum bandwidth of system. The sampling rate of the recordings needs to be very high for the integration time of the PMT to start acting as a filter.

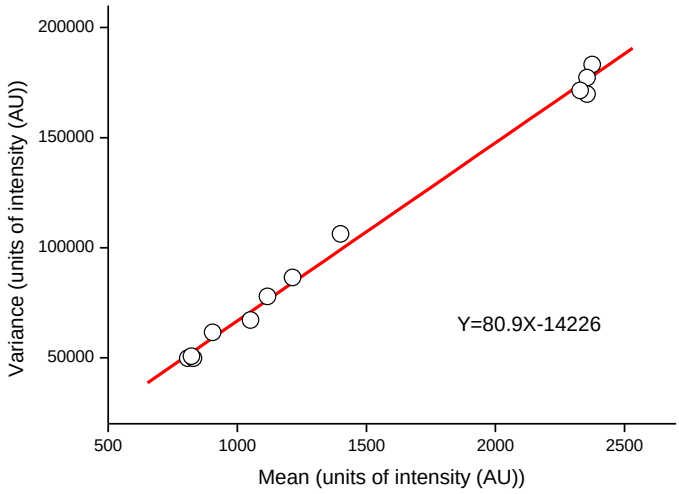

Figure 3.28 this graph shows the variance of signals plotted against the mean signal, taken from a 510 2P system.

The average signal to noise ratio for PSF measurements was 52% signal to 48% noise from the bead measurements and 85% signal to 15% noise from the Chroma test slide in the ESF measurements. There is a linear relationship between the mean and variance

(figure 3.32). In theory, photon noise is a Poisson distribution where the mean is equal to the variance. The dark noise and read noise from the system was measured. The effect of this type of noise was very low. As the linear fit is very close with an R^2=0.99, the gradient of the linear fit was at 81. This provides the conversion factor to allow the data to be transformed to allow the variance to be equal to the mean value if necessary,

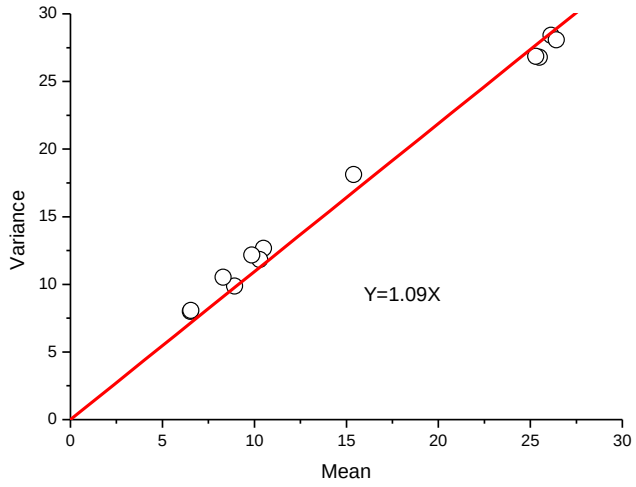

Figure 3.29 this graph shows the same data set but with the amplitude of the signal divided by the gradient of the linear fit from the last plot. This makes the data set representative Poisson distribution of the photon noise.

Simulations of the measured photon noise were run on a theoretical PSF that had a measured FWHM of 2.3µm after running several noise simulations on the PSF using noise values measured by the Zeiss 510 PMT at a gain of 629, the results from the PSF measurements consistently measured at 3.0µm ± 0.01µm.

A

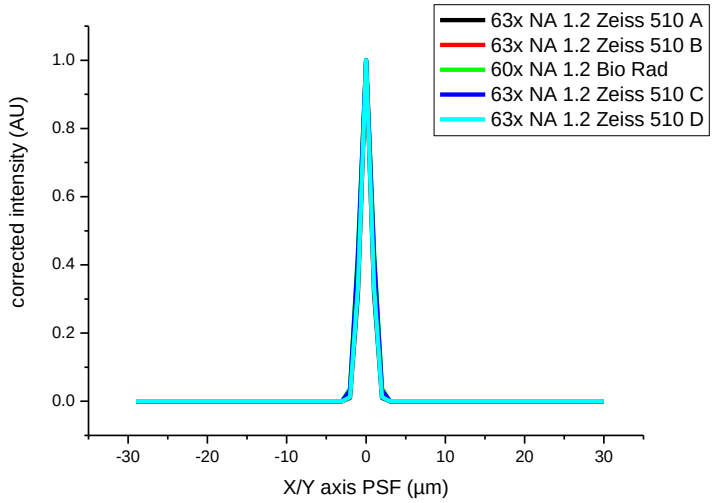

B

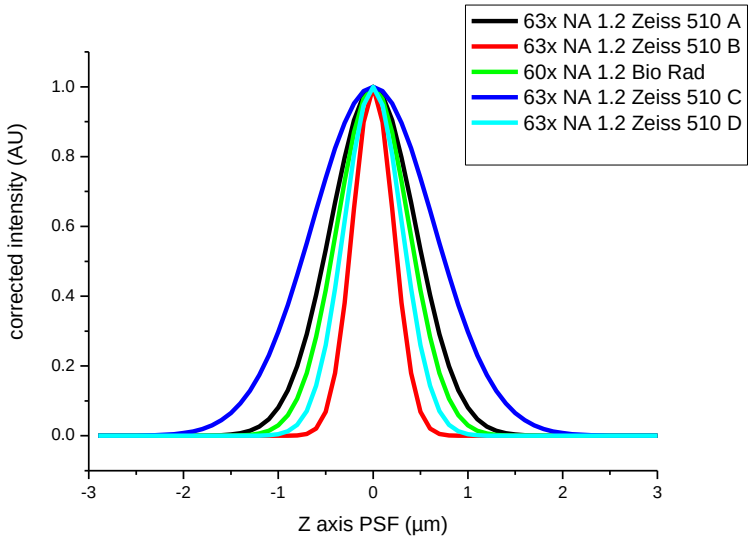

Figure3.29 Shows the super-imposed measurements from similar set-us (all 63x NA1.2 lenses using 488nm on a confocal set up. Figure A shows the lateral measurements which are very similar, Figure B shows the axial resolution varies significantly. In this chapter the causes of the variation of axial resolution have been investigated. The measured amount of noise on the systems used effects the Z- resolution by a constant amount as discussed in 3.4.2, there is little resolution difference across the field of view. The

accuracy of the Z-stage was found to be inconsistent and varied greatly in different systems.

3.5 Z-Axis Measurements used to correct PSF values.

It is now possible to correct the PSF measurement on the Z-axis by estimating the distance the Z-stage actually moves and applying it to the PSF. The protocol on most microscopes was to start well above the bead and take 100 x 0.2-µm Z samples. This is a total of 20 µm and the Z-PSF is at most 3 µm in size. It is therefore safe to assume that the larger underestimation that applies to the first 3 µm of the stages movement does not need to be taken into account. Three microscopes underwent a more accurate measurement system where the stage was moved 0.2 µm five times and then a measurement was taken. These results were as follows:

BioRad		GCRC Zeiss 510		Zeiss Two-Photon	
Mean 1-3 µm	Stdev 1-3	Mean 1-3µm	Stdev 1-3	Mean 1-3 µm	Stdev 1-3
0.52	0.28	0.75	0.13	0.22	0.10
Mean 4-10 µm	Stdev 4-10	Mean 4-10µm	Stdev 4-10	Mean 4-10 µm	Stdev 4-10
0.88	0.12	0.96	0.09	0.66	0.33
Z-PSF = 2.52 µm		Z-PSF = 2.97 µm		Z-ESF = 3.5 µm	
Corrected PSF = 2.21± 0.30		Corrected PSF = 2.85 ± 0.26		Corrected ESF = 2.31 ± 0.73	

Table 3.4 shows the corrected resolution measurements with the z-stage stepping error taken into account. All of the Z axis measurements were recorded with at least 100 z-slices so first 3 will be out of the Z axis measurements and therefore discounted, therefore a constant correction factor was applied to the Z axis measurements.

It is interesting that the Z-stage movements were very variable. The original hypothesis was the weight of the objectives or specimen stage causes hysteresis as there could be an

uneven load on the stepping motors dependent on which direction the stage was travelling. However this was examined and none of the systems demonstrated this. Most of the systems demonstrated an underestimation of movement on the first three steps. This could possibly be due to an uneven torque load on the motor.

3.6 Refractive index changes and the Z-position

Another factor that affects the position of the focal plane that is being imaged is mismatches in refractive index. This is caused by the photons changing the angle they travel at with every refractive index interface that they come across, as described by Snell's Law:

Equation 3.1

$$\frac{\sin\theta_1}{N_1} = \frac{\sin\theta_2}{N_2}$$

where θ describes the angle the photons encounter the interface and N describes the refractive indexes of the two substances. Water immersion lenses are designed to have a cover slip of 170 μm (Glass N=1.515) between the element and the specimen. Most water objective lenses also have correction collars to compensate for different thicknesses of cover slips. It is important to set these correctly as spherical aberrations can be introduced. Due to the smaller working distances of the objectives used for confocal microscopy the effects of refractive index mismatch will not be very pronounced. However, in two-photon deep tissue imaging, the effects can be quite pronounced due to the large working distance of the objective from the plane of focus, which can shift by hundreds of microns. The diagrams in Figure 3.36 show an estimation of how far the plane of focus is expected to shift due to refractive index mismatching. The refractive index of the Tyrode's solution was measured and found to be n=1.335 at 600 nm. Due to the complexity of measuring cardiac muscle refractive index, a reference bovine cardiac muscle is used which was found to be at N=1.383.(Dirckx *et al.*, 2005) Because the front aperture of the Achroplan IR 40x/0.80 W is unknown it was calculated from the numerical aperture and working distance.

Working distance = 3.6 mm

NA = 0.8

NA= n sin θ

sin θ-1 =NA/n

sin θ-1 =0.8/1.333

=36.8

A

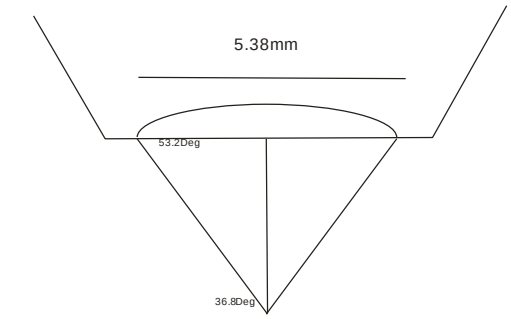

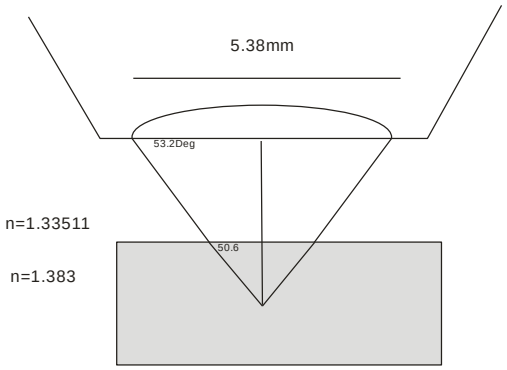

B

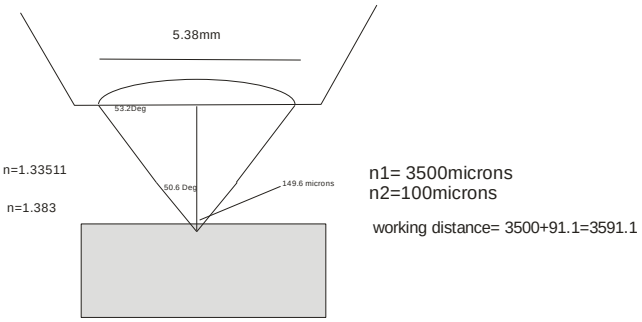

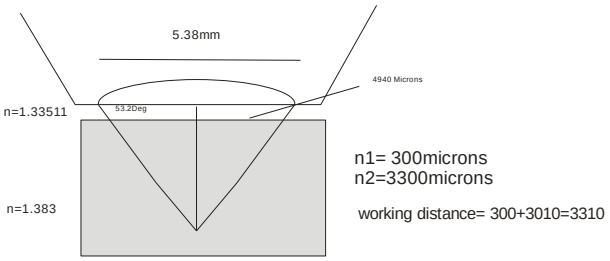

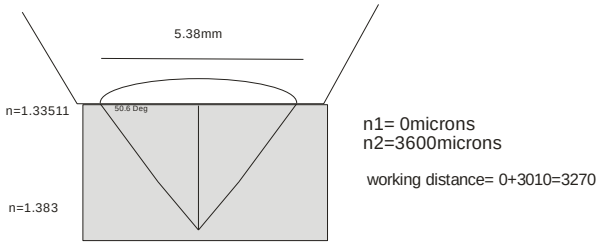

Figure 3.36 describes the error in reported depth as the aberration caused by refractive index becomes more severe. n1 and n2 refer to two mediums n1 has a refractive index of 1.33 while n2 has a refractive index of 1.38 As the photons enter the cardiac muscle there is a small change of angle. This could result in a focal plane shift of up to 330μm if the full 3.6mm working distance was used.

3.8 Conclusions

The results from this chapter highlight the importance of performing proper controls on optical sectioning microscopes before attempting biological experiments, as the measured results are often much larger than the calculated results. The noise on the system can cause problems for making fine resolution measurements as well as the misreported Z-stage positions causing a disproportionate elongation of the Z-axis resolution. However the z-axis error do not full explain degradation of the PSF and ESF measurements that were observed in this chapter.

The selective illumination microscope prototype was found to have no benefits in optical sectioning compared to a conventional wide field system; this is contrary to what previous studies have found. The selective illumination microscope prototype that was used had not been used in some time and had been transported from another lab. It is very possible that the optical surfaces had become contaminated with dust that could generate diffraction problems or the components had moved out of alignment. To rectify these issues the selective illumination microscope prototype would have to be sent to Cairn Research to be serviced, however the senior managers in the company felt the selective illumination microscope prototype system was not of sufficient commercial priority to warrant the cost of a servicing/repair of the selective illumination microscope prototype system, at the time of writing, no systems have been sold commercially.

4 Chapter 4: Artificial myocardium

4.1 Introduction

The previous chapter described the measured resolution performance of various imaging systems. There measurements were made under "ideal" conditions where the fluorescent objects were bright relative to the background and the optical properties of the specimen were not significantly different from water. However, these measurements are not necessarily realistic representations of the conditions present in biological studies, particularly studies involving muscle tissue. Previous studies have shown that the PSF of an imaging system is dependent on the intervening depth of tissue, this is thought to be a consequence of one or more aspects of the optical properties of biological tissues (Shaevitz & Fletcher, 2007). In this chapter, different aspects of the optical properties of cardiac muscle are investigated in an effort to determine the basis for (and quantify) the optical distortion at wavelengths use for multiphoton imaging.

The major focus of this chapter is resolution issues associated with two-photon imaging. The larger working distance of many two-photon systems mean that there is the potential for a considerable distance of the optical path to contain biological tissue. There have been previous attempts to study resolution of two-photon resolution in vivo however these have encountered complications. These included sub-resolution beads exhibiting oscillatory motion when located inside the cardiac muscle. There where also recorded instances of refractive index heterogeneity (Beckerle, 1984;Eschenhagen & Zimmermann, 2005;Kofidis *et al.*, 2002;Subbarao *et al.*, 1995;Young *et al.*, 2011). For these reasons, assessment of resolution in biological material can be very difficult and the use of phantom tissue is preferable.

On the basis of the analysis of optical properties described in Chapter 1, Section 6 - 3 main optical phenomena were chosen which together account for the means through which light can interact with biological tissue, i.e. light scattering, refractive-index, intrinsic fluorescence. The aims of this chapter are:

(i) Investigate the effects of light scattering on two-photon imaging.

(ii) Investigate the effects of refractive index changes on two-photon imaging.

(iii) Investigate the effects of intrinsic fluorescent dyes on two-photon imaging.

4.2 Methods

The following results where all obtained under the same standardised conditions using the upright Zeiss 510 two photon system, with the PMTs set at a constant gain of 629 and the laser power at 5% and the same objective lens, i.e. a Zeiss Achroplan IR 40x/0.8 W. the artificial myocardium samples where immersed in a sample bath in a similar set up to that used to image isolated heart tissue.

4.2.1 Back ground signal measurements

It is important to ascertain the contribution of the background light and PMT dark current to the signal on the individual non-descanned detectors. Figure 4.1 shows the results of scans done above a test specimen in view of the objective to measure the effects of ambient light on.

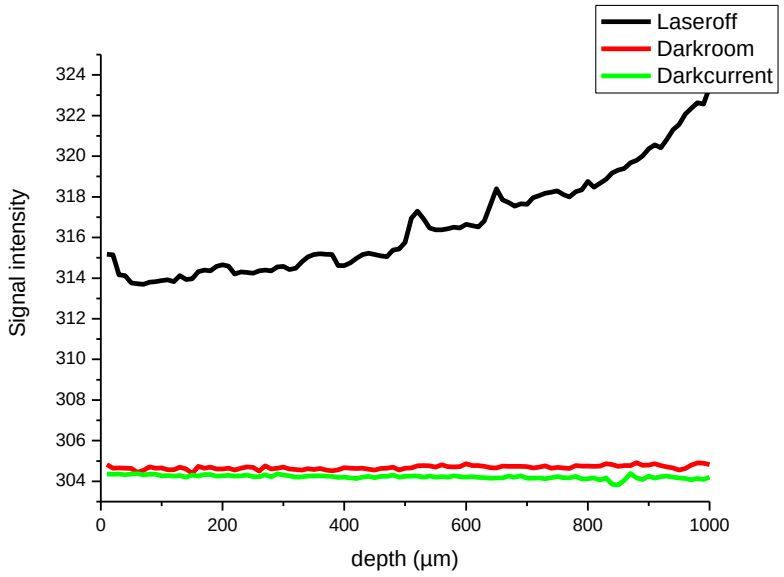

Figure 4.1 shows the results from when the dark current and ambient room light was measured. Over 1mm with a stepping interval of 10µm. to investigate where the major contributions of the noise from the signal arises from, this graph shows very small noise signal showing that the major source of noise is photon noise.

The “darkcurrent scan was done with the shutter to the PMTs closed. The “darkroom” scan was done with the shutter open. The “laseroff” scan was done with the room lights off but the room was illuminated by two large computer monitors.

All experiments using the two-photon system where conducted under “darkroom” conditions. Using a standardised gain setting for the PMT, a signal magnitude of ~300 units was recorded when the shutter to the PMT was closed (~8% of the maximum recordable signal i.e. 4096). This background signal represents the PMT “dark current” i.e. light independent signal and the minimum value that can be measured under these conditions, as expected this value showed no dependence on objective position. Opening the shutter and recording over 1 mm range of objective position registered as a slight increase in signal the further away the sample was from the objective. This is possibly due to the distance increasing and allowing greater amounts of ambient light to enter the objective. However, it is not a significant amount to warrant taking into consideration when imaging. This effect was greater when both monitors were switched on (i.e. normal operating mode), but even under these conditions the background signal was only ~5% above the dark current signal and does not represent a large contaminating signal.

4.2.2 Line spread function measurement.

As discussed in Chapter 2 section 6 it can be difficult to obtain a valid PSF measurement from some imaging systems due low signal/noise and uncertainty over the position of the standard. This is particularly the case with 2P system that has been optimised for deep tissue imaging, where the tissue scatters a considerable amount of light reducing excitation and emission signals. To overcome this, an alternative to sub-resolution beads was used, namely the imaging of a solid fluorescent surface (Perspex slide) which provides a sub-resolution transition from zero to maximum fluorescence in the Z axis to generate a line spread function. This was achieved by imaging an edge of a fluorescent Perspex surface in the z axis, differentiating the signal and taking a FWHM measurement as shown in figure 4.2. The scan was conducted with excitation at 930nm, the PMTs gain was set at 629 units and the laser power was kept at 5%.

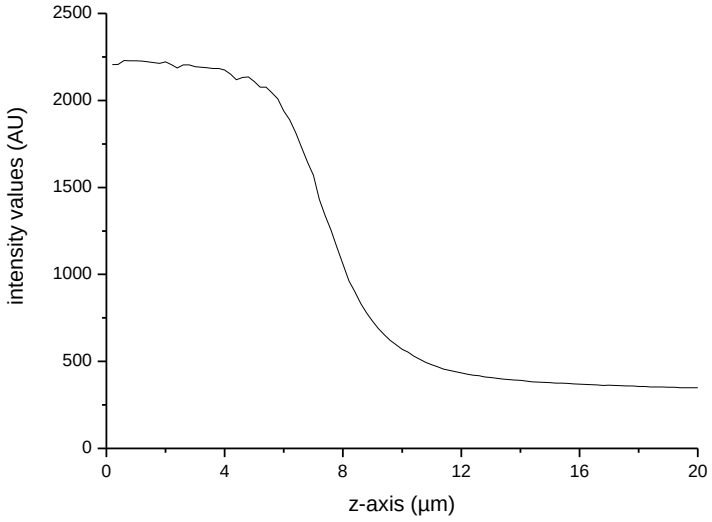

Figure 4.2 shows the original sigmoidal curve of a Z-section through the z axis.

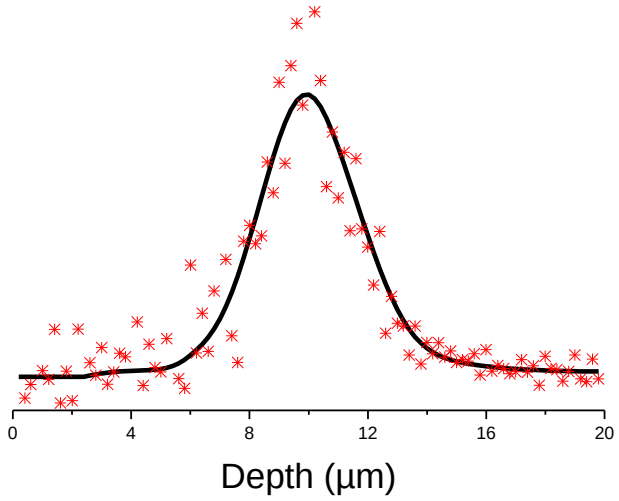

Figure 4.3: Shows the differentiated version of the rising part of Figure 4.1**.** The edge spread function FWHM is 2.22 µm.

4.3 Reproducibility of fluorescent standard

Fluorescent slides were obtained from Chroma and the consistency of the Chroma Perspex standards were examined, each slide fluoresced to varying extents; however within each Chroma slide the fluorescent value is highly consistent across the slide and on both sides of the slide. As Shown in figure 4.4

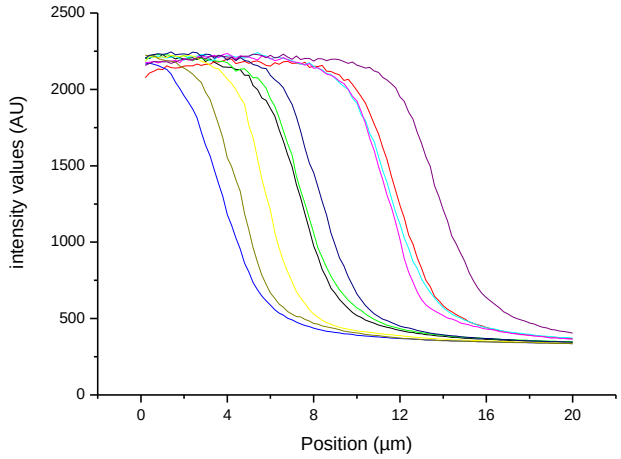

Figure 4.4 shows the summation of the X and Y pixels of a z stack to generate a singlez slice value of the surface of the slide taken from different sides of the Chroma test slide. The different curves represent individual measurements.

The fluorescent slide was tested to make sure that constant fluorescent intensity was being given off throughout the slide at the standard setting used. This was found to be the case. The laser was also tested at the start and end of the experiments to check its stability, and the laser was found to output 128 mw at 920 nm when set to 99% power. This was done when the system was in frame-scanning mode, so the laser output will have been disabled some of the time during the fly back, so this value is averaged power intensity at the objective. The system was set with the laser power at 5% and the PMTs where set to 629 units throughout all of these experiments, and the 40x NA 0.8 lens was used.

The measurements from these slides are taken by sampling 100 x 0.2 µm steps at the surface of the slide. During these measurements there is a non-uniformity of the illumination of the field of view as shown below in Panel 4.5.

A B

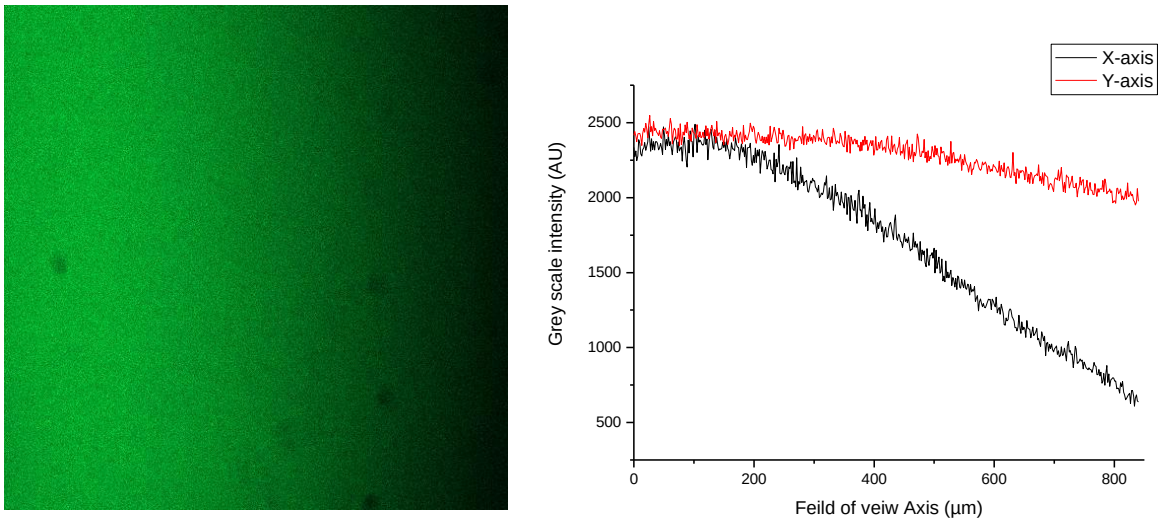

Figure 4.5A shows the illumination pattern when a uniform fluorescence is imaged. This image should be a uniform intensity across the field. **Figure 4.5B** shows a cross section across the X and Y axis of the image. There was also a small difference in the intensity profiles from the two PMTs on the system.

Great care was taken to insure the slide was seated perfectly level, many sprate measurements where taken and the slide was moved many times, this image was highly reproducible, if there was an issue with the slide there would have been many different results depending on how the slide was moved. This illumination defect is caused by a misalignment of the IR laser and not causing correct illumination of the back aperture of the objective lens and is very difficult to correct. For this reason the images are cropped at the most evenly illuminated field of view, this is at the top right hand corner. This region is approximately 100x100 pixels. Care was taken to exclude any dirt or fluorescent inhomogeneities.

This 100x100 image is then averaged into a single average greyscale value for that z stack. This shows a sigmoidal curve of the intensity profile as the scanning plane leaves the surface of the test slide. To measure the ESF the profile must be differentiated at FWHM measured from the curve.

4.3.1 Ascertaining the imaging depth

It is important that the base substances used to create the artificial myocardium are not fluorescent. However because of this it is difficult to ascertain the depth of artificial myocardium that is being imaged. The following method describes how this problem was circumvented.

A set-up was devised where a standard test slide was used as a base and then two wedges of artificial myocardium where moulded on top of the slide with the use of two cover slips. Once the agar had set, the cover slips were removed and a suspension of 5 µm fluorescent beads was used to coat the top surface of the artificial myocardium so that the depth of artificial myocardium could be measured.

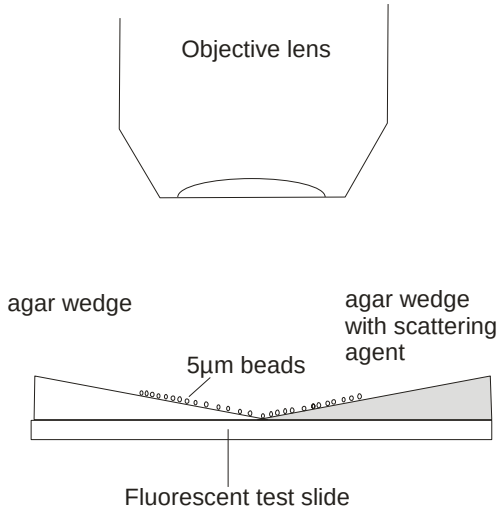

Figure 4.6 shows a schematic representation of the set up used for various test substances.

Figure 4.6 shows Z-stack intensity values the peaks on the left hand side of the graph represent the fluorescence signal emitted from the test slide, while the peaks on the right denote the signal from the fluorescent beads and mark the top surface of the artificial myocardium.

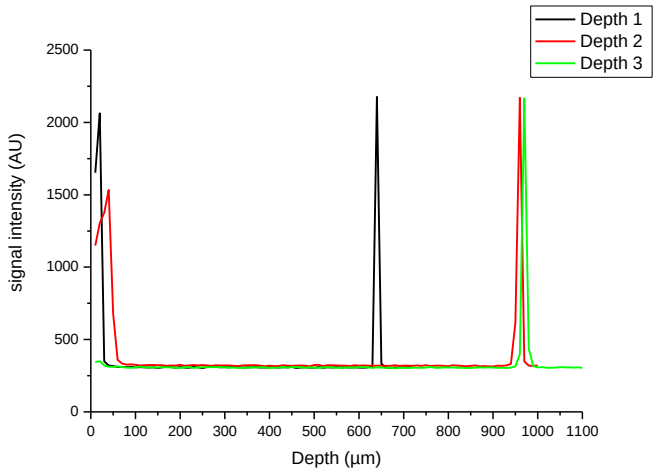

Figure 4.7 shows the analysed traces the area around a bead was selected in the X and Y axis and cropped. The peak on the right hand side denotes where the bead was located on the surface of the agar. The peak on the left hand side is the fluorescence from the test slide.

It would be impractical to sample 1.1mm at the necessary 200nm steps need to take the edge spread function. There fore these data sets where sampled at 10µm. and a Second data set was then taken immediately bellow the bead at 200nm steps to resolve the edge. There is a large distance in the depth of the ager that is dependant on where in the wedge the measurement was taken, it is evident from figure 4.7 that there are larger light levels from the shallower depth, which is expected. The data for every plane in Z was summed and averaged by the pixel count. In Figure 4.7, there is a steep drop off of fluorescence the deeper into the Perspex that is imaged. This is due to the absorbent properties of the Perspex. A Matlab program was written that detects the peak from the edge of the test slide and aligns all the measurements so that the edge is known. This enables multiple measurements to be compared.

4.3.2 The refractive index

In this study, the refractive index (RI) was measured using a refractometer (see Chapter 2 section 10). The refractive index of water was 1.332 , i.e. similar to published values (Klar *et al.*, 2000) and that of the standard Krebs' solution as 1.335. This technique was

subsequently used to measure the refractive index of the materials used to simulate the optical properties of the myocardium.

One issue is whether these changes in refractive index and large disparity from that of glass (1.515) can cause degradation of the image quality. There have been many previous studies that show image degradation caused by refractive index mismatch (de Grauw *et al.*, 1999;Dong *et al.*, 2003;Booth & Wilson, 2001;Hell *et al.*, 1993;Jacobsen *et al.*, 1994). Most water immersion lenses come with a correction collar to compensate for these factors. One example where image degradation might occur is when two-photon microscopy is used for deep tissue imaging. The ceramic immersion lenses are not fitted with a correction collar. This makes it difficult to correct for aberrations caused by refractive index mismatch. The expected refractive index of water is 1.332 and the Krebs' solution that is used to perfuse the heart has a measured refractive index of 1.335. The refractive index of cardiac muscle is 1.383, so the light must undergo changes to its path, caused by the cardiac muscle/Krebs' solution interface and the Krebs' /lens interface. One idea is to match the refractive index of the Krebs' solution to that of cardiac muscle so that the light undergoes a single (larger) refractive index change.
Sucrose is well documented as an agent that will increase the refractive index, however, the concentration needed to match that of cardiac muscle is in excess of one molar. The effects of addition of 1 molar of any solute to physiological saline would be dramatic as it would increase the osmotic strength of the solution (normally ~300mOsmoles) considerably. Pronounced effects of increased osmotic pressure of physiological saline on isolated heart preparations has been reported previously and prolonged exposure can cause considerable cell damage (Allen & Smith 1987). Therefore, an inert molecule with a much larger molecular weight is required. The large molecular weight polymer Dextran is an obvious choice, using a 40,800kDa form of Dextran, a much lower concentration is needed to match the refractive index of tissue (Fig 4.5). The effects of the additional osmotic pressure of ~10mM Dextran would be predicted to have minimal effects on cardiac muscle function (Allen & Smith, 1987).

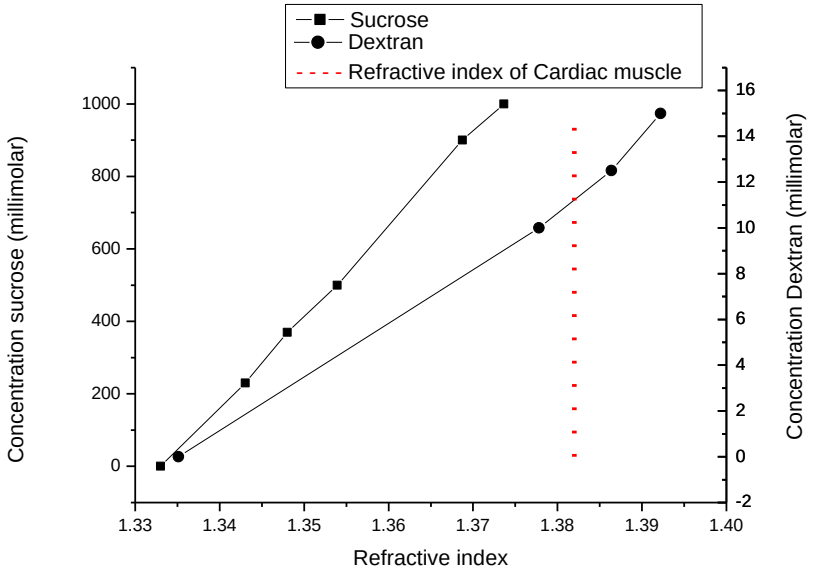

Figure 4.8 this graph shows the concentration differences need to change refractive index.

The disadvantage of the solution with the refractive index matched is that it has a considerably higher viscosity (~10 times higher) compared to normal saline and the increased perfusion pressure required to ensure proper perfusion of the heart, these high pressures could not be tolerated by the coronary circulation. Although where feasible, super-fusion of a sample of heart tissue may be possible.

4.4 Results

The first aim was to ascertain how much light loss happens in cardiac muscle as the depth of cardiac muscles being imaged increases. Both rat and rabbit cardiac muscle were studied and both healthy cardiac muscle and infarcted regions were considered.

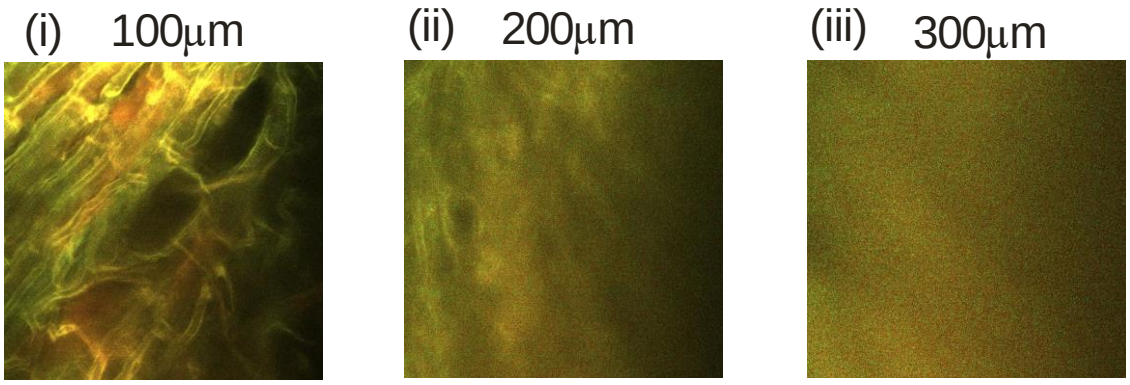

Figure 4.9 show two-photon imaging of the myocardium stained with Di-4-ANEPPS and 100µm, 200µm and 300µm, the lost of resolution is obvious although it is still possible to take functional ratiometric voltage measurements from the lower resolution images

The results shown are taken from Langendorff perfused heart preparations where the whole heart was perfused by retrograde perfusion of the aorta. These hearts where stained with Di-4-ANNEPS as part of an experimental protocol, so that voltage measurements could be made from the cardiac muscle. The signal and apparent resolution decreased the deeper into the tissue. The following graphs show the signal drop off in relation to the depth that is being imaged.

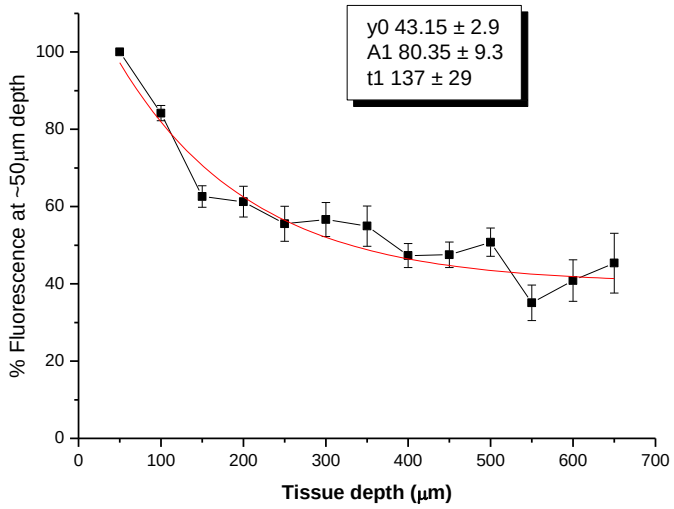

Figure 4.10 shows the signal intensity in healthy rat cardiac ventricle muscle through depth, the epicardium was being imaged. The background intensity for these readings is around 40%. The data was fitted using the following formula $y = y_0 + A_1 e^{-(x-X_0)/t_1}$ the results from these measurements where fitted to an exponential decay, "t1" denotes the rate of decay, while "y0" denotes the value at which the signal levels off. "A1" amplitude of exponential decay, the error bars show the standard error of the measurements as this graph is composed from multiple datasets. (Data supplied by Iffath Ghouri). The background stays at 40% as it is the base level of the background light lights. The fluorescence levels being measured are extremely small even at 100%.

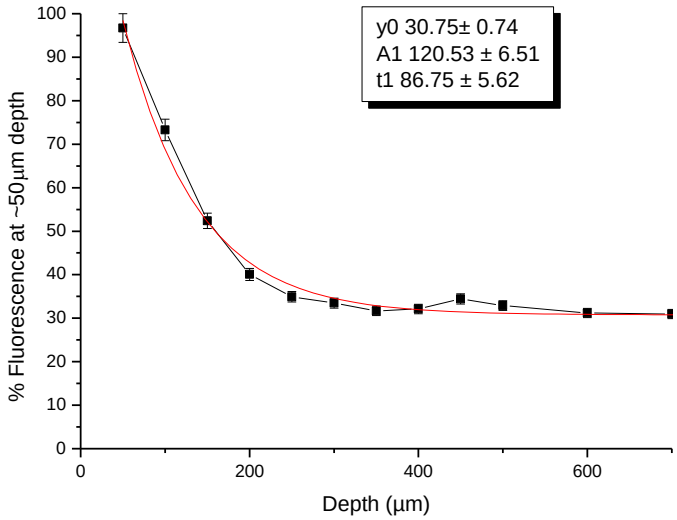

Figure 4.11 shows the signal intensity in infarcted rat cardiac ventricle muscle through depth, the epicardium was being imaged. The background intensity for these readings is around 40%. The data was fitted using the following formula $y = y_0 + A_1 e^{-(x-X_0)/t_1}$ the results from these measurements where fitted to an exponential decay, "t1" denotes the rate of decay, while "y0" denotes the value at which the signal levels off. "A1" amplitude of exponential decay the error bars show the standard error of the measurements as this graph is composed from multiple datasets. (Data supplied by Iffath Ghouri).

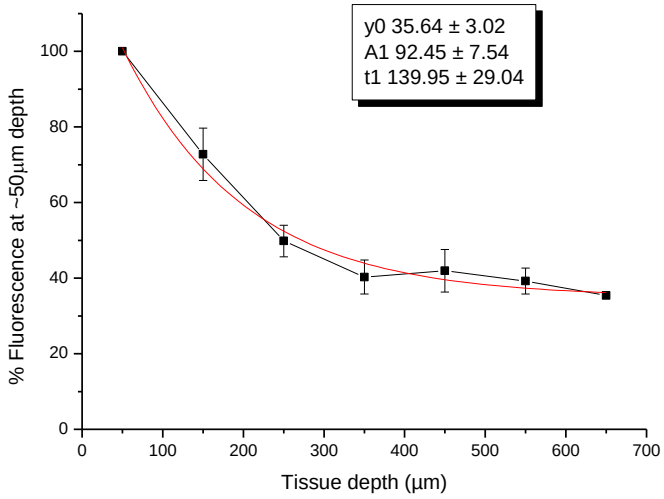

Figure 4.12 this figure shows the signal intensity in healthy rabbit cardiac ventricle muscle through depth, the epicardium was being imaged. The data was fitted using the following formula $y = y_0 + A_1 e^{-(x-X_0)/t_1}$ the results from these measurements where fitted to an exponential decay, "t1" denotes the rate of decay, while "y0" denotes the value at which the signal levels off. "A1" amplitude of exponential decay. The error bars show the standard error of the measurements as this graph is composed from multiple datasets. (Data supplied by Allen Kelly).

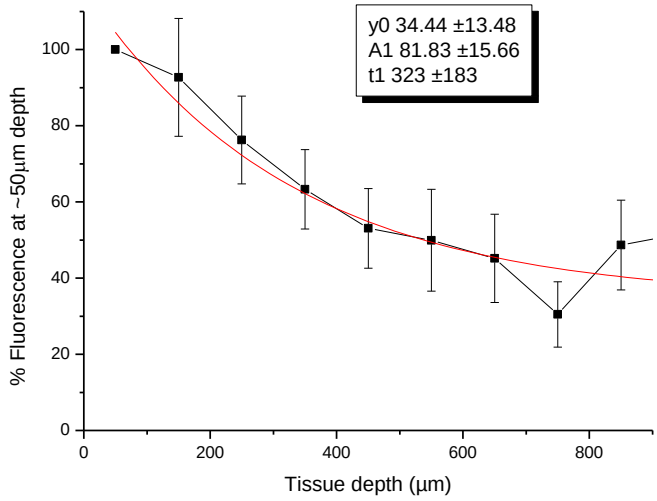

Figure 4.13 this figure shows the signal intensity in infarcted rabbit cardiac muscle through depth. The data was fitted using the following formula $y = y_0 + A_1 e^{-(x-X_0)/t_1}$. The results from these measurements where fitted to an exponential decay, "t1" denotes the rate of decay, while "y0" denotes the value at which the signal levels off. "A1" amplitude of exponential decay The error bars show the standard error of the measurements as this graph is composed from 3 datasets hence the error bars are larger. (Data supplied by Allen Kelly).

The causes of the differences in the extent of loss of signal (T1 values) between rat and rabbit and in infarcted material is unknown. One potential explanation is that variation is due to differences in the degree of light scattering between the different tissues. The most likely cause of light scatter in cardiac tissue is mitochondria, i.e. small sub-micron dense objects within heart cells. The relative volumes of mitochondria of Rat and mouse in the ventricle are shown in the graph below (DM Bers, 2002;Barth *et al.*, 1992). The higher mitochondrial content in rat relative to rabbit is consistent with the smaller T1 values observed. Furthermore, infarcted myocardium has few cardiomyocytes and therefore mitochondria, again consistent with the concept that mitochondria are responsible for the loss of signal.

	% volume of mitochondria	Measured T1 Value of healthy tissue (μm)	Measured T1 Value of infarct tissue (μm)
Rabbit	28%	150	323
Rat	34%	78	131
Mouse	37%		

Table 4.1 shows the mitochondria concentration in healthy ventricle muscles of various species. Along with the measured rate of decay of healthy and infarcted tissue.

Scattering and absorption properties of cardiac muscle

This section investigates the effects of scattering agents on signal intensity and resolution. It is thought that the main scattering agent in cardiac muscle is the mitochondria (Su *et al.*, 2009;Beauvoit *et al.*, 1995). This would mean that the majority of light scattering in the cardiac muscle can be described by Rayleigh scattering as described in Chapter 1 Section 1.3.1.3.1. In order to mimic the scattering properties of cardiac muscle 100nm non-fluorescent polystyrene microspheres where used in agar. These were added into the wedge structures that are built onto of the chroma test slide described in Chapter 4 Section 3.1.

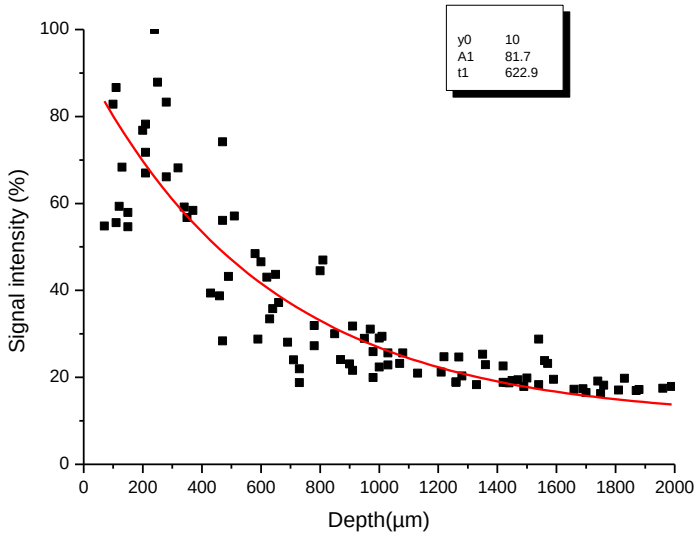

Figure 4.14 shows the intensity measurements of the Chroma test slide taken at different depths of the scattering agent at 0.1% scatter medium in agar. The data was fitted using the following formula $y = y_0 + A_1 e^{-(x-X_0)/t_1}$

As a check that the loss of signal was the result of the inclusion of the scattering medium, parallel measurements were done on agar. The results of this are shown in figure 4.13.

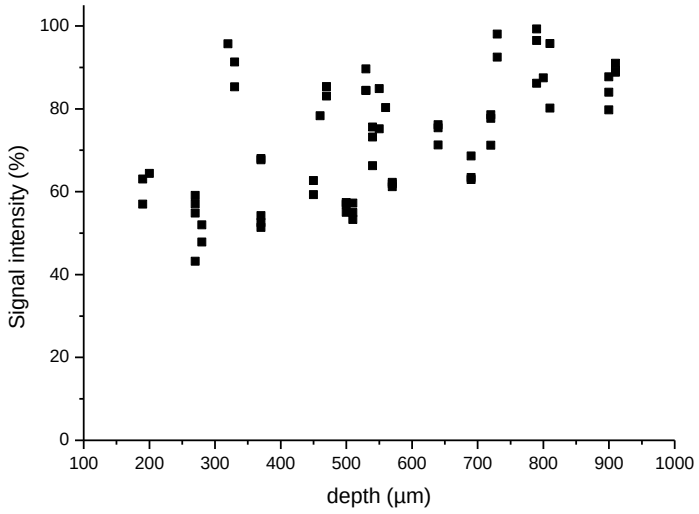

Figure 4.15 shows a trace through the Agar medium with no scattering agents. Showing that there is a slight increase in the change of light intensity in depths under 1mm

In order to assess the relative effects of light scattering the entire immersion medium was modified to have a constant concentration of scattering medium in it.

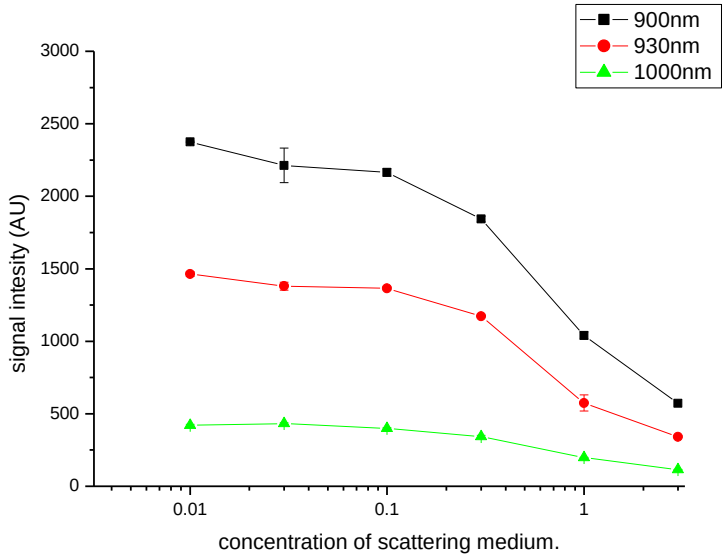

Figure 4.16 shows the intensity signal the three different wavelengths as the concentration of scattering medium increases the intensity drops. These traces have been corrected for the dark current base line. As the scattering medium concentration was being changed the imaging depth was kept the same, and was kept at a constant 3.6mm (the working distance of the Zeiss 40x 0.8NA objective)

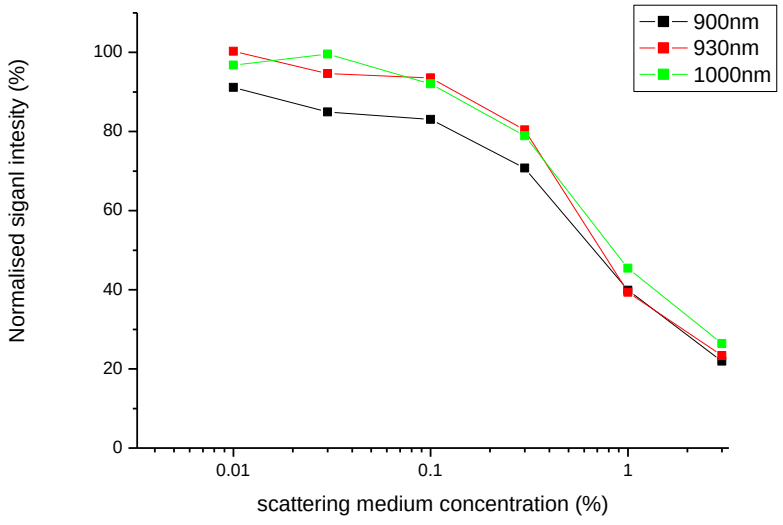

Figure 4.17 shows a normalised version so that the wavelengths are directly comparable.

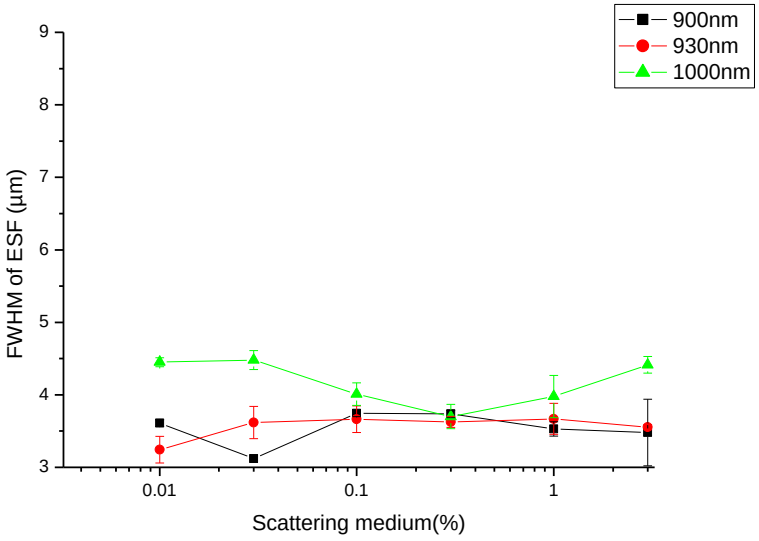

Figure 4.18 shows the edge spread function of the surface of the test slide at three different wavelengths. The longer wavelengths have a slightly larger ESF which is expected. The ESF is not changed by the amount of scattering medium.

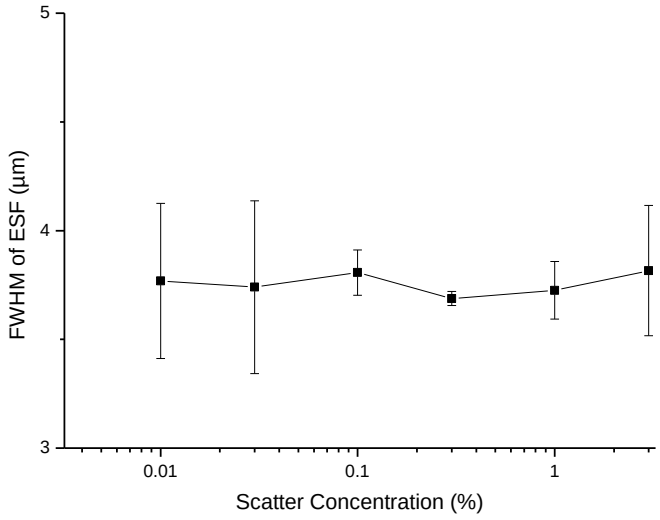

Figure 4.19 shows multiple measurements of the scattering concentration taken using 930 nm excitation. The ESF is not changed by the amount of scattering medium.

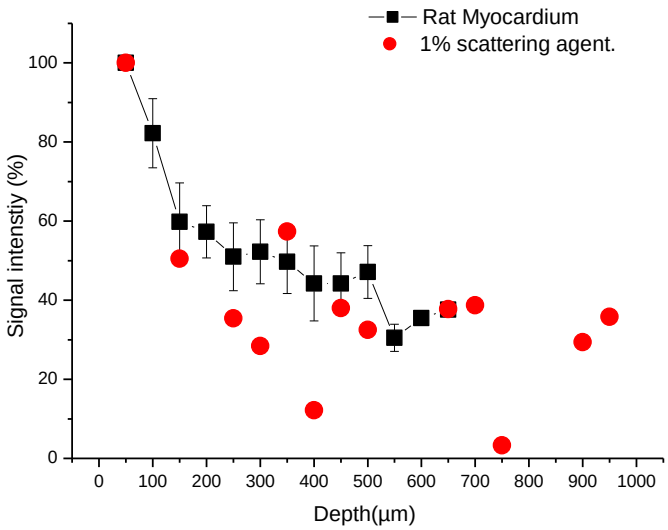

Figure 4.20 show the lost loss of signal intensity in rat myocardium (figure 4.9) Along with the 0.1% scattering light loss data (figure 4.19).

4.5 Intrinsically fluorescent substances

It is a possibility that the emitted light from dyes maybe exciting the intrinsic fluorescent properties of FAD and NADH in the mitochondria (Chapter 1 section 1.7). It is extremely difficult to estimate the amount of FAD in cardiac muscle while NADH is estimated at 20-25 µM (Coremans *et al.*, 1997;Umemura & Kimura, 2005;Bessho *et al.*, 1989).

NADH is excited most efficiently with a single photon at 350 nm (see figure 1.16), in this study, a variety of commonly used wavelengths were used (740 nm, 900 nm, 930 nm and 1000 nm) and recordings were taken from two channels: Channel 1 records the wavelengths 440 nm-480 nm where any NADH fluorescence should be detectable; Channel 2 recorded wavelengths greater than 515 nm (typically used for voltage sensitive dyes).

The NADH solution was made up as a mock intercellular solution in distilled water with 120 mM, 50 µM EGTA, 1 mM $MgCl_2$ the PH was set to 7.2 with KOH.

Figure 4.19

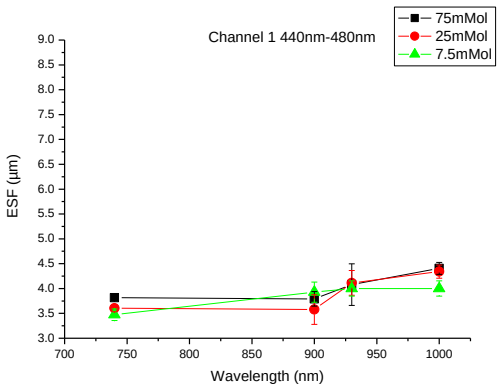

Figure 4.20

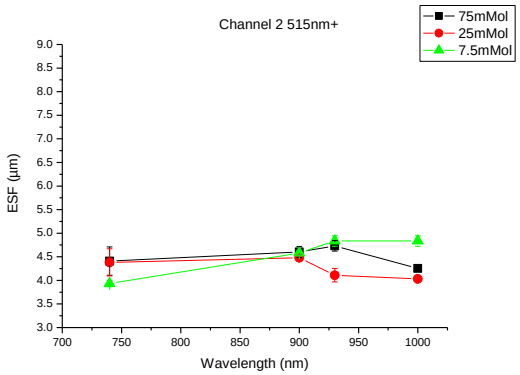

Figures 4.21 and **4.22** shows the results from the ESF measurements with the NADH solution at different concentration and wavelengths. As shown in Figs 4.19 and 4.20 the presence of these intrinsically fluorescent mitochondrial metabolites has no effect on the resolution of the system.

4.6 The effects of refractive index change

This section shows the effects of refractive index changes have in two-photon resolution and sensitivity. It is known that the refractive index of cardiac muscle is 1.38, this was simulated by adding 30% sucrose to an agar gel. Later by using an optical gel (NuSil, Unit 2, Network 4, Cressex Business Park, Lincoln Road, High Wycombe, Buckinghamshire HP12 3RF) with a refractive index of 1.38 These where added into the the wedge shaped structures the where built on the Chroma test slide, as described in Chapter 4 Section 3.1.

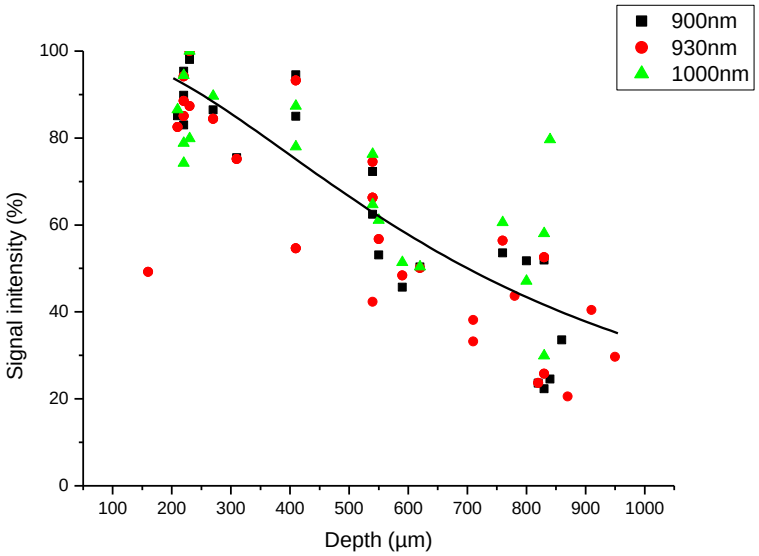

Figure 4.23 shows a scatter plot of the effects of imaging through increasing depth of a gel which has a refractive index of 1.38 at three different wavelengths. The intensity measurements have been measured from the surface of a Chroma test slide. The data was fitted using the following formula $y = \frac{A_1 - A_2}{1 + (X / X_0)^p} + A_2$ where A_1=1, A_2=0, X_0= 0.827, p = 0.983 as this gave a better fit than an exponential decay.

There appears to be no wavelength dependent effects, however there is a loss of signal intensity that is dependent on the depth of imaging. This graph has been fitted with the curve, A1=1 A0=0 X0+638 P=1.865

Figure 2.24 Shows an orthogonal view of a Chroma test slide sampled at 0.2µm, the uneven appearance is due to uneven laser illumination. Only a small segment of this data, only a few pixels in the X and Y axis where sampled when analysing the data so that the uneven laser illumination would not become and issue.

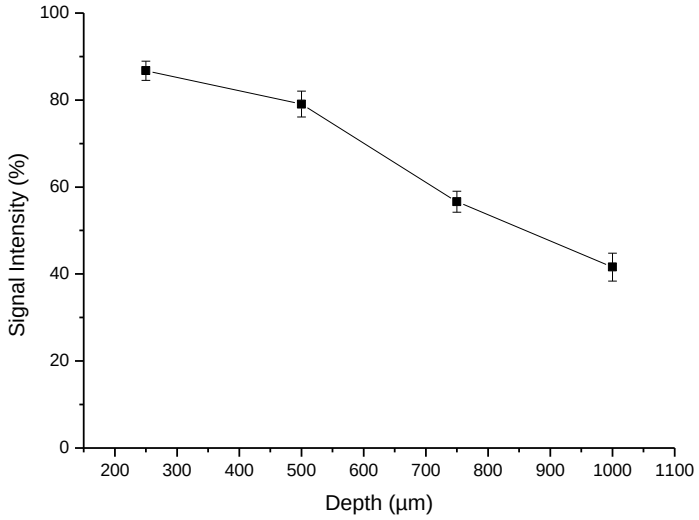

Figure 4.25 shows the light loss through depth of imaging at the refractive index 1.38, taken using 930 nm with data points grouped into the nearest 250 µm in depth.

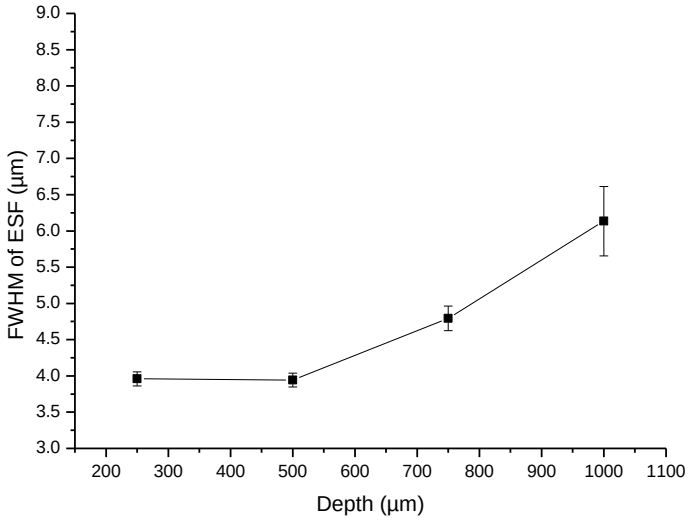

Figure 4.26 shows the increase of ESF measurements through depth of imaging at the refractive index 1.38.

This shows that there is a depth dependent loss of resolution as well as signal loss in two-photon imaging related to refractive index miss match.

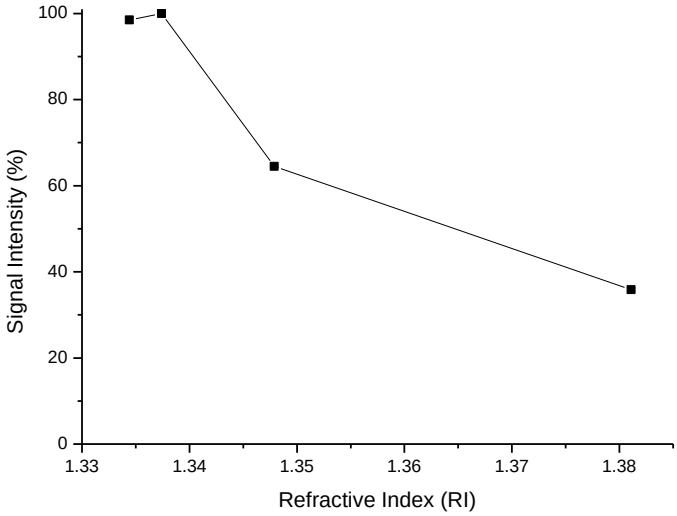

Figure 4.27 shows the effects light intensity of the Chroma test slide when the refractive index is varied. As the refractive index was varied the depth was keep constant at 3.6mm (the working distance of the Zeiss 40x 0.8NA lens)

This was done by modifying the immersion solution the lens was in. Again, figure 4.25 shows that there is a dependence on signal intensity based on refractive index mismatch.

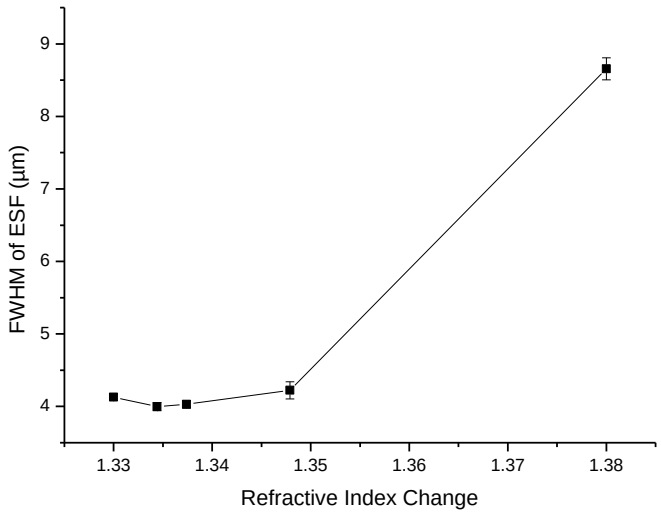

Figure 4.28 shows the effects of refractive index on the FWHM of the ESF.

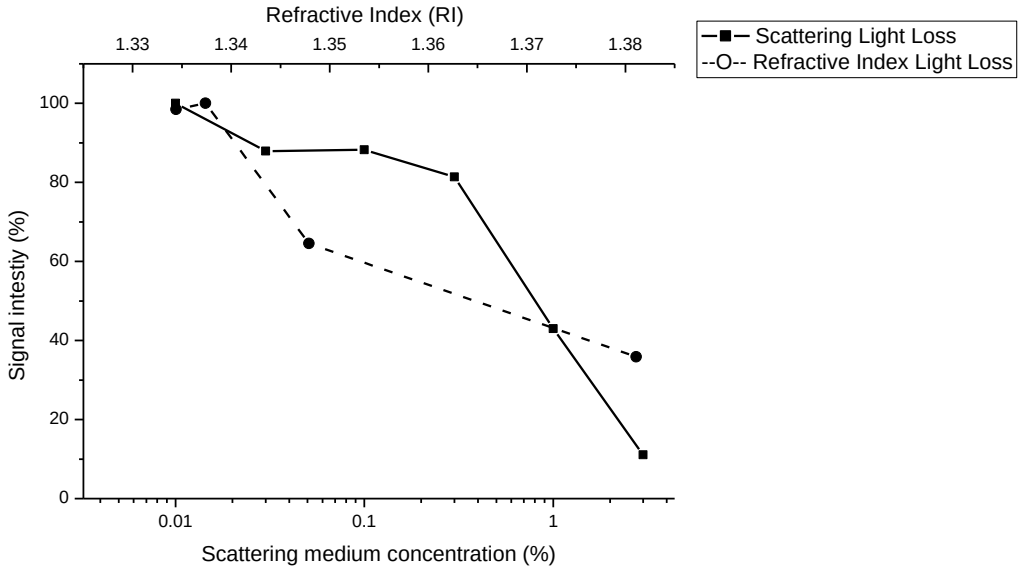

Figure 4.29 compares the effects of scattering light loss as well as the light loss from refractive index mismatch .there is a larger light loss caused by a change of scattering medium intensity than with refractive index change. This is an important issues when

trying to compose a substance that will mimic both light loss and resolution loss of cardiac muscle.

Discussion

4.6.1 Comparison of Edge and PSF

ESF measurements is expected to be larger than PSF measurements this is because of the extended nature of the object being imaged (Cheng *et al.*, 1996;Rossmann, 1969). Theoretically, the edge spread functions can be related to point spread functions. However the relationship is not a simple linier relationship. It is s hard to determine the theoretical values for microscope optics. (B Dorband *et al.*, 2009)

In this study the edge and point spread functions where measured on the Zeiss 510 confocal systems using a 63x NA1.3 lens. The FWHM of the PSF on the Z axis was found to be 2.8 µm while the ESF was 3.7 µm. PSF measurements from the Zeiss 510 two-photon system where hard to obtain as described in Chapter 2 Section 2.6.

4.6.2 Analysis of the artificial myocardium results.

Now that the effects of the myocardium have been documented it is now possible to recreate an artificial myocardium from the known effects of scattering and refractive index miss-match. The addition of intrinsic fluorophores such as NADH may be added if excitation wavelengths close to the NADH excitation wavelength are to be studied.

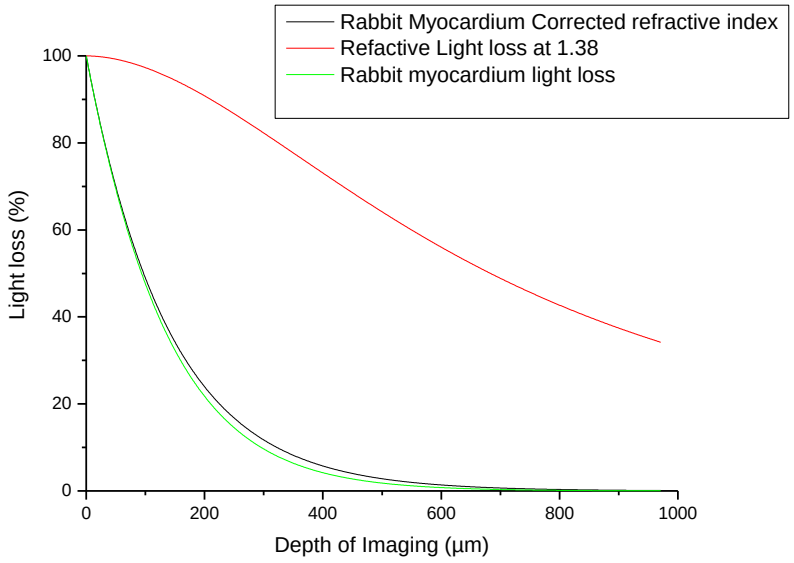

Figure 4.30 shows the relative light loss due to various depths of material of refractive index at 1.38 compared with the light loss measured by various depths of rabbit myocardium. These lines where drawn based on the fits to the earlier measured data in this chapter. The black line shows the light loss from the rabbit myocardium once it has been corrected for by its light loss from the refractive index mismatch of 1.38.

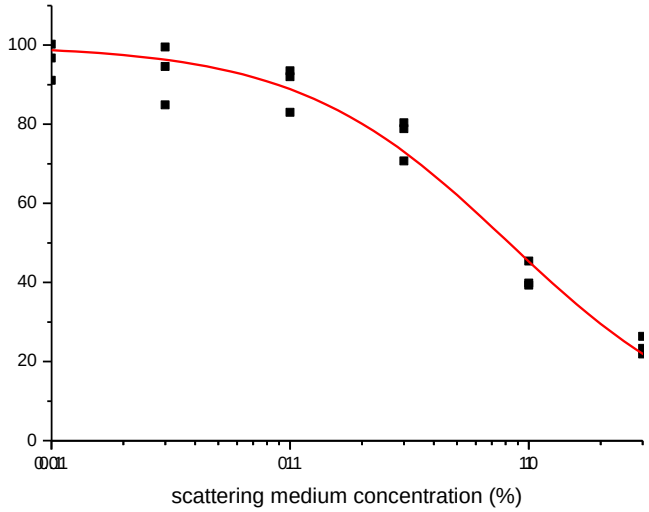

Figure 4.31 shows measured light loss from a variety of different scattering concentrations.

The red line shows a fit though this data using the Equation $y = y_0 + A_1 e^{-(x-X_0)/t_1}$ from the data shown in Figure 4.30 and from the measured decay from figure 4.12 (which is -0.0077) it is now possible to estimate the gradient of light loss induced by scattering of any concentration. The depth was kept constant at 3.6mm.

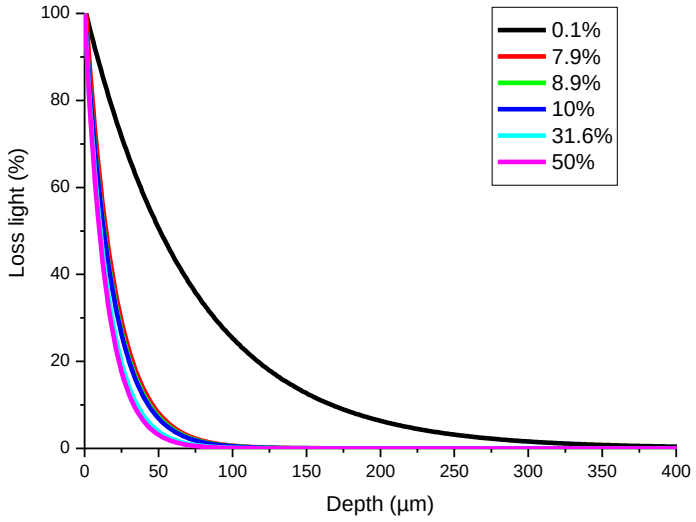

Figure 4.32 shows the calculated decay for six different concentrations of scattering medium within agar using 100nm beads.

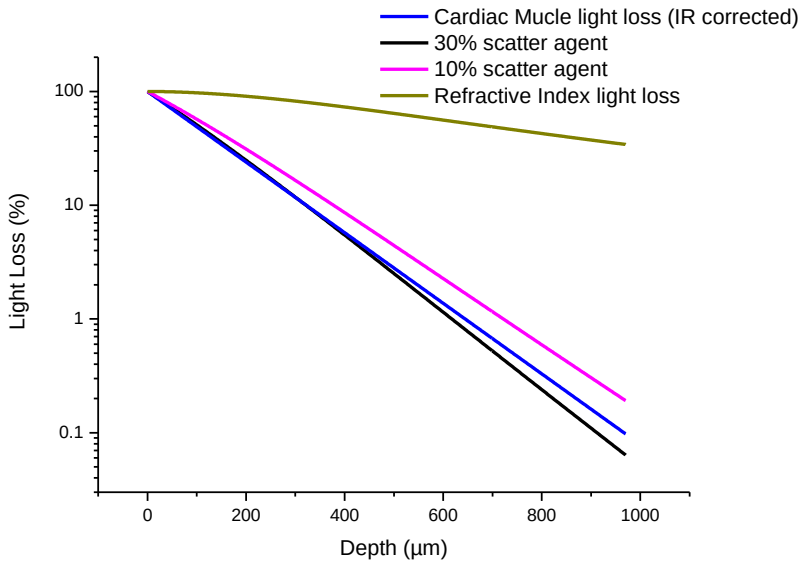

Figure 4.33 shows the merged effect of a refractive index gel at 1.38 and varying scattering concentrations (10-30%) and the cardiac muscle that has been corrected for IR light loss.

This shows that a scattering concentration of 100 nm beads needs to be around 10-30% in order to mimic cardiac muscles optical proprieties.

4.6.3 Conclusions

Scattering has a strong effect on the loss of signal intensity but no effect on the measured resolution of the system, as demonstrated in figure 4.18. The relatively small shift of the refractive index from 1.33 to 1.38 produces a significant degradation of the measured FWHM of ESF as well as a small loss of signal through depth. However the ESF measurement was still useable when wanting to acquire an intracellular signal of cardiac myocytes, as of cardiac myocytes are 20µm by 10µm in size the smallest recording point of a degraded PSF in deep tissue is still small than the size of the cells being imaged. In order to generate an artificial rabbit myocardium a gel with a refractive index of 1.38 should be used with a concentration of 100nm beads between 10-30%.

5 Chapter 5: Dual axis imaging of live cell specimens.

5.1 Introduction

As previous chapters have discussed and assessed, optical aberrations lead to a substantial degradation of the optical signal in the axial dimension (Z-axis) when compared to the lateral resolution. This chapter attempts to create novel imaging methods that can overcome the z axis image degradation. It is proposed that the Z-axis degradation is overcome by obtaining orthogonal images of the same cell using as high a numerical aperture objective lens as possible. Once this has been achieved it is possible to convolve these orthogonal images to make high resolution 3 dimensional images of the cell. As described in Chapter 1, living cardiac myocytes have rod-like dimensions of approximately 120x20x10 µm. T-tubules have an approximate diameter of 100 nm and run though-out the internal structure of the myocyte. Mitochondria are present in large numbers throughout the cell, with a higher concentration around the nucleus. Thus accurate representation of a single heart cell in 3 dimensions presents a challenge to conventional microscopy because the poor resolution in the Z-axis obscures the real structure of both mitochondria and T-tubule system (Gordienko *et al.*, 2001;Kettlewell *et al.*, 2009).

There is recent evidence in the literature to support the theory that viewing cardiac myocytes on their end will yield higher resolution of the T-tubule structures and other intracellular structures However, all of the techniques used to date have not been able to image live myocytes.(Chen-Izu *et al.*, 2006;Schaffer *et al.*, 1994;Mastronarde, 1997)
In these chapter two new methods to image myocytes are described. The first method is to conventionally image the cell and then manipulate the cell into an upright position and re image the cell. The second method involves producing an angled micro-mirror and positioning it close to the cell in order to produce a second image orthogonal image of the cell (Wang *et al.*, 2003)

5.1.1 Convolving the images

As discussed previously, further increases in optical resolution can be achieved by convoluting a series of images. It is possible to combine orthogonal images by combining

the phase and amplitudes of each Fourier component of an image after correcting as much as possible for the known PSF, there is no current commercial software that does this so some programming is required in order to achieve convolved images(Shaw *et al.*, 1989;Liu *et al.*, 2010). Methods

5.1.2 Manoeuvring cells into micro structures

The micro-structure is mounted onto a cover slip and then immersed in a physiological salt solution (based on Krebs' solution). The solution used in these experiments contained no added Ca^{2+} to ensure the cardiac myocytes did not spontaneously contract during the imaging. The microstructures were generated from hydrophobic materials; therefore it was normal for the wells will contain air bubbles after submerging in solution. To avoid this, a pipette was lowered into each well and the air removed by suction. Once the pipette has been loaded with Krebs' solution, and the pressure allowed to equalise, the pipette is then lowered back into a solution containing cardiomyocytes. Using a Nikon 10X objective to view the cell, pippette and chamber, a single cell is drawn up into the pipette tip, and the pipette is then lowered into one of the wells of the microstructure. The cell is then ejected out of the pipette, and into the well where the cell is manoeuvred into an upright position.

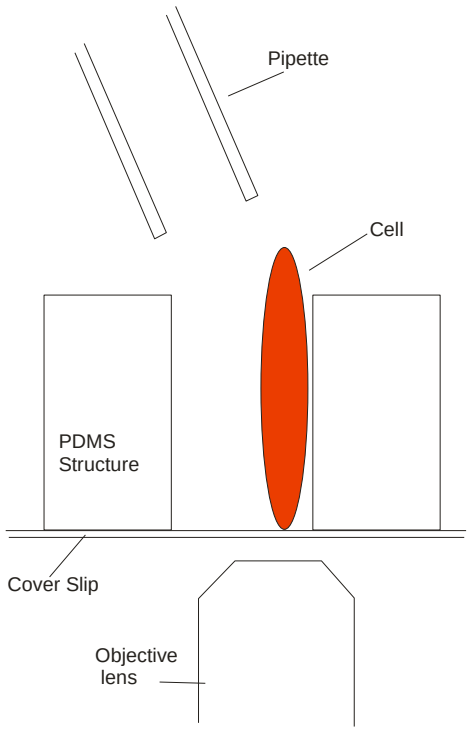

Figure 5.1 is a diagram of how a cell is manipulated into a structure.

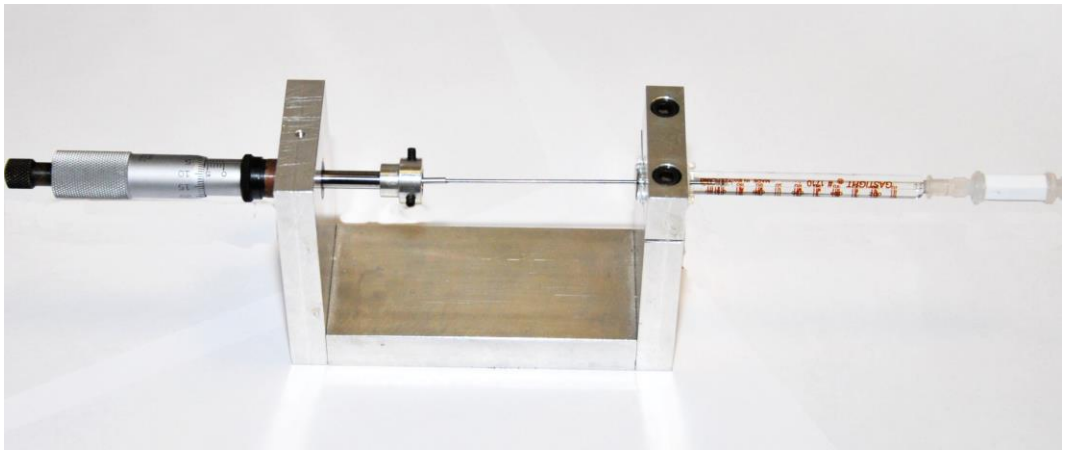

Figure 5.2 shows the syringe driver system used to control the fluidics.

5.2 Microstructures to hold cells vertically

PDMS microstructures designed to hold cardiac cells vertically were made as described in Chapter 2.

The SU8 towers where created to be 90 µm high using the methods described in section 2.12, originally circular wells were constructed with a diameter of 100 µm. Later in the project, square posts were fabricated as it was easier to place the cardio myocytes in a vertical position in the corners of the wells. This also gave the cells more support and eliminated movement artefacts.

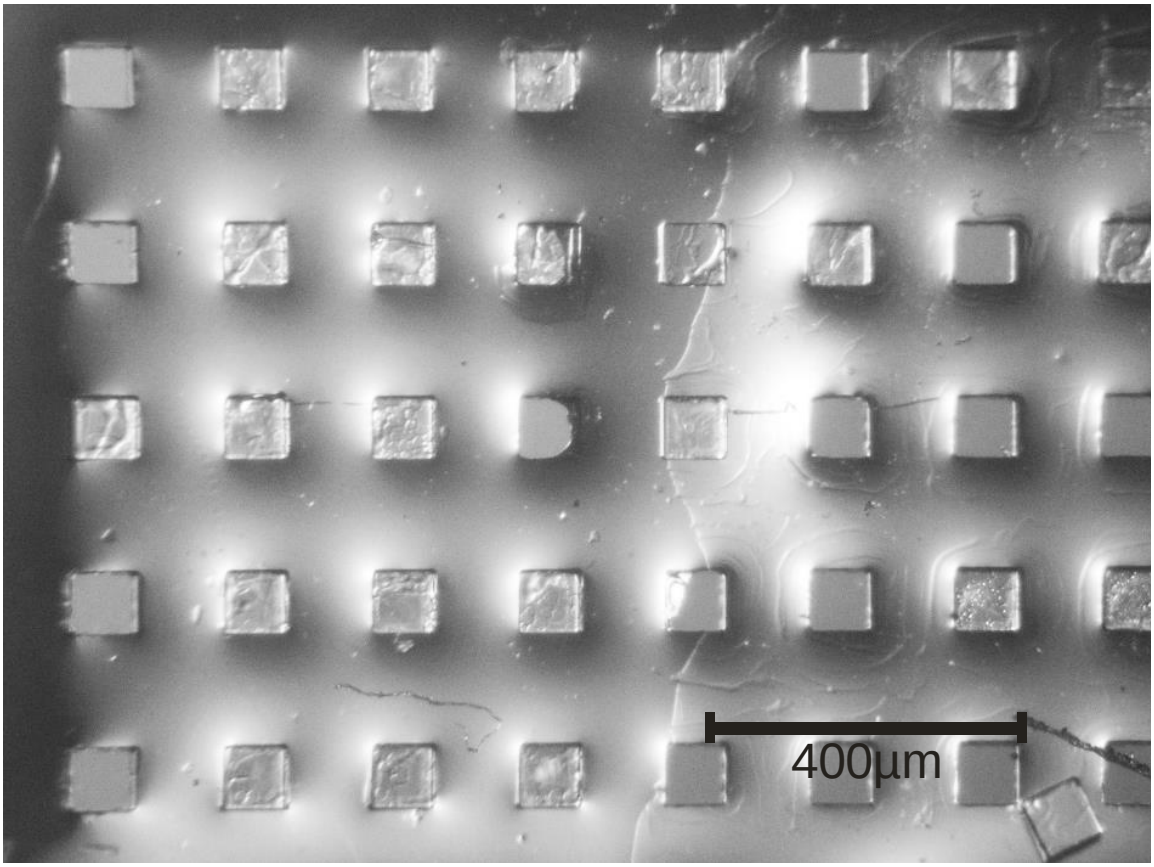

Figure 5.3: Example of a finished PDMS structure that is used in experiments this is a series of wells, an SU-8 post is visible in the bottom right corner that has become detached from the glass substrate, Viewed from the top looking directly down.

5.2.1 Vertical cell imaging using microstructures

It is proposed that living single cardiac cells cell can be orientated vertically to allow measurements of cell structure (e.g. mitochondria/nucleus) or function (intracellular Ca^{2+} measurements during field stimulation) to be made. Chapter 2 Section 2.12.1 describes the techniques involved in generating a micro-structure comprising of an array of "wells" of appropriate diameter to hold cardio myocytes vertically

5.3 Results of Cell orientation

An array of micro wells were manufactured as described above and placed on a coverslip. Cardiomyocytes were placed adjacent to the micro wells and one lying flat on the coverslip was imaged using conventional line-scanning confocal microscopy. Cells were stained either with the membrane dye (Di-4-ANEPPS) or a mitochondrial dye (TMRE). Once a 3-D stack of images were generated in this conventional mode, the same cell was picked up by the micro-pipette and placed in the well so the cell stood upright and the whole cell was re-imaged in this new attitude. Figure 5.4a and b shows images of cells within the micro-wells after staining with Di-4-ANEPPS.

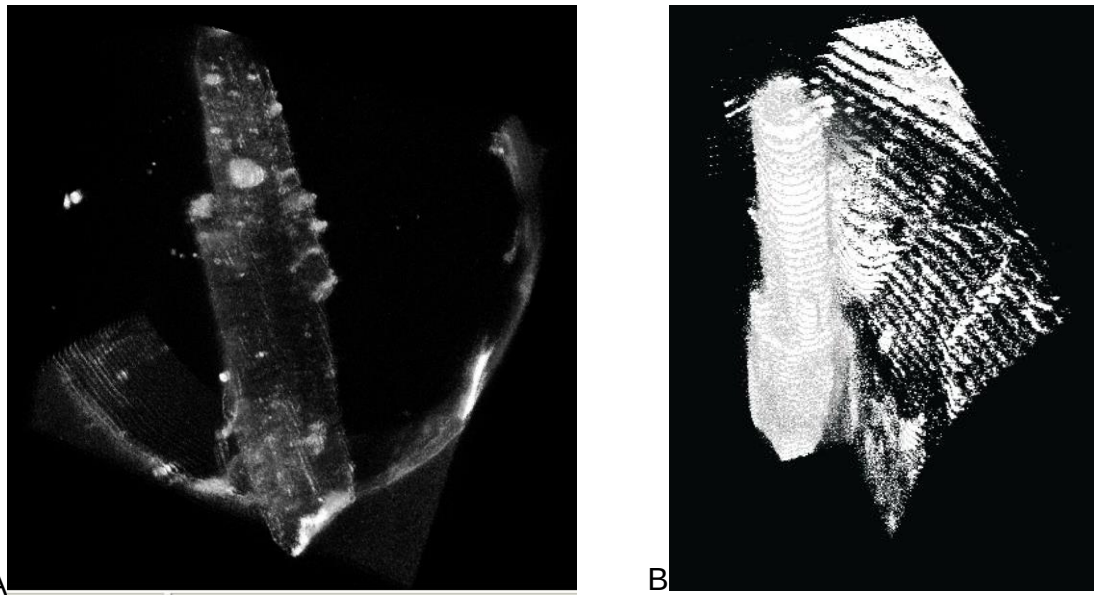

Figure 5.4a shows a 3D Z-stack cell and structure that has been placed in a prototype well structure that was only 35 µm high, both the cell and structure have been stained

with Di-4-ANEPPS and is being imaged using a Nikon 60X NA1.2 lens on the Biorad confocal system, the excitation wavelength was 470nm and the signal was collected using a 530nm long pass filter.

Figure 5.4b shows a 3D Z-stack confocal image of a cell orientated vertically within a well that is 100µm high, redrawn as a 3D representation of a finished structure with a live cardiomyocyte orientated at 90 degrees. This image was taken using a Nikon 60X NA1.2 lens on the Biorad confocal systemthe excitation wavelength was 470nm and the signal was collected using a 530nm long pass filter.

5.3.1 Imaging T-tubules in vertically arranged cardiac cells

Figure 5.5: shows an image which is part of a Z-stack of a rabbit cell stained with Di-4-ANEPPS which stains the outer membrane and the tubules. This cell has been placed in an upright position; The T-tubule network is clearly visible.

There are some limitations with this setup. For the resolution to be high enough to deconvolved the image, the scan speed has to be relatively slow. As the cell is upright the entire cell is exposed to the column of light when using confocal imaging, thus photo-bleaching is a significant problem. One approach to solve this problem is to use an extracellular solution with dextran-linked fluorescein. This will not cross the membrane but will diffuse through the T-tubules. However the smallest molecules on the market are 5 kDa, which diffuse very slowly (20mins-40mins) therefore when photo-bleaching occurs the recovery time is impracticallylong,(Ghauharali & Brakenhoff, 2000).

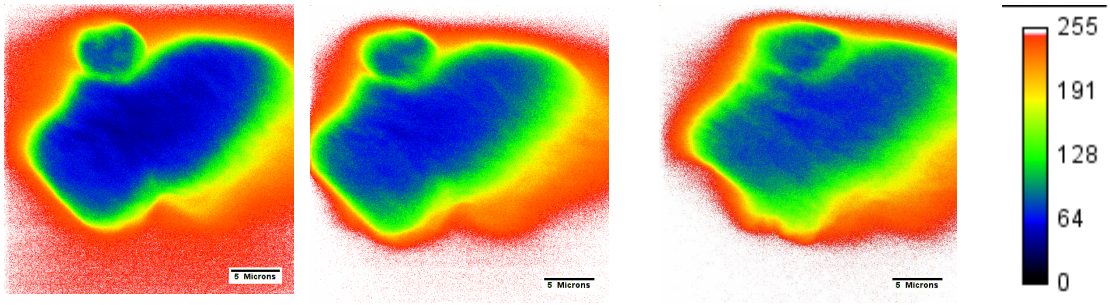

Figure 5.6 These three images are of the same cell and taken 15 minutes apart that is in an upright postion, the progressive changes indicate that the 5 kDa dextran linked fluorescence diffuse through the T-tubule network. In the finial image it is possible to make out the t-tuble network, however this image has far less contrast than figure 5.5 which is stained with Di-4-ANEPPS. The scale bar represents 5µm.

Figure 5.6 illustrates that the low molecular weight dextran can slowly enter the T-tubule network however as it take minutes to enter and seconds to bleach the signal it is a less effective method than staining the cell with DI-4-ANEPPS. Furthermore, when the cell is on its end, serial section of >100microns are necessary to image the complete cell length. As shown in Figure 5.7 and quantified in Figure 5.8, imaging high into the cell revealed a blurring of detail at the higher sections. This cannot be due to progressive entry of dextran linked fluorescence into the cell since it cannot cross the cell membrane. The blurring is due to the progressive loss of resolution deeper into the tissue.

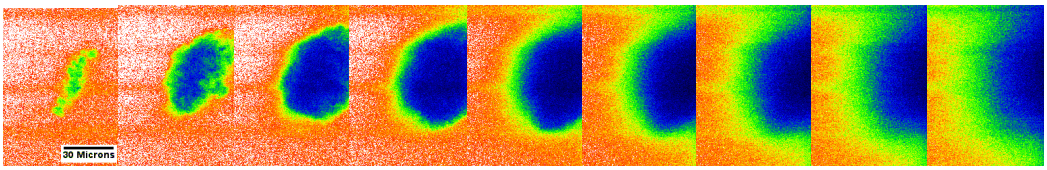

Figure 5.7 shows an upright cell sectioned every 10 µm with the image on the left hand side being closest to the objective and moving upwards towards the top of the cell. Image degradation can be seen the higher up the cell is imaged. The resolution measurement results from this can be seen in figure 5.20. The scale bar in the first image represents 30µm and is constant for all the images. The scale bar represents 5µm.

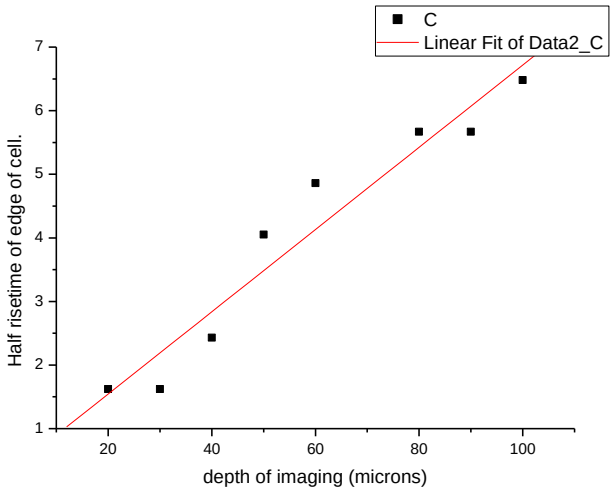

Figure 5.8 shows that there is a 7 fold loss in resolution within a 100 µm in the lateral resolution as attempts to image deeper into the tissue is made. As the specimen was unstable to take ESF measurements from, the distance it took to reach half the maximum intensity of the fluorescent signal from that depth was measured.

When imaging the intercalated disc this technique is very useful however there is a point where this technique offers comparable or lower resolution results to that of conventionally imaged cells due to the image degradation of imaging through cardiac muscle (as described in chapter 4) therefore if image structures that are deeper than 20µm into a cell then orientating the cell into an upright position offers little advantage over imaging the cell in a conventional orientation.

5.4 Images of Mitochondria in vertically arranged cells

Using the same experimental setup as described above fresh cardio myocytes were stained with the mitochondrial dye TMRE imaged conventionally and then placed into the micro wells for a second round of imaging. Using z steps of 0.1 µm, a limited section of the cell could be imaged and the data set used for deconvolution as shown below in Figures 5.7 and 5.8.

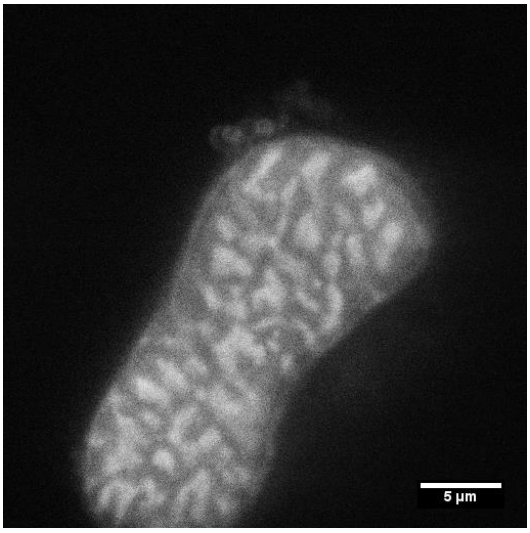

Figure 5.9 shows a cross section of a cardiomyocyte stained with TMRE, this dye stains mitochondria. The cell has been oriented in an upright position sectioned at 10µm into the cell the cell. a total of 86 sections where made in order to gain the be results from the Huygens deconvolution software A Biorad Radiance 2000 was used with a Nikon 60x 1.2NA lens using single photon excitation with a 488nm laser.

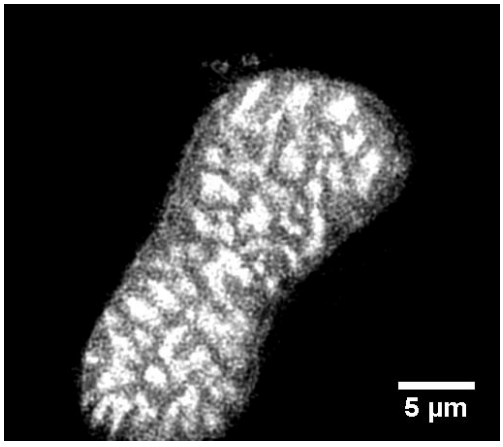

Figure 5.10: This image is the deconvolved image from figure 5.9 deconvolution was done using Huygens software. The staining pattern due to mitochondria in the cell are much better defined than that shown in Figure 5.9.

5.4.1 Creating devices that can generate a second image of the cell.

5.4.1.1 Quartz prism

Micro prisms are commercially available at a size that could be used as the auxiliary mirror for imaging, the smallest available is 500 µm on the dimension of the legs of the prism (the dimensions opposite from the hypotenuse (Tower Optical, 3600 S Congress Ave, J Boynton Beach, FL 33426). In the original design it was proposed that an inverted microscope could be used, and the orthogonal image could be obtained by imaging through a 500 µm prism. However, due to the large working distances needed, only low numerical aperture objectives could be used. This would have an adversely effect on the resolution of the image. This prism method would need a large working distance because the light that is being projected orthogonally closest the coverslip would need to travel the 500µm through the glass in the prism before being refracted down towards the objective lens. A second problem is that the edges of the prism need to be infinitely sharp (meaning that the point would need to be perfect) as the cell and prism are sitting on the cover slip surface. In practice this is not possible to achieve (Choi *et al.*, 2010). Figures 5.11 and 5.12 show schematic representations of the prism and cardiac myocyte alignment of optimal imaging.

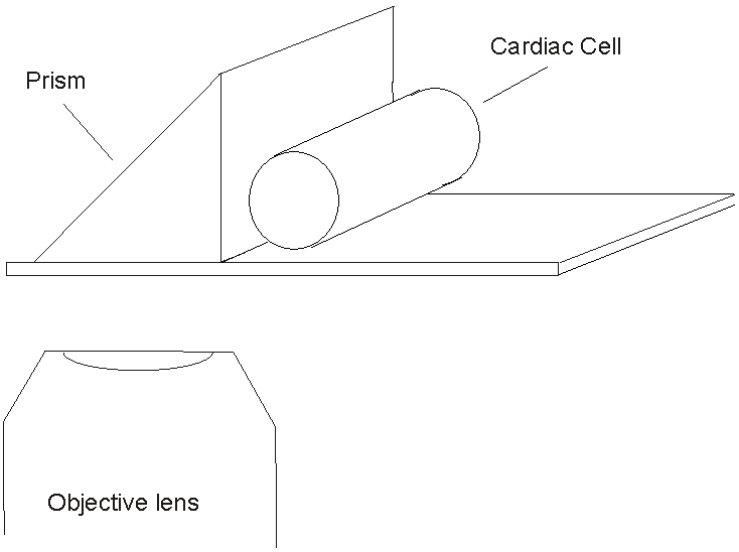

Figure 5.11 shows the schematic representation of the prism imaging set-up. It illustrates the issues over working distance when the dimensions of the prism are 50 and 500 µm. as demonstrated in the earlier results there is image degradation when trying to image through a cell. Therefore it is desirable to image the cell running along side the prism or mirror to minimize the distance that is being imaged through the cardio myocyte.

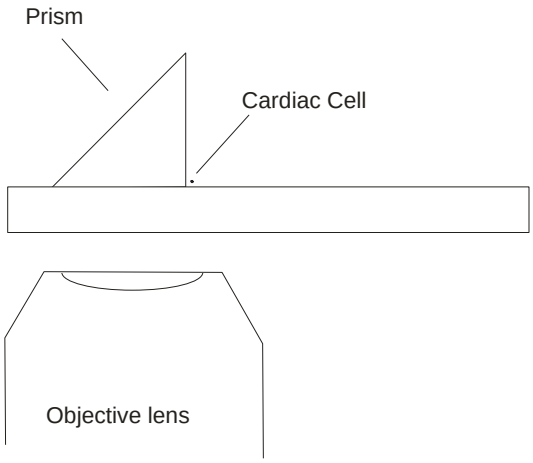

Figure 5.12 is a scaled representation of figure 5.11, it highlights the problems of using a 500 µm prism and the need for very well defined corners of the prism.

5.4.1.2 Micro Mirror

The second version of this approach was considered involving an upright water-dipping objective (as high as possible NA). But this would require a mirror rather than prism element. As demonstrated in figure 5.13

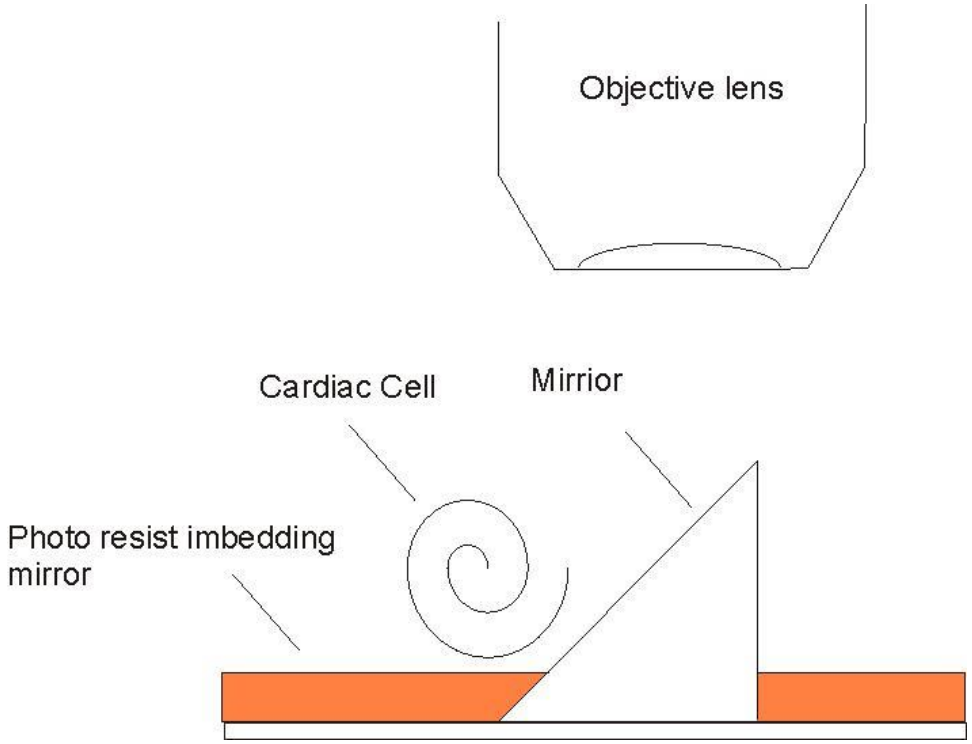

Figure 5.13 Shows a schematic representation of the structure used to create a mirror image in an upright setup. The proposed photoresist to use is S1818 spun to 20µm thickness.

This was created by coating the hypotenuse surface of a microprism with an optically flat reflective surface such as 100 nm platinum and embedding the prism in a photo resist so that the middle of the hypotenuse surface was being used. This technique has a few difficulties associated with it: (i) due to the small size of the prisms they are difficult to clean effectively, as a result the surface of the prism was not perfectly flat; (ii) the surface would be easily damaged even using 10 nm of titanium to act as a bonding agent for the platinum; (iii) positioning the prism next to a cell is challenging; (iv) using an upright microscope with water dipping lenses is a significant limitation because the upright objectives available in this project did not have high NA; (v) manoeuvring cells beside

the mirror using upright objectives is difficult due to the limited space between the objective and the specimen.

An inverted microscope set-up would be more desirable. As demonstrated in figure 5.14, if the specimen was able to sit on the cover slip, all of the specimen would be able to be imaged and it is easier to manipulate so that the specimen is not touching the mirror.

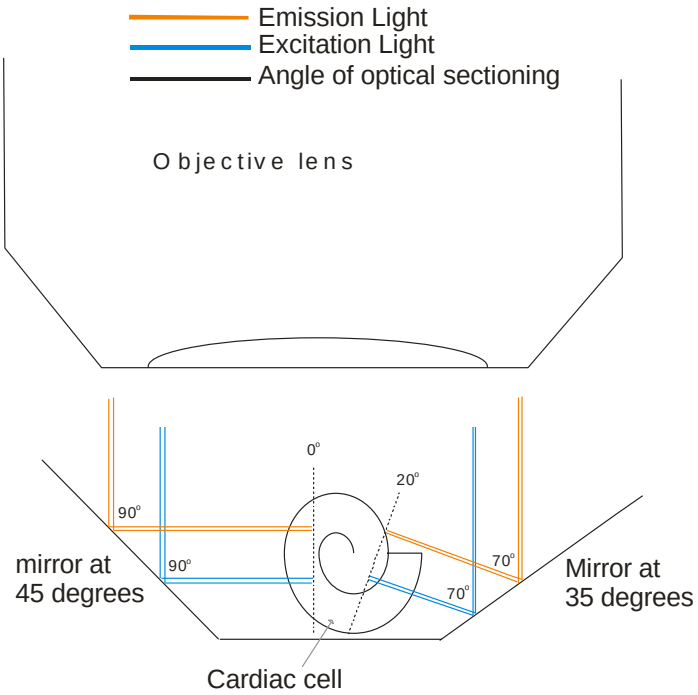

Figure 5.14 shows the optical sectioning angles of mirrors placed at different angles.

The next step is to create a structure that can be used with an inverted microscope, a PDMS cast of the prisms and coated in a reflective metal. This cast was placed on top of a cell and used on an inverted microscope. However there are some problems with this design since PDMS floats. This is normally overcome by the ability of PDMS to stick to glass. The cast needed to be made from a perfect prism with extremely well defined edges. However, the major problem with using PDMS is that it will also absorb the water from the solution bathing the structure hence disrupting the shape of 45 degree edge to change shape, which eventually fractures the platinum surface.

5.4.2 Silicon etching to generate a mirrored cell imaging technique

A variety of methods were employed in order to generate a suitable angled micro mirror that was capable of acquiring an orthogonal image of a cardiac cell. The next design is a cell bath that is approximately 2x1 cm built from a silicon wafer sloped at 55 degrees. As explained in Chapter 2, this is the preferential angle of silicon with a surface orientation of 100, silicon orientation is described in section 2.12. This is not perfect as the optical sectioning is angled at 20 degrees to the vertical plane as shown in figure 5.7.

The ideal mirror angle would be less than 45 degrees in order for it to be used on an inverted microscope system. In order to achieve an etch at this angle, 110 silicon wafers were used and the patterns were aligned to the 111 plane in order to give an etch at 35 degrees (Strandman *et al.*, 1995).

It is ideal that the imaging is sectioned 90 degrees from the original image in order to gain the highest resolution results possible. However there are practical reasons to have a mirror at an angle other than 45 degrees, the main reason is that a 45 degree mirror will always depend on having a perfect edge. In practice this will be difficult to achieve and to not damage. Silicon etching will also generate imperfect edges while leaving the middle surface with only minor defects i.e. in the single nanometre range thus providing a optically flat surface (Poate *et al.*, 1994).

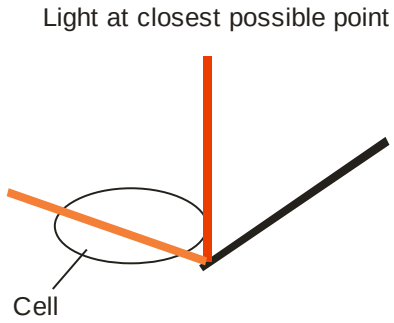

Figure 5.15 Demonstrates the problem with using a mirror at a 55 degree angle.

The main problem with a mirror at 55 degrees is that the cell cannot touch the mirror otherwise it will be impossible to tell which axis the cell is being imaged from. A

disadvantage of this technique is that only the top half of the cell will be captured making a super resolution image of only part of the cell. This problem only applies to upright microscopes. Figures 5.16, 5.17 and 5.18 show scanning electron microscope images of the initial silicon etching results showing the angles of the etch and the smoothness of the etching.

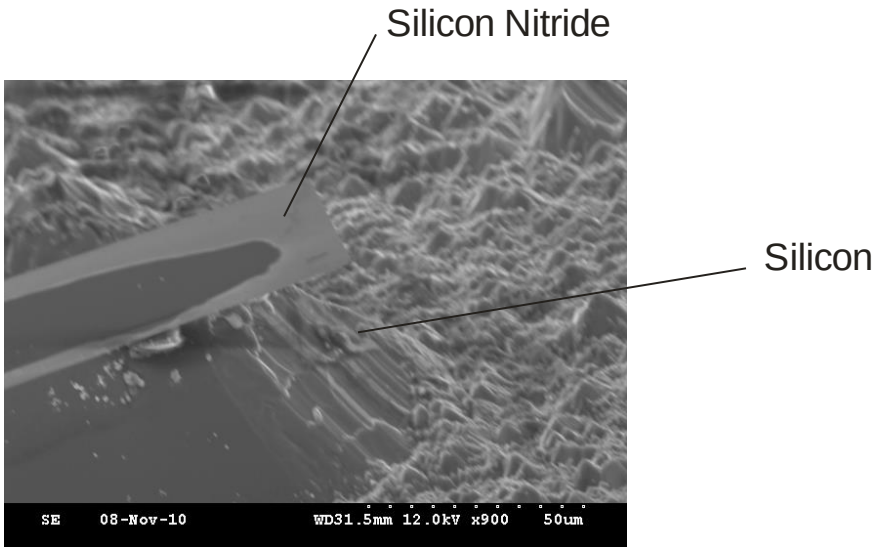

Figure 5.16 is a scanning electron microscope image showing an example of silicon etching away underneath a silicon nitride layer.

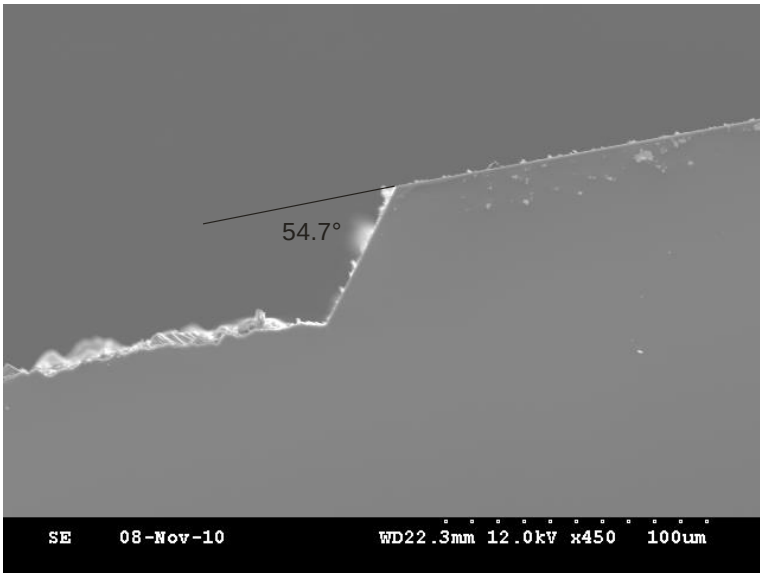

Figure 5.17 is a scanning electron microscope image showing the *54.74°* angle that the silicon has been etched at the upper surface is the original polished surface of the 100 orientation silicon that has been protected by the silicon nitride and the lower rough surface is the silicon that has been etched away.

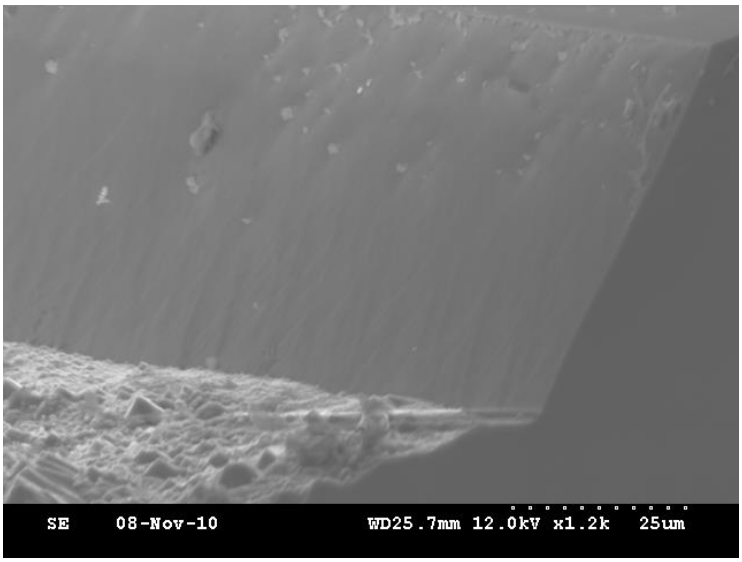

Figure 5.18 is a scanning electron microscope image showing the surface of the silicon etching, there are clearly defects on the surface of the mirror that are in the micron range.

5.4.3 Improving the smoothness of the etched surface,

Although the surface shown above is not as usable as a mirror, it can be improved by two methods: The first is a method where silicon oxide is grown on the silicon wafer. This oxide can vary in thickness from 50-1000 nm, in this case the oxide was grown thermally in a furnace at 1200^{o}C. Once the silicon oxide is grown to the desired thickness, a hydrofluoric acid etch will remove the silicon oxide and not react with the silicon, (Buhler *et al.*, 1997; Cui & Takoudis, 2001; Deal & Grove, 1965)

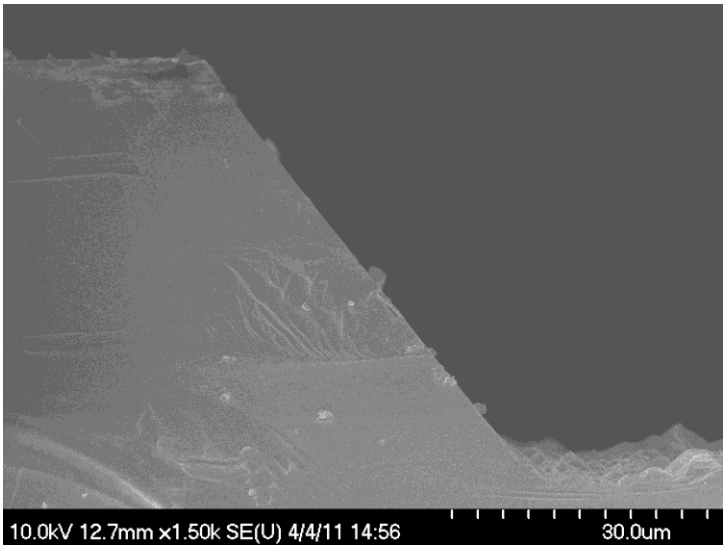

Figure 5.19 This figure shows that the angle of the silicon mirror has not changed with the silicon oxide growth or the hydrofluoric acid etch.

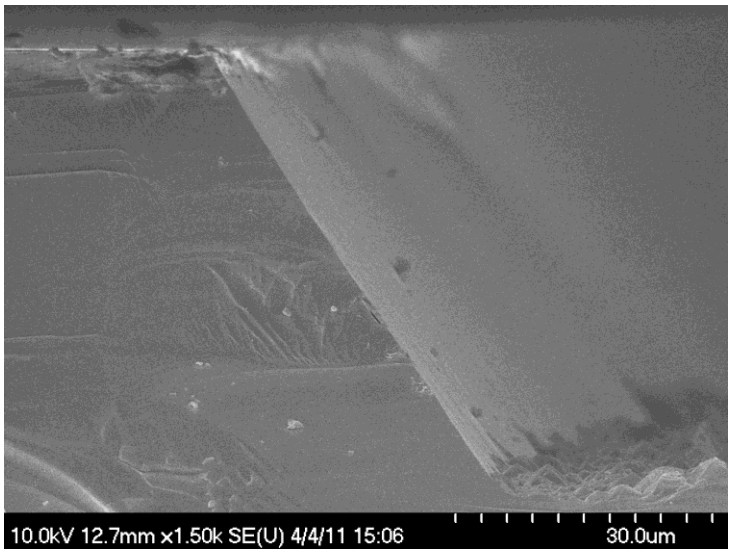

Figure 5.20 shows the surface of the mirror after the oxide layer had been removed.

As shown in Figure 5.20, there is an obvious improvement in surface smoothness although the surface is not perfect.

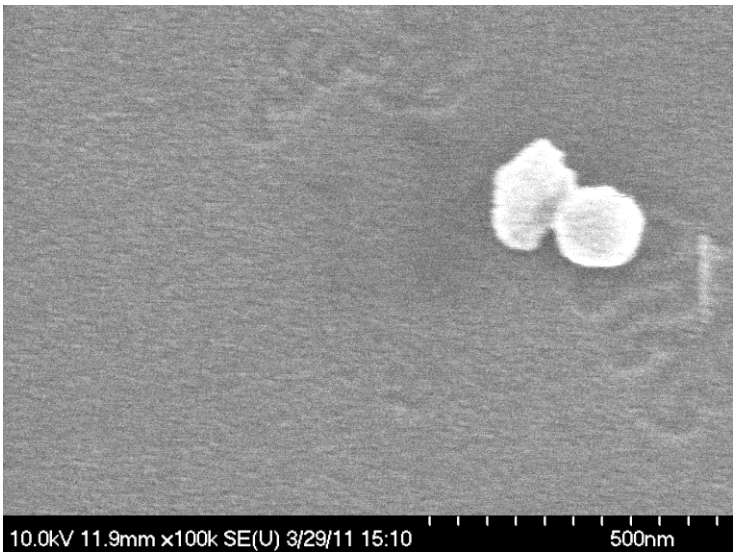

Figure 5.21 This is a high magnification image of the smooth silicon surface. Some debris is obvious along with some minor defects on the surface of the silicon .

Slower etch rates with a weaker KOH solution was able to produce a smoother etch.

A second method to smooth the surface of the silicon is to deposit metal layers on the silicon that can be up to 100nm thick. In this project 10nm of titanium was deposited to work as a bonding agent and then 50nm of platinum was deposited to act as the mirror surface. One of the issue with this approach is that inorder to deposit the metal so that it is as smooth as possible the surface needs to be at a 90-degree angle from the metal vaporization source, which requires angling the rest of the silicon wafer at a 55 degree angle. This was done in the modified evaporator that had a silicon wafer holder that could be set to a 55 degree angle. Silver was chosen as the metal for the mirror as it would reflect the wavelengths evenly (see Figure 5.21) and would not adversely affect living cells in solution.

5.5 Metal choice

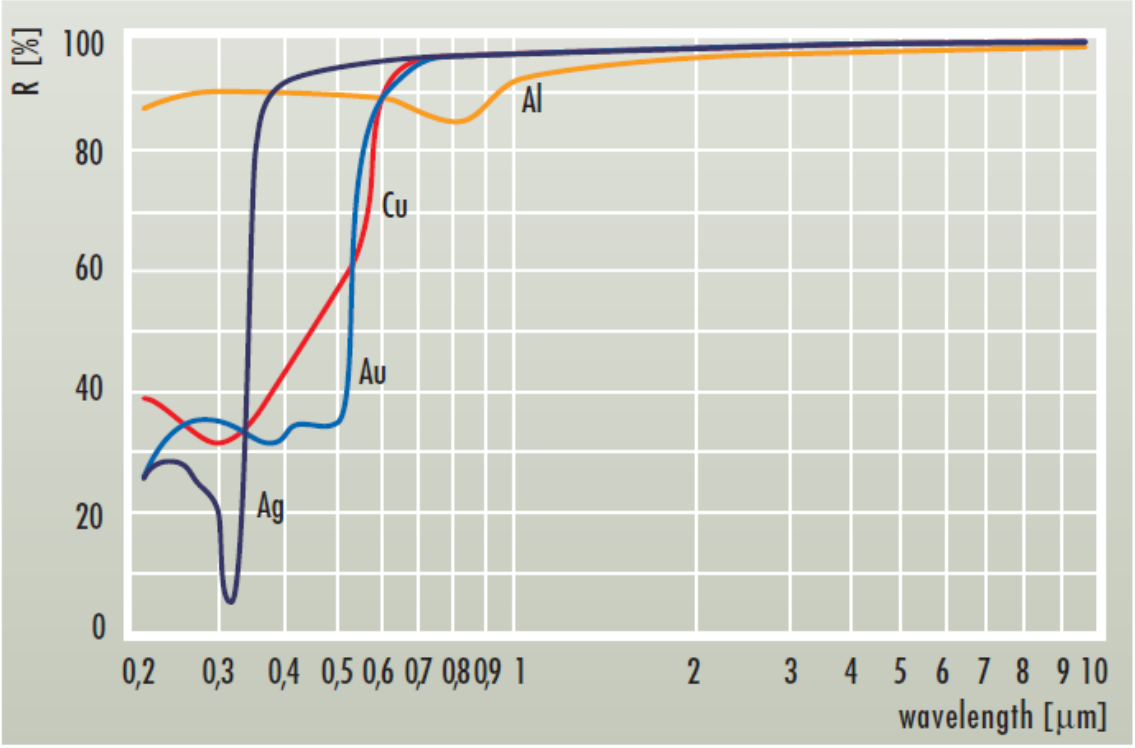

Figure 5.21 This graph shows the reflection properties of various metals (Figure from LayerTec, optical coatings and optics).

Aluminium would not be a suitable material as it would grow an oxide layer on the surface and the Al^{3+} ions would kill the cells. Silver and gold are both suitable metals.

5.6 Imaging cardiac mitochondria throughout a complete cell.

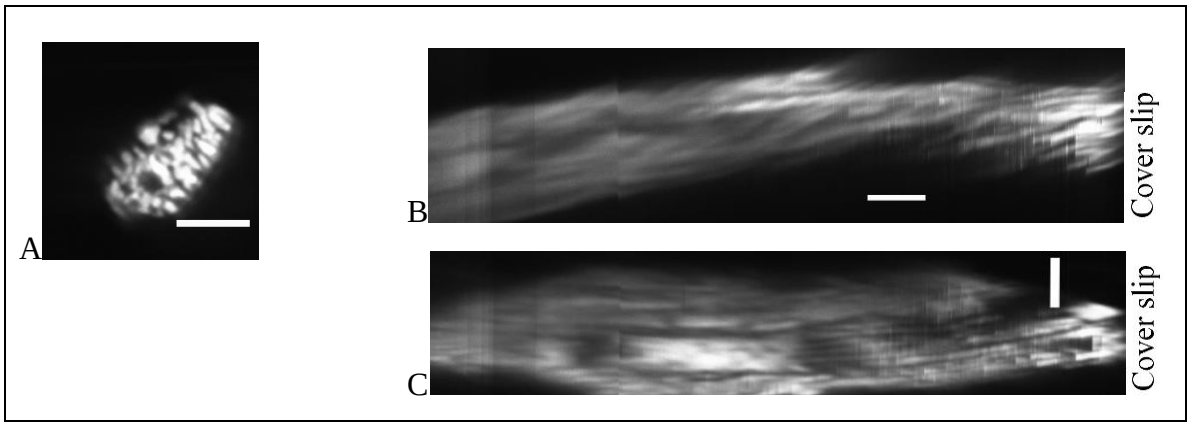

Figure 5.22a: This figure shows a two-photon image of a vertical myocyte stained with TMRE. The image is constructed from 600 256X256 images 0.2 µm apart. The resolution is not sufficient for deconvolution. **Figure 5.22b** and **5.22c**: These figures are XZ and YZ orthogonal slices. It is obvious that the large Z PSF has degraded the image. The scale bars represent 10 µm

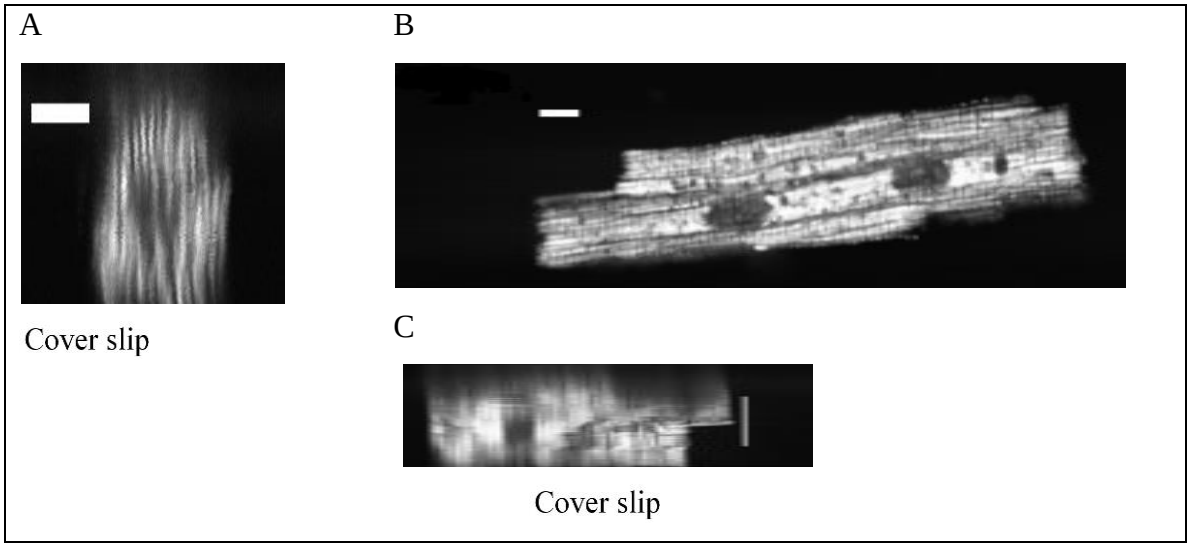

Figure 5.23a: This figure shows a conventional two-photon image where the myocyte is imaged horizontally, it is stained with TMRE. **Figure 5.23b** and **5.23c**: These figures are

XZ and YZ orthogonal slices. It is obvious that the large Z PSF has degraded the image the scale bars represent 10 µm.

5.7 Mirrored cell imaging

Due to the limited use of reorienting the cell, a much better method is to image a cell and then image the mirror image of the same cell so that there are two z stacks of the same cell that can then be convolved to create a high resolution image,

There are two challenges to creating this experimental setup, the first is to build a mirror or prism to gain a second image, the second problem is to convolve the image once the two images have been acquired.

5.7.1 Preliminary results

The mirror shown in Figure 5.11 was used by placing it on top of a cover slip. This formed a 60 µm gap in between the cover slip and the silicon on the edge of which the mirror was placed. A rod and ball suspension of cardiomyocytes was then placed next to the channel so that fluid would fill the channel via capillary motion. It appeared that the balls entered the channel while the rods did not. There was no way of manipulating the specimens in the channel. Below is an image of a ball along with the composite mirror image.

A

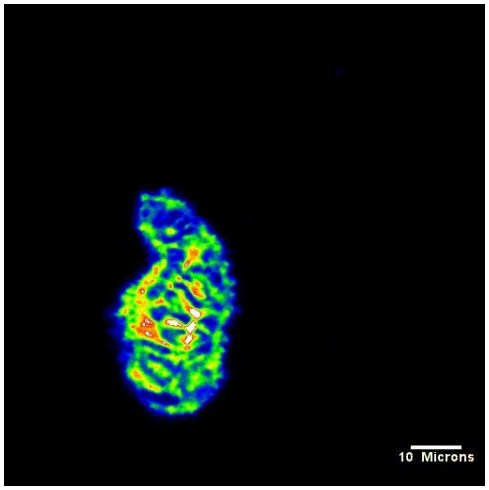

B

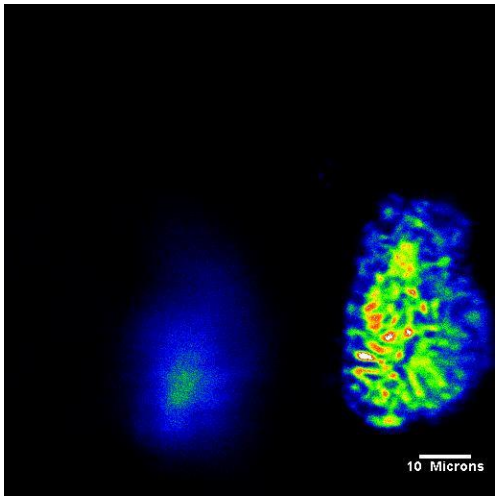

Figure5.24A shows the conventional two-photon image of a dead cardiac cell. The mirror is not visible but is place just to the right of the cell. **Figure B** shows the mirror image of the same cell, the edge of the original image is still in view. They are not visible on the same plane because the light path of the two photon beam in the mirror image is increased due to the distance the cell is from the mirror.

Figure 5.25 is an XZ image of Figure5.23A the image is sectioned at 90 degrees
Figure 5.25 is an equivalent image Figure5.23B, the image is sectioned at 70 degrees.

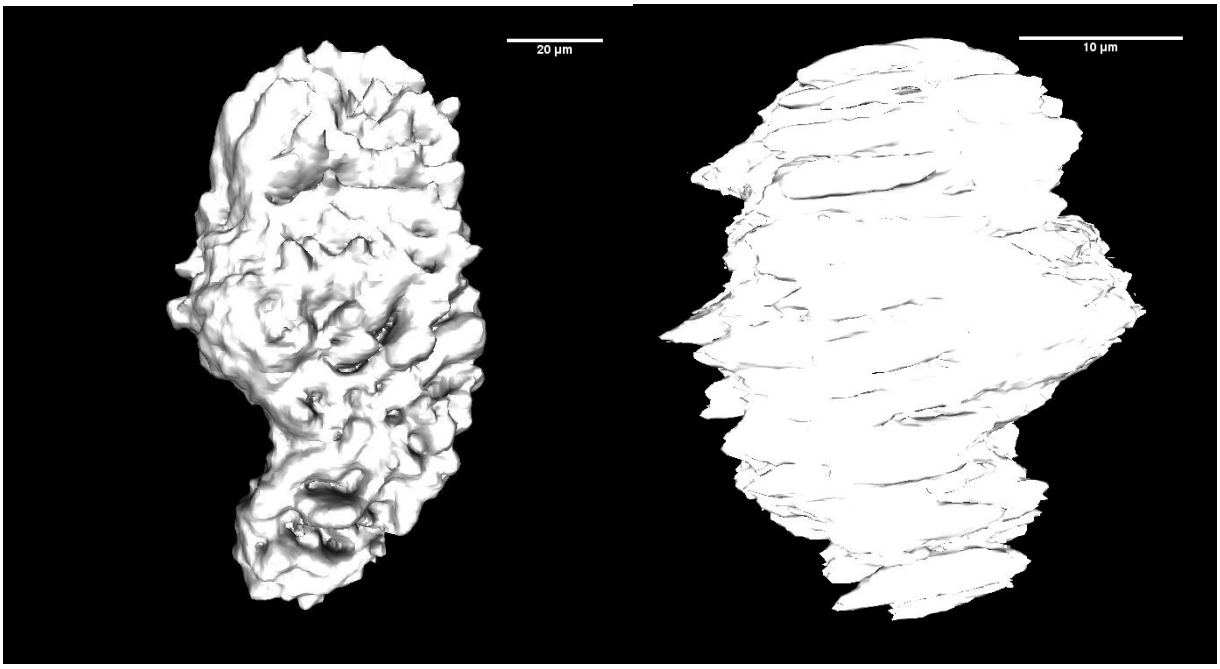

Figure 5.26 shows the a surface 3D rendering of the conventionally imaged dead cardiac cell

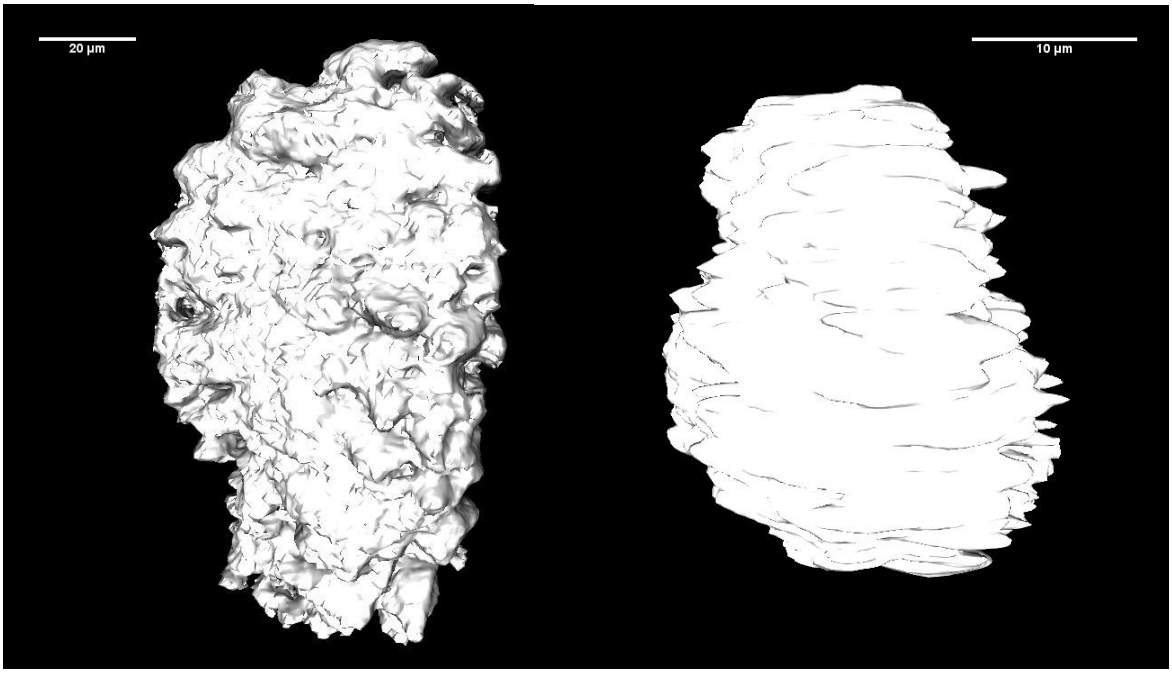

Figure 5.27 shows the a surface 3D rendering of the mirror imaged dead cardiac cell.

5.8 Discussion

5.8.1 Loss of resolution and signal

The technique of physically orientating the cells was found to have limited depth penetration. This is highlighted by Figure 5.8. Where the resolvable edge becomes less well defined at a rapid rate. The extent of the aberration is dependant on the NA of the lens used. The higher the NA the more serve the aberrations become. Imaging T-tubules was impractical as there was a small signal from them in the vertical orientation due to only a small proportion of the T-tuble is in the scanning point of the confocal system compared to a T-tuble being images in a horizontal position. A side effect of only imaging a small amount of the die is this caused rapid bleaching of the dye which meant that fine enough sample sections to enable deconvolution was not possible. Attempts to use fluorescein as a replenishable die was not possible due to the slow diffusion rates as shown in figure 5.6. Therefore a different attempt was made in which a mirror was fabricated. The attempts to fabricate the intended micro mirror where cells could be manipulated into position where unsuccessful thus no images of live cells could be acquired, however the preliminary results from the early structure are promising. There is a noticeable improvement in the z axis resolution in the mirror image shown in figures 5.24-27. Fabrication of the suitable mirror should be possible although the angle of etch may need to be different.

5.9 Conclusion

The use of vertical cell imaging is a very good method for imaging the intercalated disc and structures a few µm into the cell, however light scattering worsens the further into the cell that the light travels, until the optical quality degraded to such a point that it is better to image the cell in a conventional orientation. The future of this project has various options available to it:

(1) Electrical stimulation of vertically positioned cardiomyocytes into the walls of the microfabricated chamber. The main advantage of this is to allow imaging of intracellular regulation of Ca^{2+} on a new (radial axis).

(2) The mirror technique could be improved with a higher quality mirror as well as a design that makes the mirror surface more accessible to pipettes in order to manipulate and position the cells.

6 Chapter 6: General discussion

6.1 System resolution

One of the primary aims of this study was to investigate the abilities of optically sectioning fluorescent microscopes. This thesis presents data showing that the measured PSF and ESF measurements can be much larger than theoretically expected. The poor reproducibility and resolution in the Z axis can be partially attributed to poor performance of the Z-axis translation mechanism -stage accuracy cannot be depended on to produce accurate results and can cause and elongation to the z-axis projection by which consistently underestimates the Z step size. The results also show that there can be an even greater inconsistency within the first few movements of the z-stage motor; therefore it is an advisable to start any Z-stack acquisitions with the first 3-5 sections well above or below the specimen in order to get as constant as possible results. Furthermore, having z-sections of "nothing" i.e. non-tissue above the plane of the specimen can be extremely useful as it means it is possible to measure the background signal associated with the system at the acquisition settings being used. The data in the thesis also showed that signal noise can affect the ability to measure resolution of an optical system since curve fitting these noisy signals can generate spurious values and under-estimate resolution.

6.2 The optical effects of the specimen

The second aspect part of these studies was to examine the effects that the optical properties of the specimen had on the resolution of imaging systems. This study found that the resolution of the imaging system is reduced when imaging through significant amounts of biological material because of the difference in refractive index of biological tissue, particularly the heart from that of water. This miss-match of refractive index can generate spherical aberrations that could reduce the resolution of the objective and reduce the intensity of the signal which will indirectly reduce resolution by increasing the noise on an optical signal of equivalent fluorescence. Tissue such heart muscle also scatters light thereby reducing excitation light intensity and reducing resolution via increasing the noise on an equivalent optical signal. There are various methods of altering the

specimen's optical properties, such as specimen clearing, in order to optimise the optical properties of the specimen; however these methods are not feesible if live physiological recordings are being taken from the specimen.

6.3 PSF Vs ESF

Point spread functions are the standard method of describing the minimum resolution of an imaging system. PSFs can be used to describe the minimum resolution in the X, Y and Z axis, and they can also be used to detect aberrations within the lens. However, when PSF values are quoted, they seldom take into account the distance or position from the optical axis. Knowing the lateral axis resolution can be useful, however if the Z axis resolution is much larger than expected, one can expect the optical section to be thicker when imaging real specimens which will interfere with the lateral measurements.

The major disadvantage of measuring the PSF with sub resolution beads is the fact that the user is forced to make the assumption that the sub-resolution beads have not adhered to each other. Polystyrene beads are very prone to adhering to themselves. This coupled with the difficulty in locating beads and low signal to noise makes acquisition and analysis difficult.

As used in these studies, a substitute to the PSF is measurement of the ESF, which is feasible to measure despite a considerable amount of intervening optically dense material. However, when taking an ESF, only the Z-axis resolution is revealed at any point in the field of view. This technique also reveals the uniformity of the illumination/excitation across the field; this is vitality important as many experiments depend on comparing intensity results across the lateral axis. Uniformity of illumination/excitation is affected by the alignment of the laser in the microscope optics, this is done on site and can vary from system to system.

6.4 System improvement with the use of microfabrication

Data from the cell orientation method has shown some limited success. It is not possible or desirable to merge the orthogonal images due to changes the cell may have undergone while being manipulated by the pipette. The limited working distance into the cell also limits the usefulness of the technique.

Imaging an orthogonal view of the specimen with the use of a micro fabricated mirror shows promising potential. Orthogonal images can be convolved, as the specimen has not been disturbed and the images have been acquired within minutes. Production of a mirror should be possible with further work. Once a technique has been found and mask plates with the correct angle have been created, then recreating the mirror structure should be a relatively straightforward process.

7 Reference List

Allen, D. G. & Smith, G. L. (1987). The Effects of Hypertonicity on Tension and Intracellular Calcium-Concentration in Ferret Ventricular Muscle. *Journal of Physiology-London* **383**, 425-439.

Amos, W. B. Instruments for Fluorescence Imaging. Protein Localization by Fluorescence Microscopy 1, 67-108. 2000.
Ref Type: Generic

Andreas Ohler, Jutta Weisser-Thomas, Valentino Piacentino 3rd, Steven R.Houser, Gordon F.Tomaselli, & Brian O'Rourke. Two-Photon Laser ScanningMicroscopy of the Transverse-Axial Tubule System in Ventricular Cardiomyocytes from Failing and Non-Failing Human Hearts. Cardiology Research and Practice 1, 1-9. 2009.
Ref Type: Generic

B Dorband, H Muller, & H Gross. The Handbook of Optical Systems. 5, 919. 2009.
Ref Type: Generic

Barth, E., Stammler, G., Speiser, B., & Schaper, J. (1992). Ultrastructural Quantitation of Mitochondria and Myofilaments in Cardiac-Muscle from 10 Different Animal Species Including Man. *Journal of Molecular and Cellular Cardiology* **24**, 669-681.

Bass, M. & Van Stryland. Handbook of Optics. 2. 2010.
Ref Type: Generic

Beauvoit, B., Evans, S. M., Jenkins, T. W., Miller, E. E., & Chance, B. (1995). Correlation Between the Light-Scattering and the Mitochondrial Content of Normal-Tissues and Transplantable Rodent Tumors. *Analytical Biochemistry* **226**, 167-174.

Beckerle, M. C. (1984). Microinjected Fluorescent Polystyrene Beads Exhibit Saltatory Motion in Tissue-Culture Cells. *Journal of Cell Biology* **98**, 2126-2132.

Bessho, M., Tajima, T., Hori, S., Satoh, T., Fukuda, K., Kyotani, S., Ohnishi, Y., & Nakamura, Y. (1989). Nad and Nadh Values in Rapidly Sampled Dog Heart Tissues by 2 Different Extraction Methods. *Analytical Biochemistry* **182**, 304-308.

Bishop, M. J., Rodriguez, B., Qu, F., Efimov, I. R., Gavaghan, D. J., & Trayanova, N. A. (2007). The role of photon scattering in optical signal distortion during arrhythmia and defibrillation. *Biophysical Journal* **93**, 3714-3726.

Booth, M. J. & Wilson, T. (2001). Refractive-index-mismatch induced aberrations in single-photon and two-photon microscopy and the use of aberration correction. *Journal of Biomedical Optics* **6**, 266-272.

Brandes, R. & Bers, D. M. (1999). Analysis of the mechanisms of mitochondrial NADH regulation in cardiac trabeculae. *Biophysical Journal* **77**, 1666-1682.

Brette, F. & Orchard, C. (2003). T-tubule function in mammalian cardiac myocytes. *Circulation Research* **92**, 1182-1192.

Campagnola, P. J., Wei, M. D., Lewis, A., & Loew, L. M. (1999). High-resolution nonlinear optical imaging of live cells by second harmonic generation. *Biophysical Journal* **77**, 3341-3349.

Centonze, V. E. & White, J. G. (1998). Multiphoton excitation provides optical sections from deeper within scattering specimens than confocal imaging. *Biophysical Journal* **75**, 2015-2024.

Chen-Izu, Y., McCulle, S. L., Ward, C. W., Soeller, C., Allen, B. M., Rabang, C., Cannell, M. B., Balke, C. W., & Izu, L. T. (2006). Three-dimensional distribution of ryanodine receptor clusters in cardiac myocytes. *Biophysical Journal* **91**, 1-13.

Cheng, H., Lederer, M. R., Lederer, W. J., & Cannell, M. B. (1996). Calcium sparks and [Ca2+](i) waves in cardiac myocytes. *American Journal of Physiology-Cell Physiology* **39**, C148-C159.

Cheng, H., Song, L. S., Shirokova, N., Gonzalez, A., Lakatta, E. G., Rios, E., & Stern, M. D. (1999). Amplitude distribution of calcium sparks in confocal images: Theory and studies with an automatic detection method. *Biophysical Journal* **76**, 606-617.

Choi, S., Kim, S. H., & Park, J. K. (2010). Optical path-length modulation for three-dimensional particle measurement in mirror-embedded microchannels. *Lab on A Chip* **10**, 335-340.

Coremans, J. M. C. C., Ince, C., Bruining, H. A., & Puppels, G. J. (1997). (Semi-)quantitative analysis of reduced nicotinamide adenine dinucleotide fluorescence images of blood-perfused rat heart. *Biophysical Journal* **72**, 1849-1860.

de Boer, J. F., Milner, T. E., & Nelson, J. S. (1999). Determination of the depth-resolved Stokes parameters of light backscattered from turbid media by use of polarization-sensitive optical coherence tomography. *Optics Letters* **24**, 300-302.

de Grauw, G. J., Vroom, J. M., van der Voort, H. T. M., & Gerritsen, H. C. (1999). Imaging properties in two-photon excitation microscopy and effects of refractive-index mismatch in thick specimens. *Applied Optics* **38**, 5995-6003.

Dirckx, J. J. J., Kuypers, L. C., & Decraemer, W. F. (2005). Refractive index of tissue measured with conflocal microscopy. *Journal of Biomedical Optics* **10**.

DM Bers. Excitation contraction coupling and cardiac contractile force. Kluwer Academic . 2001.
Ref Type: Generic

DM Bers. Cardiac excitation-contraction coupling. Nature 415, 198-205. 2002.
Ref Type: Generic

Dong, C. Y., Koenig, K., & So, P. (2003). Characterizing point spread functions of two-photon fluorescence microscopy in turbid medium. *Journal of Biomedical Optics* **8**, 450-459.

Dumas, J. H. & Kinisley, S. B. (2005). Two-photon excitation of di-4-ANEPPS for optical recording of action potentials in rabbit heart. *Annals of Biomedical Engineering* **33**, 1802-1807.

Erdemoglu, S., Aksu, S. K., Sayilkan, F., Izgi, B., Asilturk, M., Sayilkan, H., Frimmel, F., & Gucer, S. (2008). Photocatalytic degradation of Congo Red by hydrothermally synthesized nanocrystalline TiO2 and identification of degradation products by LC-MS. *Journal of Hazardous Materials* **155**, 469-476.

Eschenhagen, T. & Zimmermann, W. H. (2005). Engineering myocardial tissue. *Circulation Research* **97**, 1220-1231.

F B Sachse, eleonora savio-galimberti, joshua i.goldhaber, & john h.b.bridge. Sub-micrometer anatomical models of the sarcolemma of cardiac myocytes based on confocal imaging. Pacific Symposium on Biocomputing 13, 390-401. 2008.
Ref Type: Generic

Faivre Olivier. Programmable array microscopy and its application to neurobiology. 1-304. 2012.
Ref Type: Generic

Fedosseev, R., Belyaev, Y., Frohn, J., & Stemmer, A. (2005). Structured light illumination for extended resolution in fluorescence microscopy. *Optics and Lasers in Engineering* **43**, 403-414.

Gandjbakhche, A. H., Bonner, R. F., Arai, A. E., & Balaban, R. S. (1999). Visible-light photon migration through myocardium in vivo. *American Journal of Physiology-Heart and Circulatory Physiology* **277**, H698-H704.

Garini, Y., Young, I. T., & McNamara, G. (2006). Spectral imaging: Principles and applications. *Cytometry Part A* **69A**, 735-747.

Ghauharali, R. I. & Brakenhoff, G. J. (2000). Fluorescence photobleaching-based image standardization for fluorescence microscopy. *Journal of Microscopy-Oxford* **198**, 88-100.

Goldman, B. I. & Wurzel, J. (1995). Human Fetal Cardiocytes in Enriched Culture. *In Vitro Cellular & Developmental Biology-Animal* **31**, 731-734.

Gordienko, D. V., Greenwood, I. A., & Bolton, T. B. (2001). Direct visualization of sarcoplasmic reticulum regions discharging Ca2+ sparks in vascular myocytes. *Cell Calcium* **29**, 13-28.

Gorodetsky, M. L., Savchenkov, A. A., & Ilchenko, V. S. (1996). Ultimate Q of optical microsphere resonators. *Optics Letters* **21**, 453-455.

Haemmerle, G., Moustafa, T., Woelkart, G., Buttner, S., Schmidt, A., van de Weijer, T., Hesselink, M., Jaeger, D., Kienesberger, P. C., Zierler, K., Schreiber, R., Eichmann, T., Kolb, D., Kotzbeck, P., Schweiger, M., Kumari, M., Eder, S., Schoiswohl, G., Wongsiriroj, N., Pollak, N. M., Radner, F. P. W., Preiss-Landl, K., Kolbe, T., Rulicke, T., Pieske, B., Trauner, M., Lass, A., Zimmermann, R., Hoefler, G., Cinti, S., Kershaw, E. E., Schrauwen, P., Madeo, F., Mayer, B., & Zechner, R. (2011). ATGL-mediated fat catabolism regulates cardiac mitochondrial function via PPAR-alpha and PGC-1. *Nature Medicine* **17**, 1076-1U82.

Han, M., Hyun, D. H., Park, H. H., Lee, S. S., Kim, C. H., & Kim, C. (2007). A novel fabrication process for out-of-plane microneedle sheets of biocompatible polymer. *Journal of Micromechanics and Microengineering* **17**, 1184-1191.

Hanley, Q. S., Verveer, P. J., Gemkow, M. J., Arndt-Jovin, D., & Jovin, T. M. (1999). An optical sectioning programmable array microscope implemented with a digital micromirror device. *Journal of Microscopy-Oxford* **196**, 317-331.

Heintzmann, R. & Ficz, G. (2007). Breaking the resolution limit in light microscopy. *Digital Microscopy, 3Rd Edition* **81**, 561-+.

Heintzmann, R., Hanley, Q. S., Arndt-Jovin, D., & Jovin, T. M. (2001). A dual path programmable array microscope (PAM): simultaneous acquisition of conjugate and non-conjugate images. *Journal of Microscopy-Oxford* **204**, 119-135.

Hell, S., Reiner, G., Cremer, C., & Stelzer, E. H. K. (1993). Aberrations in Confocal Fluorescence Microscopy Induced by Mismatches in Refractive-Index. *Journal of Microscopy-Oxford* **169**, 391-405.

Helmchen, F. & Denk, W. (2005). Deep tissue two-photon microscopy. *Nature Methods* **2**, 932-940.

J R Levick. An Introduction to Cardiovascular Physiology. 2003.
Ref Type: Generic

Jacobsen, H., Hanninen, P., Soini, E., & Hell, S. W. (1994). Refractive-Index-Induced Aberrations in 2-Photon Confocal Fluorescence Microscopy. *Journal of Microscopy-Oxford* **176**, 226-230.

Jacques Boutet de Monvel, Sophie Le Calvez, & Mats Ulfendahl. Image Restoration for Confocal Microscopy: Improving the Limits of
Deconvolution, with Application to the Visualization of the Mammalian
Hearing Organ. Biophysical Journal 80, 2455-2470. 2001.
Ref Type: Generic

James Pawley. Handbook of Biological Confocal Microscopy. 2006.
Ref Type: Generic

Katerina Fialova, Jana Kolarova, Ivo Provaznik, & Marie Novakova1. Comparison of Voltage-Sensitive Dye di-4-ANNEPS Effects in Isolated Hearts of Rat, Guinea Pig, and Rabbit. Computing in Cardiology 37, 565-568. 2010.
Ref Type: Generic

Kettlewell, S., Cabrero, P., Nicklin, S. A., Dow, J. A. T., Davies, S., & Smith, G. L. (2009). Changes of intra-mitochondrial Ca2+ in adult ventricular cardiomyocytes examined using a novel fluorescent Ca2+ indicator targeted to mitochondria. *Journal of Molecular and Cellular Cardiology* **46**, 891-901.

Klar, T. A., Jakobs, S., Dyba, M., Egner, A., & Hell, S. W. (2000). Fluorescence microscopy with diffraction resolution barrier broken by stimulated emission. *Proceedings of the National Academy of Sciences of the United States of America* **97**, 8206-8210.

Klauke, N., Smith, G. L., & Cooper, J. (2003). Stimulation of single isolated adult ventricular myocytes within a low volume using a planar microelectrode array. *Biophysical Journal* **85**, 1766-1774.

Kofidis, T., Akhyari, P., Boublik, J., Theodorou, P., Martin, U., Ruhparwar, A., Fischer, S., Eschenhagen, T., Kubis, H. P., Kraft, T., Leyh, R., & Haverich, A. (2002). In vitro engineering of heart muscle: Artificial myocardial tissue. *Journal of Thoracic and Cardiovascular Surgery* **124**, 63-69.

Kraus, T., Malaquin, L., Schmid, H., Riess, W., Spencer, N. D., & Wolf, H. (2007). Nanoparticle printing with single-particle resolution. *Nature Nanotechnology* **2**, 570-576.

Kuypers, L. C., Decraemer, W. F., Dirckx, J. J. J., & Timmermans, J. P. (2005). A procedure to determine the correct thickness of an object with confocal microscopy in case of refractive index mismatch. *Journal of Microscopy-Oxford* **218**, 68-78.

Laasmaa m. The Analysis of Richardson-Lucy Deconvolution Algorithm with Application to Microscope Images. 1-39. 2010.
Ref Type: Generic

Lee, J. Y., Noordhoek, M. J., Smereka, P., Mckay, H., & Millunchick, J. M. (2009). Filling of hole arrays with InAs quantum dots. *Nanotechnology* **20**.

Leray, A., Lillis, K., & Mertz, J. (2008). Enhanced background rejection in thick tissue with differential-aberration two-photon microscopy. *Biophysical Journal* **94**, 1449-1458.

Leung, A. F. (1982). Calculation of the Laser Diffraction Intensity of Striated-Muscle by Numerical-Methods. *Computer Programs in Biomedicine* **15**, 169-174.

Liu, T., Sim, L. M., & Xu, J. (2010). Targeted reconstruction with differential planar computed tomography. *Ndt & e International* **43**, 116-122.

Loew, L. M. (1996). Potentiometric dyes: Imaging electrical activity of cell membranes. *Pure and Applied Chemistry* **68**, 1405-1409.

Loew, L. M., Carrington, W., Tuft, R. A., & Fay, F. S. (1994). Physiological Cytosolic Ca2+ Transients Evoke Concurrent Mitochondrial Depolarizations. *Proceedings of the National Academy of Sciences of the United States of America* **91**, 12579-12583.

Lyon, A. R., MacLeod, K. T., Zhang, Y. J., Garcia, E., Kanda, G. K., Lab, M. J., Korchev, Y. E., Harding, S. E., & Gorelik, J. (2009). Loss of T-tubules and other changes to surface topography in ventricular myocytes from failing human and rat heart. *Proceedings of the National Academy of Sciences of the United States of America* **106**, 6854-6859.

M Nováková, K Nogová, J Bardonová, & I Provazník. Comparison of Two Procedures of Loading with Voltage-Sensitive Dye Di-4 ANEPPS in Rabbit Isolated Heart. Computers in Cardiology , 1081-1084. 2008.
Ref Type: Generic

Maisch, B. (1981). Enrichment of Vital Adult Cardiac-Muscle-Cells by Continuous Silica Sol Gradient Centrifugation. *Basic Research in Cardiology* **76**, 622-629.

Mastronarde, D. N. (1997). Dual-axis tomography: An approach with alignment methods that preserve resolution. *Journal of Structural Biology* **120**, 343-352.

McDonald, A., Harris, J., MacMillan, D., Dempster, J., & McConnell, G. (2012). Light-induced Ca2+ transients observed in widefield epi-fluorescence microscopy of excitable cells. *Biomedical Optics Express* **3**, 1266-1273.

Miks, A., Novak, J., & Novak, P. (2007). Calculation of point-spread function for optical systems with finite value of numerical aperture. *Optik* **118**, 537-543.

Millard, A. C., Jin, L., Wei, M. D., Wuskell, J. P., Lewis, A., & Loew, L. M. (2004). Sensitivity of second harmonic generation from styryl dyes to transmembrane potential. *Biophysical Journal* **86**, 1169-1176.

Mirzoyan, R., Laatiaoui, M., & Teshima, M. (2006). Very high quantum efficiency PMTs with bialkali photo-cathode. *Nuclear Instruments & Methods in Physics Research Section A-Accelerators Spectrometers Detectors and Associated Equipment* **567**, 230-232.

Montana, V., Farkas, D. L., & Loew, L. M. (1989). Dual-Wavelength Ratiometric Fluorescence Measurements of Membrane-Potential. *Biochemistry* **28**, 4536-4539.

Mortimer Abramowitz, Kenneth R.Spring, H.Ernst Keller, & Michael W.Davidson. Basic Principles of Microscope Objectives. BioTechniques 33 4, 772-780. 2002.
Ref Type: Generic

Murthy, S. K., Sethu, P., Vunjak-Novakovic, G., Toner, M., & Radisic, M. (2006). Size-based microfluidic enrichment of neonatal rat cardiac cell populations. *Biomedical Microdevices* **8**, 231-237.

Neil, M. A. A., Juskaitis, R., & Wilson, T. (1997). Method of obtaining optical sectioning by using structured light in a conventional microscope. *Optics Letters* **22**, 1905-1907.

Nicolas DEY, Laure BLANC-F´ERAUD, Christophe ZIMMER, Pascal ROUX, Zvi KAM, Jean-Christophe OLIVO-MARIN, & Josiane ZERUBIA. 3D Microscopy Deconvolution using Richardson-Lucy Algorithm with Total Variation Regularization. 2010.
Ref Type: Generic

Ntziachristos, V. (2010). Going deeper than microscopy: the optical imaging frontier in biology. *Nature Methods* **7**, 603-614.

Patterson, G., Davidson, M., Manley, S., & Lippincott-Schwartz, J. Superresolution Imaging using Single-Molecule Localization. Annual Review of Physical Chemistry 61, 345-367. 2010.
Ref Type: Generic

Pawley J. Handbook of Biological Confocal Microscopy. 2006.
Ref Type: Generic

Pawley, J. B. (2002). Limitations on optical sectioning in live-cell confocal microscopy. *Scanning* **24**, 241-246.

Peter Bankhead. Computer software for the automated analysis of calcium signalling events and vessel diameters in the retinal vasculature. 1-227. 2009.
Ref Type: Generic

Peter Bankhead. Computer software for the automated analysis of calcium signalling events and vessel diameters in the retinal vasculature. 1-227. 2012.
Ref Type: Generic

Poate, J. M., Eaglesham, D. J., Gossmann, H. J., Higashi, G. S., & Pietsch, G. (1994). Silicon Processing and Atomic-Level Defects. *Defect Recognition and Image Processing in Semiconductors and Devices* 1-10.

Popp, A. K., Valentine, M. T., Kaplan, P. D., & Weitz, D. A. (2003). Microscopic origin of light scattering in tissue. *Applied Optics* **42**, 2871-2880.

Qing Ye, Jin Wang, Zhi-Chao Deng, Wen-Yuan Zhou, Chun-Ping Zhang, & Jian-Guo Tian. Measurement of the complex refractive index of tissue-mimicking phantoms and biotissue by extended differential total reflection method. Journal of Biomedical Optics 16(9). 2011.
Ref Type: Generic

Radwanski, P. B., Veeraraghavan, R., & Poelzing, S. (2010). Cytosolic calcium accumulation and delayed repolarization associated with ventricular arrhythmias in a guinea pig model of Andersen-Tawil syndrome. *Heart Rhythm* **7**, 1428-14U1.

Rauf, S., Glidle, A., & Cooper, J. M. (2010). Application of quantum dot barcodes prepared using biological self-assembly to multiplexed immunoassays. *Chemical Communications* **46**, 2814-2816.

Rocheleau, J. V., Head, W. S., & Piston, D. W. (2004). Quantitative NAD(P)H/flavoprotein autofluorescence imaging reveals metabolic mechanisms of pancreatic islet pyruvate response. *Journal of Biological Chemistry* **279**, 31780-31787.

Rossmann, K. (1969). Point Spread-Function, Line Spread-Function, and Modulation Transfer Function - Tools for Study of Imaging Systems. *Radiology* **93**, 257-&.

Rubart, M., Wang, E. X., Dunn, K. W., & Field, L. J. (2003). Two-photon molecular excitation imaging of Ca2+ transients in Langendorff-perfused mouse hearts. *American Journal of Physiology-Cell Physiology* **284**, C1654-C1668.

Sarder, P. & Nehorai, A. (2006). Deconvolution methods for 3-D fluorescence microscopy images. *Ieee Signal Processing Magazine* **23**, 32-45.

Schaffer, P., Ahammer, H., Muller, W., Koidl, B., & Windisch, H. (1994). Di-4-Anepps Causes Photodynamic Damage to Isolated Cardiomyocytes. *Pflugers Archiv-European Journal of Physiology* **426**, 548-551.

Scherschel, J. A. & Rubart, M. (2008). Cardiovascular Imaging Using Two-Photon Microscopy. *Microscopy and Microanalysis* **14**, 492-506.

Schmitt, J. M. & G.Kumar. *Optical scattering properties of soft tissue: a discrete particle model*. Applied Optics 37(13), 2788-2797. 1998.
Ref Type: Generic

Shaevitz, J. W. & Fletcher, D. A. (2007). Enhanced three-dimensional deconvolution microscopy using a measured depth-varying point-spread function. *Journal of the Optical Society of America A-Optics Image Science and Vision* **24**, 2622-2627.

Shaw, P. J., Agard, D. A., Hiraoka, Y., & Sedat, J. W. (1989). Tilted View Reconstruction in Optical Microscopy - 3-Dimensional Reconstruction of Drosophila-Melanogaster Embryo Nuclei. *Biophysical Journal* **55**, 101-110.

Soeller, C. & Cannell, M. B. (1999). Examination of the transverse tubular system in living cardiac rat myocytes by 2-photon microscopy and digital image-processing techniques. *Circulation Research* **84**, 266-275.

Soeller, C., Crossman, D., Gilbert, R., & Cannell, M. B. (2007). Analysis of ryanodine receptor clusters in rat and human cardiac myocytes. *Proceedings of the National Academy of Sciences of the United States of America* **104**, 14958-14963.

Soeller, C., Jayasinghe, I. D., Li, P., Holden, A. V., & Cannell, M. B. (2009). Three-dimensional high-resolution imaging of cardiac proteins to construct models of intracellular Ca2+ signalling in rat ventricular myocytes. *Experimental Physiology* **94**, 496-508.

Strandman, C., Rosengren, L., Elderstig, H. G. A., & Backlund, Y. (1995). Fabrication of 45 degrees mirrors together with well-defined V-grooves using wet anisotropic etching of silicon. *Journal of Microelectromechanical Systems* **4**, 213-219.

Su, X. T., Singh, K., Rozmus, W., Backhouse, C., & Capjack, C. (2009). Light scattering characterization of mitochondrial aggregation in single cells. *Optics Express* **17**, 13381-13388.

Subbarao, M., Wei, T. C., & Surya, G. (1995). Focused Image Recovery from 2 Defocused Images Recorded with Different Camera Settings. *Ieee Transactions on Image Processing* **4**, 1613-1628.

Swedlow, J. R. & Platani, M. (2002). Live cell imaging using wide-field microscopy and deconvolution. *Cell Structure and Function* **27**, 335-341.

Tearney, G. J., Brezinski, M. E., Southern, J. F., Bouma, B. E., Hee, M. R., & Fujimoto, J. G. (1995). Determination of the Refractive-Index of Highly Scattering Human Tissue by Optical Coherence Tomography. *Optics Letters* **20**, 2258-2260.

Teh, W. H., Durig, U., Drechsler, U., Smith, C. G., & Guntherodt, H. J. (2005). Effect of low numerical-aperture femtosecond two-photon absorption on (SU-8) resist for ultrahigh-aspect-ratio microstereolithography. *Journal of Applied Physics* **97**.

Tellier, C. R. (1998). Anisotropic etching of silicon crystals in KOH solution - Part III - Experimental and theoretical shapes for 3D structures micro-machined in (hk0) plates. *Journal of Materials Science* **33**, 117-131.

Thompson, C. B., Galli, R. L., Melaragno, A. J., & Valeri, C. R. (1984). A Method for the Separation of Erythrocytes on the Basis of Size Using Counterflow Centrifugation. *American Journal of Hematology* **17**, 177-183.

Umemura, K. & Kimura, H. (2005). Determination of oxidized and reduced nicotinamide adenine dinucleotide in cell monolayers using a single extraction procedure and a spectrophotometric assay. *Analytical Biochemistry* **338**, 131-135.

Vorndran, C., Minta, A., & Poenie, M. (1995). New fluorescent calcium indicators designed for cytosolic retention or measuring calcium near membranes. *Biophysical Journal* **69**, 2112-2124.

Walsh, C. B. & Franses, E. I. (2003). Ultrathin PMMA films spin-coated from toluene solutions. *Thin Solid Films* **429**, 71-76.

Wang, E., Babbey, C. M., & Dunn, K. W. (2005). Performance comparison between the high-speed Yokogawa spinning disc confocal system and single-point scanning confocal systems. *Journal of Microscopy-Oxford* **218**, 148-159.

Wang, T. D., Mandella, M. J., Contag, C. H., & Kino, G. S. (2003). Dual-axis confocal microscope for high-resolution in vivo imaging. *Optics Letters* **28**, 414-416.

Wokosin, D. Objective lens selection within fluorescence microscopy. 2007.
Ref Type: Generic

Wokosin, D. L., Loughrey, C. M., & Smith, G. L. (2004). Characterization of a range of fura dyes with two-photon excitation. *Biophysical Journal* **86**, 1726-1738.

Xu, C. & Webb, W. W. (1996). Measurement of two-photon excitation cross sections of molecular fluorophores with data from 690 to 1050 nm. *Journal of the Optical Society of America B-Optical Physics* **13**, 481-491.

Yeh, Y. & Pinsky, B. G. (1983). Optical Polarization Properties of the Diffraction Spectra from Single Fibers of Skeletal-Muscle. *Biophysical Journal* **42**, 83-90.

Yoon, Y. K., Park, J. H., & Allen, M. G. (2006). Multidirectional UV lithography for complex 3-D MEMS structures. *Journal of Microelectromechanical Systems* **15**, 1121-1130.

Young I, J J.Gerbrands, & L J.van Vliet. Fundamentals of Image Processing. 1-112. 2010.
Ref Type: Generic

Young, P. A., Clendenon, S. G., Byars, J. M., & Dunn, K. W. (2011). The effects of refractive index heterogeneity within kidney tissue on multiphoton fluorescence excitation microscopy. *Journal of Microscopy* **242**, 148-156.